Doctoral theses at NTNU, 2020:82

Fabian Imanasa Azof

Pyrometallurgical and Hydrometallurgical Treatment of Calcium Aluminate-Containing Slags for Alumina Recovery

Doctoral thesis

NTNU
Norwegian University of Science and Technology
Thesis for the Degree of
Philosophiae Doctor
Faculty of Natural Sciences
Department of Materials Science and Engineering

NTNU
Norwegian University of
Science and Technology

Fabian Imanasa Azof

Pyrometallurgical and Hydrometallurgical Treatment of Calcium Aluminate-Containing Slags for Alumina Recovery

Thesis for the Degree of Philosophiae Doctor

Trondheim, May 2020

Norwegian University of Science and Technology
Faculty of Natural Sciences
Department of Materials Science and Engineering

NTNU
Norwegian University of
Science and Technology

NTNU
Norwegian University of Science and Technology

Thesis for the Degree of Philosophiae Doctor

Faculty of Natural Sciences
Department of Materials Science and Engineering

ISBN 978-82-326-4516-9 (printed ver.)
ISBN 978-82-326-4517-6 (electronic ver.)
ISSN 1503-8181

Doctoral theses at NTNU, 2020:82

Printed by NTNU Grafisk senter

Preface

This thesis is submitted to NTNU, the Norwegian University of Science and Technology, as partial fulfillment of the requirements for the degree of Philosophiae Doctor. The present work has been conducted at the Department of Materials Science and Engineering at the Norwegian University of Science and Technology (NTNU), Trondheim, Norway. A portion of the experimental work was carried out at the School of Mining and Metallurgical Engineering, National Technical University of Athens (NTUA), Athens, Greece.

The NTNU has funded the research and supported by the Research Domain – 5 Materials and the Society in SFI Metal Production (Project number 237738). The work also has been scientifically supported by ENSUREAL "Ensuring Zero Waste Production of Alumina in Europe," EU Horizon 2020.

The author has conducted all of the experimental works. Kai Tang (SINTEF) has carried out modeling works for $CaO–Al_2O_3–SiO_2$ phase diagrams. The electron probe microanalysis was carried out in collaboration with Morten Peder Raanes (NTNU). And Syverin Lierhagen (NTNU) has carried out the mass spectrometry analysis for pregnant solutions using an inductively coupled plasma.

Acknowledgments

First and foremost, my supervisor, Associate Professor Jafar Safarian. He has been available for me from the day one I came to Norway in February 2017. He has a clear direction and plan for my Ph.D. study. At the same time, he also leaves me a room to be independent with my experiments and makes sure that I get every necessary help, instrument, knowledge, and networks. Every discussion and supervisory meeting with him were always enjoyable, positive, and productive.

Also, I would thank my co-supervisors, Prof. Leiv Kolbeinsen, and Associate Professor Yongxiang Yang. Their lectures, ideas, and constructive comments during meetings and paper reviews have helped me to understand the hydrometallurgy process significantly better.

I would like to thank all administrative staff of the Department of Materials Science and Engineering, as well as the engineers: Dmitry Slizovskiy and Arman Hoseinpur Kermani for their assistance with my experimental works using the IF-75 instrument, Yingda Yu for his training and help with SEM analysis, Morten Peder Raanes for his help with EPMA analysis. Also, Syverin Lierhagen from the Department of Chemistry for his help with ICP-MS analysis.

My humble respect goes to Prof. Dimitrios Panias from the National Technical University of Athens (NTUA) for his kindness and openness on sharing his vast knowledge of alumina production. Moreover, I would like to acknowledge the help from one of his Ph.D. students, Michail Vafeias, who makes my days as a visiting researcher at NTUA so effective and pleasantly memorable.

I would also like to thank the staff from SINTEF Industry: Casper van der Eijk, Ingeborg Solheim, and Michal Ksiazek for their support and assistance with my works in ENSUREAL project, and Kai Tang for his thermodynamic calculations in CaO-Al_2O_3-SiO_2 systems at different atmospheres.

Thank you to my office mate and dear friends, Jian Meng Jiao and Are Bergin, of whom I spent my lunch and free time with for the last years. I would also like to thank my friends in the SiManTi group for all of the sharing, gatherings, and fun trips we had.

To my dear brothers from the Indonesian Moslem Community in Trondheim (KMIT), Gema Sakti Raspati, Dicky Harishidayat, Wahyu Wijanarko, and Saeful, jazakumullah khoiron katsiro. And the Indonesian Student Association in Trondheim

(PPIT) for their honest support and all of the cheerful activities that always make me feel like at home.

In the end, I would like to acknowledge my family, especially my mother, Murni Hayati, who mentions my name in her prayers every day and night, she is a superwoman and my living inspiration. And my wife, Putri Nurul Fadillah, who has been supporting me 101% from the beginning. She is the mother of my two charming sons, Arslan and Zhafran. Without her on my side, this journey would never be accomplished.

Abstract

In the present thesis, the pyrometallurgical and hydrometallurgical parts of the Pedersen process have been studied. The process can be seen as one of the most potent alternative methods to recover alumina from bauxite more sustainably than the well-known Bayer process. It does not produce bauxite residue (red mud) that has numerous issues concerning its disposal and environmental risk. It is also evidenced that low-grade bauxite ores, i.e., diasporic bauxite, high iron oxide contents, are not suitable in the conventional Bayer process. By using low-grade bauxite in the Bayer process, it generates more red mud, requiring extensive energy for high leaching temperatures, and accompanying lower alumina yield than high-grade ones. And it is a fact that the deposit of high-grade bauxite ores is limited to geological conditions.

In the pyrometallurgical part, the thermodynamics and characterization of calcium aluminate slags and pig iron produced from the smelting-reduction of low-grade bauxites have been studied. Coke and limestone were used to reduce the iron oxide and adjust the basicity of slag during smelting. It was observed that complete iron separation from bauxite was feasible through the smelting-reduction process, and up to 99.9 wt.%Fe was eliminated. Moreover, it was shown that silicon, titanium, and other elements partial separation from the Al_2O_3-containing slag occurred. The phase compositions and the distribution of elements between the metal and slag phases also provide information about the high-temperature behavior of the bauxite components during smelting-reduction. The phase composition of the obtained slag shows that the slag has leachable phases, i.e., $12CaO{\cdot}7Al_2O_3$ and $CaO{\cdot}Al_2O_3$, that are necessitated for the next leaching process in the Pedersen process.

Moreover, to investigate the stability of the $12CaO{\cdot}7Al_2O_3$ phase in a CaO–Al_2O_3 slag at room temperature, a synthesis of crystalline slags of the phase from a corresponding melt composition in different atmospheric conditions and different purities have been studied. Observations using a thermogravimetry coupled with differential thermal analysis showed that the dehydration of a zeolitic $12CaO{\cdot}7Al_2O_3$ phase occurs at 770 – 1390 °C before it congruently melts at 1450 °C. X-ray diffraction (XRD) pattern of the slag showed that a single $12CaO{\cdot}7Al_2O_3$ phase is produced from a mixture, which has small SiO_2 impurity with 49:51 mass ratio of CaO to Al_2O_3. Scanning electron microscope (SEM) and electron probe micro-analyzer (EPMA) results show that a minor Ca-Al-Si-O-containing phase is in equilibrium with a grain-less

$12CaO \cdot 7Al_2O_3$ phase. The $12CaO \cdot 7Al_2O_3$ phase is unstable at room temperature when the high purity molten slag is solidified under oxidizing conditions, contained in an alumina crucible.

On the other hand, a high-temperature in-situ Raman spectroscopy of a slag that was made of higher purity $CaO–Al_2O_3$ mixture showed that $5CaO \cdot 3Al_2O_3$ phase is an unstable/intermediate phase in the $CaO\text{-}Al_2O_3$ system, which is decomposed to $12CaO \cdot 7Al_2O_3$ above 1100 °C upon heating in oxidizing conditions. It is proposed that low concentrations of silicon stabilize $12CaO \cdot 7Al_2O_3$ (or also known as mayenite mineral), in which silicon is a solid solution in its lattice, which is named Si-mayenite. Regarding the calculated $CaO\text{-}Al_2O_3\text{-}SiO_2$ diagram in the study, this phase may contain a maximum of 4.7 wt.%SiO_2, which is depending on the total SiO_2 in the system and the Ca/Al ratio.

In the hydrometallurgical part, the leaching characteristics and mechanism of synthetic $CaO\text{-}Al_2O_3$ slags in alkaline solution at atmospheric pressure have been studied. The purpose of the study was to have a better understanding of the leaching part of the Pedersen process. The crystalline slags containing $CaO \cdot Al_2O_3$, $3CaO \cdot Al_2O_3$, $CaO \cdot 2Al_2O_3$, and $12CaO \cdot 7Al_2O_3$ phases, and leaching residues (predominantly $CaCO_3$) are characterized by XRD and semi-quantitative analysis. Of the leaching characteristics in a solution containing 120 g/L Na_2CO_3, the slag with the highest amount of $12CaO \cdot 7Al_2O_3$ phase is the most leachable one in the $CaO\text{-}Al_2O_3$ system with about 95% of alumina extraction. The leaching extent is confirmed by employing Inductively Coupled Plasma-High Resolution-Mass Spectrometer (ICP-HR-MS) analysis, and it decreases by 0.4% for every percent of the bayerite ($Al(OH)_3$) formation during the leaching. The less stable form of $CaCO_3$, i.e., vaterite, is formed over the leached slag particles that consist 33 – 49 wt% CaO. At the same time, $3CaO \cdot Al_2O_3 \cdot 6H_2O$, a hydrogarnet phase, precipitated at relatively low concentrations (< 6 wt%) in all residue. The non-bridging oxygen (NBO) over tetrahedral structure (T) index shows that the atomic structure may affect the leaching extent of the slags, the lower NBO/T index of the phase is the more difficult for the phase to leach or depolymerize. However, the $12CaO \cdot 7Al_2O_3$ phase is an exceptional case where it has “free” O-ions at the center of the cage structure, which makes it easily depolymerize. Therefore, the NBO/T index for the $12CaO \cdot 7Al_2O_3$ phase becomes irrelevant. Furthermore, the morphology and size evolution of the obtained residue measured with a laser particle analyzer indicates the agglomeration behavior of the residue particles during the leaching process.

In an investigation on leaching kinetics and mechanism, the highest alumina recovery up to 90.5 % is obtained after the slag is leached by 10 wt.% Na_2CO_3 solution, at low temperatures (30 – 45 °C) within 90 min. It is shown that the rate of alumina recovery is high at the beginning of leaching and is then slow down due to the calcite layer product nucleation and growth at the surface of slag. The wet-grinding leaching and vigorous stirring increase the possibility of the collision between both particles and the stirrer that breaks the calcite layer, yielding less residue agglomeration and better recovery compared to the slow and mild agitations. A surface observation of the slag using electron microscopy shows that the calcite starts to nucleate at the unleachable phase as the best deposition site, which has the least mass transfer barrier in the system. The apparent activation energy of the leaching reaction is calculated as 10.8 – 19.9 kJ/mol, which indicates the reaction is diffusion rate-limited as revealed by the applied kinetic models.

List of Papers

This thesis is based on the following papers, which were submitted and published in peer-reviewed scientific journals or conferences. The list is in chronological order from the most recent work.

Peer-reviewed journal papers:

1. Azof, F. I., Tang, K., You, J., and Safarian, J. *Synthesis and characterization of $12CaO{\cdot}7Al_2O_3$ slags: the effects of impurities and atmospheres on the phase relations*. Submitted to a journal.
   Author contributions:
   Azof: methodology, experimental work, analysis, writing – original
   Tang: modeling work, analysis
   You: experimental work
   Safarian: conceptualization, analysis, writing – review, and editing

2. Azof, F.I., and Safarian, J. *Leaching kinetics and mechanism of slag produced from smelting-reduction of bauxite for alumina recovery*. Submitted to a journal.
   Author contributions:
   Azof: methodology, experimental work, analysis, writing – original
   Safarian: conceptualization, analysis, writing – review, and editing

3. Azof, F.I., Vafeias, M., Panias, D., and Safarian, J., 2020. *The leachability of a ternary CaO-Al_2O_3-SiO_2 slag produced from the smelting-reduction of low-grade bauxite for alumina recovery*. Hydrometallurgy, 191, pp. 105184.
   DOI: 10.1016/j.hydromet.2019.105184
   Author contributions:
   Azof: methodology, experimental work, analysis, writing – original
   Vafeias: analysis, writing – review, and editing
   Panias: analysis, writing – review, and editing
   Safarian: conceptualization, analysis, writing – review, and editing

4. Azof, F.I., Kolbeinsen, L., and Safarian, J., 2018. *Characteristics of calcium-aluminate slags and pig iron produced from the smelting-reduction of low-grade bauxites*. Metallurgical and Materials Transactions B, 49(5), pp. 2400-2420.
   DOI: 10.1007/s11663-018-1353-1
   Author contributions:
   Azof: methodology, experimental work, analysis, writing – original
   Kolbeinsen: analysis, writing – review, and editing
   Safarian: conceptualization, analysis, writing – review, and editing

5. Azof, F.I., Yang, Y., Panias, D., Kolbeinsen, L., and Safarian, J., 2019. *Leaching characteristics and mechanism of the synthetic calcium-aluminate slags for alumina recovery*. Hydrometallurgy, 185, pp. 273-290.
   DOI: 10.1016/j.hydromet.2019.03.006
   Author contributions:
   Azof: methodology, experimental work, analysis, writing – original
   Yang: analysis, writing – review, and editing
   Panias: analysis, writing – review, and editing
   Kolbeinsen: analysis, writing – review, and editing
   Safarian: conceptualization, analysis, writing – review, and editing

Peer-reviewed conference papers:

1. Azof, F.I., Kolbeinsen, L., and Safarian, J., 2019. *Kinetics of the leaching of alumina-containing slag for alumina recovery*. In European Metallurgical Conference 2019, GDMB Verlag GmbH Germany, June, pp. 511-526.
   Author contributions:
   Azof: methodology, experimental work, analysis, writing – original
   Kolbeinsen: analysis, writing – review, and editing
   Safarian: conceptualization, analysis, writing – review, and editing

2. Azof, F.I., Safarian, J., and Kolbeinsen, L., 2017. *The leachability of calcium aluminate phases in slags for the extraction of alumina*. In Travaux 46, Proceedings of 35th International ICSOBA Conference, 42, pp. 243 – 253.
   Author contributions:
   Azof: methodology, experimental work, analysis, writing – original
   Safarian: conceptualization, analysis, writing – review, and editing
   Kolbeinsen: analysis, writing – review, and editing

Table of Contents

List of Figures

List of Tables

Chapter 1

Introduction

Brief information and challenges concerning the use of bauxite as one of the sources to produce metallurgical grade alumina are presented. This chapter also shows the motivation behind the investigation and scope of work of the thesis.

1.1 Bauxite, as a source of alumina

According to data statistics from The International Aluminum Institute [1], the total amount of metallurgical grade alumina (hereafter named as alumina) in the world has been exceeding more than 1 billion metric tons for the past ten years. Safarian and Kolbeinsen [2] reported that the annual production of alumina is 120 million tons in 2016, and the number goes up as the demand from the aluminum industry unceasingly increases. Almost 90% of alumina produced in the world is used as a raw material to produce Aluminum. Aluminum is considered one of the most sustainable materials in the current society due to its attractive properties, i.e., high strength and durability, completely recyclable, and lightweight material.

Alumina can be found in many potential sources in nature, i.e., bauxite, coal ash, steelmaking slag, clay, etc. However, producing alumina from bauxite through the well-known Bayer process is the most common route in alumina industries due to the enormous reserve of bauxite and viable of the process. More details about the Bayer process will be described later in chapter 2, in the literature review. Moreover, it was reported that there are more than 27 billion tons of bauxite reserves in 2011 with Guinea, Australia, Brazil, Vietnam, and Jamaica are holding over 70% of the reserves [3].

The bauxite ore was discovered in 1821 by a professor at the School of Mines in Paris, Pierre Berthier (1782 – 1861), while he was sourcing iron ores in the southern part of France [4]. Berthier thought it was an iron ore as the dark reddish-brown color looks that the bauxite ore has, which is relatively similar to the color of iron ore. However, it was observed that the ore has a high content of alumina. The name of bauxite is derived after the village of Les Beaux, where he discovered the ore. In literature [5],

bauxite is regarded as an ore that is produced from Al-Fe-Si containing parent rocks with an exception that the Al content is relatively high up to 60 wt.%.

Bauxite deposits are primarily divided into two groups according to their host rock, which are laterite and karst bauxites. Lateritic bauxite mostly found in equatorial regions and is formed by laterization/weathering under the intense wet and warm condition of silicate rocks, e.g., granite and gneiss, and mafic rocks that are rich in magnesium and iron oxides [6]. On the other hand, karst bauxites are formed by weathering processes that occur upon carbonate rocks such as limestone and dolomite [7], where the deposit occurrence is known preferentially in Europe and Northern Asia [8,9]. These two type-bauxites, however, have different mineralogical compositions that eventually affect the efficacy of alumina recovery extent after a digestion treatment. Lateritic bauxite is dominated by gibbsite, which is considerably easy to digest in the Bayer process, whereas karst bauxite has a high amount of boehmite and diaspore, which are more challenging to digest [8,10]. **Table 1.1** shows an approximate mineralogical composition of lateritic and karst bauxites, as reported by Smith [9].

Table 1.1
Mineralogical compositions of lateritic and karst bauxites [9]

Constituent	Lateritic bauxite	Karst bauxite
Al_2O_3	gibbsite, boehmite	boehmite, diaspore
SiO_2	kaolinite, quartz	kaolinite, quartz, chamosite, illite
Fe_2O_3	goethite, hematite	hematite, goethite, maghemite, magnetite
TiO_2	anatase, rutile	anatase, rutile, ilmenite
CaO	calcite, apatite, crandallite	calcite, apatite, crandallite

As mentioned previously, a different source of bauxite deposits may give different results on the Bayer digestion yields, which means the economic feasibility of the process is also dependent on the minerals that constitute the bauxite. This is one of the disadvantages of the process. On the other hand, intensive exploitation of preferable sites of bauxite deposits questions the sustainability of bauxite mining activities in those particular areas. As a reference, a summary of the quantitative phase analysis for bauxites taken from several locations is shown in **Table 1.2** after Gan et al. [10].

Table 1.2
A summary of the quantitative phases analysis of bauxites taken from several locations [10]

Mineral	Chemical formula	Wt. %			
		Jamaican	Australian	North European	Vietnamese
Gibbsite	$Al(OH)_3$	49.3	53.3	NA	70.6
Boehmite	γ-Al(O(OH)	1.3	13.9	42.3	0.1
Diaspore	α-AlO(OH)	NA	0.1	1.6	NA
Goethite	FeOOH	25.1	1.2	3.4	14.7
Hematite	Fe_2O_3	0.6	7.8	12.4	2.4
Anatase	TiO_2	1.6	2.4	0.5	0.7
Rutile	TiO_2	1.5	2.1	0.2	0.9
Quartz	SiO_2	0.1	3.3	0.5	0.1
Kaolinite	$Al_2Si_2O_5(OH)_4$	0.4	6.1	0.8	8.1
Ilmenite	$FeTiO_3$	0.5	NA	NA	1.9
Magnetite	Fe_3O4	0.2	NA	0.2	0.2
Crandalllite	$Ca_{1.002}P_2Al_3O_{14}$	3.9	NA	NA	NA
Larnite	$Ca_2(SiO_4)$	NA	NA	0.1	NA
Chamosite	$(Mg_{2.518}Fe_{2.482})(Al_{1.2}Si_{3.8})O_{18}$	NA	NA	14.4	NA
Muscovite	$KAl_2(Si_3Al)O_{10}(OH)_2$	NA	NA	3.9	NA
Illite	$KAl_2(Si_3Al)O_{10}(OH)_2H_2O$	NA	0.5	NA	NA
Nahcolite	$NaHCO_3$	NA	2.9	NA	NA
Dozyite	$Mg_3Si_2O_9$	NA	NA	0.6	NA
Sodalite	$Na_8Al_6Si_6O_{24}(OH)_2$	NA	NA	0.1	NA
Calcite	$CaCO_3$	NA	NA -	0.1	NA
Dawsonite	$NaAlCO_3(OH)_2$	NA	NA	0.2	NA
Hollandite	$KAlSi_3O_8$	NA	NA	NA	NA
Sum		84.5	93.5	81.3	100.0
100-Sum*		15.5	6.5	18.7	0.0

*(100-Sum) includes amorphous and undetected phase(s)

Furthermore, schematic diagrams of bauxite composition according to their mineralogy in a typical laterite ore are shown in **Fig. 1.1(a) – (b)** after Aleva [5]. **Fig. 1.1(a)** shows the tetrahedron composition of laterite ore with Al_2O_3, SiO_2, Fe_2O_3, and H_2O at each axis, where a green triangle indicates the position of gibbsite, kaolinite, and hematite that are attributed to bauxite ore. Meanwhile, **Fig. 1.1(b)** shows the compositional diagram of the green triangle in **Fig. 1.1(a)**. As seen on the diagram, a bauxite ore may have bauxitic, kaolinitic, or ferruginous properties, depending on its $Al_2O_3/(SiO_2+Fe_2O_3)$ mass ratios.

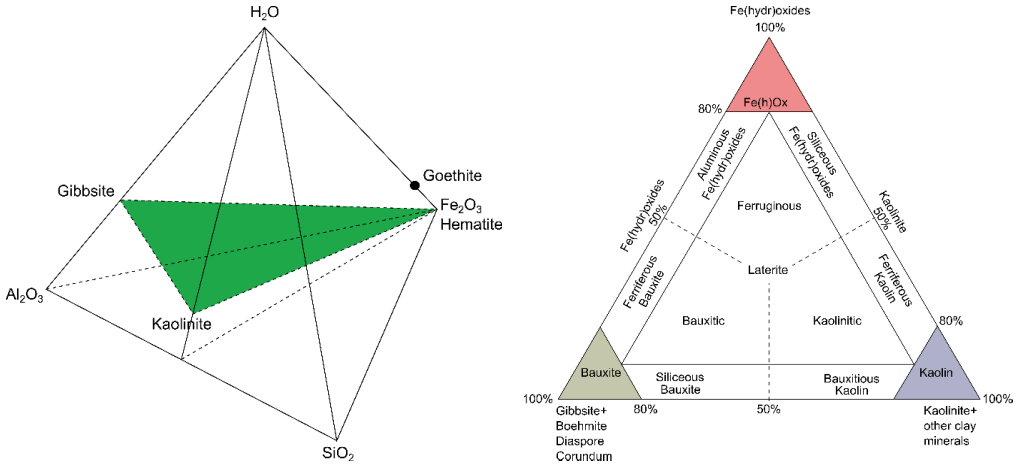

Fig. 1.1 (a) Tetrahedron composition of laterite ore with Al_2O_3, SiO_2, Fe_2O_3, and H_2O at each axis. (b) Equilateral triangle of the ternary compositional diagram of the green area in Fig. 1.1(a).

Of various chemical properties of the bauxite, the one that has a relatively high Fe_2O_3 content (ferriferous/ferruginous bauxite) becomes the main object of investigation of the current study. This is due to the respected compound that is hardly digested in the Bayer process that leads to massive accumulation of bauxite residue (also known as red mud) in alumina refineries. The red mud has low added value and numerous disposal and environmental issues.

1.2 Bauxite residue (red mud) issues

Red mud is a solid waste residue of the digestion of bauxite ores with NaOH for alumina production in the Bayer process. In 2016, more than 150 million tons of red mud was produced annually [11,12]. In the Bayer process, the global average for the production of red mud per tonne of alumina is 1 – 1.5 tons [12]. According to the commission decision of the European Parliament and of the Council in 2014 [13], red mud is identified as either a mirror hazardous (MH) or a mirror non-hazardous (MNH) entries. On technical guidance of the classification of waste [14], mirror entries are defined as two or more related entries where one is hazardous, and the other is not. Red mud can be classified as an MH or hazardous waste (code number 01-03-10*) when it contains substances that exceed to some extents, so that the red mud has following

properties, but not limited to: explosive, oxidizing, flammable, irritant, aspiration and/or acute toxicity, carcinogenic, corrosive, and releasing acute toxic gas. Whereas, it is classified as an MNH entry or a non-hazardous waste (code number 01-03-09) when it does not have hazardous substances as mentioned before.

Red mud has a relatively small particle size, high alkalinity, and a considerable amount of production annually creates a significant problem for the disposal as well as the environment [15]. Notably, several accidents regarding the handling and storage of the red mud, as shown in **Fig. 1.2** raise public awareness, questioning the sustainability and environmental footprint of alumina industries more than before.

(a) (b)

Fig. 1.2 Aerial images of (a) Red mud dam failure in Hungary in 2010 that causes casualties and injuries to residents nearby and ca. 40 km^2 land affected by alkaline and caustic substance [16], (b) Red mud dam failure in Henan province, China, in 2016, the dam held ca. 2 million m^3 of red mud [17].

On the other hand, the red mud deposit has been seen as a potential resource of byproducts that can be valorized and transformed into a valuable raw material. In the last decade, researches employing red mud as a binder in a cement-making process [18] as a source of inorganic polymers [19], refractory metals [20], rare earth elements (REE) [21], and other potential valorizations. Unfortunately, many of the researches and pilot-scale experiments are not successfully upscaled to an industrial process due to the feasibility or economic reasons.

1.3 Motivation

The environmental risk mentioned above has driven me to seek and study an alternative process for alumina recovery from bauxite ores that could potentially yield zero amount or significantly reduce the amount of red mud. There has been no alumina produced commercially without yielding red mud since the invention of the Bayer process. It was until a combination of the pyro-hydrometallurgical process that was patented by Harald Pedersen in 1927 [22]. The process is also known as the Pedersen process. It is shown that the process can separate Al and Fe-containing materials from the bauxite through a smelting-reduction reaction, and CO_2 gas generated from the reaction can be utilized in the precipitation of alumina. No red mud is produced in every stage of the process. The process allows the industry to highly recovers alumina and iron oxides and has a low environmental footprint at the same time. Also, the Pedersen process produces non-hazardous leaching residue (hereafter named as grey mud) that can be potentially used as a flux in fertilizer and REE source. However, literature regarding the process was very few due to the confidentiality of unpublished reports and the limitation of instruments at that time, which motivates me to fill in the gap of knowledge.

1.4 Scope of the thesis

The alumina recovery from alumina-containing materials employing the original or modification of the Pedersen process has been reported by several researchers. Most of the publications related to the process are about the leaching characteristics of calcium aluminate slags produced by smelting reduction of bauxites in sodium carbonate (Na_2CO_3) solutions. Unfortunately, there was little information available regarding the leaching treatment and other aspects of the process in the literature that stands as the basis of the observation and also the scope of the current study, which includes:

1. Thermodynamic study of the smelting and leaching process,
2. Characteristics of slags produced from the smelting-reduction treatment of bauxite,
3. Elemental composition and concentrations of the leachate produced from the leaching treatment,
4. Microstructure and morphology of slags and grey mud, and

5. The leaching kinetics and mechanism, and the effect of different leaching conditions to alumina recovery extent

The current thesis is divided into six chapters. Chapter 1 comprises the background, objectives, and scope of the thesis. Chapter 2 consists of an overview concerning the history of alumina production, the introduction of various bauxite processing for alumina recovery that is highlighted in the Pedersen process. Chapters 3 and 4 contain summaries, methodologies, and theoretical background of the published and/or submitted manuscripts that are classified into pyrometallurgical and leaching part of the Pedersen process, respectively. Chapter 5 is the research conclusion and future works. Chapter 6 contains a copy of peer-reviewed publications and a draft of submitted articles.

Chapter 2

An Overview of Alumina Production

The production of alumina from bauxite has been rooted in mankind's history for more than 150 years. In this chapter, the origin of alumina production before the invention of the Bayer process, the sustainability as well as the challenges of the Bayer process, and also several alternative processes that include the Pedersen process are presented.

2.1 Development of alumina production in the early years

Following the discovery of bauxite in 1821, Louis Le Chatelier (1815 – 1873), a chief inspector of mines in France, invented a process to recover $Al(OH)_3$ from bauxite in 1855 [4]. At that time, $Al(OH)_3$ was used in textile industries as a mordant for dyeing cotton, wool, and silk. The Le Chatelier process consists of pyro- and hydrometallurgical treatment. The bauxite is sintered at about 1000 °C with Na_2CO_3, which is subsequently followed by water leaching and CO_2 precipitation on the produced pregnant liquor. It was known that the CO_2 gas was taken from the gas generated by the calcination step of $Al(OH)_3$ [4]. The $Al(OH)_3$ is then obtained after the filtration stage, while Na_2CO_3 can be reused in the process after evaporating the spent liquor. Furthermore, in 1888, the process was then modified by an Austrian chemist, Karl Josef Bayer (1847 – 1904). Bayer introduced the use of a fresh precipitate of $Al(OH)_3$ in the pregnant liquor to substitute the use of CO_2 gas during the precipitation [23]. The suitable method was documented as having a pure product, and it was easily filtered and washed [24]. Both Le Chatelier and its modified process are shown schematically in **Fig. 2.1(a)** and **2.1(b)**, respectively.

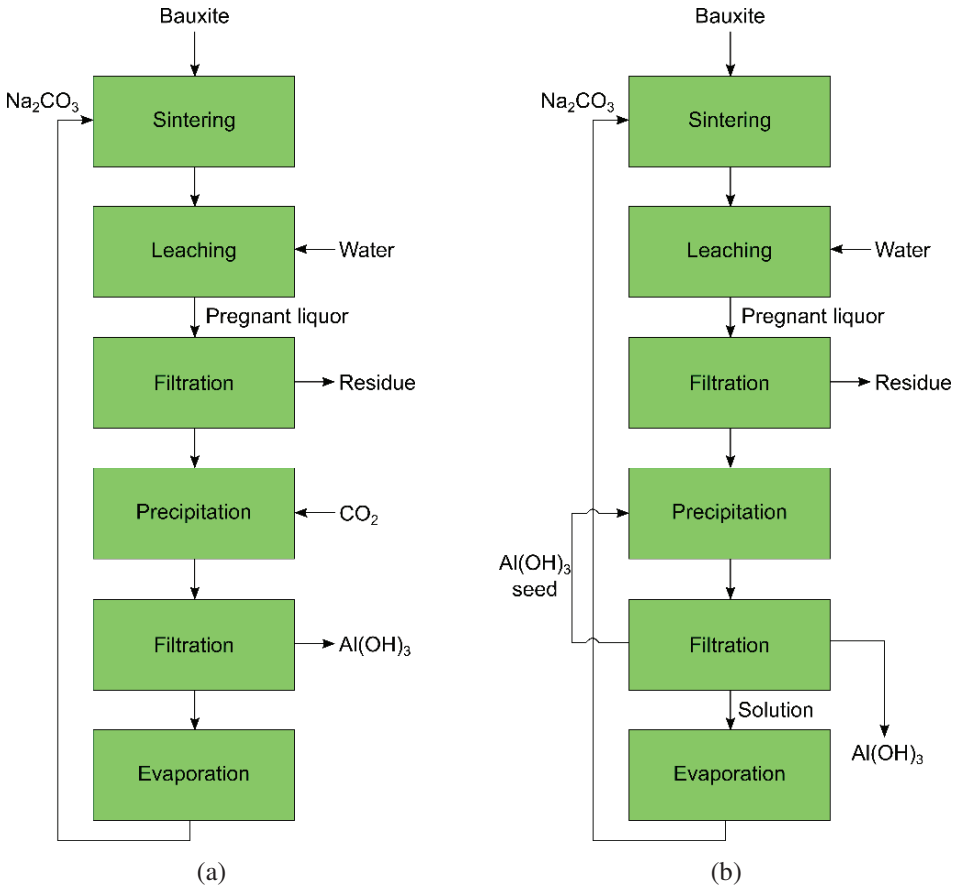

Fig. 2.1 Process flow of $Al(OH)_3$ recovery from bauxite with pyro- and hydrometallurgical route, which was invented by (a) Louis Le Chatelier in 1855, and (b) Karl Josef Bayer in 1888 that was adapted from the Chatelier process.

2.2 Modern Bayer process

The revolution of the alumina industry begins after the development of a fully hydrometallurgical route on alumina recovery by Karl Josef Bayer in 1892, four years after his modification on the Chatelier process. Instead of sintering bauxite at elevated temperatures, Bayer used a pressurized reactor, or as known as an autoclave, to leach the bauxite directly in a NaOH solution, as illustrated in **Fig. 2.2**. Bayer also introduced precipitation tanks for $Al(OH)_3$ seeding. The process is then known as the Bayer process and has been implemented for more than 100 years in most of the alumina industries in

the world without significant changes. In the US patent number 515895 [25], the Bayer process is performed by digesting bauxite with NaOH at 3 – 4 atm within 160 – 170 °C.

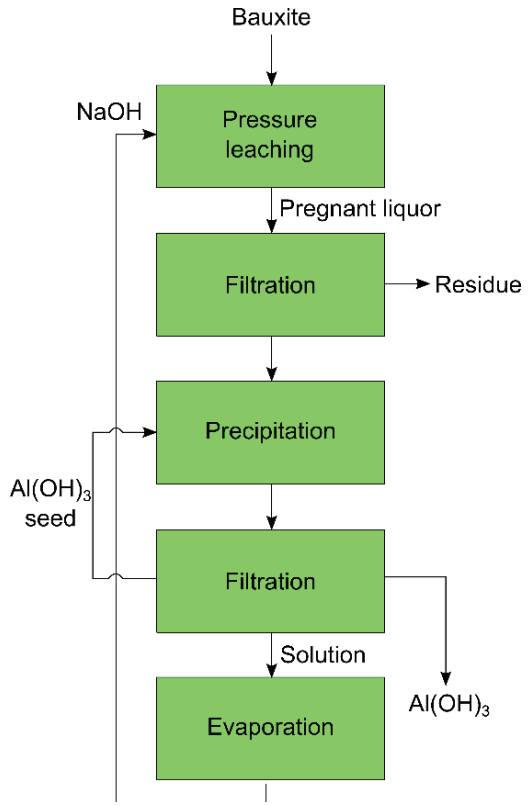

Fig. 2.2 A simplified process flow of the Bayer process that was invented by Karl Josef Bayer in 1892.

The Bayer process can be divided into three steps. The first step is the pressure leaching of bauxite by NaOH to obtain a sodium aluminate solution in its unhydrated ($NaAlO_2$) or hydrated ($NaAl(OH)_4$) phase. The second step is the precipitation of pure $Al(OH)_3$ produced by seeding the solution with fine crystals of $Al(OH)_3$ in vigorous agitation. And the final step is the calcination, in which the $Al(OH)_3$ is calcined, and pure alumina is produced. The reactions of every step can be described as follow:

a) Pressure leaching of bauxite and NaOH

Depending on the type of bauxites, leaching reactions between NaOH and bauxite can be written as in **reactions (2.1)** and **(2.2)**. Gibbsitic bauxite is normally digested at around 150 °C, while boehmitic and diasporic bauxite are treated at around 250 °C or higher [26].

Gibbsite-type bauxite: $Al(OH)_{3(s)} + NaOH_{(aq)} = NaAl(OH)_{4(aq)}$ (2.1)

Boehmite-type bauxite: $AlO(OH)_{(s)} + NaOH_{(aq)} + H_2O_{(l)} = NaAl(OH)_{4(aq)}$ (2.2)

The insoluble species that left during leaching are separated in a clarifier and regarded as a residue (red mud).

b) Precipitation of $Al(OH)_3$

The pregnant liquor of sodium aluminate then introduced with fine $Al(OH)_3$ as a seed to precipitate the crystal of $Al(OH)_3$ and reproduce NaOH that can be reused for another cycle of leaching step as in **reaction (2.3)**.

$$NaAl(OH)_{4(aq)} = Al(OH)_{3(s)} + NaOH_{(aq)} \quad (2.3)$$

Based on the change of Gibbs free energy calculated by using HSC™ ver. 9, a thermochemical software, the precipitation of $Al(OH)_3$ is favored at temperatures lower than 200 °C, as shown in **Fig. 2.3**.

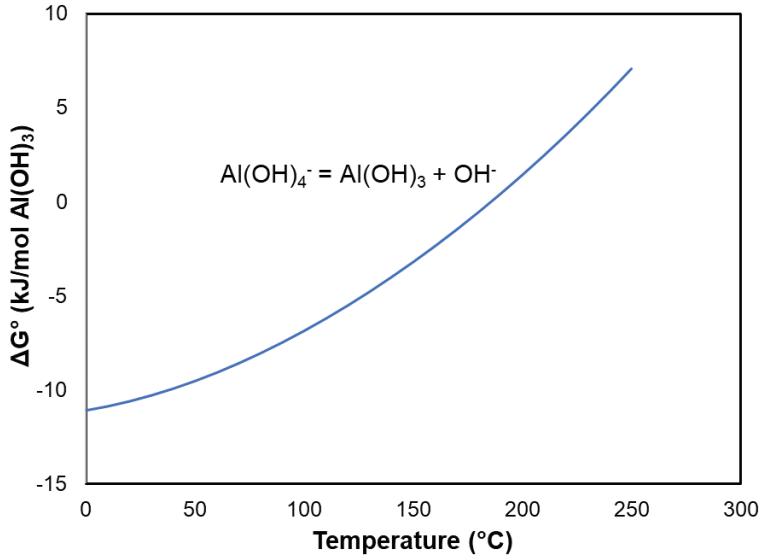

Fig. 2.3 The change of Gibbs free energy formation of $Al(OH)_3$ from soluble $Al(OH)_4^-$ at different temperatures

Concerning the size of precipitates, generally, primary aluminum manufacturer prefers a coarse size of $Al(OH)_3$ and only a small quantity (< 5 wt.%) of $Al(OH)_3$ with less than 44 μm (mesh -325) is allowed and acceptable to be consumed by the electrolytic cell in the Hall-Heroult process due to the dusting phenomenon [27].

c) Calcination

The final step of the Bayer process is the calcination of produced $Al(OH)_3$ at elevated temperatures between 950 – 1100 °C. At this step, pure alumina is obtained, as shown in **reaction (2.4)**.

$$2Al(OH)_{3(s)} = Al_2O_{3(s)} + 3H_2O_{(l)} \quad (2.4)$$

Smelter or metallurgical-grade alumina is the name given when the produced alumina is used as a raw material to manufacture aluminum. A typical composition of smelter-grade alumina produced from the Bayer process is shown in **Table 2.1** [28]. The alumina contains an α-Al_2O_3 phase that ranges from 2 – 30% [28], and it is more thermodynamically stable than a γ-Al_2O_3 phase. The α-Al_2O_3 phase may create a practical problem in the Hall-Heroult process production as it tends to settle underneath the metal pad of the pots and form "sludge" or "muck" due to its low solubility [29]. To a certain extent, it may also weaken the pot crust and making it more challenging to keep the pot sealed. Therefore, alumina that contains less than 10 wt.% of the α-Al_2O_3 phase is favorable by most smelting industries [29].

Table 2.1
Typical composition of smelter-grade alumina produced from the Bayer process [28]

Constituents	Mass fraction (wt.%)
Al_2O_3	99.3 – 99.7
Na_2O	0.3 – 0.5
SiO_2	5×10^{-3} – 25×10^{-3}
CaO	< 5×10^{-3} – 40×10^{-3}
Fe_2O_3	5×10^{-3} – 20×10^{-3}
TiO_2	1×10^{-3} – 8×10^{-3}
ZnO	< 1×10^{-3} – 10×10^{-3}
P_2O_5	< 1×10^{-4} – 15×10^{-4}
Ga_2O_3	5×10^{-3} – 15×10^{-3}
V_2O_5	< 1×10^{-3} – 3×10^{-3}
SO_3	< 5×10^{-2} – 20×10^{-2}

2.3 Challenges in the Bayer process

Several main challenges can be noted here of which the Bayer process has been dealing with in many years.

2.3.1 Environmental and ecological risk

As mentioned previously in **section 1.2**, red mud disposal is one of the significant problems in the aluminum industries. At the moment, the safest and most practical method to store and handle the red mud is by filter-press technology [30]. However, when it comes to the valorization, significant challenges remain to exist due to [30]:

1) Technical parameters, e.g., soda and Cr contents, moisture level,
2) Legislative (difficulties on waste transportation or cross border permit),
3) Financial challenges, no incentives given to cement plant or other industries for utilizing red mud or similar wastes
4) Social challenges, protests from the local societies against plants that use red mud as one of their raw materials

On the other hand, it was stated in literature [31] that aluminum industry may be considered as one of the primary sources of the increasing natural radioactivity and toxic elements in the environment due to its large areal requirements for red mud disposal storage. A result of red mud composition, which includes toxic elements from one of the aluminum plants in Turkey, is shown in **Table 2.2** [31].

Table 2.2
The concentration of several elements in a red mud from an aluminum plant in Turkey [31]

Major elements	Wt.%	Significant trace elements	ppm	Minor trace elements	ppm
Iron (Fe)	52	Arsenic (As)	63 ± 0.6	Antimony (Sb)	4.1 ± 0.1
Aluminum (Al)	25	Cerium (Ce)	514 ± 52	Caesium (Cs)	11 ± 0.5
Sodium (Na)	14	Chromium (Cr)	567 ± 23	Cobalt (Co)	43 ± 0.7
Calcium (Ca)	2	Lanthanum (La)	192 ± 11	Dysprosium (Dy)	24 ± 1
Titanium (Ti)	6	Manganese (Mn)	231 ± 9	Europium (Eu)	10 ± 2
		Nickel (Ni)	532 ± 50	Gallium (Ga)	18 ± 2
		Neodynium (Nd)	204 ± 28	Hafnium (Hf)	27 ± 0.6
		Scandium (Sc)	110 ± 0.7	Indium (In)	1.0 ± 0.01
		Thorium (Th)	95 ± 5	Rubidium (Rb)	13 ± 3
		Uranium (U)	52 ± 0.8	Samarium (Sm)	40 ± 2
		Vanadium (V)	325 ± 11	Tantalum (Ta)	5 ± 2
		Zircon (Zr)	1150 ± 226	Terbium (Tb)	5 ± 0.8
				Tungsten (W)	4.4 ± 0.2
				Ytterbium (Yb)	20 ± 5

Based on an investigation by Ozden et al. [31] regarding the potential of ecological risk of the red mud shown above is among toxic metals, Arsenic (As) has the highest ecological risk factor, which is in the range of moderate potential ecological risk. The decreasing order of potential ecological risk is As > Ni > Cr > Mn > Co. It is, therefore, a marine discharge or improper disposal of red mud led to a risk of metallic pollution in the ecosystem.

2.3.2 Energy and exergy intensive

According to the literature [32], the world's average on alumina refining energy consumption was 11.4 GJ/ton in 2016. The value was varied between 9 – 11 GJ/ton at low-temperature refineries and 9 – 14 GJ/ton at high-temperature refineries [33], whereas in other reports the range may occur around 6.5 – 33 GJ/ton [32] and 7 – 21 GJ/ton alumina [34]. Theoretically, the minimum energy required for the main steps in the Bayer process is relatively low, which is shown in **Table 2.3**.

Table 2.3
Theoretical energy requirement on the main steps of the Bayer process

Steps	Energy required (GJ/ton Al_2O_3)	Reference
Gibbsite-digestion at 25 °C	0.66	[35]
Boehmite-digestion at 25 °C	0.44	[35]
NaOH and bauxite slurry heating during digestion*	1.5	[36]
Evaporation of spent liquor*	0.5	[36]
Calcination (dry gibbsite)	1.9	[37]
Total	4.4	

**Based on the practical assumption*

The gap between theoretical and actual energy consumption in the Bayer process due to several factors: 1) the need of pre-existing thermal requirement for the digestion reaction takes place, e.g., an effective dissolution of gibbsite or boehmite require relatively high temperatures of slurry [34], (2) heat losses due to process and limitations of heat transfer and exchanger equipment [36,38]. Furthermore, in regards to the exergy consumption, Balomenos et al. [39] claimed that the Bayer process has an exergy efficiency of only 2.94% as schematically shown in **Fig. 2.4**. Balomenos suggested that the inefficiency is the result of a cyclic chemical process designed in the Bayer process to separate gibbsite from bauxite, and also a series of reactions that produces alumina and unutilized red mud in a practically 1:1 mass ratio.

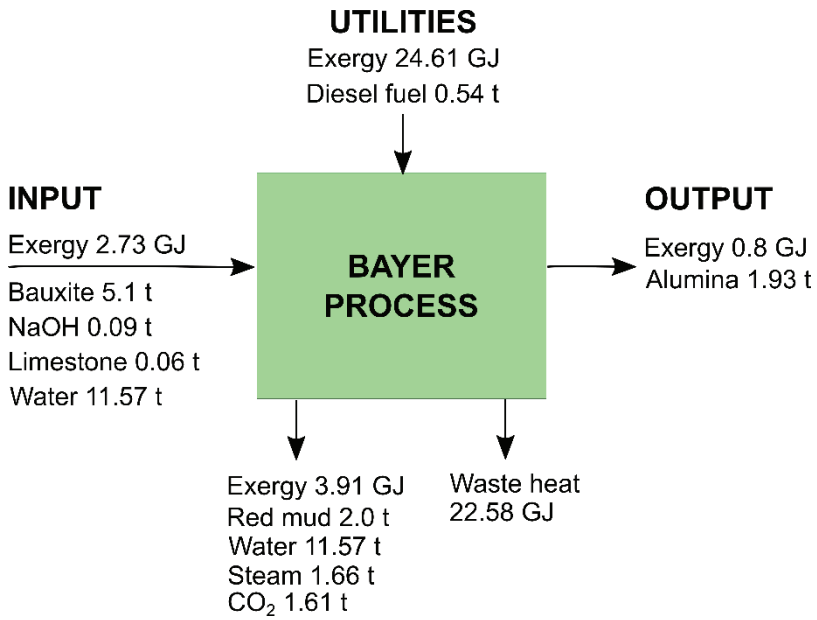

Fig. 2.4 A schematic exergy flow of the Bayer process with a coal-based electricity adapted after Balomenos et al. [39].

2.3.3 Mineralogy-dependent process

Iron and silicon are two dominant fraction elements in bauxite ores after aluminum. Therefore, it is necessary to evaluate the behavior of these two elements under the digestion step in the Bayer process. Also, bauxite ore may contain organic material, e.g., carbon, and other trace elements that may partially or entirely be dissolved in the digestion step.

2.3.3.1 Iron- and silicon-bearing minerals

Hematite (Fe_2O_3) and aluminum goethite (α-$(Fe, Al)_2O_3 \cdot H_2O$) are the majority of iron minerals in tropical bauxites, which are inert under low-temperature digestion conditions [28]. The insoluble phase of slurry is, therefore, separated in a clarifier and then practically discharged into a pond or any means of disposal storage, which leads to the situations mentioned previously in **section 2.3.1**. On the other hand, it is unlikely to always source a high-quality bauxite ore with low iron-bearing minerals due to the availability and cost-wise.

Moreover, it was reported [9] that the main reactions of the Bayer process are less effective if bauxite has Al_2O_3/SiO_2 mass ratio < 6.25 or has a reactive silica content higher than 8 wt.%. Silicate minerals, particularly kaolinite, react with NaOH at low temperatures as in **reaction (2.5)**.

$$3Al_2Si_2O_5(OH)_{4(s)} + 18NaOH_{(aq)} = 6Na_2SiO_{3(aq)} + 6NaAl(OH)_{4(aq)} + 3H_2O_{(l)} \quad (2.5)$$

In modern Bayer plants, there is a pre-desilication stage where the dissolved silica is kept at near atmospheric boiling temperatures for several hours to reprecipitate a sodium-aluminum silicate phase, also known as a Bayer sodalite or Bayer desilication product (DSP), as in **reaction (2.6)** [9].

$$6Na_2SiO_{3(aq)} + 6NaAl(OH)_{4(aq)} + Na_2X_{(aq)} = Na_6(Al_6Si_6O_{24}) \cdot Na_2X_{(s)} + 12NaOH_{(aq)} + 6H_2O_{(l)} \quad (2.6)$$

The X represents a variety of inorganic anions, e.g., CO_3^{2-}, SO_4^{2-}, $2AlO_2^-$, $2OH^-$. However, the excessive loss of NaOH and alumina as the occurrence of side reactions limit the production of alumina from high-silica bauxites, which is accounted as an uneconomical process [40].

2.3.3.2 Organic and trace elements

The organic carbon in tropical bauxites co-exists as 50 – 90% of humic acids in a pregnant solution, depending on the bauxite source and digestion temperatures [28]. The complex organic breakdowns then into several simpler organics, e.g., sodium oxalate ($Na_2C_2O_4$) and carbonate (Na_2CO_3). The formation rate of $Na_2C_2O_4$ can exceed its solubility level in Bayer solution, which leads to very little precipitation in the precipitation-classification circuit, as shown in **Fig. 2.5** [41]. Hence, the precipitates interfere with the solids separation in the classification trays [42]. On the other hand, Na_2CO_3 decreases the rate of $Al(OH)_3$ precipitation that impair the process' productivity [28].

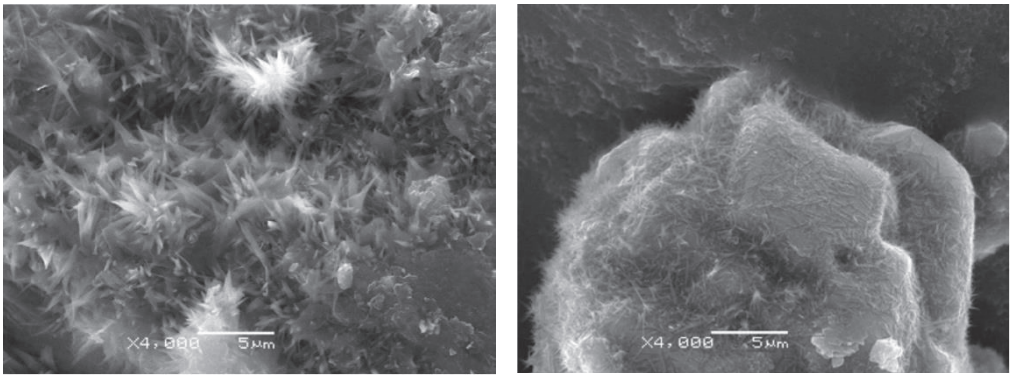

(a) (b)

Fig. 2.5 Morphologies of (a) precipitates of very fine oxalate, and (b) oxalate that precipitates on gibbsite [41].

Trace elements that may dissolve moderately or entirely into the pregnant solution during the digestion are Ga, V, Zn, and P. The presence of the elements in the liquor may cause several problems. A list of dissolution reactions from these elements and their common practical issues in the Bayer plants is shown in **Table 2.4**.

Table 2.4
Dissolution reaction of trace elements in the Bayer process [28]

Trace elements	Dissolution reactions	Remarks
Ga	$Ga_2O_{3(s)} + 6NaOH_{(aq)} = 2Na_3GaO_{3(aq)} + 3H_2O_{(l)}$	Ga is dissolved partially during the digestion. Some Ga precipitates, while the remainder accumulates in the liquor.
V	$V_2O_{5(s)} + 2NaOH_{(aq)} = Na_2V_2O_{6(aq)} + H_2O_{(l)}$	V is partially soluble in the Bayer process. A vanadium salt starts to precipitate in colder parts of the Bayer circuit, which causes flow problems.
Zn	$ZnO_{(s)} + 2NaOH_{(aq)} = Na_2ZnO_{2(aq)} + H_2O_{(l)}$	Zn is dissolved 10 – 20% into the solution, which is an undesirable impurity in the liquor as it precipitates during the Bayer precipitation step.
P	$P_2O_{5(s)} + 2NaOH_{(aq)} = Na_2P_2O_{6(aq)} + H_2O_{(l)}$	P is extracted 20 – 90% into the liquor under low-temperature digestion conditions. Phosphorous is unfavorable in certain aluminum alloys.

2.4 Alternative Processes for Alumina Recovery from Bauxite

After the invention of the Chatelier and Bayer process, there has been a number of researchers conducting experiments to seek other methods to recover alumina from bauxites. However, only a few of them have been scaled up to the commercial phase, which is described as follows.

2.4.1 The Pedersen process

In 1927 an alternative process on producing alumina was patented in Norway after Harald Christian Pedersen (1888 – 1945) [22]. Pedersen was a professor in metallurgy and also a rector (1925 – 1929) at Norges Tekniske Høgskole (NTH), or later known as NTNU [43]. The process had run commercially for approximately forty years (1928 – 1968) at Høyanger, Norway, with an annual production of about 17,000 tons [44]. It had been implemented in other parts of the world, including the USSR (now Russia), China, Manchuria (now Northern China), Japan, and Sweden [40]. The process was also economically attractive to the German industrial group, Nordag, so that they build a similar alumina plant based on the Pedersen process at Sauda, Norway, during the second world war [43]. The plant has an annual capacity of 50,000 tons Al_2O_3, and it was being commissioned when the war ended [45].

The process is based on the combination of pyro- and hydrometallurgical processes. Actually, the theoretical background of the Pedersen process has been adapted and modified accordingly for alumina recovery treatment on other sources than bauxite, e.g., coal ash [46], andalusite [47], clay [48,49], which are not in my current interest on the thesis. The Pedersen process can be divided into several steps. First, bauxite is smelted with lime and coke, and subsequently, the generated slag is leached in a Na_2CO_3 solution, and afterward, an $Al(OH)_3$ is precipitated out of the solution by the introduction of CO_2 gas. Finally, a pure Al_2O_3 is obtained after the calcination treatment. A simplified process flow of the Pedersen process is shown in **Fig. 2.6**.

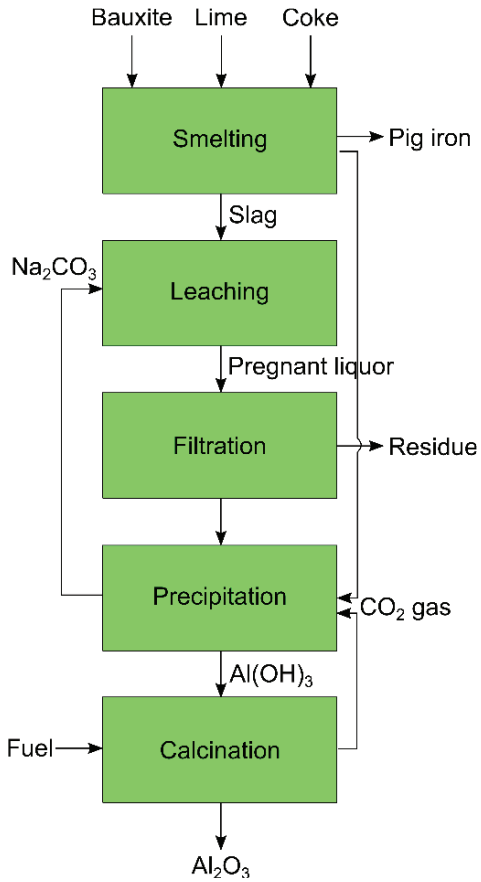

Fig. 2.6 A simplified process flow of the Pedersen process.

A more detailed explanation of the Pedersen process is described as follows:

a) Smelting of bauxite

A work after Sellæg et al. [50] shows that iron is separated from bauxite through smelting reduction technique. In their experiments, a proportioned ratio of bauxite, lime, and coke were smelted at 1600 °C with the holding time, heating and cooling rate were 1 hour, 20 °C/min and 5 °C /min, respectively. Depending ore characteristics, the main smelting-reduction reactions that occur according to the literature [51] are shown in **reactions (2.7) – (2.19)**:

$$3Fe_2O_{3(s)} + C_{(s)} = 2Fe_3O_{4(s)} + CO_{(g)} \quad (2.7)$$

$$3Fe_2O_{3(s)} + CO_{(g)} = 2Fe_3O_{4(s)} + CO_{2(g)} \quad (2.8)$$

$$Fe_3O_{4(s)} + C_{(s)} = 3(FeO) + CO_{(g)} \quad (2.9)$$

$$Fe_3O_{4(s)} + CO_{(g)} = 3\left(FeO\right) + CO_{2(g)} \quad (2.10)$$

$$\left(FeO\right) + C_{(s,\ dissolved)} = Fe_{(l)} + CO_{(g)} \quad (2.11)$$

$$\left(SiO_2\right) + 2\underline{C} = \underline{Si} + 2CO_{(g)} \quad (2.12)$$

$$\left(SiO_2\right) + CO_{(g)} = SiO_{(g)} + CO_{2(g)} \quad (2.13)$$

$$\left(SiO_2\right) + \underline{Si} = 2SiO_{(g)} \quad (2.14)$$

$$SiO_{(g)} + \underline{C} = \underline{Si} + CO_{(g)} \quad (2.15)$$

$$(TiO_2) + 2C_{(solid,\ dissolved)} = Ti_{(s)} + 2CO_{(g)} \quad (2.16)$$

$$\left(MnO\right) + \underline{C} = Mn_{(s)} + CO_{(g)} \quad (2.17)$$

$$C_{(s)} = \underline{C} \quad (2.18)$$

$$CO_{2(g)} + \underline{C} = 2CO_{(g)} \quad (2.19)$$

The underline "_" and parenthesis "()" notations indicate the element or phase that is dissolved in the Fe-liquid solution and slag at known temperature, respectively. Furthermore, as lime is used for slag making, the main reactions that occur in the process through elevated temperatures for slag formation can be expressed as in **reactions (2.20) – (2.27)** [51]:

$$CaO_{(s)} + Al_2O_{3(s)} = \left(CaO{\cdot}Al_2O_3\right) \quad (2.20)$$

$$CaO_{(s)} + 1/3\,Al_2O_{3(s)} = 1/3\,(3CaO{\cdot}Al_2O_3) \quad (2.21)$$

$$CaO_{(s)} + 7/12\,Al_2O_{3(s)} = 1/12\,(12CaO{\cdot}7Al_2O_3) \quad (2.22)$$

$$1/3\,(3CaO{\cdot}Al_2O_3) + 1/4\,Al_2O_{3(s)} = 1/12\,(12CaO{\cdot}7Al_2O_3) \quad (2.23)$$

$$CaO_{(s)} + Al_2O_{3(s)} + SiO_{2(s)} = (CaO{\cdot}Al_2O_3{\cdot}SiO_2) \quad (2.24)$$

$$CaO_{(s)} + Al_2O_{3(s)} + 2SiO_{2(s)} = (CaO{\cdot}Al_2O_3{\cdot}2SiO_2) \quad (2.25)$$

$$2CaO_{(s)} + Al_2O_{3(s)} + SiO_{2(s)} = (2CaO{\cdot}Al_2O_3{\cdot}SiO_2) \quad (2.26)$$

$$CaO_{(s)} + TiO_{2(s)} = \left(CaTiO_3\right) \quad (2.27)$$

Calcium aluminate will mainly compose the slag, while Fe (pig iron) is separated from the slag due to the difference of density; 2.5 – 2.7 g/cm^3 for a typical CaO-Al_2O_3-SiO_2 slag depending on the temperature and compositions [52], and 6.8 – 7.8 g/cm^3 for a pig iron [53].

In **chapter 6**, there is one of the published papers that is related to the characteristics of slags and pig iron produced by the Pedersen process. One of the bauxites was originated from Greece and containing a high Fe_2O_3 phase (up to 22.7 wt.%). Based on their experimental conditions, a mass and heat balance calculation of the smelting experiment for that particular bauxite using HSC™ ver. 9 can be done. The result is shown in **Fig. 2.7**. The energy needed to smelt a mixture of 1.7 tons of low-grade bauxite, 1 ton of lime, and 0.1 ton of coke is about 4.6 GJ (1275 kWh). As the available Al_2O_3 in the slag based on the X-Ray Fluorescence (XRF) result is 46 wt.%. Therefore, we can calculate the energy for producing 1 ton of Al_2O_3 is about 5 GJ (1388 kWh). The assumption used for the calculation is as follows: 1. All of the aluminum exists in the bauxite is considered as diaspore α-AlO(OH), 2. No heat loss is considered on the calculation, 3. The TiO_2 is 100% reduced, 4. The quantification of CaO-Al_2O_3-SiO_2-containing phases of the slag is based on an estimation of the literature [51] XRD results.

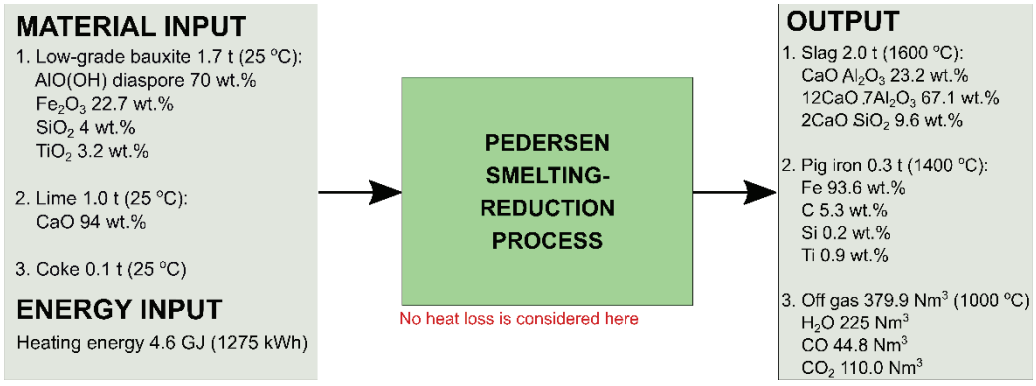

Fig. 2.7 A calculation of mass and heat balance of the Pedersen smelting-reduction process using HSC ver.9.

b) Leaching

After iron and slag are separated in smelting reduction, the next stage of Pedersen process is the wet stage starts with a leaching step. Leaching is needed to be done to digest the aluminate slag. Calcium aluminates as the major alumina-containing slag components are digested by Na_2CO_3 solution. The leaching reactions are described in the **reactions (2.28) – (2.31)**[54]:

$$CaO \cdot Al_2O_{3(s)} + Na_2CO_{3(aq)} = 2NaAlO_{2(aq)} + CaCO_{3(s)} \quad (2.28)$$

$$12CaO \cdot 7Al_2O_{3(s)} + 12Na_2CO_{3(s)} + 5H_2O_{(l)} = 14NaAlO_{2(aq)} + 12CaCO_{3(s)} + 10NaOH_{(aq)} \quad (2.29)$$

$$3CaO \cdot Al_2O_{3(s)} + 3Na_2CO_{3(aq)} + 2H_2O_{(l)} = 2NaAlO_{2(aq)} + 3CaCO_{3(s)} + 4NaOH_{(aq)} \quad (2.30)$$

$$CaO \cdot 2Al_2O_{3(s)} + Na_2CO_{3(aq)} + 2NaOH_{(aq)} + 7H_2O_{(l)} = 4NaAl(OH)_{4(aq)} + 3CaCO_{3(s)} \quad (2.31)$$

$CaO \cdot Al_2O_3$ and $12CaO \cdot 7Al_2O_3$ are most likely dissolved in Na_2CO_3 solution, $3CaO \cdot Al_2O_3$ is less than 50% soluble in a 5% Na_2CO_3 solution [55], and $CaO \cdot 2Al_2O_3$ phase has less leachability than $3CaO \cdot Al_2O_3$ at the same leaching conditions [56].

More details concerning the leaching mechanism and characteristics of the Pedersen process will be discussed later in **chapter 4**.

c) Precipitation

Sodium aluminate solution, the main product of the leaching step after the grey mud residue separation, is reacted with CO_2 (carbon dioxide) in order to get the precipitation of $Al(OH)_3$ phase. Miller and Irgens [44] proposed the precipitation to proceed as in **reaction (2.32)**:

$$2NaAlO_{2(aq)} + 3H_2O_{(l)} + CO_{2(g)} = 2Al(OH)_{3(s)} + Na_2CO_{3(aq)} \quad (2.32)$$

By means of HSC™ ver.9, we can calculate the change of Gibbs free energy of the **reaction (2.32)** at different temperatures, as shown in **Fig. 2.8**. The calculation shows

that the precipitation is favored at temperatures below 200 °C, and can occur at low temperatures.

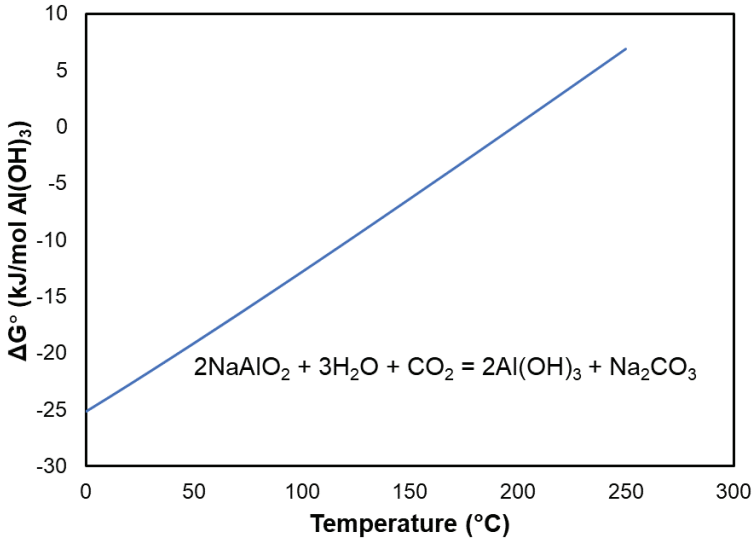

Fig. 2.8 The change of Gibbs free energy of the precipitation of $Al(OH)_3$ at different temperatures

However, depending on the concentration of Na_2CO_3 added into the solution during the leaching and the leaching reaction itself, the obtained pregnant solution is reported in a range of pH between 12.5 – 12.9 [54]. The pH is relatively high. Therefore it is likely that aqueous phases such as Na^+, $Al(OH)_4^-$, HCO_3^-, and OH^- mainly constitute the system as a result of the hydration of $NaAlO_2$ in a high pH solution [57], hydrolysis of CO_3^{2-}, and dissociation of Na_2CO_3, respectively. The reactions can be described as in **reactions (2.33) – (2.35)**[58]:

$$NaAlO_{2(aq)} + 2H_2O_{(l)} = Na^+_{(aq)} + Al(OH)^-_{4\ (aq)} \quad (2.33)$$

$$Na_2CO_{3(aq)} + H_2O_{(l)} = 2Na^+_{(aq)} + HCO^-_{3\ (aq)} + OH^-_{(aq)} \quad (2.34)$$

$$NaOH_{(aq)} = Na^+_{(aq)} + OH^-_{(aq)} \quad (2.35)$$

The result of hydration of $NaAlO_2$ into $Al(OH)_4^-$ phase is also supported by the literature [59], which showed a speciation diagram of aluminate ions in different pH (see

Fig. 2.9). The literature showed that $Al(OH)_4^-$ is favorable at pH more than 10. The Al^{3+} ion is stable at a pH between 2 – 4. Whereas, it is expected to have $Al(OH)_3$ phase at pH in the range of 6 – 8.

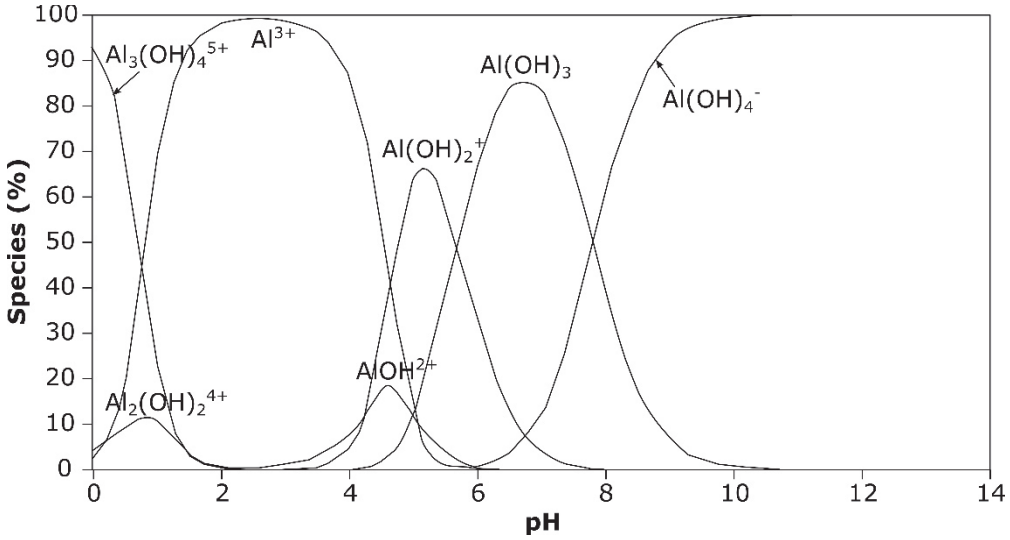

Fig. 2.9 Speciation of aluminate ions in different pH [59].

The precipitation of $Al(OH)_3$ by introducing CO_2 gas in an $Al(OH)_4^-$-rich solution is defined as a carbonation process. The carbonation is a relatively old method that was used in the early years of alumina production as in the Le Chatelier process (see **section 2.1**). There are three main steps in the carbonation, which are CO_2 absorption, hydrolysis (decomposition) of the aluminate ions, and crystallization of $Al(OH)_3$. The proposed reactions from the literature [60] are shown in **reactions (2.36)** and **(2.37)**:

$$OH^-_{(aq)} + CO_{2(g)} = CO_3^{2-}{}_{(aq)} + H^+_{(aq)} \quad (2.36)$$

$$Al(OH)_4^-{}_{(aq)} = Al(OH)_{3(s)} + OH^-_{(aq)} \quad (2.37)$$

Also, Czajkowski et al. [60] classified three regions in the carbonation based on the concentration of each known aqueous phase in the system, as shown in **Fig. 2.10**. In the first region, neutralization of OH^- takes place where CO_3^{2-} concentration increases as in the **reaction 2.36**. Second, $Al(OH)^{4-}$ ion starts to decompose and crystallize as $Al(OH)_3$ as in **reaction 2.37**. In the meantime, OH^- concentration is almost wholly

consumed at the end of stage 2. In the third region, the concentration of HCO_3^- increases due to the reaction between CO_3^{2-} and H^+ as seen in **reaction 2.38**.

$$CO_{3\,(aq)}^{2-} + H^+_{(aq)} = HCO_{3\,(aq)}^- \quad (2.38)$$

It leads to the precipitation of unfavorably sodium aluminocarbonate phases, i.e., $Na_2O{\cdot}Al_2O_3{\cdot}2CO_3{\cdot}nH_2O$, $NaAlCO_3(OH)_2$ (dawsonite). There was no information concerning the pH value of Czajkowski et al. published results. However, according to a master's thesis from Nedkvitne [61], the initial pH of the solutions (region I) was 12.8 ± 0.1, the precipitation of $Al(OH)_3$ (region II) was observed when the pH was 11.8 ± 0.2, and the precipitation of unwanted dawsonite in region 3 was observed when the carbonation was performed until the pH was 9.5. It is important to note here that temperature and initial Na_2CO_3 concentration can give different values of the pH.

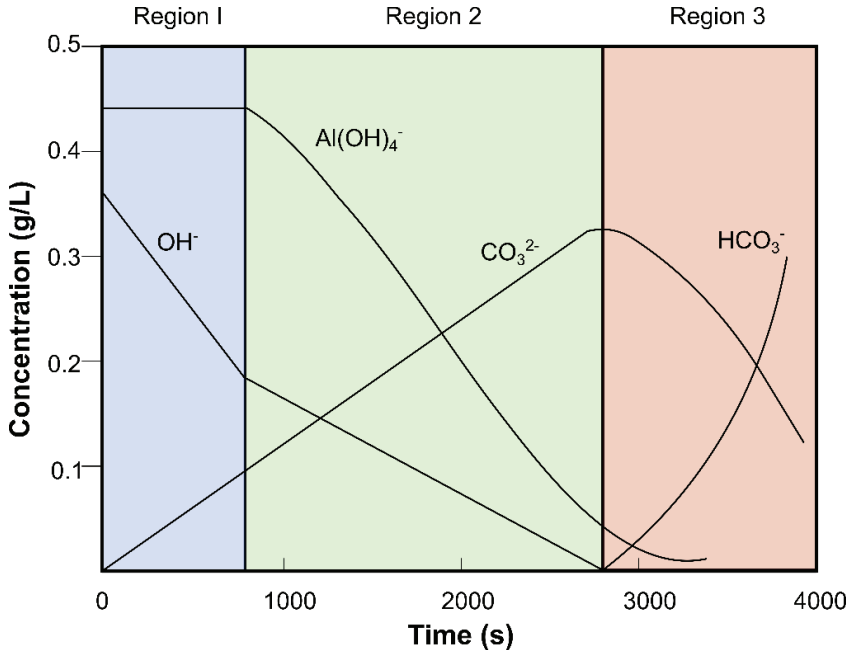

Fig. 2.10 Distribution of the concentration of the phase in the process of carbonation according to the different stages [60]

It has been mentioned before that gibbsite is obtained in the process of $Al(OH)_3$ precipitation out of from aluminate solutions. On the other hand, it was shown in the literature [60,62,63] the existence of other polymorphous forms of alumina hydroxide, i.e., boehmite and bayerite, from saturated aluminate solutions. An equilibrium condition for different forms of aluminum hydroxide in regards to the concentration ratio of $Al(OH)_4^-$ and OH^- is provided in **Fig. 2.11** [60], which includes Czajkowski et al. experimental results on the changes of $Al(OH)_4^-$ concentration at different CO_2 absorption rates.

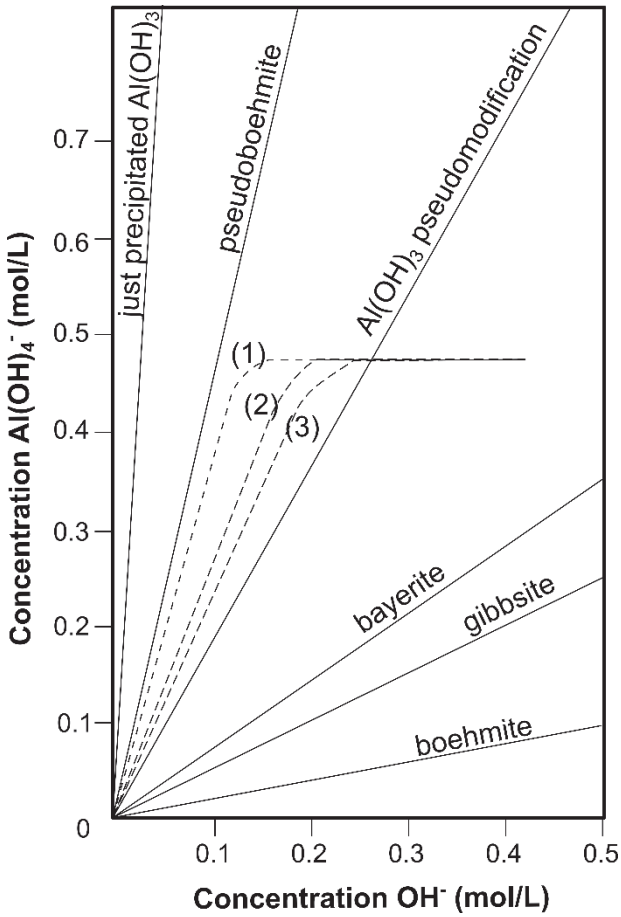

Fig. 2.11 Equilibrium in the system of aluminate solutions, which includes the changes of $Al(OH)_4^-$ concentration at different CO_2 absorption rates: (1) 1.7×10^{-4}, (2) 9.9×10^{-5}, (3) 5.4×10^{-5} mol/L·s [60]

As both the main leaching reactions and precipitation mechanism have been discussed earlier, it is worth to summarize the leaching and precipitation parameters that were stated on the original patent of Pedersen process [22] as shown in **Table 2.5**:

Table 2.5

Leaching and precipitation parameters of the Pedersen original patent [22].

Parameters	Key remarks/issues
Leaching by means of Na_2CO_3 (30 – 80 g/L)	a) By employing Na_2CO_3, the slag is dissolved, and then $Al(OH)_3$ is precipitated by carbonation treatment using CO_2 gas. b) All of the silica which was dissolved is precipitated together with the $Al(OH)_3$, thus contaminate the purity of the product unless the solvent is very dilute (< 30 g/L Na_2CO_3).
Leaching by means of NaOH (unspecified concentration)	a) If NaOH is used, then the $Al(OH)_3$ is precipitated by the well-known Bayer process where the sodium aluminate solution is hydrolyzed and $Al(OH)_3$ precipitated by gradual cooling (auto-precipitation), agitation, and $Al(OH)_3$ seed. b) The leaching rate is much slower than using Na_2CO_3. c) The alumina extraction extent is lower than using Na_2CO_3 as the calcium hydroxide is formed in a large amount and reacts with the dissolved alumina. d) The ratio of alumina to total soda and silica to alumina is consecutively lower and higher than when Na_2CO_3 is used.
Leaching by means of Na_2CO_3 (30 – 40 g/L) and "free" NaOH at 80 °C	a) The presence of a small amount of NaOH does not reduce the extent of alumina recovery significantly or reduce the ratio of alumina to soda in the solution. However, it does tend to prevent silica dissolution. b) The term "free" NaOH means that the amount is present in excess of the amount required to form sodium aluminate, $NaAlO_2$. c) The amount of "free" NaOH is about 10 wt.% of the amount of total alkali, calculated as Na_2CO_3.
Precipitation	a) Carbonation by means of CO_2 gas: the size of $Al(OH)_3$ precipitate is a relatively fine, and a large amount of it may be lost like dust in the calcination plant. b) Auto-precipitation, as in the Bayer process: the morphology of the $Al(OH)_3$ produced by the auto-precipitation of the mentioned solution satisfactorily meets the size requirement (granular). c) A combination of auto-precipitation and carbonation can be used to precipitate $Al(OH)_3$ in a shorter time than the auto-precipitation in the Bayer process. By introducing CO_2 gas during the precipitation, it neutralizes the "free" NaOH, which converts it into carbonate and is managed to be used again in the leaching process of calcium aluminate (cyclic process).

d) Calcination

Calcination is the final stage of alumina recovery in the Pedersen process. The reaction of calcination is the same as in the Bayer process in **reaction (2.4)**. It employs a high-temperature chamber with fuel to remove the moisture on alumina hydroxide and chemical reaction, which finally produces alumina concentrate and CO_2 gas. Carbon dioxide afterward will be used for the precipitation stage (cycle process).

There have been several researchers showing the composition of smelter-grade alumina produced by the Pedersen process, as shown in **Table 2.6**. Fursman et al. [64] and Miller and Irgens [44] have managed to have a purity of 98.7 and 98.9 wt.%Al_2O_3, respectively. Furthermore, Blake et al. [65] claimed that they could have a purity of up to 99.5 wt.%Al_2O_3 by implementing a desilication process after the leaching stage.

Table 2.6
Typical smelter-grade alumina produced by the Pedersen process

Constituents	Miller and Irgens [44]	Fursman et al. [64]	Blake et al.* [65]
Al_2O_3 (wt.%)	98.9	98.7	98.9 – 99.5
Na_2O (wt.%)	0.6	> 1.0	1.1 – 1.3
SiO_2 (wt.%)	0.1	$5 – 13 \times 10^{-2}$	$17 – 28 \times 10^{-3}$
CaO (wt.%)	0.2	$7 – 10 \times 10^{-2}$	$1 – 4 \times 10^{-2}$
Fe_2O_3 (wt.%)	12×10^{-3}	1×10^{-2}	5×10^{-3}
TiO_2 (wt.%)	3×10^{-3}	$< 1 \times 10^{-3}$	$1 – 3 \times 10^{-3}$
ZnO (wt.%)	NA	NA	1×10^{-3}
P_2O_5 (wt.%)	NA	$10 – 13 \times 10^{-3}$	$2 – 6 \times 10^{-3}$
Ga_2O_3 (wt.%)	NA	NA	NA
V_2O_5 (wt.%)	4×10^{-3}	NA	NA
SO_3 (wt.%)	NA	$6 – 20 \times 10^{-3}$	NA

**Using a desilication process as an addition to the original Pedersen patent*

Sustainability of the Pedersen process

In regards to environmental and economic perspectives, the Pedersen process can be seen as one of the potential alternatives to produce alumina more sustainably than in the current situation using the Bayer process. The process does not produce red mud and unutilized byproduct. On the contrary, most of its byproduct is a consumable material of other processes; pig iron and the grey mud.

Pig iron is favored in foundries to cast engine blocks, automotive parts, or another end-use. Depending on the bauxite deposits, the chemical composition of typical pig iron produced from the smelting-reduction process of bauxite is shown in **Table 2.7**.

Table 2.7

Chemical composition of typical pig iron produced from smelting-reduction treatment of bauxites

Origin of bauxites (reference)	Fe (Wt.%)	C_{sat} (Wt.%)	Si (Wt.%)	Mn (Wt.%)	Ti (Wt.%)	P (Wt.%)	S (Wt.%)
Brazil [51]	89.9	4.6	4.0	0.5	0.6	4×10^{-2}	NA
Greece [51]	92.0	5.3	0.2	0.2	0.9	9×10^{-2}	7×10^{-3}
Iran [51]	92.7	4.9	1.2	0.4	0.2	0.1	7×10^{-3}
Salem Hills, USA, low-silica [64]	91.9	NA	5×10^{-2}	NA	0.2	1.4	3×10^{-3}
Salem Hills, USA, mid-silica [64]	93.8	3.8	3×10^{-2}	NA	0.3	1.8	NA
Salem Hills, USA, high-silica [64]	93.3	4.0	3×10^{-2}	NA	0.5	1.7	NA
Salem Hills, USA [65]	89.6	5.1	3×10^{-2}	NA	5×10^{-2}	1.4	NA
Guangxi, China [66]	93.3	4.2	0.1	1.6	NA	6×10^{-3}	4×10^{-3}

In the meantime, grey mud can be used in cement, fertilizer, or lime and CO_2 source industries due to its high content of $CaCO_3$ [67]. A typical of grey mud produced from the leaching of calcium aluminate slags, and the differences between grey mud and the red mud are shown in **Table 2.8** [58] and **2.9** [67], respectively.

Table 2.8
Chemical composition of typical grey mud produced from different leaching temperatures, after a loss on ignition test [58].

Constituents	Leaching temperature		
	45 °C (Wt.%)	60 °C (Wt.%)	75 °C (Wt.%)
CaO	64.0	57.9	63.8
Al_2O_3	7.8	5.9	5.9
SiO_2	2.2	1.8	1.7
TiO_2	2.9	3.1	3.1
Na_2O	2.2	2.1	2.1
Fe_2O_3	1.0	1.3	1.5
MgO	0.6	0.5	0.5
P_2O_5	0.1	4.2×10^{-2}	1.1×10^{-2}
V_2O_5	4.3×10^{-2}	3.5×10^{-2}	3.3×10^{-2}
Cr_2O_3	5.9×10^{-2}	5.3×10^{-2}	5.9×10^{-2}
MnO	6.4×10^{-2}	6.5×10^{-2}	6.4×10^{-2}
LOI	17.7	25.9	19.9

Tabel 2.9
Main differences between grey and red mud [67]

Parameter	Grey mud	Red mud
Main components	$CaCO_3$, CaO, SiO_2	Fe-oxides, Al_2O_3,
Al_2O_3 losses	8% (low)	15% (moderate)
Na_2O losses	2%	5%
Mud : alumina mass ratio*	1.5 – 2 : 1	1 – 1.2 : 1
Alkalinity	Low	High

**Depending on the bauxite compositions*

Moreover, Safarian and Kolbeinsen [2] highlighted several differences between the Bayer and Pedersen process, as shown in **Table 2.10**.

Table 2.10
Comparison of the Bayer and Pedersen Process [2]

Parameter	Bayer Process	Pedersen Process
Overall process characteristic	Hydrometallurgical	Pyrometallurgical Hydrometallurgical
Ore type	High Al_2O_3:Fe_2O_3 ratio	Low Al_2O_3:Fe_2O_3 ratio
Main byproducts	Red mud (not consumable)	Pig iron (consumable) Grey mud (consumable)
Leaching conditions	Digestion by NaOH 150-250 °C High pressure	Digestion by Na_2CO_3 40-80 °C Atmospheric pressure
$Al(OH)_3$ precipitation	45-80 °C; 48-70 hour	70-80 °C; 6-10 hour
Electric energy consumption	Reference process	10% higher
Using TiO_2 and SiO_2 containing ores	Reference process	More flexible
Raw materials costs	Reference process	Higher (~40% on average)
Process costs for a unit mass of Alumina	Reference process	30-50% lower

2.4.2 Soda-lime sintering

A region that has high reserves of low-grade diasporic bauxite might find problems on the losses of NaOH during the leaching step in the Bayer process due to its high reactivity with silica. Thus, the bound-soda losses can be reduced by utilizing a soda-lime sintering process, as reported by Cao et al. [68]. In a soda-lime sintering process, aluminosilicate-containing bauxite is reacted with limestone and Na_2CO_3 at elevated temperatures (> 1100 °C) to form a sodium aluminate phase, which is soluble in an alkaline solution and an insoluble Ca_2SiO_4 phase that can be filtered afterward [69]. The bauxite is heated to sintering temperatures along with $CaCO_3$ or Na_2CO_3 to increase the leachability of material that is necessary for its next leaching process. A simplified flow sheet of the soda-lime sintering process is shown in **Fig. 2.12**.

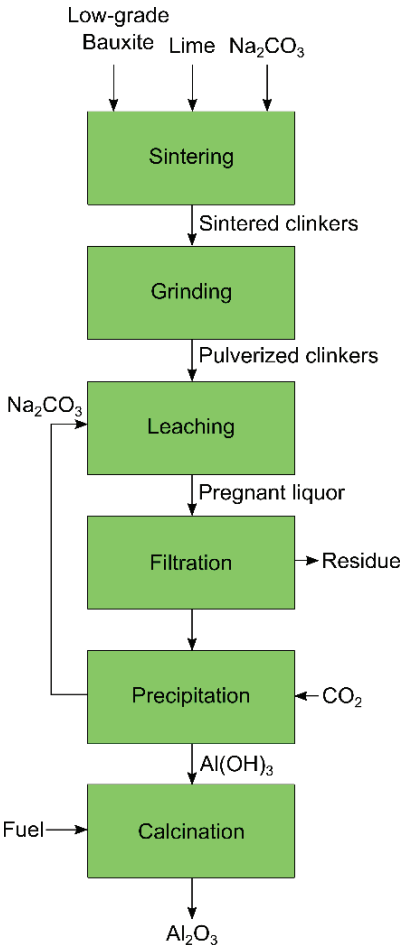

Fig. 2.12 A simplified flow sheet of the soda-lime sintering process.

Depending on the composition of bauxites, the reactions that occur during sintering can be presented as in **reactions (2.38) – (2.43)**:

$$2CaCO_{3(s)} + SiO_{2(s)} = 2CaO \cdot SiO_{2(s)} + 2CO_{2(g)} \quad (2.38)$$

$$12CaCO_{3(s)} + 7Al_2O_{3(s)} = 12CaO \cdot 7Al_2O_{3(s)} + 12CO_{2(g)} \quad (2.39)$$

$$2Al(OH)_{3(s)} = Al_2O_{3(s)} + 3H_2O_{(l)} \quad (2.40)$$

$$Fe_2O_{3(s)} + Na_2CO_{3(aq)} = Na_2O \cdot Fe_2O_{3(aq)} + CO_{2(g)} \quad (2.41)$$

$$4CaCO_3 + Al_2O_3 \cdot 2SiO_2 = 2(2CaO \cdot SiO_2) + Al_2O_3 + 4CO_2 \quad (2.42)$$

$$Al_2Si_2O_{7(s)} + Na_2CO_{3(aq)} + 4CaCO_{3(s)} = 2NaAlO_{2(aq)} + 2Ca_2SiO_{4(s)} + 5CO_{2(g)} \quad (2.43)$$

Furthermore, Ostrowski and Zelazny [70] suggested that a $CaO \cdot Al_2O_3$ phase can be transformed into $Na_4Ca_3(AlO_2)_{10}$ and $12CaO \cdot 7Al_2O_3$ in a Na_2O-doped CaO-Al_2O_3 system. The leachability of $Na_4Ca_3(AlO_2)_{10}$ phase was reported better than that of $CaO \cdot Al_2O_3$ and $12CaO \cdot 7Al_2O_3$ phase by Tian et al. [71]. They have claimed that almost all of the $12CaO \cdot 7Al_2O_3$ and $Na_4Ca_3(AlO_2)_{10}$ phases can be leached when the leaching time of sintered clinkers is 120 min and the Al-containing residue is in the form of $2CaO \cdot Al_2O_3 \cdot SiO_2$. Tian et al. [71] stated that the leaching efficiency is above 95%. Therefore, the formation of $2CaO \cdot Al_2O_3 \cdot SiO_2$ is one of the reasons why the leachability of the Na_2O-CaO-Al_2O_3-SiO_2 system is lower than a single $Na_4Ca_3(AlO_2)_{10}$ phase [71].

2.4.3 Roast-leaching

Researchers have tried to extract alumina from a low grade of bauxite ores by roasting it prior to leaching. Li et al. [72] investigated the reduction roasting effect on the Fe-Al separation of gibbsite prior to magnetic separation, of which the process flow is shown in **Fig. 2.13**. Li et al. discovered that the appropriate roasting temperature was 1000-1100 °C. Based on their results, a metallic iron that contains 93.3 wt.%Fe_{total} and non-magnetic product with 40 wt.%Al_2O_3 can be obtained from high-iron gibbsite bauxite containing 31.2 wt.%Fe_{total} and 26.3 wt.%Al_2O_3.

Valeev et al. [73] reported the leaching behavior of high-silica bauxite by hydrochloric acid with a preliminary roasting method. Roasting is used to increase the extraction ratio of aluminum bauxite as it changes the low-soluble boehmite and kaolinite phases into acid-soluble forms, which are γ-Al_2O_3 and $Al_2Si_2O_5$, respectively. Valeev et al. found that preliminary roasting of high-silica bauxite at 700 °C for 0.5 h leads to a significant increase of the extraction ratio of aluminum in solution, which becomes 89%, in comparison with the leaching of uncalcined bauxite, which is only 23%.

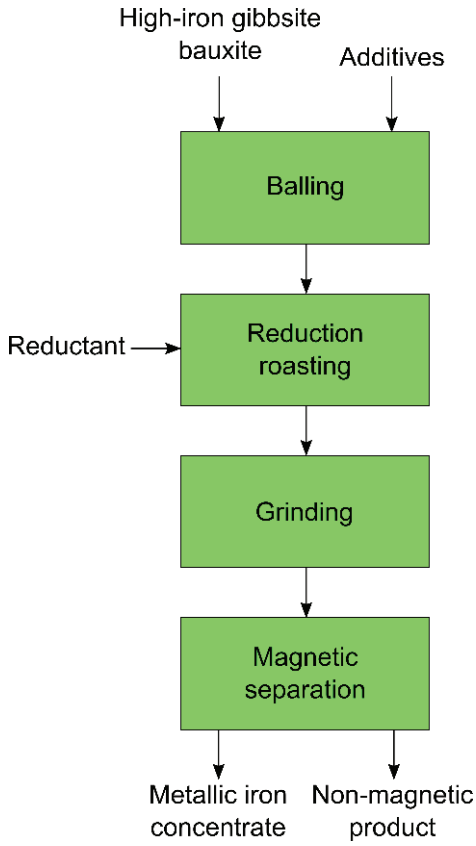

Fig. 2.13 Flow sheet of reduction roasting followed by magnetic separation for bauxite beneficiation.

Chapter 3

Pyrometallurgical Part of the Pedersen Process

This chapter is written based on following papers 1 and 2 in **chapter 6** entitled "Synthesis and characterization of $12CaO{\cdot}7Al_2O_3$ slags: the effects of impurities and atmospheres on the phase relations" and "Characteristics of calcium-aluminate slags and pig iron produced from smelting-reduction of low-grade bauxites," respectively. The first paper has been submitted to a peer-reviewed journal, and the second paper has been published on Metallurgical and Materials Transactions B, volume 49(5), pp. 2400-2420 (DOI: 10.1007/s11663-018-1353-1).

3.1 Summary of paper 1 – The stability of $12CaO{\cdot}7Al_2O_3$ phase in $CaO\text{-}Al_2O_3$ system

The stability of $12CaO{\cdot}7Al_2O_3$ (denoted as $C_{12}A_7$) phase at room temperature produced from melts that are exposed to different atmospheric conditions and various raw materials purity was investigated. The $C_{12}A_7$ phase is one of the essential phases that exist in the $CaO\text{-}Al_2O_3$ system due to its high leachability in Na_2CO_3 solution [54,58], which is beneficial for alumina recovery in the Pedersen leaching process. The $C_{12}A_7$ phase has unique properties that also attract many researchers that have an interest in manufacturing stable inorganic electrides at room temperature [74–77]. It has a unit cell that consists of $(Ca_{24}Al_{28}O_{64})^{4+}{\cdot}2O^{2-}$, where the first part is a lattice framework with 12 sub-nanocages, and the latter is called an extra-framework oxide ion that is randomly distributed in the cages [78]. Nurse et al. [79,80] reported that the phase is unstable at elevated temperatures and in anhydrous or moist-free $CaO\text{-}Al_2O_3$ system.

Based on DT-TGA experiments, it was found that the dehydration of the $C_{12}A_7$ phase takes place at 770 – 1390 °C upon heating, before it melts congruently at 1450 °C. A stable $C_{12}A_7$ phase at room temperature is evident that is enforced by impurities, i.e., SiO_2, which plays a significant role in maintaining the $C_{12}A_7$ structure with good

reproducibility. As the silicon stabilizes the $C_{12}A_7$ phase (Si-mayenite), then it is possible to produce a stable $C_{12}A_7$ phase in either reducing or oxidizing atmosphere by using a single smelting process.

On the other hand, it was observed that the $5CaO \cdot 3Al_2O_3$ (C_5A_3) phase is an unstable/intermediate phase in the ternary $CaO\text{-}Al_2O_3\text{-}SiO_2$ system. It is decomposed to $C_{12}A_7$ above 1100 °C. In the current paper, it is evident that the phase exists only at room temperature when the $C_{12}A_7$ dissociates to a mixture of C_5A_3, $3CaO \cdot Al_2O_3$ (denoted as C_3A), and $CaO \cdot Al_2O_3$ (denoted as CA) phases during the gradual cooling of slag at 1180 ± 20 °C in a reducing atmosphere and is made from a pure 99.9 %CaO – 99.95 $\%Al_2O_3$ mixture.

3.1.1 Methodology

The $C_{12}A_7$ phase has a mass ratio of 49:51 of CaO to Al_2O_3 (C/A), which is equivalent to 12 moles CaO and 7 moles Al_2O_3. In paper 1, four slags were made in a mass ratio of 49:51 C/A, and four other slags were in a ratio of 54:46 C/A. The reason for making slags at different C/A ratio is to investigate if the chemical composition affects the stability of $C_{12}A_7$ phase. The slags were made from different raw materials, purity, and atmospheric conditions. The pure mixtures were made from 99.9 wt.%CaO and 99.95 wt.$\%Al_2O_3$. On the other hand, the less pure mixtures were made from 96 wt.%CaO and the same 99.95 wt.$\%Al_2O_3$. Furthermore, the slags were subjected to be exposed in three different melting atmospheric conditions; reduction with $O_{2(g)}$ present, reduction without $O_{2(g)}$ present, and oxidation. The partial pressure of O_2 or $CO_{2(g)}$ was conditioned by the use of different crucibles and the use of lid to limit the contact of the melts with the surrounding air. In addition, a slag with a ratio of 49:51 C/A was re-melted in different atmospheric conditions than the slag has in its previous treatment to observe the stability of the phases. **Table 3.1** shows the slag composition and melting parameters of each sample. On the other hand, **Fig. 3.1(a)** shows an image of slags smelted inside of an induction furnace, while **Fig. 3.1(b)** shows a cross section of the slag produced in different crucibles.

Table 3.1
Target slags composition that are classified by different raw materials purity, crucible types, and melting atmospheric conditions

Sample name	Composition		Raw materials purity	Crucible type	Use a graphite or alumina lid	Melting atmospheric condition
	CaO (wt.%)	Al_2O_3 (wt.%)				
Slag 3(a)	49	51	Less pure	Graphite	No	Reduction with $O_{2(g)}$ present
Slag 3(b)	49	51	Pure	Graphite	No	Reduction with $O_{2(g)}$ present
Slag 3(c)	49	51	Pure	Graphite	Yes, graphite lid	Reduction
Slag 3(d)	49	51	Pure	Alumina	Yes, alumina lid	Oxidation
Slag 4(a)	54	46	Less pure	Graphite	No	Reduction with $O_{2(g)}$ present
Slag 4(b)	54	46	Pure	Graphite	No	Reduction with $O_{2(g)}$ present
Slag 4(c)	54	46	Pure	Graphite	Yes, graphite lid	Reduction
Slag 4(d)	54	46	Pure	Alumina	Yes, alumina lid	Oxidation
Slag 3(a)-remelted	49	51	Less pure	Graphite	Yes, graphite lid	Reduction

(a) (b)

Fig. 3.1(a) shows an image of slags smelted inside of an induction furnace, while (b) shows a cross section of the slag produced in different crucibles.

Furthermore, a high-resolution imaging, Energy Dispersive Spectroscopy (EDS) analysis, and X-ray element mapping of slags were carried out using Hitachi SU6600™ SEM. A high-resolution EPMA JXA-8500F™, supported by Wavelength Dispersive Spectroscopy (WDS), also used to get high accuracy on quantitative analysis of elements in selected phases of the slags. Phase identification of the slags and residues were undertaken with a Bruker D8 A25 DaVinci™ XRD machine with CuKα radiation, between 10 - 75° diffraction angle, 0.01° step size, and 2.5° for both primary and secondary soller slit. The identification and qualitative phase analysis of the obtained XRD peaks were made by using DIFFRAC.EVA™.

For thermal analysis, a Thermogravimetry (TG) and Differential Thermal Analysis (DTA) NETZSCH STA 449C™, combined with mass spectrometry QMS 403C™ was used. Alumina crucible was used and exposed in synthetic air that flows at 30 mL/min and was heated at a ramp of 10 °C/min up to 1500 °C. Thus, after 30 min it was cooled down to room temperature at 10 °C/min. Furthermore, High-Temperature Raman spectrometer Jobin Y'von LabRAM HR Evolution™ was used to determine the Raman spectra of the slags. It uses a visible pulse laser with a wavelength of 532 nm. The laser output power, slid width, scanning wavenumber range are 100 mW, 200 μm, 200 – 1200 cm^{-1}, respectively. A platinum crucible with 5 mm of diameter and 2 mm of depth was used when experimenting with the measurement. The heating rate from room temperature to 1000 °C was 500 °C/min, in which the spectrum was measured after holding at 500, 800, and 1000 °C for 10 min. Furthermore, from 1000 – 1485 °C, the heating rate was 200 °C/min, in which the spectrum was measured after 10 min at 1200, 1300, 1400, 1450, 1485 °C. The measurements were carried out under ambient pressure. Images of the slags that were taken when performing Raman spectroscopy at 1400 °C are shown in **Fig. 3.2**.

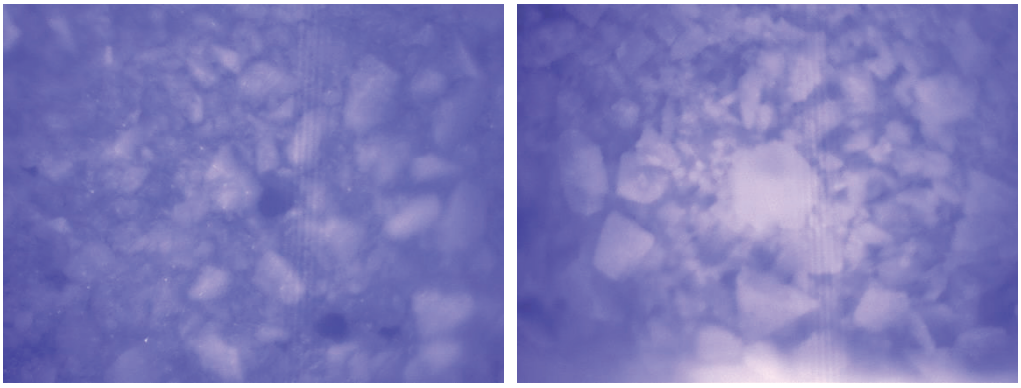

(a) (b)

Fig. 3.2 Images of the slags that were taken when performing Raman spectroscopy at 1400 °C, which have the same 49:51 C/A mass ratio that were made from (a) less pure mixtures and (b) pure mixtures.

3.1.2 Theoretical background

The paper describes the phase relation of $C_{12}A_7$ in the CaO – Al_2O_3 system at different atmospheric conditions and the effect of impurities on the phase stability. Therefore, the theoretical background concerning the phase diagram of CaO-Al_2O_3 and the structure of the $C_{12}A_7$ phase is deemed necessary.

3.1.2.1 CaO–Al_2O_3 system

In 1909, the binary CaO–Al_2O_3 phase diagram was initially reported by Shepherd et al., as shown in **Fig. 3.3** [81] . In addition to pure CaO and Al_2O_3 phases, they observed four compounds in a range of 15 to 70 wt.%Al_2O_3, which were CA, C_5A_3, C_3A, and an unstable form of both $3CaO{\cdot}5Al_2O_3$ (denoted by C_3A_5) and C_5A_3. The approximate melting temperature of CaO was not known, and there was no eutectic between CaO and C_3A. It is shown that the C_3A is unstable at its melting point. The eutectic reaction between C_3A and C_5A_3 occurs at 51 wt.%Al_2O_3 at 1382 °C. Meanwhile, the eutectic between C_5A_3 and CA occurs at 53 wt.%Al_2O_3 at the same temperature, 1382 °C.

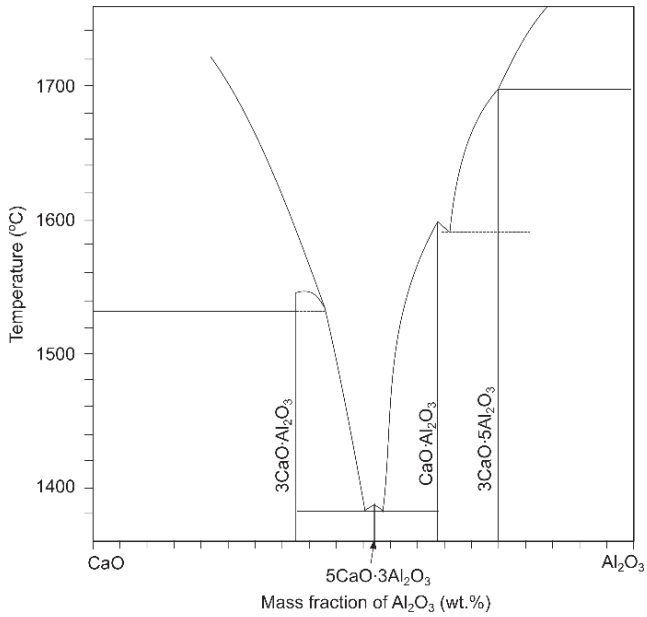

Fig. 3.3 A binary $CaO–Al_2O_3$ phase diagram as constructed by Shepherd et al. in 1909 [81].

In 1911, they published a preliminary report on the ternary $CaO–Al_2O_3–SiO_2$ system [82], which was of great importance on a study of the constitution of Portland cement clinker. Later on, Rankin and Wright [83] in 1915, documented the ternary $CaO–Al_2O_3–SiO_2$ phase diagram, as shown in **Fig. 3.4**, which was an updated version of the preliminary report. They had stated that C_5A_3 formation occurred in two forms; a stable and an unstable monotropic form. The stable form melts at 1455 ± 5 °C and has two eutectic mixtures with C_3A and CA phases. On the other hand, the unstable form has neither a definite melting point nor any range of temperatures regarding its stability.

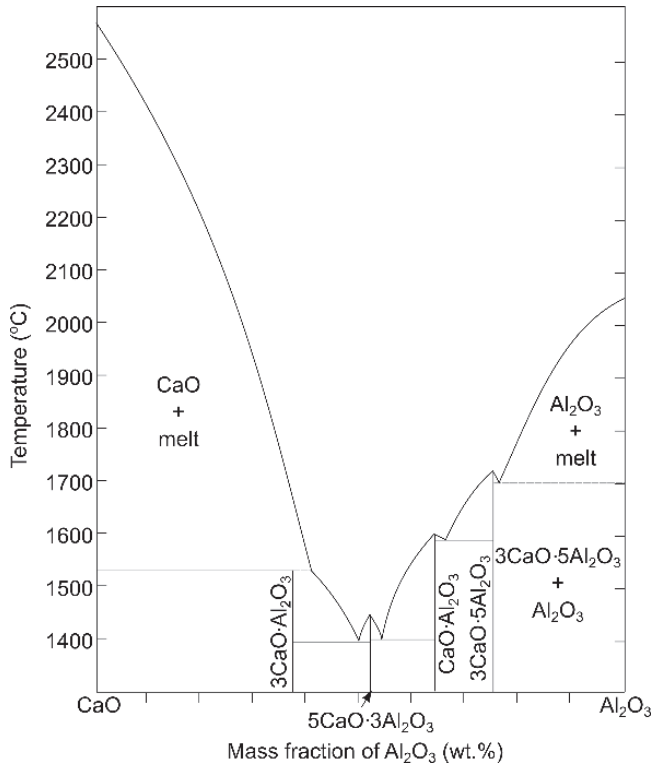

Fig. 3.4 A binary CaO – Al_2O_3 phase diagram as constructed by Rankin and Wright in 1915 [83].

As per today, the phase diagram of CaO–Al_2O_3 has been assessed intensively and reported by many researchers who have been working on the phase equilibrium [84–86]. A CaO–Al_2O_3 system in the range of 1000 – 2000 °C has been calculated by using Fact Sage™ with the FToxid database, and the result is shown in **Fig 3.5**. The C_5A_3 phase is unregistered on the Fact Sage™ FToxid database due to its unstable characteristics in nature. Also, there is a change regarding the existence of the C_3A_5 phase. It has been acknowledged from relatively recent works of literature [84–86] that the correct stoichiometry of the phase would be $CaO{\cdot}2Al_2O_3$ (denoted as CA_2), and, in addition, it was proposed that $CaO{\cdot}6Al_2O_3$ (denoted as CA_6) phase exists at ca. 91 wt.%Al_2O_3.

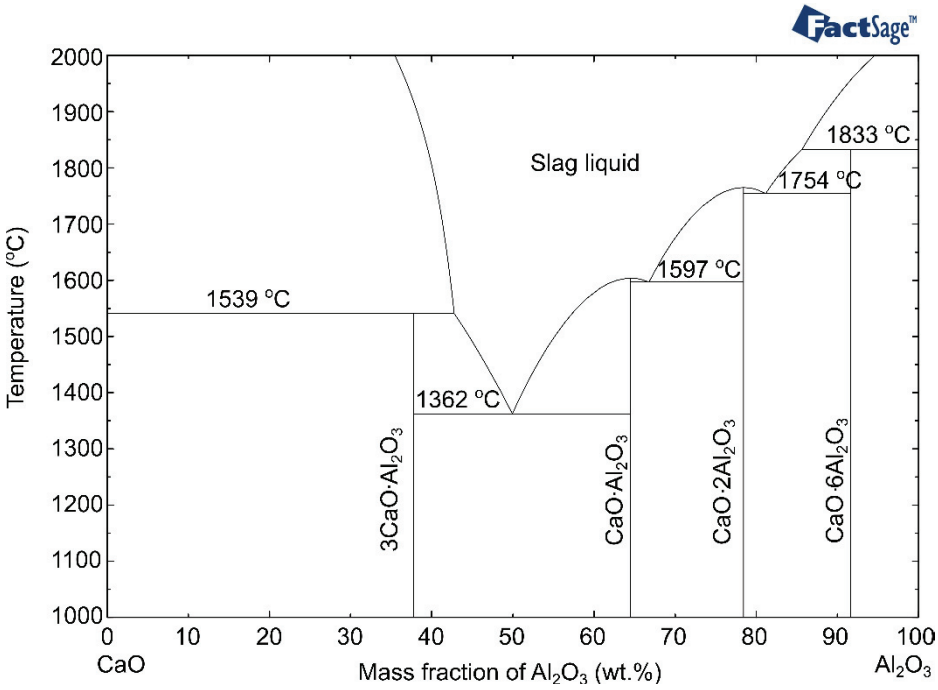

Fig. 3.5 Phase diagram of $CaO–Al_2O_3$ system as constructed using Fact Sage™ with FToxid database.

3.1.2.2 $C_{12}A_7$ Structure

It was until 1936, Büssem and Eitel [87] showed that the $CaO:Al_2O_3$ ratio of the synthesized stable C_5A_3 phase from Rankin and Wright's study was 12:7 rather than 5:3, in which they suggested chemical compound was $C_{12}A_7$. According to Büssem and Eitel, the $C_{12}A_7$ phase in its anhydrous form has the following physical properties: a = 11.982 Å, V = 1720.24 $Å^3$, bulk density = 2.85×10^3 $kg.m^{-3}$, in cubic I-43d (220) space group. In 1962, Jeevaratnam et al. [88] used a petrographic microscope to investigate the $C_{12}A_7$ crystal structure and showed results that were in agreement with the work of Büssem and Eitel as well. The unit cell is composed of 12 cages, two of which are occupied with O^{2-} ion. In the literature [89], the occupied cage is relatively mobile. Thus $C_{12}A_7$ phase has a high ionic conductivity due to diffusion of the ions between 500 – 1200 °C.

Regarding the phase, Nurse et al. [79,80] found that at elevated temperatures, $C_{12}A_7$ is unstable in anhydrous or moist-free $CaO-Al_2O_3$ system. It is in equilibria with H_2O above 950 °C and forms $Ca_{12}Al_{14}O_{32}(OH)_2$ when it is fully saturated (the water present as hydroxyl ions in the crystal structure). The observation was in agreement with

Roy and Roy [90], which had previously reported the zeolitic behavior of the phase. Zeolitic behavior means that the phase absorbs and desorbs water as a function of temperature (with pH_2O fixed). They found that $C_{12}A_7$ could absorb water vapor even at 1000 °C at a pH_2O of 1.6×10^{-3} atm. The hydration and dehydration occur reversibly, and the reaction was proposed by Hayashi et al. [91] as in **reaction (3.1)**:

$$(Ca_{12}Al_{14}O_{32})^{2+} \cdot O^{2-} + H_2O = (Ca_{12}Al_{14}O_{32})^{2+} \cdot 2(OH)^- \quad (3.1)$$

Where $(Ca_{12}Al_{14}O_{32})^{2+}$ indicates the lattice framework, and O^{2-} and OH^- are the extra-framework anions. A crystal structure of $C_{12}A_7$ that shows its nanoporous lattice framework and OH^- as the extra-framework anion is shown in **Fig. 3.6** [91].

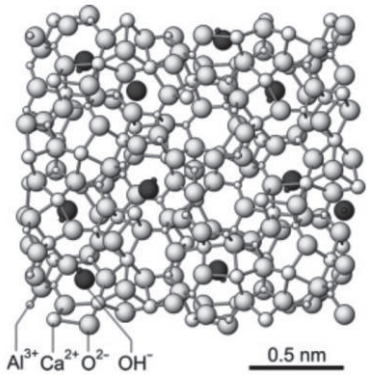

Fig. 3.6 Crystal structure of $C_{12}A_7$ that shows the nanoporous lattice framework and the OH^- as the extra-framework anion [91]

In a similar conclusion, Imlach et al. [92] claimed that the $C_{12}A_7$ phase is stable at high temperatures as it absorbs excess of oxygen from an oxidizing atmosphere, even where pO_2 is as low as 10^{-8} atm. In other words, the phase is very efficient at extracting oxygen from the surrounding atmosphere.

3.1.2.3 Anion effects on the $C_{12}A_7$ stability

As shown previously, moisture (H_2O) affects the stability of $C_{12}A_7$ at elevated temperatures, which forms $Ca_{12}Al_{14}O_{32}(OH)_2$ when it is fully saturated. Also, O^{2-} and/or OH^- act as extra-framework anions on the $C_{12}A_7$ lattice framework. Interestingly, it has

been observed that several other anions can substitute the extra-framework anions and stabilize the phase, as listed in **Table 3.2**.

Table 3.2
Selectively anion substitution of the extra-framework ions on $C_{12}A_7$ phase

Anion	Remarks	Ref.
F^- and Cl^-	It has been observed that halogenated compounds, $C_{11}A_7{\cdot}CaX$, where X is F_2 or Cl_2, can be prepared by heating $C_{12}A_7$ with CaF_2 or $CaCl_2$ at 900 – 1300 °C. If the $C_{11}A_7{\cdot}CaCl_2$ is heated with an excess of CaF_2, the Cl^- ions are exchanged for F^-. The relative stability of the compound is proposed as follows: $Ca_{24}Al_{28}O_{64}F_4 > Ca_{24}Al_{28}O_{64}Cl_4 > Ca_{24}Al_{28}O_{64}(OH)_4$	[93]
O_2^- and O^-	It has been found that O_2^- occurs in the $C_{12}A_7$ crystal prepared by the solid-state reaction between $CaCO_3$ and Al_2O_3 or $Al(OH)_3$ powder. The concentration of O_2^- is measured up to ca. 4×10^{18} units/g. The formation of oxygen radicals (O_2^- and O^-) are formed mainly through the oxidation of the extra-framework O^{2-} ions by absorbed O_2 molecules. The reaction and its enthalpy are shown in **reaction (3.2)**. $O^{2-}(\text{cage}) + O_2(\text{gas}) \rightarrow O^-(\text{cage}) + O_2^-(\text{cage})$ (3.2) $\Delta H = -131\ \text{kJ/mol}O_2$	[94–96]
CN^-	CN-mayenite was synthesized by a solid-gas reaction under vacuum condition at 1100 °C. The reaction is proposed as in **reaction (3.3)**. $12CaO + 6Al_2O_3 + 2AlN + 2CO = Ca_{12}Al_{14}O_{32}(CN)_2$ (3.3)	[97]
H^-	H^- ions are incorporated into the cages of $C_{12}A_7$ by a thermal treatment in a hydrogen atmosphere. When the sample was heated in a He carrier gas, hydrogen molecules were released at 500 – 750 °C. In addition, applying an electric field at 700 °C induced H^- emission. The proposed incorporation mechanism of H^- anions in $C_{12}A_7$ is shown in **reaction (3.4)** and/or **(3.5)**. $O^{2-}(\text{cage}) + H_2(\text{atmosphere}) \rightarrow OH^-(\text{cage}) + H^-(\text{cage})$ (3.4) $O^{2-}(\text{cage}) + H_2(\text{atmosphere}) \rightarrow 1/2O_2(\text{atmosphere}) + 2H^-(\text{cage})$ (3.5)	[98]
S^{2-}	It is claimed by Zhmoidin [99] that the crystalline structure of $C_{12}A_7$ can be achieved when the melt absorbs certain gases from the atmosphere (O_2, H_2O, CO_2, CO, SO_3) or when CaF_2, $CaCl_2$, CaS, $CaSO_4$, $CaCO_3$ are added to the melt. When CaS is introduced, it has a chemical composition of $C_{11}A_7{\cdot}CaS$, and has the following characteristics:	[99]

Refractive index 1.643, density 2.619 g/cm^3, and incongruent phase.

C_2^{2-}	The C_2^{2-} ions may dissolve into the melt to compensate for the oxygen deficiency in $C_{12}A_7$, which makes the $C_{12}A_7$ phase stable in reducing atmosphere. The C_2^{2-} and O^{2-} have close anion sizes, which are 1.2 and 1.4 Å, respectively. Thus, the C_2^{2-} ions may act as a template instead of the extra-framework O^{2-} in the cages. The proposed mechanism is shown in **reaction (3.7)** and/or **(3.8)**.	[77]

$$C_2^{2-}(\text{melt or glass}) \rightarrow C_2^{2-}(\text{cage}) \rightarrow C_2(\text{atmosphere}) + 2e^-(\text{cage}) \quad (3.7)$$

$$C_2^{2-}(\text{cage}) + 2O^{2-}(\text{cage}) \rightarrow 2CO(\text{atmosphere}) + 6e^-(\text{cage}) \quad (3.8)$$

3.2 Summary of paper 2 - Smelting-reduction mechanism and slag phases formation

The characteristics of calcium aluminate-containing slags and pig iron produced from low-grade bauxite ores were studied. The thermochemistry of oxides reduction, elements distribution between the slag and metal products, and mechanisms of the formation of phases in them can be explained. Iron from bauxite ores is removed from 94.8 to 99.9 wt.% during smelting-reduction by carbon and yields the alumina-containing slag containing less than 1 wt.%Fe, dependent on the slag chemistry.

It is evident that the partial separation of Mn, Si, Ti, V, and P oxides occurs through the smelting-reduction, and therefore, the distribution coefficient (L_i) is calculated. Low L_{Mn}, L_P, and L_V values are observed, whereas L_{Si} and L_{Ti} values ranges are considerably wide depending on the characteristics of the produced slag.

The viscosity in calcium-aluminate slags with CaO/SiO_2 mass ratio less than three is higher compared to other compositions at elevated temperatures. It causes less of Fe-removal and gives the more porous product. Furthermore, silicon loss from high SiO_2-containing bauxites may occur at elevated temperatures through the SiO gas formation.

Concerning the leachable slag phases (CA, $C_{12}A_7$), which are observed in one of the slags, are obtained after the smelting-reduction of bauxite that has $Al_2O_3/(Fe_2O_3 + SiO_2)$ mass ratio higher than two. It is also worth noting that the complex bonding between titanium and aluminum oxides in slag is not favorable for the leaching process and is likely to occur in the $CaO{\cdot}Al_2O_3{\cdot}SiO_2$ phase.

3.2.1 Methodology

This section describes the applied experimental activities about the pyro-metallurgical part of the Pedersen process for treating selected low-grade bauxites. Consecutively, the procedure consists of materials preparation and characterization, and the details of smelting-reduction treatment.

3.2.1.1 Materials preparation and characterization

Brazilian, Greek, and Iranian low-grade bauxite ores were used in the study, as shown in **Fig. 3.7**, which were denoted as B-, G-, and I-bauxite in the paper, respectively. The bauxite ore was mixed with lime and coke, which corresponds to the Pedersen smelting process [44]. The amount of lime and coke used were based on the characteristics of the bauxites, and the lime/bauxite ratios for B-, G-, and I- are 0.55, 0.8, and 0.44, respectively.

Fig. 3.7 Brazilian, Greek, and Iranian low-grade bauxites used in the study.

Pig iron and slag are the products of the smelting-reduction treatment. For the targeted slag compositions, the CaO/Al_2O_3 (C/A) mass ratios were in the range of 0.65 to 0.75. The amount of coke in the current paper was 1.5 times larger than the stoichiometric needed to assure the complete reduction of iron oxides. Coke was dried in an oven at 100 ^oC for 12 hours before use to remove any free-moisture content.

The mass of bauxite ore, lime, and coke required for the smelting trial are calculated based on the following **Equations (3.2) – (3.4)**:

$$\text{Bauxite ore mass}\ (\text{g}) = \frac{m_{\text{calcined bauxite}} \times (100 + \text{wt.\%LOI}_{(\text{bauxite})})}{100} \tag{3.2}$$

$$\text{Lime mass}\ (\text{g}) = \frac{\left(m_{Al_2O_3\,(\text{bauxite})} + m_{Al_2O_3\,(\text{coke})}\right) \times \left(\frac{\text{wt.\%CaO}_{(\text{slag})}}{\text{wt.\%Al}_2\text{O}_{3(\text{slag})}}\right)}{\text{wt.\%CaO}_{(\text{lime})}} \times 100 \tag{3.3}$$

$$\text{Coke mass}\ (\text{g}) = \frac{\left(m_{Fe_2O_3\,(\text{bauxite})} \times \left(\frac{n_C \times A_C}{n_{Fe_2O_3} \times A_{Fe_2O_3}}\right)\right)}{\text{wt.\%C}_{(\text{coke})}} \times 100 \times 1.5 \tag{3.4}$$

Where $m_{\text{calcined bauxite}}$, $m_{Al_2O_3\,(\text{bauxite})}$, $m_{Al_2O_3\,(\text{coke})}$, and $m_{Fe_2O_3\,(\text{bauxite})}$ represent the masses of calcined bauxite, Al_2O_3 phase in both bauxite and coke, and Fe_2O_3 in bauxite, respectively. Also, wt.%$LOI_{(bauxite)}$, wt.%$CaO_{(lime)}$, wt.%$CaO_{(slag)}$, wt.%$Al_2O_{3(slag)}$, denote the weight percentage of loss on ignition of bauxite during heating, the weight percentage of CaO phase in lime, and the weight ratio of CaO and Al_2O_3 in the targeted slag. While n_C, $n_{Fe_2O_3}$, A_C, $A_{Fe_2O_3}$ are the mol and relative atomic mass of both C and Fe_2O_3, which refer to the carbothermic reduction of Fe_2O_3 phase in a bauxite ore as in **reaction (3.5)**.

$$Fe_2O_{3(s)} + 3C_{(s)} \rightarrow 2Fe_{(s)} + 3CO_{(g)} \tag{3.5}$$

Part of the ores and products were ground by a ring mill into powder size for phase identification using Bruker D8 A25 DaVinci™ XRD with CuKα radiation, 10 - 75° diffraction angle, 0.01° step size, and 2.5° for both primary and secondary soller slit. The slag and pig iron samples were mounted in epoxy, polished, and carbon-coated before employing Hitachi SU6600™ SEM to capture the secondary electron (SE) and backscattered electron (BSE) images, X-ray element mapping, and use of EDS. XRF analysis was used to identify the overall composition of the ores and pig iron and slag products. Moreover, a JXA-8500F™ EPMA, supported by WDS, was applied for high accuracy on quantitative analysis of elements in selected phases of the products.

3.2.1.2 Smelting-reduction treatment

The mixture of starting materials was set into an open graphite crucible with 115 mm of inner diameter. The crucible was placed in a 75-kVA induction furnace and heated relatively slow until it reached 1650 °C. The partial pressure of the gas (O_2, N_2, CO, CO_2, etc.) inside of the crucible was not measured during the smelting trial. However, an oxidizing atmosphere (with less oxygen than air) during the smelting reduction process can be considered to exist because the experiments were in the open furnace. The smelting-reduction duration was one hour at 1650 °C, while the top of the crucible was partially closed by refractories to minimize the dissipation of the heat. However, the top was opened at intervals to crush the sintered materials or a solidified foamy-slag, while stirring of the melts was proper due to the induction in pig iron and gas bubbles movements in the slag. To compensate for the heat loss, I heated the mixture until 1750 °C for the last ten minutes of the treatment. Consecutively, the mean and standard deviation of B-, G-, and I-Bauxite smelting temperature is 1664 ± 44 °C, 1662 ± 54 °C, and 1637 ± 38 °C. Fig.

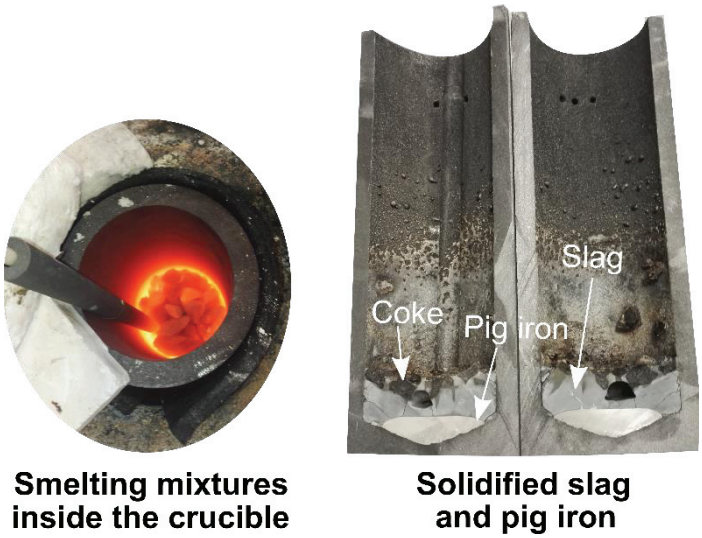

Fig. 3.8 Images taken during the smelting trials which show the heated mixtures inside the crucible and the cross-section of crucible after the smelting that shows solidified slag, pig iron and coke.

3.2.2 Theoretical background

The theoretical background of the paper is based on the smelting-reduction thermochemistry, which includes the Ellingham diagram, and also the graphite morphologies in cast-iron.

3.2.2.1 Smelting-reduction thermochemistry

The Gibbs energy change when one mole of a compound is formed from elements at 1 atm pressure is also known as the standard Gibbs energy change of formation, $\Delta G°$. At different temperatures, it can be calculated as in **Equation (3.6)**.

$$\begin{aligned}\Delta G^o &= \Delta H^o - T\Delta S^o \\ &= \left[\Delta H^o_{25^oC} + \int_{25^oC}^{T} \Delta C p dT\right] - T\left[\Delta S^o_{25^oC} + \int_{25^oC}^{T} \left(\Delta Cp/T\right) dT\right]\end{aligned} \tag{3.6}$$

Where $\Delta H°$, T, and $\Delta S°$ is the change of enthalpy formation, temperature, and the change of entropy. In 1944, H. J. T. Ellingham [100] made a diagram, which is later known as the Ellingham diagram, that shows the variation with temperature of the $\Delta G°$ of the oxides and sulfides of metals and of certain non-metals commonly used in metallurgical reduction processes. A reconstruction of the diagram showing the $\Delta G°$ of several oxides in regards to the temperatures and partial pressure of CO/CO_2, H_2/H_2O, and O_2 is shown in **Fig. 3.9**. Consider an equilibrium condition of a metal (M), O_2(gas), and its oxide (M_xO_y) as in **reaction (3.7)**. If both M and M_xO_y are in their standard states, then the equilibrium constant (K) would be expressed as in **Equation (3.8)**.

$$(2x/y)\mathrm{M} + \mathrm{O}_{2(\mathrm{gas})} = (2/y)\mathrm{M}_x\mathrm{O}_y \tag{3.7}$$

$$K = 1/pO_2 \tag{3.8}$$

Furthermore, the equilibrium oxygen partial pressure of **reaction (3.7)** at a given temperature can be given as in **reaction (3.9)**.

$$\Delta G^o = -RT \ln K = RT \ln pO_2 \tag{3.9}$$

The reaction above means that if at any temperature, the actual partial pressure of oxygen is higher than the calculated value, spontaneous oxidation of metal M occurs, while oxide M_xO_y decomposes to metal M and O_2(gas) at the oxygen partial pressure less than the equilibrium value.

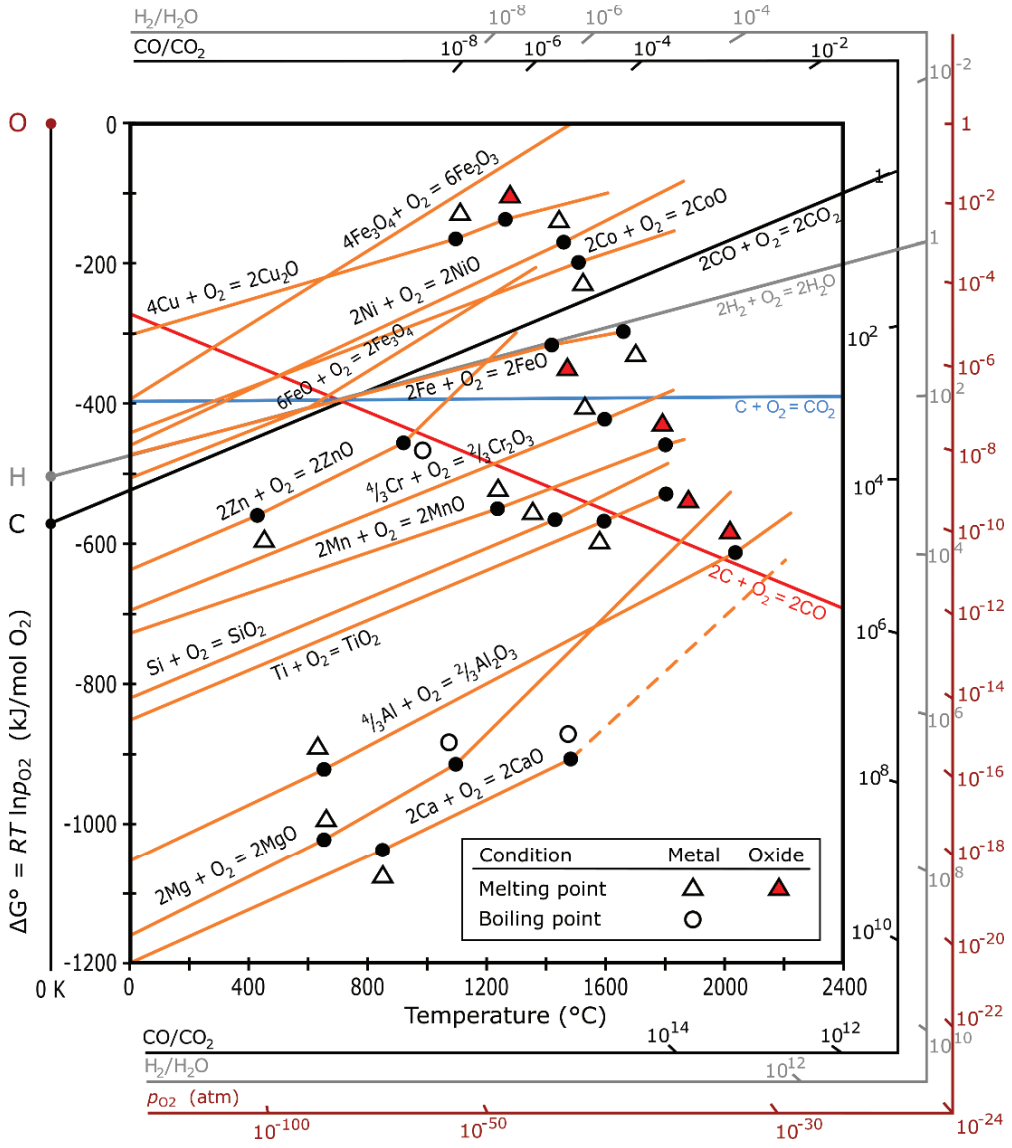

Fig. 3.9. Ellingham diagram for several oxides with the temperatures and partial pressure of CO/CO_2, H_2/H_2O, and O_2 [100].

From the Ellingham diagram, we can see that the CO_2 (gas) is in favor to be produced from the oxidation of carbon at low temperatures, whereas the partial pressure of CO (gas) increases at high temperatures (> ca. 700 °C). As the CO (gas) is a more potent reducing agent than the carbon at temperatures below 700 °C, then it is likely that the reduction of Fe_2O_3 to Fe_3O_4 (**reaction 2.8**) and Fe_3O_4 to FeO (**reaction 2.10**) by means of CO (gas) occurring at that range of temperatures. While the reduction of FeO to Fe (**reaction 2.11**) is suggested to occur when the FeO reacts with a dissolved carbon in a slag phase [51]. In the meantime, the reduction of MnO, SiO_2 and TiO_2 by CO (gas) favorably happens at high temperatures ca. 1400, 1550 and 1610 °C, respectively.

By means of reaction equations module in HSC™, a calculation of $\Delta G°$ of several reactions during smelting-reduction and slag making at a temperature range up to 1785 °C is shown in **Fig. 3.10**. It is worth to note that the calculation was made using an assumption that the reactions occur in equilibrium conditions.

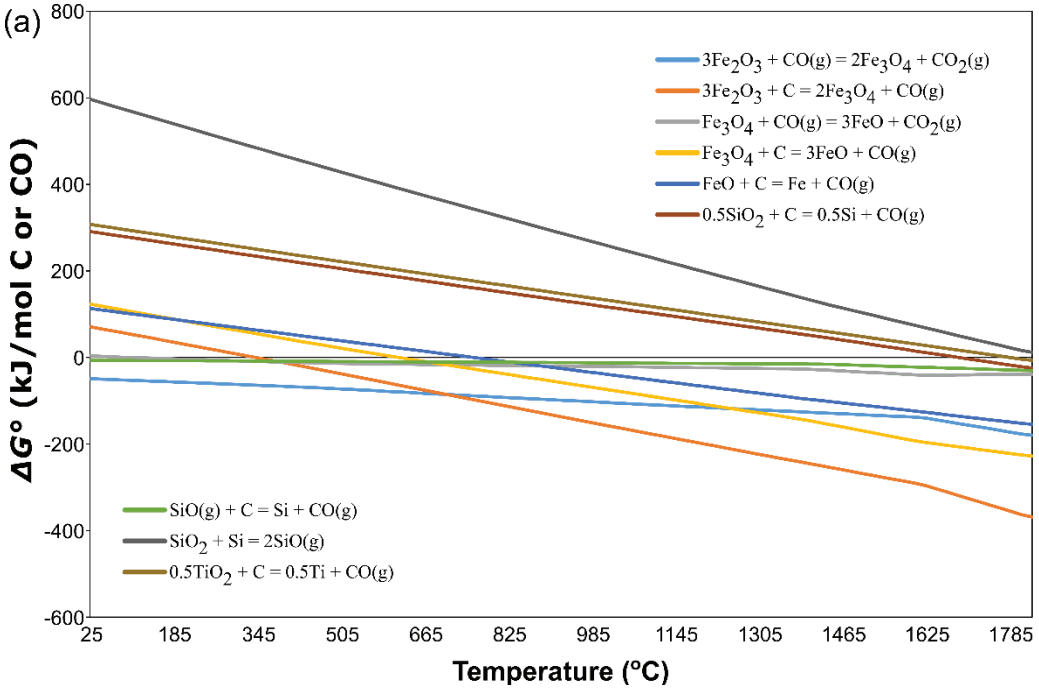

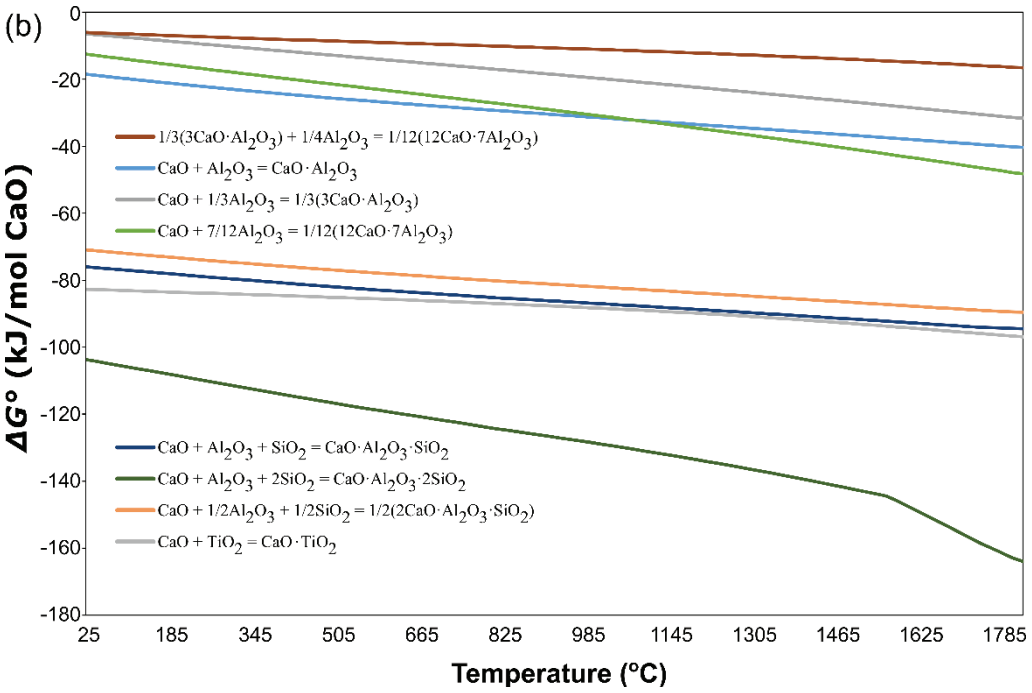

Fig. 3.10 The standard Gibbs energy change of formation of several reactions of (a) oxides reduction, and (b) slag-making oxidation during the smelting process.

3.2.2.2 Graphite structures and distribution in a cast-iron

In the paper, the composition and microstructure of cast iron produced from the smelting-reduction treatment of bauxite were investigated. The cast iron primarily consists of Fe_{metal} as the matrix and graphite. Flakes and spheres are the two most commonly observed graphite shapes in cast iron [101,102], as shown in **Fig. 3.11**. While other morphologies, including compacted graphite, star-like graphite, and single-layer graphene, also have been reported [101]. It was reported in the literature [103] that in a "clean" melt, of which oxygen, sulfur, and possibly phosphorous have been removed, a spherulitic growth is preferred as it can occur with minimum activation energy. In other words, the spherodizer elements, e.g., magnesium and cerium, do not directly assist the growth of the sphere, but rather scavenge the oxygen and sulfur as oxides and sulfides so that they let the graphite sheets wrapping as shown in **Fig. 3.11(b)**.

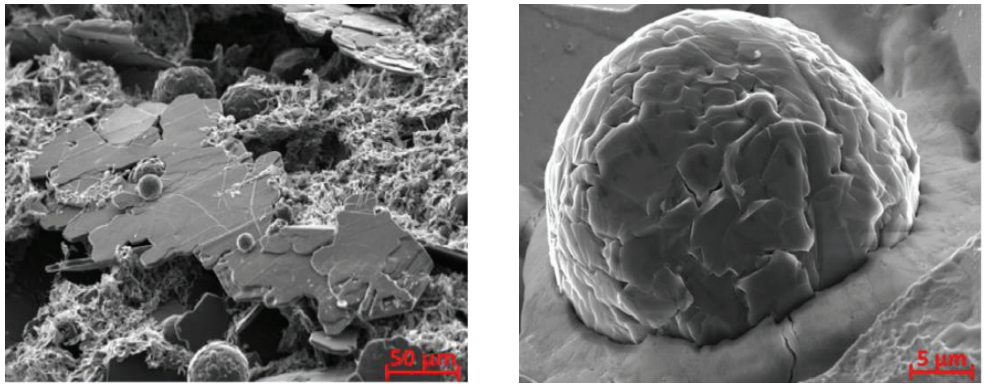

(a) (b)

Fig. 3.11 SEM images of graphite morphologies in a profoundly etched samples (a) flake and (b) sphere, after Amini and Abbaschian [101].

Moreover, **Fig. 3.12** shows an illustration of the graphite distribution in five different types [104]. Type A is random flake graphite in a uniform distribution. Type B is a rosette flake graphite, which is a type of reasonably rapid cooling and is common with moderately thin sections and along the surfaces of thicker sections, and sometimes results from poor inoculation [105]. Type C is a kish (large flake) graphite with a hyper-eutectic composition. Type D is undercooled flake graphite, and type E is interdendritic flake graphite with a hypo-eutectic composition. In addition, **Fig. 3.13** shows an example of the microstructure of cast iron obtained from a hypoeutectic, eutectic, and hypereutectic melt.

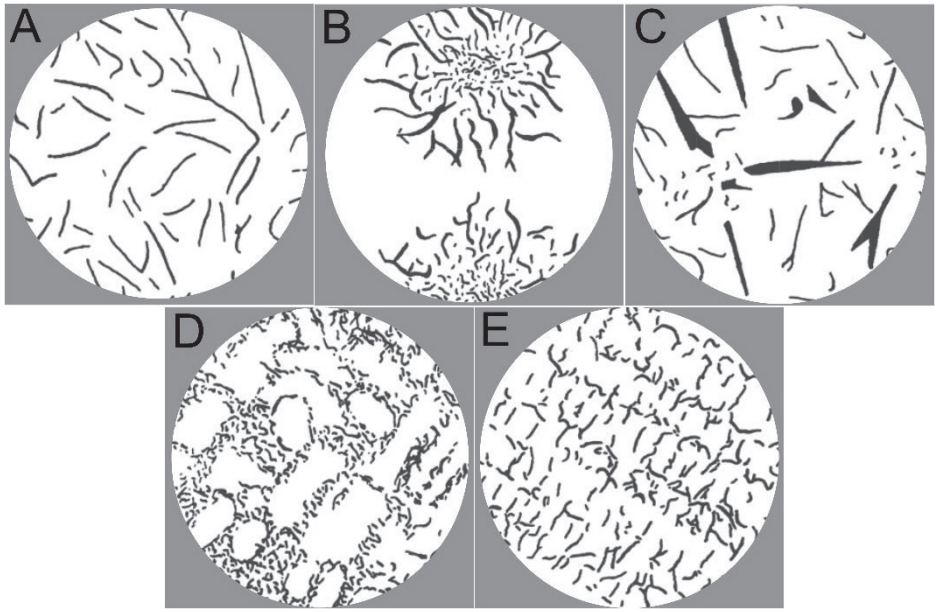

Fig. 3.12 An illustration of graphite distribution that show type "A" random flake, type "B" rosette flake, type "C" kish or large flake, type "D" undercooled flake, and type "E" interdendritic flake graphite [104]

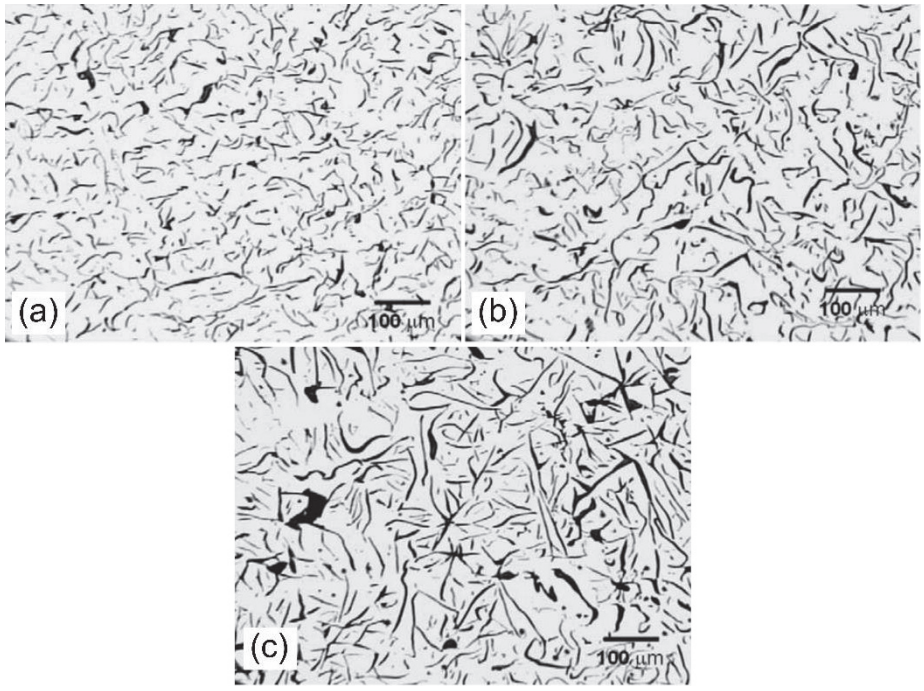

Fig. 3.13 Microstructure of (a) hypoeutectic melt, (b) eutectic melt, (c) hypereutectic melt [106].

Chapter 4

Leaching Part of the Pedersen Process

This chapter is written based on papers 3 – 7 in **chapter 6,** which covers the leaching part of the Pedersen process. The third and fourth papers discussed the leaching thermochemistry of calcium aluminate slags in Na_2CO_3 – NaOH solution, which is titled "The leachability of calcium aluminate phases in slags for the extraction of alumina" and "Leaching characteristics and mechanism of the synthetic calcium-aluminate slags for alumina recovery." Both papers were published in Proceedings of 35th International ICSOBA Conference, and Hydrometallurgy journal, volume 185, respectively. The fifth paper discussed the leaching mechanism of slag and grey mud characteristics. It is titled "The leachability of a ternary CaO-Al_2O_3-SiO_2 slag produced from smelting-reduction of low-grade bauxite for alumina recovery," and was published in Hydrometallurgy journal, volume 191. Moreover, the sixth and seventh papers showed the leaching kinetics of the CaO–Al_2O_3–SiO_2 slag in the Na_2CO_3 solution. The papers titled "Kinetics of the leaching of alumina-containing slag for alumina recovery" and "Leaching kinetics and mechanism of slag produced from smelting-reduction of bauxite for alumina recovery." The sixth paper was published in European Metallurgical Conference 2019. While the seventh paper was submitted to a peer-review journal.

4.1 Summary of paper 3 and 4 – Leaching thermochemistry

The papers investigated several synthetic calcium aluminate slags leachability in solutions containing Na_2CO_3 and NaOH at different temperatures and durations. Depending on the type and number of phases in the slags, it is shown that increasing temperature enhances the leachability and leaching extent. The rate of leaching is fast, and significant digestion occurs within relatively short reaction times. In binary calcium aluminate slags, the leachability of one phase affects the leaching behavior of the other ones. The leachability of the CA phase in slag is hindered by the presence of the less leachable CA_2 phase. The leachability of the observed calcium aluminate phases in binary slags from the highest to the lowest order is CA, C_3A, and CA_2.

Furthermore, a calcium aluminate slag, which consists only $C_{12}A_7$ phase, is seen as the most leachable slag in a Na_2CO_3 solution compared to the other slag compositions in the CaO-Al_2O_3 binary system. The leaching recovery may decrease with the precipitation of $Al(OH)_3$ in bayerite form, and $Ca_3Al_2(OH)_{12}$, a hydrogarnet phase. However, a "free-NaOH" can suppress the formation of those two compounds, accordingly. The less stable form of $CaCO_3$, vaterite, is likely formed in the residue from a relatively low calcium-containing slag (33 – 49 wt.%CaO), and the stable form, calcite, is optimally formed from slag which contains CaO more than 49 wt.%. The non-bridging oxygen (NBO) over the tetrahedral structure (T) index shows that the atomic structure may affect the leaching extent of the slags, wherein decreasing order the index of NBO/T of the calcium aluminate phases is C_3A > CA > CA_2. The $C_{12}A_7$ phase is an exceptional case where it has "free" O-ions at the center of the cage structure, which makes it easily depolymerize. The morphology and size changes of the obtained residues are apparent and clustered in the range of small (< 15 μm), moderate (30 – 40 μm), and large (100 – 170 μm), whereas the agglomeration of individual $CaCO_3$ particle might be the dominant mechanism of increasing particle size compared to the primary crystal growth.

4.1.1 Methodology

4.1.1.1 Slags preparation

In both papers 3 and 4, synthetic slags were prepared by smelting the proportioned mixture of high purity CaO (96 wt.%) and Al_2O_3 (99.9 wt.%) powders inside graphite crucibles at 1650 °C for 1 hour by means of 75 kVA induction furnace. The heating rate was kept slow at 15 °C/min up to 1000 °C to remove hydrates and moisture in the mixture, then 30 °C/min until reaching the targeted smelting temperature. The crucible was air-cooled inside the furnace at 28 °C/min from 1650 °C to 1300 °C, and the cooling rate exponentially decreased until it reached room temperature. A Tungsten/Rhenium alloy thermocouple with alumina insulating tube and wired with molybdenum alloy was inserted in a graphite thermo-well and fixed to the wall of the graphite crucible to measure the temperature inside of the crucible. The crucible was crushed, and the slags were collected and ground with a vibratory ring mill at 800 rpm for one minute. The size distribution was measured by a laser particle analyzer Horiba LA-960 in a wet analysis.

4.1.1.2 Leaching of the slags

The leaching parameters used in the papers are as follows: 100 – 120 g/L of Na_2CO_3 and up to 7 g/L of NaOH for the leaching solutions, 45 - 75 °C for the leaching temperature, 10 - 120 min for the leaching duration, and 400 rpm for the stirring magnetic speed. The leaching experiment was performed inside an open beaker glass, which was heated on top of a hot plate and measured with a pH meter at the same time, as shown in **Fig. 4.1**. The loss of solution due to the evaporation was neglected, and in order to minimize the loss, the top of the beaker was sealed by using a plastic paraffin film. At the end of leaching, the leachate and the residue were filtered by an ashless grade of quantitative filter paper. The pregnant liquid solution (PLS) was stored in a vial, whereas, the residue was stored in a dryer at 100 °C for an overnight to remove the contained moisture.

Fig. 4.1 Leaching experiment using a hot plate, beaker glass, and pH meter. pH meter was used to measure pH value continuously during the leaching trials.

4.1.2 Theoretical background

The theory covers the leaching thermochemistry of calcium aluminate slags and Na_2CO_3 solution, and also its relations with the pH value.

4.1.2.1 Leaching reactions

The leaching reactions between CA, $C_{12}A_7$, C_3A, and CA_2 phases and Na_2CO_3 solutions have been shown earlier in **reactions (2.28) – (2.31)**, respectively. As the leaching reactions are the main topics in the current section, then the reactions are presented again here to ease the reader.

$$CaO \cdot Al_2O_{3(s)} + Na_2CO_{3(aq)} = 2NaAlO_{2(aq)} + CaCO_{3(s)} \quad (2.28)$$

$$12CaO \cdot 7Al_2O_{3(s)} + 12Na_2CO_{3(s)} + 5H_2O_{(l)} = 14NaAlO_{2(aq)} + 12CaCO_{3(s)} + 10NaOH_{(aq)} \quad (2.29)$$

$$3CaO \cdot Al_2O_{3(s)} + 3Na_2CO_{3(aq)} + 2H_2O_{(l)} = 2NaAlO_{2(aq)} + 3CaCO_{3(s)} + 4NaOH_{(aq)} \quad (2.30)$$

$$CaO \cdot 2Al_2O_{3(s)} + Na_2CO_{3(aq)} + 2NaOH_{(aq)} + 7H_2O_{(l)} = 4NaAl(OH)_{4(aq)} + 3CaCO_{3(s)} \quad (2.31)$$

The product of the reactions contains: (a) Sodium aluminate in hydrated ($NaAl(OH)_4$) or un-hydrated ($NaAlO_2$) aqueous phase, (b) NaOH such as in **reactions (2.29)** and **(2.30)**, and (c) Solid $CaCO_3$. It needs one mole of Na_2CO_3 and two moles of NaOH to leach one mole of the CA_2 phase (**reaction 2.31**). While other calcium aluminates need no addition of NaOH in their leaching reactions.

The equilibrium amount of thermodynamic **reactions (2.28) – (2.31)** at temperature 25 – 100 °C in 1 atm is calculated using HSC Chemistry™ with Equilibrium Compositions module is shown in **Fig. 4.2**. The modeling is based on the Pitzer (1973) theory on calculating the activity coefficient of electrolytes. The input amount and output species used for the calculation are shown in **Table 4.1** and **4.2**. The input species and the amount used in the calculation are chosen as an attempt to indicate the experimental leaching conditions in the papers. The same amount of $H^+_{(aq)}$ and $OH^-_{(aq)}$ is introduced to maintain the electronic neutrality of the system.

Table 4.1
The list of input species that is used in the thermochemical simulation

Input species	Figure	Quantity	
		(mol)	(g/L)
$CaO \cdot Al_2O_{3(s)}$	4.2(a)	0.3	50
$Na_2CO_{3(aq)}$		0.9	102.6
$H_2O_{(l)}$		55.5	1000
$OH^-_{(aq)}$		1×10^{-7}	1.7×10^{-6}
$H^+_{(aq)}$		1×10^{-7}	1×10^{-7}
$12CaO \cdot 7Al_2O_{3(s)}$	4.2(b)	4×10^{-2}	50
$Na_2CO_{3(aq)}$		0.9	102.6
$H_2O_{(l)}$		55.5	1000
$OH^-_{(aq)}$		1×10^{-7}	1.7×10^{-6}
$H^+_{(aq)}$		1×10^{-7}	1×10^{-7}
$CaO \cdot 2Al_2O_{3(s)}$	4.2(c)	0.24	50
$Na_2CO_{3(aq)}$		1.13	120
$H_2O_{(l)}$		55.5	1000
$OH^-_{(aq)}$		1×10^{-7}	1.7×10^{-6}
$H^+_{(aq)}$		1×10^{-7}	1×10^{-7}

Table 4.2
The selected output species that is used in the thermochemical simulation

Output species in Al – O – H – Ca – C – Na aqueous solution			
$Al(OH)_2^+{}_{(aq)}$	$AlOH^{2+}_{(aq)}$	$CaHCO_3^+{}_{(aq)}$	$CO_{2(aq)}$
$Al(OH)_{3(aq)}$	$Ca^{2+}_{(aq)}$	$CaO \cdot Al_2O_{3(s)}$	$HCO_3^-{}_{(aq)}$
$Al(OH)_4^-{}_{(aq)}$	$CaC_2H_3O_2^+{}_{(aq)}$	$12CaO \cdot 7Al_2O_{3(s)}$	$HCO_2^-{}_{(aq)}$
$Al_{13}O_4(OH)_{24}{}^{7+}_{(aq)}$	$CaC_2H_3O_3^+{}_{(aq)}$	$Ca(CHO_2)_{2(aq)}$	$Na^+_{(aq)}$
$Al_2(OH)_2{}^{4+}_{(aq)}$	$CaCHO_2^+{}_{(aq)}$	$Ca(OH)_{2(aq)}$	$OH^-_{(aq)}$
$Al_3(OH)_4{}^{5+}_{(aq)}$	$CaCO_{3(aq)}$	$CaOH^+_{(aq)}$	$H^+_{(aq)}$
$AlO^+_{(aq)}$	$CaCO_{3(s)}$	$Ca(OH)_{2(s)}$	

In an equilibrium system, **Fig. 4.2** indicates that the amount of calcium aluminate phases are considerably low compared to the $Al(OH)_4^-$ or $NaAl(OH)_4$ aqueous phases at temperature 25 – 100 °C. This means according to their thermodynamic properties, CA, $C1_2A_7$, and CA_2 phases are leachable in the Na_2CO_3 solution. However, it is evident that side reactions could happen during the leaching, and some calcium aluminate phases could be identified as the less leachable ones [64].

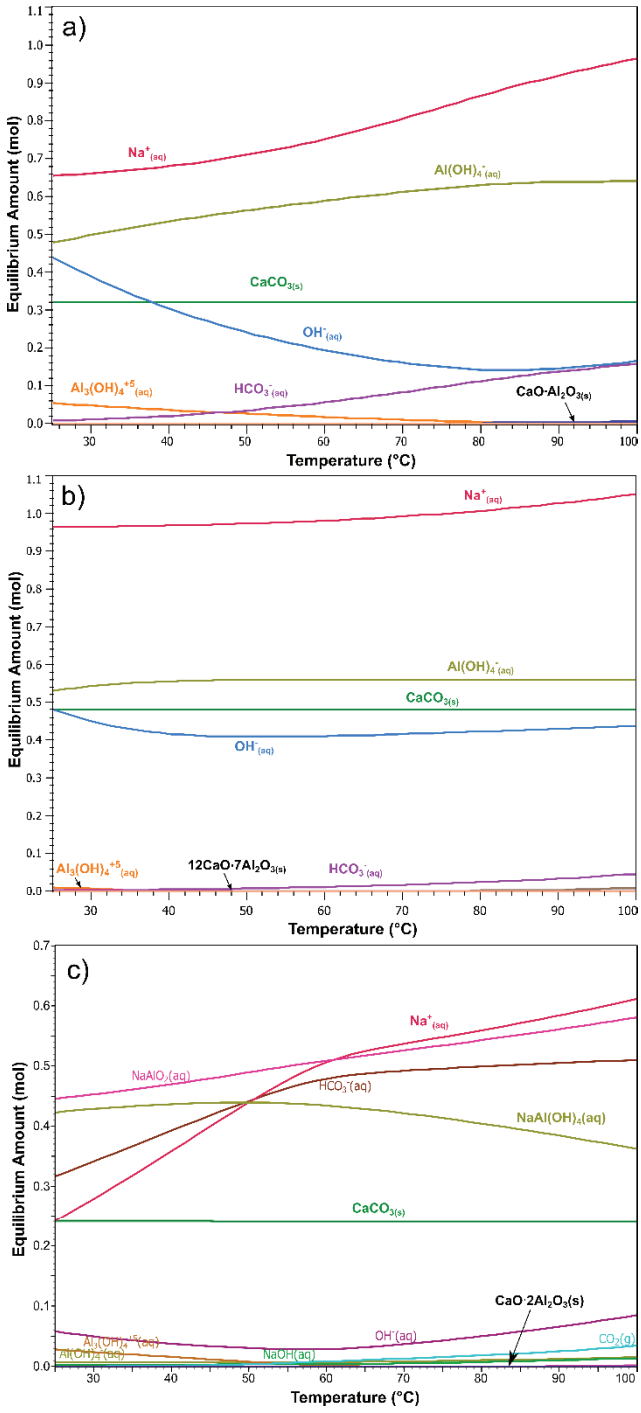

Fig. 4.2 Equilibrium amount of (a) CA, (b) $C_{12}A_7$, and (c) CA_2 phase and selected species in the leaching experiments.

4.1.2.2 Slag structure

As the equilibrium condition of CA, $C_{12}A_7$, and CA_2 phases in Na_2CO_3 solution showed that the phases are leachable (easy to depolymerize), it is then necessary to study the slag structure to understand the reason of depolymerization. There are two popular theories around the slag structure, which are the molecular and ionic theory.

The Molecular Theory

The molecular theory proposes that a liquid slag is composed of individual oxides, fluorides, e.g., MnO, SiO_2, Al_2O_3, FeO, CaO, etc. and that these can combine to form $CaO{\cdot}Al_2O_3$, $CaO{\cdot}SiO_2$, $CaO{\cdot}Al_2O_3{\cdot}SiO_2$, etc. This means every individual oxide in the slag can affect the activity of one another. Rao and Gaskell [108] measured the activity of SiO_2 in MnO-SiO_2 melts at 1400, 1500, and 1600 °C as shown in **Fig. 4.3**. The result implies that the increasing amount of MnO in MnO-SiO_2 gives a negative deviation to the activity of SiO_2 from the ideality.

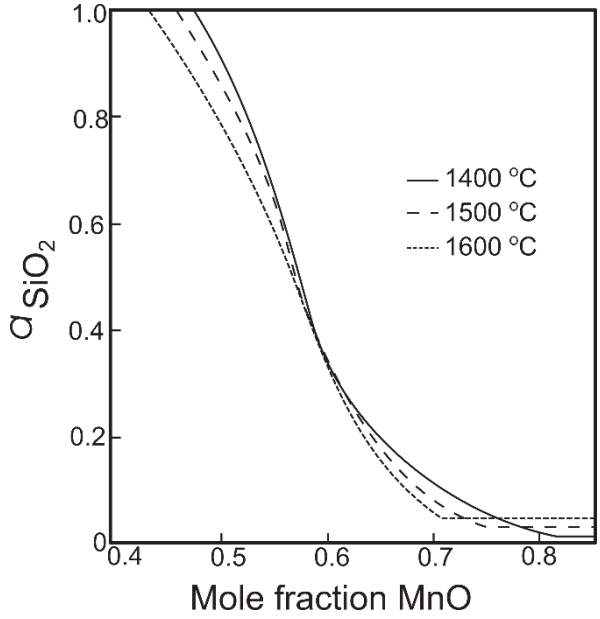

Fig. 4.3 The activity of SiO_2 in MnO-SiO_2 melts at 1400, 1500, and 1600 °C [108].

Furthermore, Olsen et al. [109] comprehensively calculated the phase and liquidus relations, as well as the activities in the slag system of Mn-Si-Ca-Al-Mg-O,

which is the predominant system of slag in the ferromanganese production. **Fig. 4.4** shows the calculated phase and liquidus relations for the MnO-SiO_2-CaO-Al_2O_3-MgO (Al_2O_3/SiO_2 = 0.425; CaO/MgO = 7) system[109], which is a type of high carbon ferromanganese slag system.

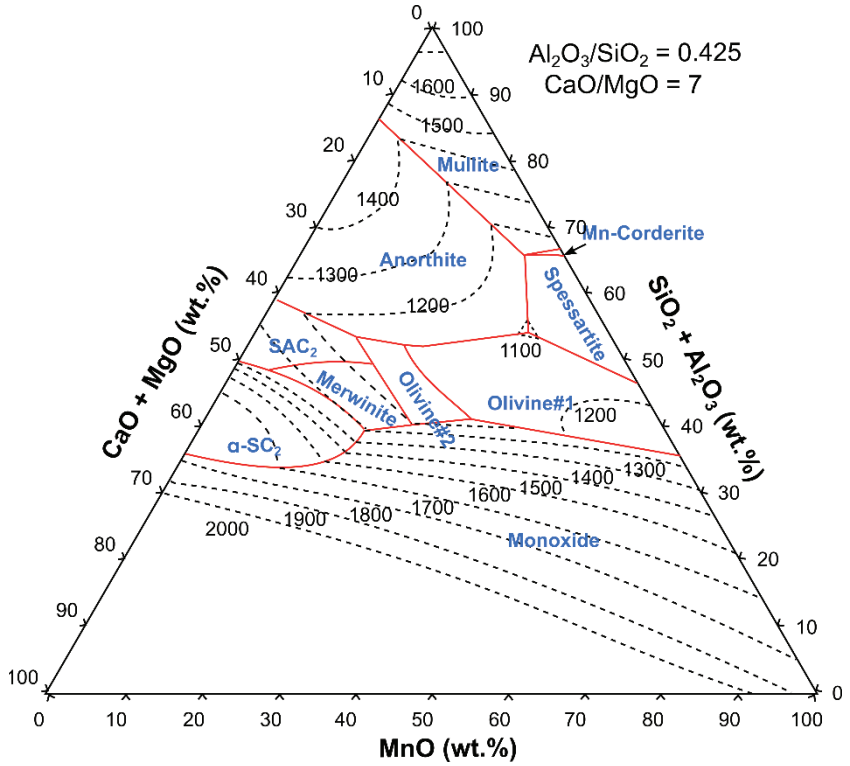

Fig. 4.4 Calculated phase and liquidus relations for the MnO-SiO_2-CaO-Al_2O_3-MgO (Al_2O_3/SiO_2 = 0.425; CaO/MgO = 7).

Another example of the phase and liquidus relation is shown in **Fig. 4.5**, which represents the CaO–Al_2O_3–SiO_2 ternary system. The phase diagram is constructed by FactSage with the FTOxid database. The experimental and calculated works show the phase and liquidus relation and activity of each oxide that constitutes the slag, which occurs both in ferromanganese and CaO–Al_2O_3–SiO_2 slag. However, the molecular theory cannot clearly explain one of the physical properties of slag, which is electrical conductivity.

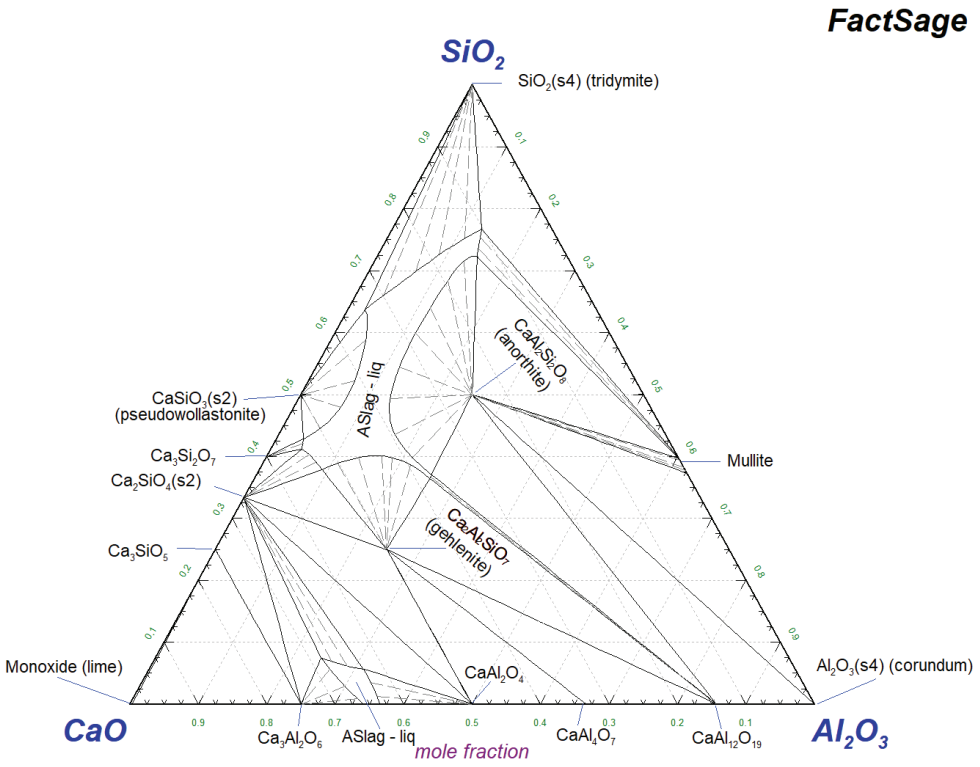

Fig. 4.5 Phase diagram of CaO – Al_2O_3 – SiO_2 at 1400 °C as in FactSage FTOxid database

The Ionic Theory

In 1938, Herasymenko [110] initially proposed the ionic theory of slag when investigating the equilibria between acid slags and liquid steel containing small amounts of chromium in the open-hearth furnace. Herasymenko stated that liquid slags consisted of (I) cations, such as Ca^{2+}, Fe^{2+}, etc., (II) anions such as O^{2-}, F^{2-}, S^{2-}, and (III) anion complexes such as SiO_4^{4-}, PO_4^{3-}, AlO_3^{3-}. At that time, the structure of slag was deduced from the physical properties and phase of equilibria's data, which is most likely rely on the knowledge of the researcher to see the structure effects on the particular physical property. Recently, researchers have used spectroscopic techniques to determine the slag structure, and some insights on the mechanism accounted for the structure-property relationship.

Slag can be divided into two different types, acid, and basic oxides. The first type contains network forming oxides that produce anion, such as SiO_2. While the latter one has significant network breaking oxide that forms a cation, such as MnO, CaO, FeO,

and MgO. Aluminum oxide may act as a network forming and breaking oxide, depending on the slag composition. Some examples of the classification presented in **Table 4.3**.

Table 4.3
Examples of different types of oxides.

Basic oxide	Acid oxide	Amphoteric oxide
Na_2O	TiO_2	Al_2O_3
BaO	SiO_2	Cr_2O_3
SrO	P_2O_5	Fe_2O_3
CaO		
MnO		
FeO		
ZnO		
MgO		
BeO		

Before discussing the mechanism of network breaking and forming oxides, it is worth to know the factor that controls the structure of oxides. And it appears that the dimension relativity of cations and anions and type of bonds between them are the critical factors. **Table 4.4** shows the radius of common cations (R_c) and anions (R_a) [111]. Thus, with the information given above, the coordination number, R_c/R_a ratio, and structure of solid oxides are presented, as shown in **Table 4.5** [112].

Table 4.4
Radius of common cations (R_c) and anions (R_a) [111]

Cations	K^+	Ca^{2+}	Mn^{2+}	Fe^{2+}	Fe^{3+}	Mg^{2+}	Cr^{3+}	Al^{3+}	Si^{4+}	P^{5+}
R_c (nm)	0.133	0.099	0.08	0.074	0.061	0.066	0.063	0.051	0.042	0.035
Anions	I^-	S^{2-}	Cl^-	O^{2-}	F^-					
R_a (nm)	0.220	0.184	0.181	0.140	0.133					

Table 4.5
The structure, coordination number, and R_c/R_a ratio

Structure	Coordination number	R_c/R_a	Examples
Cubic	8	1 - 0.732	-
Octahedral	6	0.732 - 0.414	CaO, MgO, MnO, FeO
Tetrahedral	4	0.414 - 0.225	SiO_2, P_2O_5
Triangular	3	0.225 - 0.155	

Many metallurgical slags contain silica and are a relatively strong acid oxide that constructs the structure and behavior of the slag. In the case of SiO_2, four O^{2-} ions provide the frame of the tetrahedron, and the smaller Si^{4+} ion is situated within the frame, as

shown in **Fig. 4.6(a)**. Since the neighboring cations (Si^{4+}) are mutually repellent, the interval between two Si^{4+} ions should be maximum. The crystalline silica network is shown in **Fig. 4.6(b)** and will be distorted when it melts in a liquid phase, as shown in **Fig. 4.6(c)**.

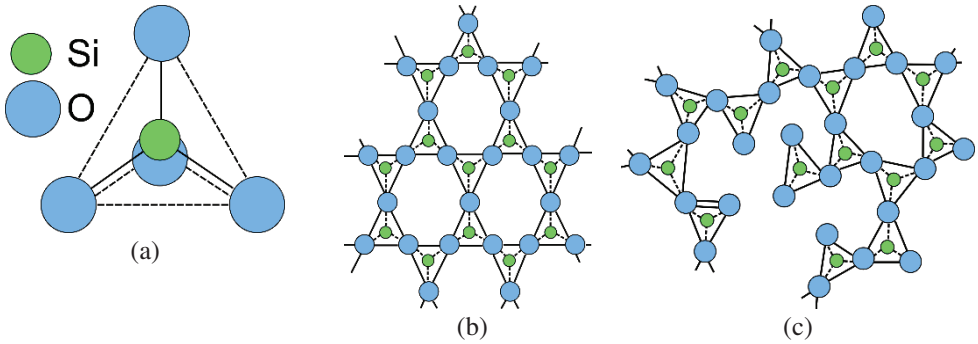

Fig. 4.6 Structure of silica as in (a) tetrahedral structure of SiO_4^{4-}, (b) crystalline network, (c) melts.

As can be seen above, the SiO_4^{4-} tetrahedral are joined together in chains or rings by bridging oxygens (BO). Cations such as Na^+, Ca^+, Mg^{2+}, Fe^{2+} tend to break these bonded oxygens and form non-bridging oxygen (NBO), O^-, and free oxygen, O^{2-}. The degree of depolymerization of a silicate melt can be expressed by the ratio of (non-bridging oxygen atoms/number of tetrahedrally - coordinated atoms) this is usually denoted as NBO/T ratio, and the physical properties such as viscosity, thermal conductivity, etc., are very dependent upon the NBO/T ratio [52]. In other words, with an increasing amount of network breaking oxides, the distorted crystalline network will change into complex rings and chains, and when the total amount of network breaking oxides exceeds 67 mol%, there will only be simple SiO^{4-} anions in the mix[109]. A simple illustration of the mechanism of the network breaking oxides is given in **Fig. 4.7**[113].

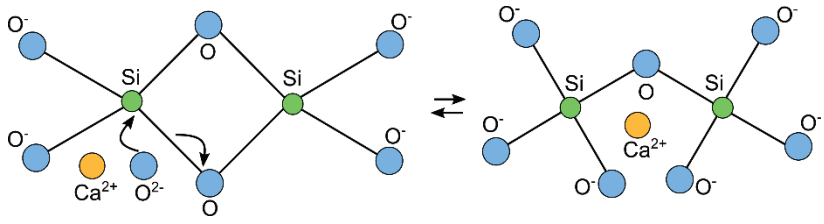

Fig. 4.7 The mechanism of the network breaking oxides (CaO) in a silicate network.

The silicate melts contain various 3-dimensionally, interconnected anion units such as SiO_4^{4-}, $Si_2O_7^{6-}$, $Si_3O_9^{6-}$, $Si_4O_{12}^{8-}$, $Si_6O_{18}^{12-}$, which coexist in the melt (see **Fig.4.8**). The nature of the cation affects the proportion of these anionic units.

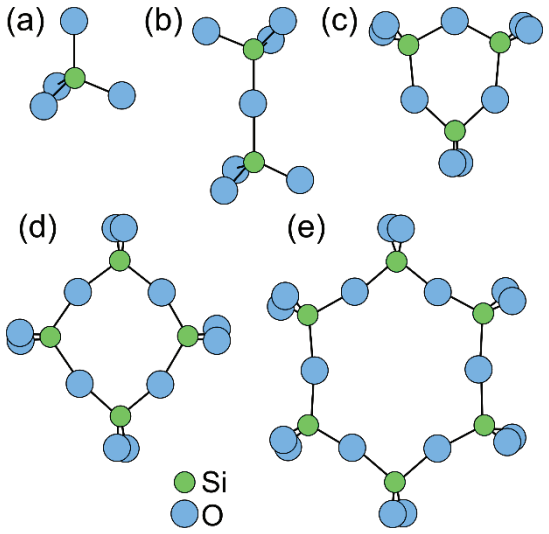

Fig. 4.8 The schematic representation of 3-dimensions of silicate structure in different anionic units (a) SiO_4^{4-}, (b) $Si_2O_7^{6-}$, (c) $Si_3O_9^{6-}$, (d) $Si_4O_{12}^{8-}$, and (e) $Si_6O_{18}^{12-}$.

Molten silica is a poor electrical conductor. However, its conductivity increases mainly by the addition of basic oxides, i.e., CaO, FeO, or MnO as flux. This change is likely due to the formation of ions. The electrical conductivity of slags depends on the number of ions present and the viscosity of the liquid slag. Thus, conductivity will be higher in the liquid state and further increases with the temperature.

Liu et al. [114] found that for the silicate melt without Al_2O_3, more and more bridging oxygen will be broken by the production of non-bridging oxygen with increasing basic oxide content. Therefore, the melt will change its structure from a network of silica to small structural units composed of chains or rings, etc. as mentioned earlier. However, in the $CaO–Al_2O_3–SiO_2$ system, the situation is much more complicated because of the amphoteric behavior of Al_2O_3. In the $CaO–Al_2O_3–SiO_2$ system, there are two types of Ca^{2+} cations: one compensates Al^{3+} ion, and the other forms non-bridging oxygen. **Fig. 4.9** shows the schematic diagrams of these two types of Ca^{2+} cations[114].

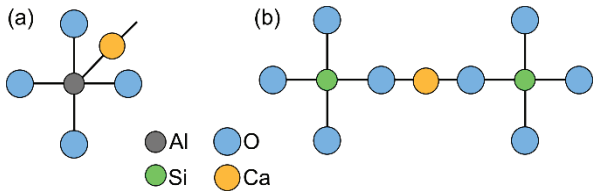

Fig. 4.9 Schematic diagrams of two types of Ca^{2+} ions.

When the basicity of melt is high enough, there are enough metal cations (Ca^{2+}) to participate in the charge compensation. Al^{3+} ions have strong preferences to form AlO_4^{5-} tetrahedral and incorporate into the network of SiO_4^{4-}. Therefore, the degree of polymerization of the melt increases with increasing CaO content until all Al^{3+} ions form AlO_4^{5-} tetrahedrons. After that, CaO will act as the network modifier, and the melt will begin to depolymerize.

4.2 Summary of paper 5 – Leaching mechanism

The leaching treatment of a ternary CaO-Al_2O_3-SiO_2 slag produced from the smelting-reduction of low-grade bauxite was carried out at different temperatures and mixed proportion of Na_2CO_3 and NaOH. Some conclusions can be taken from the experimental works. It is shown that the leaching reaction of calcium-aluminate phases in Na_2CO_3 solution is fast, and temperature gives mild effect to the aluminum extraction in the first 30 min of the reaction. The addition of NaOH in the solution decreases the aluminum dissolution of the slag, while it increases the silicon dissolution into the pregnant liquid solution. The calcite-containing layer formed and distributed around the surface of the slag as the leaching reactions progress. The kinetics of the leaching reaction appears to be diffusion rate-limited as the passive calcium carbonate-containing layer formed at the unreacted surface of slag and may inhibit the progress of leaching reactions.

The results obtained from the current study may pave a new way to utilize CaO-Al_2O_3-SiO_2 slag more effectively. The slow diffusion of Na_2CO_3 to the unreacted $12CaO{\cdot}7Al_2O_3$ phase due to the formation of the calcite-containing layer at the surface of slag is suggested to be the reaction limiting. Therefore, leaching that employs a mechanochemical treatment such as wet grinding, or a sonochemical treatment using ultrasound, can be used to break the layer during the leaching. Such treatments may

allow the Na_2CO_3 diffuse to and attack the unreacted $12CaO \cdot 7Al_2O_3$ and achieve a high aluminum extraction extent.

4.2.1 Methodology

4.2.1.1 Leaching setup

The leaching treatment was performed inside a Parr 4563 mini reactor, which is an Inconel alloys-based vessel with 600 mL capacity that is resistant to chemical attack. The reactor was heated through convection heating using a heating element. It has a lid that is made of Teflon, which is fitted with a condenser for condensing the water vapors that allows the pressure inside of the reactor remained in ambient pressure, and at the same time keeps the liquid-solid (L/S) weight ratio of the system relatively constant. The temperature was measured with a Pt thermocouple, and the stirring was performed through a mechanical stirrer. The thermocouple, stirrer, and heater were connected to Parr 4841, a Programmable Logic Controller (PLC), to set and measure the necessitate parameters during the leaching treatment. An image of the leaching setup is shown in **Fig. 4.10**.

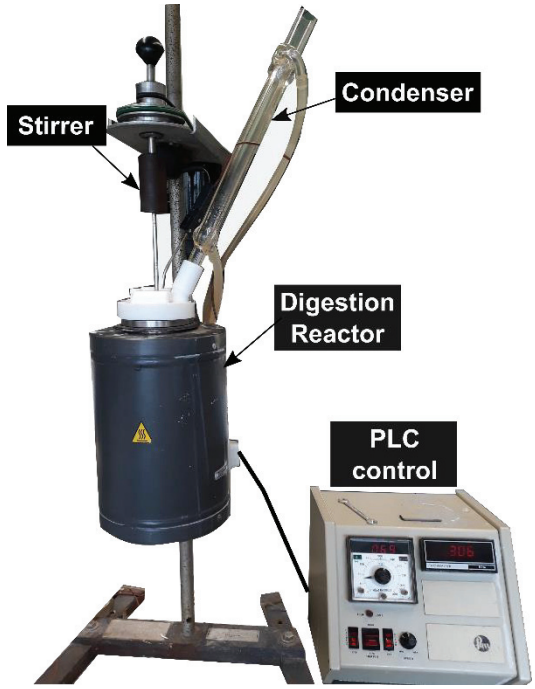

Fig. 4.10 A leaching setup using a 1 L digestion reactor that is equipped with a mechanical stirrer and condenser.

Moreover, the pregnant liquid solution (PLS) and grey mud obtained after the leaching trials were filtered using a Büchner funnel and Erlenmeyer flask to ensure that the solid-liquid were separated adequately, as shown in **Fig. 4.11**. Furthermore, the PLS was contained in a plastic flask to avoid silicon contamination during the waiting time before it was diluted accordingly for ICP-OES analysis purposes, as seen in **Fig. 4.12**.

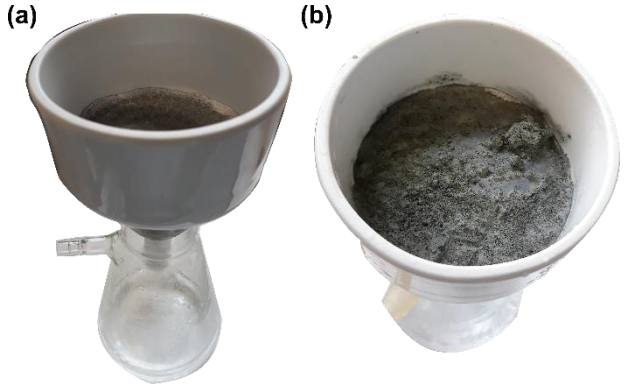

Fig. 4.11 (a) Büchner funnel and Erlenmeyer flask were used for the filtration of solid-liquid after the leaching trials, (b) grey mud obtained on top of the filter paper after the filtration.

(a) (b)

Fig. 4.12 Preparation of the PLS from the leaching trials for an ICP-OES analysis (a) plastic flasks were used instead of a glass-made container to avoid silicon contamination and (b) dilution of the solution

4.2.1.2 Leaching parameters

The leaching solution used in the experiments has a constant concentration of 60 g/L Na_2O, which was made by mixing distilled water, Na_2CO_3 powder, and NaOH pellet with 99.8 wt.% and 99.0 wt.% purity, respectively. The dissolved Na_2CO_3 and NaOH give an extent of Na_2O concentration of the solution that can be denoted as $Na_2O_{(carbonate)}$ and $Na_2O_{(caustic)}$, respectively. The list of leaching parameters that were performed in the experiments is shown in **Table 4.6**.

Table 4.6
Leaching parameters that were performed in the paper 5

Temperature (°C)	Solvent concentration	Na_2O concentration (g/L)	Liquid to solid ratio (mL:g)	Leaching duration (min)
45	100% Na_2CO_3	60	20	30
45	85% Na_2CO_3 + 15% NaOH	60	20	30
45	75% Na_2CO_3 + 25% NaOH	60	20	30
45	50% Na_2CO_3 + 50% NaOH	60	20	30
60	100% Na_2CO_3	60	20	30
60	85% Na_2CO_3 + 15% NaOH	60	20	30
60	75% Na_2CO_3 + 25% NaOH	60	20	30
60	50% Na_2CO_3 + 50% NaOH	60	20	30
75	100% Na_2CO_3	60	20	30
75	85% Na_2CO_3 + 15% NaOH	60	20	30
75	75% Na_2CO_3 + 25% NaOH	60	20	30
75	50% Na_2CO_3 + 50% NaOH	60	20	30

4.2.2 Theoretical background

4.2.2.1 Dissolution of solid phases in aqueous solutions

Leaching is one of the hydrometallurgical processes that employ a dissolution of solid in aqueous solutions as its main activity. In the extractive metallurgical process, a solvent is chosen to dissolve a particular phase selectively in ore or/and concentrate, leaving behind impurities or byproduct, which can be separated by filtration. The process can be classified as physical, chemical, and electrochemical, or an electrolytic process [115]. However, the first two processes are the most relevant in the leaching of alumina from slag and, therefore, the main interest in the current thesis.

Physical dissolution process

An example of the physical process is the dissolution of salt in the water where there is no chemical transformation occurs, as shown in **reaction (4.1)**[115].

$$NaCl_{(s)} + (n+m)H_2O \rightarrow Na(H_2O)_n^+ + Cl(H_2O)_m^- \qquad (4.1)$$

It is known that ionic salts are soluble, whereas covalent salts are not. However, pure ionic or pure covalent are not common. Thus, many anions form coordination bonds by sharing the non-bonded pair of electrons, which are partly covalent.

In the kinetics perspective, a German chemist, Walther Nernst, introduced the concept of the boundary layer in 1904 that paved a way to understand the mechanism of the process. When a solid is in contact with an aqueous phase, it is covered by a thin layer of a stagnant or immobile solution. The layer adheres to the solid, which causes ions or molecules have to diffuse, either to or from the solid surface (reaction interface), abiding the laws of diffusion established by Adolf Fick in 1855[116]. In other words, upon the immersion of crystal of salt in water, it will be covered by a layer of a salt-saturated solution which will then slowly diffuse to the bulk of aqueous phase (bulk fluid) following the **Equation (4.2)** [116]:

$$\frac{dC}{dt} = \frac{D}{\delta} \cdot \frac{A}{V}(C_s - C) \qquad (4.2)$$

Where C is the concentration of the solute at time t, C_s is its solubility in water at the experimental temperature, A is the surface area, V is the volume of solution, D is the diffusion coefficient, δ is the thickness of the boundary layer.

In the same perspective, a boundary layer is created between the interfaces of the solid with the bulk fluid. The boundary layer is the layer of a medium that is not very mobile due to solvent molecules are bound to the surface, and layers of solvent molecules near the surface tend to associate with surface and near-surface molecules [116]. As the distance from the surface of the reaction interface increases, the solvent molecules become more mobile, as illustrated in **Fig. 4.13**. A solution in the bulk fluid moves due to natural or forced convection. Subsequently, bulk fluid transports ions to the boundary layer. However, bulk fluid flow cannot transport ions into areas where the solvent is immobile. As a result, the boundary layer represents the distance where there is little or no bulk fluid flow to or from the reaction interface.

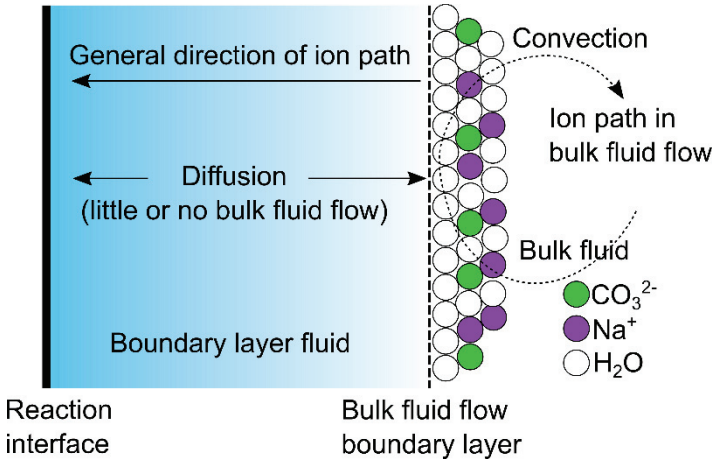

Fig. 4.13 Illustration of bulk fluid flow, boundary layer, and ion transport near a reaction interface.

Chemical dissolution process

Usually, a crystalline solid that has a covalent bond is insoluble in the water; however, due to the presence of a particular ion in solution, it disrupts the bond. Consider a solid phase AB is in contact with water. Then the equilibrium condition is shown as in **reaction (4.3)**.

$$AB_{(s)} = A^{2+}{}_{(aq)} + B^{2-}{}_{(aq)} \tag{4.3}$$

Where the equilibrium constant is $K = [A^{2+}][B^{2-}]$. Whenever the concentration of any of the ions A^{2+} or B^{2-} is decreased, then K is disrupted, which means more solid will go into solution. A neutralization reaction or complex formation may decrease the concentration of any of these ions.

For example, $Al(OH)_3$ has low solubility in water. It is an amphoteric hydroxide, i.e., it may behave as an acid or alkali. As an acid, it has an equilibrium condition, as shown in **reaction (4.4)**.

$$Al(OH)_{3(s)} = AlO(OH)_2^-{}_{(aq)} + H^+{}_{(aq)}; K = 4\times10^{-13} \tag{4.4}$$

In the Bayer process, the presence of NaOH neutralizes the H^+ and, therefore, shifts the equilibrium to the right, which dissolves more $Al(OH)_3$ into the solution as in **reaction (4.5)**.

$$Al(OH)_{3(s)} + OH^-{}_{(aq)} = AlO(OH)_2^-{}_{(aq)} + H_2O_{(l)} \tag{4.5}$$

A further example is for the complex formation. Lead sulfate ($PbSO_4$) has low solubility in the water (see the **reaction (4.6)**). However, in the presence of chloride ions, the complex chloro-plumbate ion is formed as in **reaction (4.7)**, which disrupts the equilibrium of Pb^{2+} as the solid phase $PbSO_4$, thus more solid goes into the solution [115].

$$PbSO_{4(s)} = Pb^{2+}_{(aq)} + SO_4^{2-}{}_{(aq)} \quad (4.6)$$

$$Pb^{2+}_{(aq)} + 4Cl^{-}_{(aq)} = PbCl_4^{2-}{}_{(aq)} \quad (4.7)$$

In literature [115], a chemical dissolution process contains two steps:

1. A physical process, where it establishes an equilibrium between the solid and the aqueous phase.
2. A homogenous chemical reaction in the vicinity of the solid between the ions that just left the solid and the reagent present in the aqueous phase.

As mentioned earlier, on the physical dissolution process, if the solid is in contact with water, it forms an immobile saturated solution at the surface. Subsequently, when the attacking reagent is added to the water, it will diffuse through this boundary layer, where it will neutralize the system or will complex the ions, thus diminishing their concentrations in this region and favoring more dissolutions take place.

In regards to the kinetics, if the reactions in the boundary layer are fast, the process will be controlled by the rate of diffusion of the attacking reagent (diffusion-controlled process). On the other hand, if the rate of the reaction in the boundary layer is slow, it will control the overall process, and the process will be chemically controlled. In other words, a leaching process may be entirely controlled by a physical dissolution process, which is the diffusion of the reagent through the boundary layer is limited, or chemically controlled through the chemical dissolution process, or maybe both.

4.2.2.2 The leaching side reactions

The main reactions of calcium aluminate slags in Na_2CO_3 solution have been presented in **reactions (2.28) – (2.31)**. However, practically, a detrimental side reaction may occur, as reported in the literature [117,118]. **Fig. 4.14** shows the relationship between the mixed solution ratio of $NaOH:Na_2CO_3$ to the number of precipitated compounds in the residue as reconstructed from Lundquist and Leitch [117].

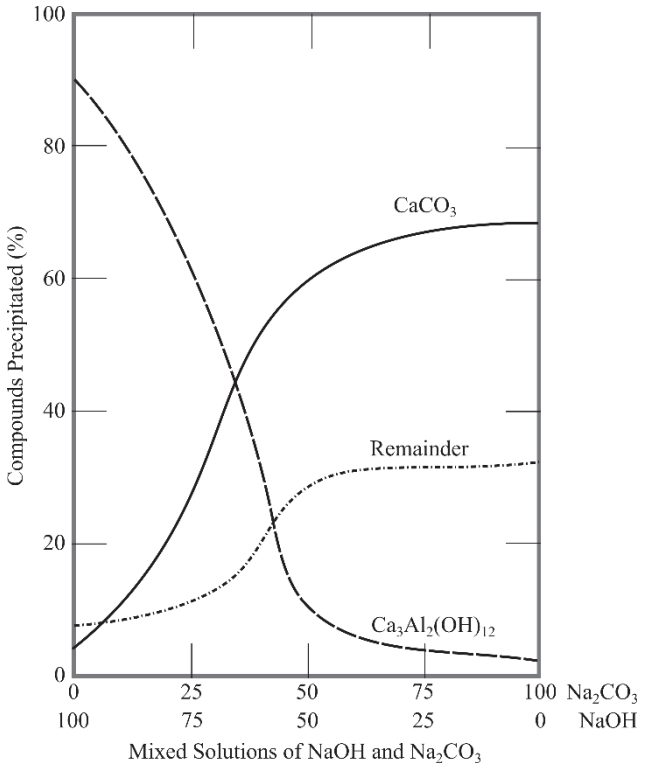

Fig. 4.14 Mixed solutions of NaOH and Na_2CO_3 in accordance with the precipitated compounds as reconstructed from Lundquist and Leitch [117].

As the carbonate ion concentration increases from 0 to 100 wt.%, the $Ca_3Al_2(OH)_{12}$ phase (denoted as $3CaO{\cdot}Al_2O_3{\cdot}6H_2O$ or C_3AH_6) decreases and $CaCO_3$ is precipitated instead. These results show the influence of the calcium ion in sodium aluminate solutions in causing the detrimental precipitation of C_3AH_6. Whittington et al. [119] reported that the free-CaO had been observed to lower alumina recoveries, suggesting that it contributes to the precipitation of C_3AH_6 as in **reaction (4.8)**.

$$2NaAl(OH)_{4(aq)} + 3CaO_{(s)} + 3H_2O_{(l)} = 3CaO \cdot Al_2O_3 \cdot 6H_2O_{(s)} + 2NaOH_{(aq)} \quad (4.8)$$

The reaction indicates that the carbonate anions in the solution are necessitated to the alumina loss prevention as it reacts with the calcium cations and replacing the hydroxyl ion, $Al_2(OH)_{12}^{2-}$, so that $CaCO_3$ precipitation is more favorable than the C_3AH_6 precipitation.

4.2.2.3 The pH calculation

One of the leaching agents used in the experiment on the paper contains 60 g/L $Na_2O_{(carbonate)}$, which means it was prepared by dissolving 103 g of Na_2CO_3 in 1 L of water (0.97 M Na_2CO_3). Therefore, the complete dissolution of Na_2CO_3 is shown by **reaction (4.9)**.

$$Na_2CO_{3(aq)} = 2Na^+_{(aq)} + CO_3^{2-}{}_{(aq)} \quad (4.9)$$

The reaction of sodium cations and water yield a neutral solution. However, the carbonate anions act as weak alkali and can contribute to the pH of the solution as in **reaction (4.10)**.

$$CO_3^{2-}{}_{(aq)} + H_2O_{(l)} = HCO_3^-{}_{(aq)} + OH^-_{(aq)} \quad (4.10)$$

As the initial concentration of CO_3^{2-} is known, we may set an initial, change, and equilibrium table for the above reaction as **Table 4.7**.

Table 4.7
Initial, change, and equilibrium condition of CO_3^{2-} reaction with water.

Condition	$[CO_3^{2-}]$	$[HCO_3^-]$	$[OH^-]$
Initial	0.97	0	0
Change	$-x$	$+x$	$+x$
Equilibrium	$0.97 - x$	x	x

Based on the HSC Chemistry™ database, the equilibrium constant (K_b) of **reaction (4.10)** is known as 2.049×10^{-4}, which gives **Equation (4.11)**.

$$K_b = \frac{a_{HCO_3^-} \cdot a_{OH^-}}{a_{CO_3^{2-}} \cdot a_{H_2O}} = 2.094\times10^{-4} \quad (4.11)$$

Where $a_{HCO_3^-}$, a_{OH^-}, $a_{CO_3^{2-}}$, a_{H_2O} are the activities of HCO_3^-, OH^-, CO_3^{2-}, and H_2O in a solution, respectively. Assume the solution is an ideal mixture, then the activity is as same as the molar concentration. Consider the activity of water is unity and, thus, taking into account the equilibrium condition in **Table 4.7**, the **Equation (4.11)** becomes **Equation (4.12)**.

$$2.094\times10^{-4} = \frac{x^2}{0.97 - x} \tag{4.12}$$

The x value is considerably small, thus neglecting x value in denominator gives $x = 1.4 \times 10^{-2}$. As pOH = -log [OH^-] and pH = 14 – pOH, then the theoretical pH in the leaching solution is 12.1.

Moreover, if we consider the slags leaching **reactions (2.28)** – **(2.31)** in the solution, the leaching product (i.e., $NaAlO_2$) can be hydrated with water and produce aluminate ion, whereas in a high pH solution it is in the form of $Al(OH)_4^-$ [57], as seen in **reaction (4.13)**. Furthermore, **reactions (2.29)** and **(2.30)** give NaOH as the leaching product, which is a strong alkali and can dissociate entirely in the solution, as seen in **reaction (4.14)**.

$$2NaAlO_{2(aq)} + 4H_2O_{(l)} = 2Na^+_{(aq)} + 2Al(OH)_4^-{}_{(aq)} \tag{4.13}$$

$$NaOH_{(aq)} = Na^+_{(aq)} + OH^-_{(aq)} \tag{4.14}$$

The $NaAlO_2$ aqueous solution could be considered as a weak alkali where the only fraction of it accepts protons from water, which means along with the dissociation of NaOH in **reaction (4.14)**, both of these reactions most likely increase the pH extent of the leachate during the leaching.

4.3 Summary of papers 6 and 7 – Kinetics modelling

A series of leaching treatment of a calcium aluminate slag in Na_2CO_3 solution has been done. It was observed that the leaching reactions between leachable phases, e.g., $C_{12}A_7$, CA phase, and Na_2CO_3, are relatively fast. High alumina recovery up to 90.5 % is obtained within 90 min after the slag is leached at 10 wt.% Na_2CO_3 solution, high stirring rates, at 30 – 45 °C.

In regards to the solid product of the leaching reaction, the calcite phase starts to nucleate at the surface of the adjacent unleachable phase in the slag. Calcite crystals can grow up to large sizes (over 10 micrometers), and bridging occurs between them (agglomeration tendency). The use of stirrer and PTFE-ball during the leaching (wet-grinding) increases the collision frequency between both slag and stirrer that breaks the calcite layer and the agglomerates that leads to higher alumina recovery.

Moreover, different kinetic models were tried to find out the rate-limiting step during the leaching, and it was found that the process rate is controlled by the diffusion of reactant and product ions through the product calcite layer. The calculated apparent activation energy of the leaching reaction is 10.8 – 19.9 kJ/mol, which is relatively low, and it indicates the reaction is diffusion rate limited.

4.3.1 Methodology

Two different setups were performed to investigate the kinetics and leaching mechanism of calcium aluminate slags.

4.3.1.1 Leaching kinetics experimental setup

In the kinetics experiment, a slag that was produced from the smelting of bauxite was leached with Na_2CO_3 solution in a borosilicate glass at several different temperatures. No silicon contamination from the glass container was detected on the blank solution. There are 3 and 10 wt.%Na_2CO_3 solvent concentrations were chosen to observe different concentrations effect to the aluminum recovery. The first concentration represents the Pedersen original leaching process, as was mentioned in **section 2.4.1**.

The ratio of solid to liquid is assumed to be constant throughout the leaching treatment, as the water evaporation was considered small. The solid and liquid were stirred at different speeds using a magnetic bar stirrer. The leaching time was up to 90 min and was taken as a sample in different periods. The samples were filtered by using a Büchner funnel and an ashless grade of quantitative filter paper, which then separated the liquor and the solid (grey mud). In addition, PTFE-balls were used in the leaching trials to increase the agitation and collision effects.

Moreover, to study the effect of stirring or agitation, a digestion reactor that can be shaken is used. The reactor is a Polytetrafluoroethylene (PTFE)-base with a capacity of 45 mL and covered with stainless steel as the outer body. It was placed on a tilting plate that can move ± 45°from the horizontal situation, which gives a shaking effect to the solution inside the reactor. Both the reactor and the plate were installed inside of an oven that can be run under controlled temperature, as shown in **Fig. 4.15**.

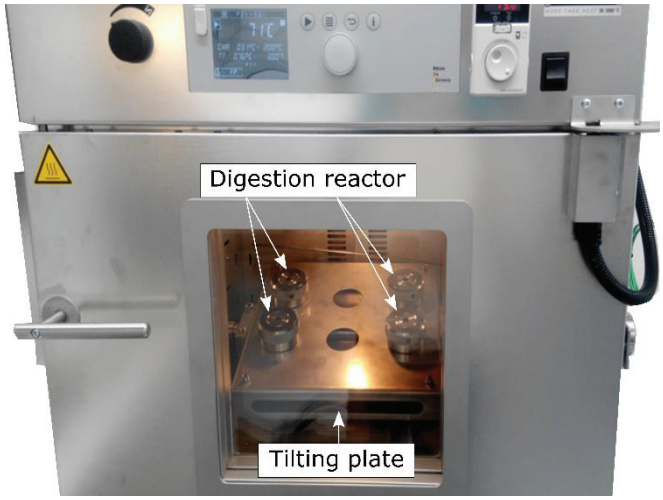

Fig. 4.15 Digestion reactors are placed on a plate that can be tilted ± 45° in an oven that gives a shaking effect to the solution.

4.3.1.2 Leaching mechanism experimental setup

In the current setup, the objective is to study the leaching mechanism and the growth of the solid product (calcium carbonate) that occurs on the slag's surface while it is being exposed to Na_2CO_3 solution. To achieve that, I have submerged the polished slag, which was previously cast into a resin, into a Na_2CO_3 solution for short intervals while the solution was stirred at the same time. The setup is shown in **Fig. 4.16**.

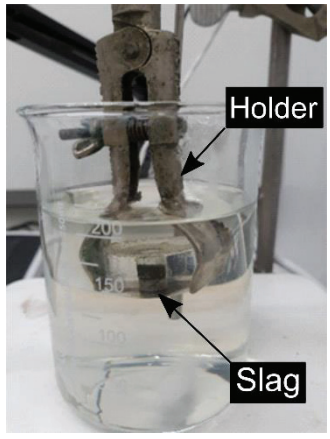

Fig. 4.16 Experimental setup to investigate the leaching mechanism and growth of the calcite on the surface.

4.3.2 Theoretical background

A leaching stage or solid-liquid reaction requires heterogeneous reactions between phases. It takes place at a phase boundary between the reacting phases, unlike homogenous reactions that take place over the entire volume of a given phase [120]. Thus, heterogeneous reactions constitute mass transfer between the reaction interface and the bulk phase, as well as the chemical reaction rate. In this reaction, there are two factors that must be accounted for; rate expression and contacting patterns for two-phase systems [121]. It is more complicated than gas-liquid, and liquid-liquid reactions since these reactions only mass transfer controlled [120]. In this chapter, though related, the thermodynamic theory that involves Gibbs free energy with regard to the alumina recovery is not discussed. It is because the values of Gibbs free energy and species of reactant and product that constitute the equation of produced alumina is known. On the other side, the theory and equation that involves the kinetic rate of leaching are of more importance, especially to industry.

If we consider a leachable solid surrounded by a sea of liquid, which has a product layer due to the continuous reaction, then we can draw a schematic of the solid-liquid reaction, as in **Fig. 4.17**.

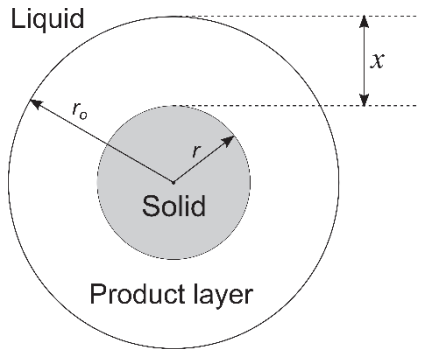

Fig. 4.17 Schematic representation of solid-liquid reactions with a growing product layer.

Referring to the figure, if the original radius is r_o and the interface of the produced layer of the reaction at time t has spread a distance x inwards. This let the radius of the remaining sphere of reactant solid be r. Thus, the relation between the radius and volume of the sphere at original (V) and at time t (V_t) are shown in **Equation (4.15) – (4.17)**.

$$r = r_o - x \tag{4.15}$$

$$V = \frac{4}{3}\pi(r_o)^3 \tag{4.16}$$

$$V_t = \frac{4}{3}\pi(r)^3 = \frac{4}{3}\pi(r_o - x)^3 \tag{4.17}$$

If the fraction degree of leachable solid that has reacted is α, then the value of the unreacted sphere (1-α) on a volume basis can be calculated as in **Equations (4.18) – (4.21)**.

$$(1-\alpha) = \frac{(4/3)\pi(r_o - x)^3}{(4/3)\pi(r_o)^3} = \frac{(r_o - x)^3}{(r_o)^3} \tag{4.18}$$

Rearranging both left and right sides,

$$(1-\alpha)^{1/3} = \frac{r_o - x}{r_o} = 1 - \frac{x}{r_o} \tag{4.19}$$

$$\frac{x}{r_o} = 1 - (1-\alpha)^{1/3} \tag{4.20}$$

$$x = r_o(1 - (1-\alpha)^{1/3}) \tag{4.21}$$

Thus, by deriving the **Equation (4.21)** on both sides, the relation between x and α on a volume basis is given in **Equation (4.22)**.

$$\frac{dx}{d\alpha} = \frac{1}{3} r_o (1-\alpha)^{-2/3} \tag{4.22}$$

Furthermore, if the model is based on a diffusion-controlled mechanism, further assumptions can be made to derive the rate equations. There are at least 12 diffusion-controlled kinetics models that can be used in a solid-liquid reaction [122]. Due to the limitation of pages, only several equations are presented in the current thesis, which is selected based on its positive correlation with the result of experiments performed in the published papers on **chapter 6**.

Jander equation

The time dependence of the growth of the product layer can be described by the parabolic law, as shown in **Equation (4.23)**[122].

$$x^2 = 2DV_mC_ot = kt \tag{4.23}$$

Where D is the diffusion coefficient, V_m is the volume of product layer formed, C_o is the concentration of the penetrating species at the surface, and k is a constant which incorporates system parameters, e.g., diffusion coefficient, penetrating species concentration, and extensive property of the product. The rate (dx/dt) varies inversely with x. Thus, by deriving the equation above will provide **Equation (4.24)** and **(4.25)**.

$$2\frac{xdx}{dt} = k \tag{4.24}$$

or

$$\frac{dx}{dt} = \frac{k}{2x} = \frac{DV_mC_o}{x} \tag{4.25}$$

By substituting **Equation (4.21)** to **Equation (4.23)**, it gives **Equation (4.26)**.

$$x^2 = r_o^2(1-(1-\alpha)^{1/3})^2 = kt \tag{4.26}$$

or

$$(1-(1-\alpha)^{1/3})^2 = \frac{k}{(r_o)^2}t \tag{4.27}$$

Equation (4.27) is known as the Jander equation for a three-dimensional diffusion type. Jander [123] derived a kinetic equation for the diffusion-controlled reaction of a spherical particle from the parabolic law. The product layer substitutes the space filled by the initial reactant solid particle with no change in volume. However, Jander used a plane surface (one-dimensional) as the basis of assumption. Also, the equation assumes that all reacting particles are homogenous in size, which has been criticized by some researchers. In general, the Jander model fits well with experimental measurements within small fraction conversions, e.g., below 50% completion.

Ginstling and Brounshtein equation

Ginstling and Brounshtein [124] stated that the Jander equation is oversimplified and holds only at low conversion values, i.e., low α, as mentioned above. They

introduced Fick's first law of steady-state solution for radial diffusion in a sphere to the parabolic law's equation. As mentioned earlier, Jander used one-dimensional assumption to make the **Equation (4.21)** as the basis of calculations. Therefore, if it is reformulated considering spherical geometry, it should be replaced with **Equation (4.28)** [121].

$$-\frac{dr}{dt} = \frac{k}{6}\left[\frac{r_o}{r(r_o - r)}\right] \tag{4.28}$$

Thus, integrating the equation yields **Equation (4.29)**.

$$r^2\left(\frac{2r}{r_o} - 3\right) = kt \tag{4.29}$$

The relationship of the reacted volume fraction of solid, α, with r and r_o in **Fig. 4.17** can be written as in **Equation (4.30)**.

$$\alpha = 1 - \left(\frac{r}{r_o}\right)^3 \tag{4.30}$$

Then, by substituting **Equation (4.29)** to **Equation (4.30)**, it yields **Equation (4.31)**, which is known as Ginstling and Brounshtein equation [124,125].

$$\frac{k}{(r_o)^2}t = 3 - 2\alpha - 3(1-\alpha)^{2/3} \tag{4.31}$$

Kröger and Ziegler equation

Kröger and Ziegler [126] proposed the equation by integrating the diffusion equation of a sphere particle and equating it with the fraction of unreacted solid reactant on a volume basis. Their main assumption is that the rate of product layer growth is inversely proportional to the product thickness and time. Consider the diffusion coefficient, D, is inversely proportional to t. Then **Equation (4.25)** can be written as **Equation (4.32)**.

$$\frac{dx}{dt} = \frac{V_m C_o}{x} \times \frac{k}{t} \tag{4.32}$$

By rearranging and integrating back the equation, then it leads to **Equation (4.33)** and **(4.34)**.

$$\int 2x dx = \int 2V_m C_o k \frac{dt}{t} \tag{4.33}$$

After the integration,

$$x^2 = 2V_m C_o k \ln t \tag{4.34}$$

Thus, by substituting **Equation (4.21)** to the equation above, it yields **Equation (4.35)**.

$$r_o^2 (1-(1-\alpha)^{1/3})^2 = 2V_m C_o k \ln t \tag{4.35}$$

or **Equation (4.36)**, which is known as Kröger and Ziegler equation.

$$(1-(1-\alpha)^{1/3})^2 = k^{'} \ln t \tag{4.36}$$

where $k^{'} = \frac{2V_m C_o k}{(r_o)^2}$.

Zhuravlev, Lesokhin, and Templeman (ZLT) equation

The ZLT equation is a modification of the Jander equation by assuming that the activity of the reacting substance is not constant. It is proportional to the fraction of unreacted material (1 – α) [122]. Referring to **Fig. 4.17** and assuming the concentration C_o is not a constant, but as a factor of reactant activity that varies with (1- α), which leads to rearrangement of **Equation (4.25)** to **Equation (4.37)**.

$$\frac{dx}{dt} = \frac{DV_m C_o (1-\alpha)}{x} = \frac{k^{"}(1-\alpha)}{x} \tag{4.37}$$

where $k^{"} = DV_m C_o$, and $\frac{xdx}{1-\alpha} = k^{"} dt$

Substituting x and dx from the **Equation (4.21)** and **(4.22)** gives **Equation (4.38)**

$$\frac{r_o (1-(1-\alpha)^{1/3}) \times (1/3) r_o (1-\alpha)^{-2/3}}{1-\alpha} d\alpha = k^{"} dt \tag{4.38}$$

Rearrange it to give the **Equation (4.39)** and **(4.40)**

$$\frac{(1/3)(r_o)^2 ((1-\alpha)^{-2/3} - (1-\alpha)^{-1/3})}{1-\alpha} d\alpha = k^{"} dt \tag{4.39}$$

$$\frac{1}{3}r_o^2\left((1-\alpha)^{-5/3}-(1-\alpha)^{-4/3}\right)d\alpha = k^{"}dt \tag{4.40}$$

Integrating the equation above yields **Equation (4.41)**

$$\frac{1}{3}r_o^2\left(\frac{3}{2}(1-\alpha)^{-2/3}-3(1-\alpha)^{-1/3}+c\right) = k^{"}t \tag{4.41}$$

at $t = 0$, $\alpha = 0$, then $c = 3/2$. Thus, substituting the c value to the **Equation (4.41)** gives **Equation (4.42)** and **(4.43)**

$$r_o^2\left(\frac{1}{2}(1-\alpha)^{-2/3}-(1-\alpha)^{-1/3}+\frac{1}{2}\right) = k^{"}t \tag{4.42}$$

$$\frac{1}{2}r_o^2\left((1-\alpha)^{-2/3}-2(1-\alpha)^{-1/3}+1\right) = k^{"}t \tag{4.43}$$

Furthermore, rearranging the equation yields **Equation (4.44)** that is known as ZLT equation.

$$\left((1-\alpha)^{-1/3}-1\right)^2 = k^{'''}t \tag{4.44}$$

where $k^{'''} = \dfrac{2k^{"}}{r_o^2}$

Chapter 5

Conclusions and Suggestions

5.1 Conclusions

The motivation of the work on the current thesis was to fill the gap of knowledge of the Pedersen process, especially on its pyrometallurgical and leaching part, so that the process advantages and also challenges in the present period can be evaluated with more details. Therefore, the conclusion will be based on the open points, where the literature of the Pedersen process was still lacking.

The thermodynamic study of the smelting and leaching process.

Based on the experimental result, it is observed that iron from the bauxite ores is removed from around 94.8 to 99.9 % during smelting-reduction, which is also supported by the Ellingham diagram that iron oxides can be reduced by carbothermic reduction. Furthermore, the smelting process yields alumina-containing slags that have iron less than 1 wt.%, dependent on the slag chemistry. In the leaching process, it is shown that $CaO{\cdot}Al_2O_3$, $12CaO{\cdot}7Al_2O_3$, and $CaO{\cdot}2Al_2O_3$ phases are leachable in Na_2CO_3 solution in equilibrium. However, it is confirmed by experiments that side reactions happen during the leaching, and the $CaO{\cdot}2Al_2O_3$ is considered as the unleachable one. Whereas the leaching reaction between $CaO{\cdot}Al_2O_3$ and/or $12CaO{\cdot}7Al_2O_3$ phase in Na_2CO_3 solution is fast. It is likely that the non-bridging oxygen (NBO) over tetrahedral structure (T) index affect the leaching extent of the slags, the lower NBO/T index of the phase is the more difficult for the phase to leach or depolymerize.

Characteristics of slags produced from the smelting-reduction treatment of bauxite.

Depending on the corresponding amount of CaO/Al_2O_3 ratio, slags produced from the smelting-reduction treatment of low-grade bauxites consist of leachable phases, i.e., $CaO{\cdot}Al_2O_3$, $12CaO{\cdot}7Al_2O_3$. Also, the partial separation of Mn, Si, Ti, V, and P oxides occurs through the smelting-reduction, where low distribution coefficients of L_{Mn}, L_P, and L_V are observed, which means these elements are favored to be co-existed in pig

iron. While L_{Si} and L_{Ti} values ranges are considerably wide depending on the characteristics of the produced slag, which means that the elements may exist either in the slag or pig iron after the smelting.

Elemental composition and concentrations of the leachate produced from the leaching treatment.

A high concentration of aluminum (high recovery) is obtained from a pregnant liquid solution (PLS) that uses a solvent, which consists of 100 – 120 g/L Na_2CO_3. Whereas, lower concentrations of aluminum (low recovery) are produced from solutions with a mixed Na_2CO_3–NaOH at any studied temperatures. The addition of NaOH in the solution decreases the aluminum dissolution of the slag, while it increases the silicon dissolution into the PLS. Furthermore, the higher the aluminum concentration of the solution is, the higher concentration of silicon will be. It is also worth noting, the aluminum and silicon concentrations from solutions that were treated at 60, and 75 °C show similar results.

Microstructure and morphology grey mud.

The residue (grey mud) produced from a Na_2CO_3 solvent consists of calcite and vaterite crystals. A calcite crystal has a cubical shape, whereas vaterite has a spherical one. Vaterite is the least stable thermodynamic form of $CaCO_3$ compared to other polymorphs (e.g., aragonite and calcite). On the other hand, a grey mud produced from a mixed Na_2CO_3–NaOH consists of calcite, $3CaO{\cdot}Al_2O_3{\cdot}6H_2O$ (hydrogarnet) phase, and a fibrous-like shape, which incorporates and forming a network structure to other grains. It is very likely that the fibrous-like shape of this grey mud is a calcium-silicate-hydrate phase that incorporates the hydrogarnet crystals.

The leaching kinetics and mechanism, and the effect of different leaching conditions to alumina recovery extent.

The calcite phase as a solid product of the leaching reaction starts to nucleate at the surface of the adjacent unleachable phase in the slag. Calcite crystals can grow up to large sizes (over 10 micrometers), and bridging occurs between them (agglomeration tendency). The use of stirrer and PTFE-ball during the leaching (wet-grinding) increases the collision frequency between both slag and stirrer that breaks the calcite layer and the agglomerates that leads to higher alumina recovery. Different kinetic models were tried to find out the rate-limiting step during the leaching, and it was observed that the process

rate is controlled by the diffusion of reactant and product ions through the product calcite layer.

5.2 Suggestions for further works

Based on experimental works and results presented in the thesis, I have several suggestions that can be assessed for further works in aluminum recovery from low-grade bauxite using the Pedersen process.

1. Investigate the leachability of slag in the CaO-Al_2O_3-SiO_2 system with an addition of the TiO_2 phase as there are low-grade bauxites at several locations consist TiO_2 in the form of anatase or rutile.
2. Study on the desilication process before the precipitation, as it is evident that a certain extent of silicon dissolves into the pregnant liquor that may deteriorate the $Al(OH)_3$ purity.
3. The use of a pressurized reactor. All of the experimental works in the present thesis were performed in 1 atm. There is no information available in the literature about the mechanism and kinetics data of a slag leached inside of a pressurized reactor. Kinetics data of the leaching experiments are necessary for upscaling the work.
4. A different leaching method to improve aluminum recovery extent. It is observed that a passive layer of calcite inhibits the mass transfer of aqueous phases during the leaching. Therefore, it is plausible to compare different leaching methods, e.g., wet grinding, ball milling, or ultrasonic, to evaluate which one is the most effective method to break the networking calcites.
5. Identify the distribution of rare earth elements (REE) in the slag and leaching residue. Many researchers have studied the valorization of red mud as one of the REE sources. Therefore, a further study on the REE recovery from the slag and/or grey mud is of interest.

References

[1] World Aluminum, The International Aluminum Institute, (2019). http://www.world-aluminium.org/statistics/alumina-production/ (accessed October 8, 2019).

[2] J. Safarian, L. Kolbeinsen, Sustainability in Alumina Production from Bauxite, in: Sustain. Ind. Process. Summit, 2016: pp. 75–82.

[3] CBIX, The Bauxite Index, (2019). https://thebauxiteindex.com/cbix/industry-101 (accessed October 14, 2019).

[4] F. Habashi, Karl Josef Bayer and his time — Part 1, CIM Bull. 97 (2004) 61–64.

[5] G.J.J. Aleva, G.J.J. Aleva (Compiler) Laterites. Concepts, Geology, Morphology and Chemistry. ISRIC, Wageningen, 1994. 169 pp. Price NLG 25. ISBN: 90.6672.053.0., Clay Miner. 31 (1996) 440–441. doi:10.1180/claymin.1996.031.3.15.

[6] G. Bárdossy, G.J.J. Aleva, Lateritic bauxites. Developments in Economic Geology., Vol. 27, Elsevier Science Ltd., 1990.

[7] G. Bardossy, Karst bauxites. Bauxite deposits on carbonate rock, Elsevier Scientific Publishing Company, Amsterdam, 1982.

[8] F.M. Meyer, Availability of Bauxite Reserves, Nat. Resour. Res. 13 (2004) 161–172. doi:10.1023/B:NARR.0000046918.50121.2e.

[9] P. Smith, The Processing of High Silica Bauxites - Review of Existing and Potential Processes, Hydrometallurgy. (2009). doi:10.1016/j.hydromet.2009.04.015.

[10] B.K. Gan, Z. Taylor, B. Xu, A. Van Riessen, R.D. Hart, X. Wang, P. Smith, Quantitative phase analysis of bauxites and their dissolution products, Int. J. Miner. Process. 123 (2013) 64–72. doi:10.1016/j.minpro.2013.05.005.

[11] Y. Pontikes, Bauxite Residue Valorization and Best Practices: Preface for the Thematic Section and Some of the Work to Follow, J. Sustain. Metall. 2 (2016) 313–315. doi:10.1007/s40831-016-0104-2.

[12] K. Tsesmelis, Bauxite Mine Rehabilitation & Bauxite Residue Management: A Global Perspective, in: Proc. 35th Int. ICSOBA Conf., ICSOBA, 2017: p. 71.

[13] The European Commission, Commission decision 2014/955/EU - List of waste, 2014. doi:http://eur-lex.europa.eu/pri/en/oj/dat/2003/l_285/l_28520031101en00330037.pdf.

[14] The European Commission, Commission notice on technical guidance on the classification of waste, 2018. https://eur-lex.europa.eu/legal-content/EN/TXT/?uri=uriserv:OJ.C_.2018.124.01.0001.01.ENG&toc=OJ:C:2018:124:TOC.

[15] E. Balomenos, I. Gianopoulou, D. Panias, I. Paspaliaris, K. Perry, D. Boufounos, Efficient and Complete Exploitation of the Bauxite Residue (Red Mud) Produced in the Bayer Process, in: EMC 2013, 2013: pp. 745–758.

[16] J. Cody, “Red mud disaster” accused receive jail sentences, FWD Aff. LLC, Budapest, Hungary. (2019). https://rmx.news/article/article/red-mud-disaster-accused-receive-jail-sentences (accessed December 25, 2019).

[17] TW, Major tailings dam failure in China’s Henan Province, Watch. (2016). https://watchers.news/2016/08/16/major-tailings-dam-failure-in-china-s-henan-province/ (accessed December 25, 2019).

[18] L. Arnout, T. Hertel, M. Liard, D. Lootens, Y. Pontikes, Use of Bauxite Residue Slurry as Single Activator in a Hybrid Binder System, Proc. 35th Int. ICSOBA Conf. Hamburg, Ger. 2 – 5 October, 2017. (2017) 2–5.

[19] T. Hertel, R.I. Iacobescu, B. Blanpain, Y. Pontikes, Large-scale Valorization of Bauxite Residue for Inorganic Polymers, Proc. 34th Int. ICSOBA Conf. (2016) 1200.

[20] J. Anawati, G. Azimi, Recovery of Rare Earth Elements and Refractory Metals from Bauxite Residue, in: Trav. 47, Proc. 36th Int. ICSOBA Conf., 2018: pp. 449–458.

[21] C. Rao Borra, Recovery of Rare Earths from Bauxite Residue (Red Mud), KU Leuven, 2016.

[22] H. Pedersen, Process of Manufacturing Aluminum Hydroxide, 1618105, 1927.

[23] K.J. Bayer, Process of Obtaining Alumina, 382505, 1888.

[24] F. Habashi, Alumina Production and the Textile Industry, J. Text. Sci. Eng. 07 (2017) 7–9. doi:10.4172/2165-8064.1000327.

[25] K.J. Bayer, Process of Making Alumina, 515895, 1894.

[26] A.R. Burkin, Production of aluminium and alumina Baffins Lane, John Wiley and Sons, Chichester, 1987.

[27] J.L. Anjier, M.L. Roberson, W.E. Atchison, Bayer Process Production of Alumina Hydrate, 4511542, 1985.

[28] M. Authier-Martin, G. Forte, S. Ostap, J. See, The mineralogy of bauxite for producing smelter-grade alumina, JOM. 53 (2001) 36–40. doi:10.1007/s11837-001-0011-1.

[29] S.J. Lindsay, SGA Requirements in Coming Years, Springer International Publishing, Cham, 2005. doi:10.1007/978-3-319-48176-0.

[30] E. Balomenos, Bauxite Residue Handling Practice and Valorisation Research in Aluminium of Greece, in: 2nd Int. Bauxite Residue Valoris. Best Pract. Conf., 2018: pp. 29–37. http://www.alhellas.com/.

[31] B. Ozden, C. Brennan, S. Landsberger, Investigation of bauxite residue (red mud) in terms of its environmental risk, J. Radioanal. Nucl. Chem. (2018). doi:10.1007/s10967-018-6355-6.

[32] L. Wu, Overview of Alumina Refining Energy Consumption, in: Trav. 46, Proc. 35th Int. ICSOBA Conf., Hamburg, 2017: p. 12.

[33] H. Mahadevan, Cost Competitiveness of Indian Alumina Refineries, in: Int. Comm. Study Bauxite Alumina Alum., 2009: pp. 2–7.

[34] A.A. Scarsella, S. Noack, E. Gasafi, C. Klett, A. Koschnick, Energy in Alumina Refining: Setting New Limits, in: Light Met. 2015, John Wiley & Sons, Inc.,

Hoboken, NJ, USA, 2015: pp. 131–136. doi:10.1002/9781119093435.ch24.

[35] S. Gu, L. Qi, Y. Zhonglin, Energy Consumption in Bayer Process, in: Light Met. 2007, 2007: pp. 55–59.

[36] D. Thomas, Heat Transfer in the Bayer Process, in: S.J. Lindsay (Ed.), Essent. Readings Light Met., Springer International Publishing, Cham, 2016: pp. 705–710. doi:10.1007/978-3-319-48176-0_98.

[37] L.M. Perander, J.B. Metson, C. Klett, Two Perspectives on the Evolution and Future of Alumina, in: Light Met. 2011, John Wiley & Sons, Inc., Hoboken, NJ, USA, 2011: pp. 151–155. doi:10.1002/9781118061992.ch26.

[38] T. Mach, Energy Consumption in the Bayer Process, in: Int. Alumina Qual. Work., 2012: pp. 375–378.

[39] E. Balomenos, D. Panias, I. Paspaliaris, Energy and Exergy Analysis of the Primary Aluminum Production Processes: A Review on Current and Future Sustainability, Miner. Process. Extr. Metall. Rev. 32 (2011) 69–89. doi:10.1080/08827508.2010.530721.

[40] O.C. Fursman, Submerged-Arc Smelting of Ferruginous Bauxite for the Recovery of Iron and Alumina, in: Proc. Electr. Furn. Conf., 1968: pp. 140–144.

[41] G. Songqing, The evolution of alumina production technology in China, new challenges and trends, in: Trav. 46, Proc. 35th Int. ICSOBA Conf., ICSOBA, Hamburg, 2017: pp. 135–144.

[42] R. Calalo, T. Tran, Effects of sodium oxalate on the precipitation of alumina trihydrate from synthetic sodium aluminate liquors, in: Light Met. Proc. Sess. TMS Annu. Meet. (Warrendale, Pennsylvania), 1993: pp. 125–133.

[43] A. Espelund, Harald Pedersen, Nor. Biogr. Leks. (2009). https://nbl.snl.no/Harald_Pedersen (accessed December 31, 2019).

[44] J. Miller, A. Irgens, Essential Readings in Light Metals, Springer International Publishing, Cham, 1974. doi:10.1007/978-3-319-48176-0.

[45] K. Nielsen, The Pedersen Process - An old process in a new light, Erzmetall. 31 (1978) 523–525.

[46] W. Jerzy Grzymek, A. Derdacka, Z. Konik, B. Werynski, Method for obtaining aluminum oxide, 4149898, 1979. doi:10.1016/0375-6505(85)90011-2.

[47] L.F.K. Barr, Alumina Production from Andalusite by the Pedersen Process, Trans. Inst. Min. Metall. Sect. C-Mineral Process. Extr. Metall. 86 (1977) C64–C70.

[48] T.P. Hignett, PILOT PLANTS: Production of Alumina from Clay by a Modified Pedersen Process, Ind. Eng. Chem. 39 (1947) 1052–1060. doi:10.1021/ie50452a028.

[49] T.P. Copson, Raymond L.; Walthall, John H.; Hignett, Extraction of Alumina from Clays by the Lime-sinter Modification of the Pedersen Process, Trans. Am. Inst. Min. Metall. Eng. 159 (1944).

[50] H. Sellaeg, L. Kolbeinsen, J. Safarian, Iron Separation from Bauxite Through Smelting-Reduction Process, in: Miner. Met. Mater. Ser., 2017: pp. 127–135. doi:10.1007/978-3-319-51541-0_19.

[51] F.I. Azof, L. Kolbeinsen, J. Safarian, Characteristics of Calcium-Aluminate Slags and Pig Iron Produced from Smelting-Reduction of Low-Grade Bauxites, Metall. Mater. Trans. B Process Metall. Mater. Process. Sci. 49 (2018) 2400–2420. doi:10.1007/s11663-018-1353-1.

[52] K.C. Mills, M. Kowalski, P.J. Spencer, D. Neuschiitz, J. Geiseler, B.J. Keene, H. Gaye, J. Lehmann, D. Kirner, D. Janke, Slag atlas 2nd edition, 2nd ed., Verlag Stahleisen GmbH, Dusseldorf, 1995.

[53] R. Walker, SI Metric, (2011). https://www.simetric.co.uk/si_metals.htm (accessed December 29, 2019).

[54] F.I. Azof, Y. Yang, D. Panias, L. Kolbeinsen, J. Safarian, Leaching characteristics and mechanism of the synthetic calcium-aluminate slags for alumina recovery, Hydrometallurgy. 185 (2019) 273–290. doi:10.1016/j.hydromet.2019.03.006.

[55] S. Marie Bø, Operating Parameters in the Leaching Stage of the Pedersen Process for Alumina Production, 2015.

[56] F.I. Azof, L. Kolbeinsen, J. Safarian, The Leachability of Calcium Aluminate Phases in Slags for the Extraction of Alumina, in: Trav. 46, Proc. 35th Int. ICSOBA Conf., ICSOBA, Hamburg, 2017: pp. 243–253. https://icsoba.org/sites/default/files/2017papers/Alumina Papers/AA13 - The Leachability of Calcium Aluminate Phases in Slags for the Extraction of Alumina.pdf (accessed February 25, 2018).

[57] R.J. Moolenaar, J.C. Evans, L.D. McKeever, The structure of the aluminate ion in solutions at high pH, J. Phys. Chem. 74 (1970) 3629–3636. doi:10.1021/j100714a014.

[58] F.I. Azof, M. Vafeias, D. Panias, J. Safarian, The leachability of a ternary CaO-Al2O3-SiO2 slag produced from smelting-reduction of low-grade bauxite for alumina recovery, Hydrometallurgy. 191 (2020) 105184. doi:10.1016/j.hydromet.2019.105184.

[59] D. Panias, P. Asimidis, I. Paspaliaris, Solubility of boehmite in concentrated sodium hydroxide solutions: Model development and assessment, Hydrometallurgy. (2001). doi:10.1016/S0304-386X(00)00146-8.

[60] A. Czajkowski, A. Noworyta, M. Krótki, Studies and modelling of the process of decomposition of aluminate solutions by carbonation, Hydrometallurgy. 7 (1981) 253–261. doi:10.1016/0304-386X(81)90006-2.

[61] E. Nedkvitne, Leaching and Precipitation Experiments Related to the Pedersen Process, 2019.

[62] B. Dash, B.C. Tripathy, I.N. Bhattacharya, S.C. Das, C.R. Mishra, B.K. Mishra, Precipitation of boehmite in sodium aluminate liquor, Hydrometallurgy. 95 (2009) 297–301. doi:10.1016/j.hydromet.2008.07.002.

[63] Z. Wang, L. Yang, J. Zhang, Z. cheng Guo, Y. Zhang, Adjustment on gibbsite and boehmite co-precipitation from supersaturated sodium aluminate solutions, Trans. Nonferrous Met. Soc. China (English Ed. 20 (2010) 521–527. doi:10.1016/S1003-6326(09)60172-2.

[64] O.C. Fursman, H.E. Blake Jr., J.E. Mauser, Recovery of Alumina and Iron from Pacific Northwest Bauxites by the Pedersen Process, Albany, 1968.

[65] H.E. Blake, O.C. Fursman, A.D. Fugate, L.H. Banning, Adaptation of the Pedersen Process to the Ferruginous Bauxites of the Pacific Northwest, 1966.

[66] Y. Zhang, W. Lü, Y. Qi, Z. Zou, Recovery of iron and calcium aluminate slag from high-ferrous bauxite by high-temperature reduction and smelting process, Int. J. Miner. Metall. Mater. 23 (2016) 881–890. doi:10.1007/s12613-016-1303-3.

[67] P. Vafeias, Michail; Marinos, Danai; Panias, Dimitrios; Safarian, Jafar; van Der Eijk, Casper; Solhem, Ingeborg; Balomenos, Efthymios; Ksiazek, Michal; Davris, From Red To Grey: Revisiting the Pedersen Process To Achieve Holistic Bauxite Ore Utilisation, in: Proc. 2nd Int. Bauxite Residue Valoris. Best Pract. Conf., 2018: pp. 111–117.

[68] W. Cao, W. Tian, Z. Hong, Study on Bayer process and Soda-lime sintering process of special diasporic bauxite with high silica, in: Miner. Met. Mater. Soc., 2010: pp. 149–153.

[69] R. Padilla, H.Y. Sohn, Sintering kinetics and alumina yield in lime-soda sinter process for alumina from coal wastes, Metall. Trans. B. 16 (1985) 385–395. doi:10.1007/BF02679731.

[70] C. Ostrowski, J. Zelazny, Solid solutions of calcium aluminates C3A, C12A7 and CA with sodium oxide, J. Therm. Anal. Calorim. 75 (2004) 867–885. doi:10.1023/B:JTAN.0000027182.40442.fe.

[71] Y. Tian, X. Pan, H. Yu, Y. Han, G. Tu, S. Bi, An Improved Lime Sinter Process to Produce Al2O3 from Low-Grade Al-Containing Resources, in: Light Met. 2016, Springer International Publishing, Cham, 2016: pp. 5–9. doi:10.1007/978-3-319-48251-4_1.

[72] G. Li, N. Sun, J. Zeng, Z. Zhu, T. Jiang, Reduction Roasting and Fe-Al Separation of High Iron Content Gibbsite-type Bauxite Ores, Light Met. 2010. (2010) 133–137.

[73] D. V Valeev, E.R. Mansurova, V.A. Bychinskii, K. V Chudnenko, Extraction of Alumina from high-silica bauxite by hydrochloric acid leaching using preliminary roasting method, IOP Conf. Ser. Mater. Sci. Eng. 110 (2016) 012049. doi:10.1088/1757-899X/110/1/012049.

[74] S.W. Kim, Y. Toda, K. Hayashi, M. Hirano, H. Hosono, Synthesis of a Room Temperature Stable 12CaO·7Al 2 O 3 Electride from the Melt and Its Application as an Electron Field Emitter, Chem. Mater. 18 (2006) 1938–1944. doi:10.1021/cm052367e.

[75] L. Palacios, A. Cabeza, S. Bruque, S. García-Granda, M.A.G. Aranda, Structure and Electrons in Mayenite Electrides, Inorg. Chem. 47 (2008) 2661–2667. doi:10.1021/ic7021193.

[76] D. Jiang, Z. Zhao, S. Mu, V. Phaneuf, J. Tong, Simple and Efficient Fabrication of Mayenite Electrides from a Solution-Derived Precursor, Inorg. Chem. 56 (2017) 11702–11709. doi:10.1021/acs.inorgchem.7b01655.

[77] S. Kim, M. Miyakawa, K. Hayashi, T. Sakai, M. Hirano, H. Hosono, Simple and Efficient Fabrication of Room Temperature Stable Electride: Melt-Solidification and Glass Ceramics, J. Am. Chem. Soc. 127 (2005) 1370–1371. doi:10.1021/ja043990n.

[78] R. Strandbakke, C. Kongshaug, R. Haugsrud, T. Norby, High-Temperature Hydration and Conductivity of Mayenite, Ca 12 Al 14 O 33, J. Phys. Chem. C. 113 (2009) 8938–8944. doi:10.1021/jp9009299.

[79] R.W. Nurse, J.H. Welch, A.J. Majumdar, The CaO-Al2O3 System in a Moisture-free Atmosphere, Trans. Br. Ceram. Soc. 64 (1965) 409–418.

[80] R.W. Nurse, J.H. Welch, A.J. Majumdar, The 12CaO.7Al2O3 Phase in the CaO-Al2O3 System, Trans. Br. Ceram. Soc. (1965) 323–332.

[81] E.S. Shepherd, G.A. Rankin, F.E. Wrigth, The Binary Systems of Alumina with Silica,Lime and Magnesia.pdf, Am. J. Sci. 28 (1909) 293–333.

[82] E.S. Shepherd, G.A. Rankin, Preliminary Report on the Ternary System CaO–Al2O3–SiO2. A Study of the Constitution of Portland Cement Clinker., J. Ind. Eng. Chem. 3 (1911) 211–227. doi:10.1021/ie50028a005.

[83] G.A. Rankin, F.E. Wright, The Ternary System CaO-Al2O3-SiO2, Am. J. Sci. 39 (1915).

[84] B. Hallstedt, Assessment of the CaO-Al2O3 System, J. Am. Ceram. Soc. 73 (1990) 15–23. doi:10.1111/j.1151-2916.1990.tb05083.x.

[85] D.. Jerebtsov, G.. Mikhailov, Phase diagram of CaO–Al2O3 system, Ceram. Int. 27 (2001) 25–28. doi:10.1016/S0272-8842(00)00037-7.

[86] E. Haccuria, T. Crivits, P.C. Hayes, E. Jak, Selected Phase Equilibria Studies in the Al 2 O 3 -CaO-SiO 2 System, J. Am. Ceram. Soc. 99 (2016) 691–704. doi:10.1111/jace.13991.

[87] W.. Büssem, A. Eitel, Die Struktur des Pentacalciumtrialuminats, Zeitschrift Für Krist. - Cryst. Mater. 95 (1936). doi:10.1524/zkri.1936.95.1.175.

[88] J.. Jeevaratnam, L.S.D.. Glasser, F.P. Glasser, Structure of Calcium Aluminate, 12CaO.7Al2O3, Nature. 194 (1962) 764–765. doi:10.1038/140607a0.

[89] M. Lacerda, J.T.S. Irvine, F.P. Glasser, A.R. West, High oxide ion conductivity in Ca12Al14O33, Nature. 332 (1988) 525–526. doi:10.1038/332525a0.

[90] D.M. Roy, R. Roy, Crystalline Solubility and Zeolitic Behavior in Garnet Phases in the System CaO-Al2O3-SiO2, 4th Int. Congr. Chem. Cem. Vol.1. (1960) 307–314.

[91] K. Hayashi, M. Hirano, H. Hosono, Thermodynamics and Kinetics of Hydroxide Ion Formation in 12CaO·7Al2O3, J. Phys. Chem. B. 109 (2005) 11900–11906. doi:10.1021/jp050807j.

[92] J.A. Imlach, L.S.D. Glasser, F.P. Glasser, Excess Oxygen and the Stability of 12CaO.7Al2O3, Cem. Concr. Res. 1 (1971) 57–61.

[93] J. Jeevaratnam, F.P. Glasser, L.S.D. Glasser, Anion Substitution and Structure of 12CaO.7Al2O3, J. Am. Ceram. Soc. 47 (1964) 105–106. doi:10.1111/j.1151-2916.1964.tb15669.x.

[94] H. Hosono, Y. Abe, Occurrence of superoxide radical ion in crystalline calcium

aluminate 12CaO.7Al2O3 prepared via solid-state reactions, Inorg. Chem. 26 (1987) 1192–1195. doi:10.1021/ic00255a003.

[95] K. Hayashi, S. Matsuishi, M. Hirano, H. Hosono, Formation of Oxygen Radicals in 12CaO·7Al 2 O 3 : Instability of Extraframework Oxide Ions and Uptake of Oxygen Gas, J. Phys. Chem. B. 108 (2004) 8920–8925. doi:10.1021/jp037916n.

[96] K. Hayashi, M. Hirano, S. Matsuishi, H. Hosono, Microporous Crystal 12CaO·7Al 2 O 3 Encaging Abundant O - Radicals, J. Am. Chem. Soc. 124 (2002) 738–739. doi:10.1021/ja016112n.

[97] A. Schmidt, M. Lerch, J.-P. Eufinger, J. Janek, R. Dolle, H.-D. Wiemhöfer, I. Tranca, M.M. Islam, T. Bredow, H. Boysen, M. Hoelzel, CN-mayenite Ca12Al14O32(CN)2: Replacing mobile oxygen ions by cyanide ions, Solid State Sci. 38 (2014) 69–78. doi:10.1016/j.solidstatesciences.2014.09.017.

[98] K. Hayashi, S. Matsuishi, T. Kamiya, M. Hirano, H. Hosono, Light-induced conversion of an insulating refractory oxide into a persistent electronic conductor, Nature. 419 (2002) 462–465. doi:10.1038/nature01053.

[99] G.I. Zhmoidin, A.K. Chatterjee, Conditions and mechanism of interconvertibility of compounds 12CaO.7Al2O3 and 5CaO.3Al2O3, Cem. Concr. Res. 14 (1984) 386–396. doi:10.1016/0008-8846(84)90057-7.

[100] H.J.T. Ellingham, Reducibility of Oxides and Sulphides in Metallurgical Processes, J. Soc. Chem. Ind. 63 (1944) 125–160. doi:10.1002/jctb.5000630501.

[101] S. Amini, R. Abbaschian, Nucleation and growth kinetics of graphene layers from a molten phase, Carbon N. Y. 51 (2013) 110–123. doi:10.1016/j.carbon.2012.08.019.

[102] D.M. Stefanescu, G. Alonso, P. Larrañaga, R. Suarez, On the stable eutectic solidification of iron-carbon-silicon alloys, Acta Mater. 103 (2016) 103–114. doi:10.1016/j.actamat.2015.09.043.

[103] D.D. Double, A. Hellawell, The nucleation and growth of graphite-the modification of cast iron, Acta Metall. Mater. 43 (1995) 2435–2442. doi:10.1016/0956-7151(94)00416-1.

[104] ISO 2017, International Standard ISO 945-1, 2017 (2017).

[105] T. Materia, Gray Iron, Key to Met. AG. (2002). https://www.totalmateria.com/page.aspx?ID=CheckArticle&site=kts&NM=84 (accessed February 5, 2020).

[106] G.L. Rivera, R.E. Boeri, J.A. Sikora, Solidification of gray cast iron, Scr. Mater. 50 (2004) 331–335. doi:10.1016/j.scriptamat.2003.10.019.

[107] K.S. Pitzer, Thermodynamics of electrolytes. I. Theoretical basis and general equations, J. Phys. Chem. 77 (1973) 268–277. doi:10.1021/j100621a026.

[108] B.K.D.P. Rao, D.D.R. Gaskell, The thermodynamic properties of melts in the system MnO-SiO2, Metall. Trans. B. 12 (1981) 311–317. doi:10.1007/BF02654464.

[109] S.E. Olsen, M. Tangstad, T. Lindstad, Production of Manganese Ferroalloys, SINTEF and Tapir Academic Press, Trondheim, 2007.

[110] P. Herasymenko, Electrochemical Theory of Slag-Metal Equilibria. Part II-The

Reactions of Chromium in the Acid Open-Hearth Furnace, (1938) 1254–1257.
[111] R.D. Shannon, Revised effective ionic radii and systematic studies of interatomic distances in halides and chalcogenides, Acta Crystallogr. Sect. A. 32 (1976) 751–767. doi:10.1107/S0567739476001551.
[112] S. Sarkar, Structure and Properties of Metallurgical Slag, National Institute of Technology, Rourkela, 2017.
[113] M. Tangstad, Lecture notes in advanced metal production course: Slag Fundamental, (2017).
[114] J.-H. Liu, G.-H. Zhang, K.-C. Chou, Study on electrical conductivities of CaO–SiO 2 –Al 2 O 3 slags, Can. Metall. Q. 54 (2015) 170–176. doi:10.1179/1879139514Y.0000000174.
[115] F. Habashi, Dissolution of minerals and hydrometallurgical processes, Naturwissenschaften. 70 (1983) 403–411. doi:10.1007/BF01047177.
[116] M.L. Free, Hydrometallurgy: fundamentals and applications, John Wiley & Sons, Inc., New Jersey, 2013.
[117] R. V. Lundquist, H. Leitch, Two hydrated calcium aluminates encountered in the lime-soda sinter process, US Dept. Inter. Bur. Mines. 6335 (1963).
[118] R. V. Lundquist, H. Leitch, Aluminum Extraction Characteristics of Three Calcium Aluminates in Water, Sodium Hydroxide, and Sodium Carbonate Solutions, Boulder City, 1964.
[119] B.I. Whittington, T.M. Fallows, M.J. Willing, Tricalcium aluminate hexahydrate (TCA) filter aid in the Bayer industry: factors affecting TCA preparation and morphology, Int. J. Miner. Process. 49 (1997) 1–29. doi:10.1016/S0301-7516(96)00035-X.
[120] S. Seetharaman, Fundamentals of metallurgy, Woodhead Publishing Limited, 2005. doi:10.1533/9781845690946.
[121] O. Levenspiel, Chemical Reaction Engineering-3rd edition, John Wiley & Sons, Inc., 1999.
[122] C.F. Dickinson, G.R. Heal, Solid–liquid diffusion controlled rate equations, Thermochim. Acta. (1999). doi:10.1016/S0040-6031(99)00256-7.
[123] W. Jander, Reaktionen im festen Zustande bei höheren Temperaturen. Säureplatzwechsel bei einigen Wolframaten und Molybdaten, Zeitschrift Für Anorg. Und Allg. Chemie. 190 (1930) 397–406. doi:10.1002/zaac.19301900139.
[124] A.M. Ginstling, B.L. Brounshtein, Concerning the diffusion kinetics of reactions in spherical particles, Appli Chem USSR. 23 (1950) 1327–1338. doi:10.1007/10722086_4.
[125] J.L. Provis, On the use of the Jander equation in cement hydration modelling, RILEM Tech. Lett. 1 (2016) 62. doi:10.21809/rilemtechlett.2016.13.
[126] C. Kroger, G. Ziegler, Über die Geschwindigkeiten der zur Glasschmelze führenden Reaktionen. III. Reaktionsgeschwindigkeiten im Quarternären System Na2O-CaO-SiO2-CO2, Glas. Ber. 27 (1954) 199–212.

Chapter 6

Peer-Reviewed Publications

Paper 1

Synthesis and characterization of $12CaO{\cdot}7Al_2O_3$ slags: the effects of impurities and atmospheres on the phase relations

Fabian Imanasa Azof[a], Kai Tang[b], Jinglin You[c], Jafar Safarian[a]

[a]Norwegian University of Science and Technology (NTNU), Department of Materials Science and Engineering, N-7491 Trondheim, Norway

[b]SINTEF Industry, NO-7465 Trondheim, Norway

[c]State Key Laboratory of Advanced Special Steel and Shanghai Key Laboratory of Advanced Ferrometallurgy, School of Materials Science and Engineering, Shanghai University, Shanghai-200072, China

Corresponding author: Fabian Imanasa Azof (fabian.i.azof@ntnu.no)

Abstract

Synthesis of crystalline slags of $12CaO{\cdot}7Al_2O_3$ phase from the corresponding melt compositions in different atmospheric conditions and different purities are investigated. Observations using a thermogravimetry coupled with differential thermal analysis showed that the dehydration of a zeolitic $12CaO{\cdot}7Al_2O_3$ phase occurs at 770 – 1390 °C before it congruently melts at 1450 °C. X-ray diffraction pattern of the slag showed that a single $12CaO{\cdot}7Al_2O_3$ phase is produced from a mixture, which has small SiO_2 impurity with 49:51 mass ratio of CaO to Al_2O_3. Scanning electron microscope and electron probe micro-analyzer showed that a minor Ca-Al-Si-O-containing phase is in equilibrium with a grainless $12CaO{\cdot}7Al_2O_3$ phase. Moreover, $12CaO{\cdot}7Al_2O_3$ is unstable at room temperature when the high purity molten slag is solidified under oxidizing conditions, contained in an alumina crucible. On the other hand, a high-temperature in-situ Raman spectroscopy of a slag that was made of higher purity CaO –Al_2O_3 mixture showed that $5CaO{\cdot}3Al_2O_3$ phase is an unstable/intermediate phase in the CaO-Al_2O_3 system, which is decomposed to $12CaO{\cdot}7Al_2O_3$ above 1100 °C upon heating in oxidizing conditions. It was found that $5CaO{\cdot}3Al_2O_3$ present at room temperature when the $12CaO{\cdot}7Al_2O_3$ dissociates to a mixture of $5CaO{\cdot}3Al_2O_3$, $3CaO{\cdot}Al_2O_3$, and $CaO{\cdot}Al_2O_3$ phases during the cooling of the slag at 1180 ± 20 °C in reducing atmosphere. It is proposed that low concentrations of Si stabilize $12CaO{\cdot}7Al_2O_3$ (mayenite), in which Si is a solid solution in its lattice, which is named Si-mayenite. Regarding the calculated CaO-Al_2O_3-SiO_2 diagram in this study, this phase may contain a maximum of 4.7 wt.%SiO_2, which is depending on the total SiO_2 in the system and the Ca/Al ratio.

Keywords: $12CaO{\cdot}7Al_2O_3$; Mayenite; Si-mayenite; Slag; Impurities

1. Introduction

In 1909, the binary $CaO–Al_2O_3$ phase diagram was initially reported by Shepherd et al. that was supported by an optical study by Wright, F. E. [1] . In addition of pure CaO and Al_2O_3 phases, they observed four compounds in a range of 15 to 70 wt.%Al_2O_3, which were $CaO·Al_2O_3$ (denoted by CA), $5CaO·3Al_2O_3$ (denoted by C_5A_3), $3CaO·Al_2O_3$ (denoted by C_3A), and an unstable form of both $3CaO·5Al_2O_3$ (denoted by C_3A_5) and C_5A_3. Also, in 1911, they published a preliminary report on the ternary $CaO–Al_2O_3–SiO_2$ system [2], which was of great importance on a study of the constitution of Portland cement clinker. Later on, Rankin and Wright [3] in 1915, documented the ternary $CaO–Al_2O_3–SiO_2$ phase diagram, which was an updated version of the preliminary report. They had stated that C_5A_3 formation occurred in two forms; a stable and an unstable monotropic form. The stable form melts at 1455 ± 5 °C and has two eutectic mixtures with C_3A and CA phases. On the other hand, the unstable form has neither a definite melting point nor any range of temperatures regarding its stability.

It was until 1936, Büssem and Eitel [4] showed that the $CaO:Al_2O_3$ ratio of the synthesized stable C_5A_3 phase from Rankin and Wright's study was 12:7 rather than 5:3, in which they suggested chemical compound was $12CaO·7Al_2O_3$ (denoted by $C_{12}A_7$). Regarding this phase, Nurse et al. [5,6] found that at elevated temperatures, $C_{12}A_7$ is unstable in anhydrous or moist-free $CaO-Al_2O_3$ system. It is in equilibria with H_2O above 950 °C and forms $Ca_{12}Al_{14}O_{32}(OH)_2$ when is fully saturated; the water present as hydroxyl ions in the crystal structure. The observation was in agreement with Roy and Roy [7], which had previously reported the zeolitic behavior of the phase. Zeolitic behavior means that the phase absorbs and desorbs water as a function of temperature (with pH_2O fixed). They found that $C_{12}A_7$ could absorb water vapor even at 1000 °C at a pH_2O of 1.6×10^{-3} atm. In a similar conclusion, Imlach et al. [8] claimed that the $C_{12}A_7$ phase is stable at high temperatures as it absorbs excess of oxygen from any oxidizing atmosphere, even where pO_2 is as low as 10^{-8} atm. In other words, according to them, the phase is very efficient at extracting oxygen from the surrounding atmosphere.

According to Büssem and Eitel [4], the $C_{12}A_7$ phase in its anhydrous form has the following physical properties: a = 11.982 Å, V = 1720.24 Å^3, bulk density = 2.85×10^3 kg.m^{-3}, in cubic I-43d (220) space group. In 1962, Jeevaratnam et al. [9] used a petrographic microscope to investigate the $C_{12}A_7$ crystal structure and showed results that were in agreement with the work of Büssem and Eitel as well. As mentioned earlier, Rankin and Wright [3] claimed that $C_{12}A_7$ melts at 1455 ± 5 °C. Whereas, Nurse et al. [6] used a high-temperature microscope and proposed that $C_{12}A_7$ crystals are seen to melt at 1392 ± 3 °C. Later, Hallstedt [10] optimized the thermodynamic data of $C_{12}A_7$ phase using CALPHAD, which stands for Calculation of Phase Diagram technique, and reported that the phase melts congruently at 1449 °C and it has a eutectic with other phases C_3A and CA on each side. Thermodynamic properties of $C_{12}A_7$ phase has been evaluated based on the phase equilibrium information given by Rankin [3], Nurse et al. [6], and Chatterjee and Zhmoidin [11]. An updated thermodynamic description of the CaO-

Al_2O_3-SiO_2 system has been established., using FactSage™, a thermochemical simulation software. A part of CaO–Al_2O_3 phase diagram that includes $C_{12}A_7$ phase is calculated and shown in Fig. 1. It is worth noting that the presented phase diagrams for this binary system in literature [12–14] may do not show $C_{12}A_7$ phase, assuming that it is not a stable phase.

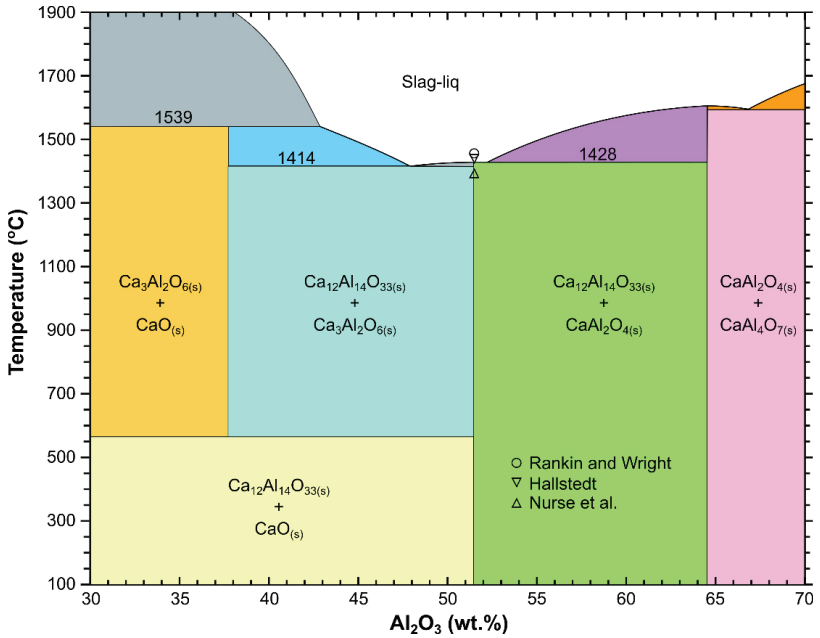

Fig. 1. A part of CaO–Al_2O_3 phase diagram as constructed using FactSage™, which includes the $C_{12}A_7$ phase and its melting point according to Hallstedt [10], Nurse et al. [5], and Rankin and Wright [3].

The stability of anhydrous $C_{12}A_7$ has been investigated intensively as the phase exhibits excellent properties as inorganic electrides [15–18]. Electrides are regarded as ionic compounds, where electrons act as anions and can be utilized in various fields, such as catalysis, batteries, reducing agents, electronic and optoelectronic devices [17,19]. A stoichiometric compound of $C_{12}A_7$ has a unit cell that consists of $(Ca_{24}Al_{28}O_{64})^{4+}\cdot 2O^{2-}$, in which the first part is a lattice framework with 12 subnanocages and the latter is called an extra framework oxide ions that are randomly distributed in the cages [20].

In 2017, the European Commission under Horizon 2020 program launched a project that is named ENSUREAL (www.ensureal.com). The project works on a sustainable alumina recovery from bauxite that is based on a smelting-reduction process that produces calcium-aluminate slags that can be further leached in Na_2CO_3 solution for alumina recovery [21–29]. One of the known leachable and favorable

phases in the slags is $C_{12}A_7$ phase, which has been reported in several studies [21,30–32]. However, the formation of $C_{12}A_7$ phase in slags produced from the smelting-reduction of bauxite, and its behavior under different conditions is still unclear [24]. Therefore, it is necessary to study the stability of $C_{12}A_7$ as well as other known metastable phase, C_5A_3, that are produced from calcium-aluminate melts at different conditions.

2. Experimental procedure

2.1 Slagmaking

The $C_{12}A_7$ phase consists of 12 moles CaO and 7 moles Al_2O_3, which is equivalent to a mass ratio of 49:51 of CaO to Al_2O_3 (C/A). In the current study, four slags (denoted as Slags 3(a) to (d)) were made in the mass ratio of 49:51 C/A, and four other slags (denoted as Slags 4(a) to (d)) were in ratio 54:46. The slag numbers here are based on the labeled slags in our previous published work and are kept in this research to be more convenient for the readers [21]. The slags were made from different raw materials purity and atmospheric conditions. The composition of CaO and Al_2O_3 powders used for the pure mixture are 99.9 wt.%CaO and 99.95 wt.%Al_2O_3. Whereas, the less pure mixtures were made from 96 wt.%CaO and the same 99.95 wt.%Al_2O_3. Table 1 shows the names, composition, and smelting parameter of each sample. In addition to the eight different slags, the Slag 3(a) was re-melted in a reducing condition to see the stability of phases that were formed in its first treatment.

Table 1. Target slags composition that are classified by different raw materials purity, crucible types, and melting atmospheric conditions.

Sample name	Composition		Raw materials purity	Crucible type	Use a graphite or alumina lid	Melting atmospheric condition
	CaO (wt.%)	Al_2O_3 (wt.%)				
Slag 3(a)	49	51	Less pure	Graphite	No	Reduction with $O_{2(g)}$ present
Slag 3(b)	49	51	Pure	Graphite	No	Reduction with $O_{2(g)}$ present
Slag 3(c)	49	51	Pure	Graphite	Yes, graphite lid	Reduction
Slag 3(d)	49	51	Pure	Alumina	Yes, alumina lid	Oxidation
Slag 4(a)	54	46	Less pure	Graphite	No	Reduction with $O_{2(g)}$ present
Slag 4(b)	54	46	Pure	Graphite	No	Reduction with $O_{2(g)}$ present
Slag 4(c)	54	46	Pure	Graphite	Yes, graphite lid	Reduction
Slag 4(d)	54	46	Pure	Alumina	Yes, alumina lid	Oxidation

Slag 3(a)-remelted	49	51	Less pure	Graphite	Yes, graphite lid	Reduction

Mixtures of CaO and Al_2O_3 powders were appropriately prepared using a mixing-jar. The weight of each mixture was 25 g. The mixtures were poured into either graphite or alumina crucible with about 30 mm and 50 mm of inner diameter and height. In the smelting of Slags 3(c), 3(d), 4(c), 4(d), and re-melted 3(a), to reduce the oxygen interference and create either a reducing or oxidizing atmosphere, the top of the crucible was closed using a lid. On the other hand, the remaining slags were not smelted using the lid. The relatively small crucibles were then placed into a larger graphite crucible. The crucibles were heated by using a 75-kVA open induction furnace slowly at the rate of 30 °C/min until the temperature has reached 1650 °C. The temperature was kept for 30 min before it was subsequently cooled down in the furnace slowly. The thermocouple used in the study was tungsten/rhenium (C-type), which was encapsulated by alumina and graphite insulation tubes. The schematic of smelting setup is shown in Fig. 2.

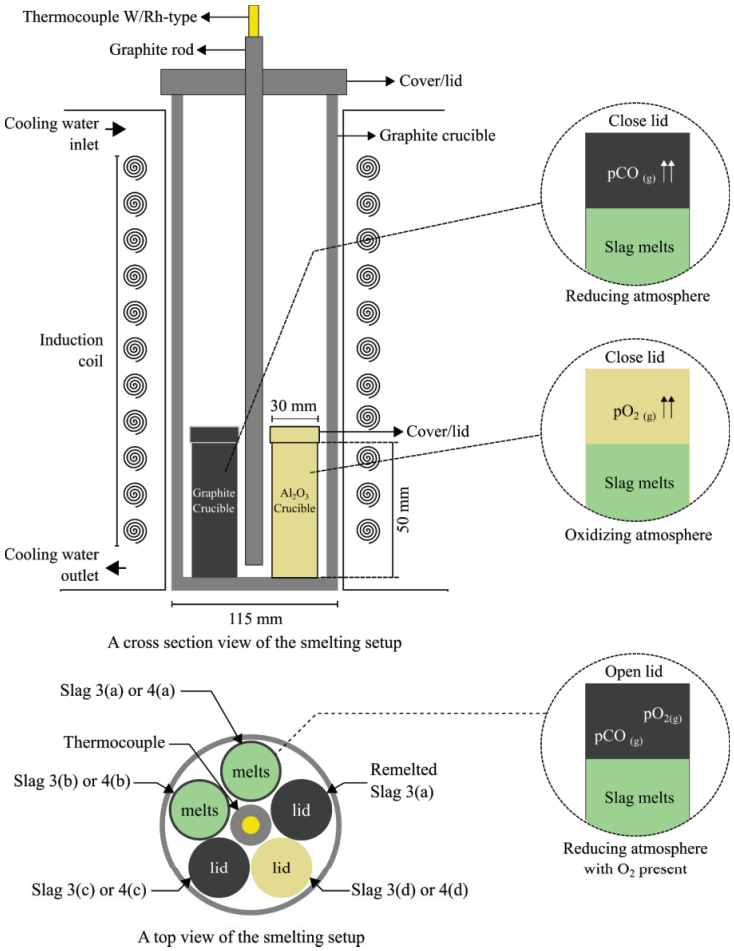

Fig. 2. A schematic diagram of smelting setup with different crucibles and atmospheric conditions.

The smelting profile of the slagmaking step is shown in Fig. 3. On average, the heating rate from the room temperature to 1000 °C and from 1000 to 1650 °C were 37.9 and 26.1 °C/min, respectively. Whereas, the cooling rate from 1650 to 1450, 1450 to 1000, 1000 to 600, and 600 to the room temperature were, respectively, 32.5, 29.2, 10.0, and 1.1 °C/min, on average.

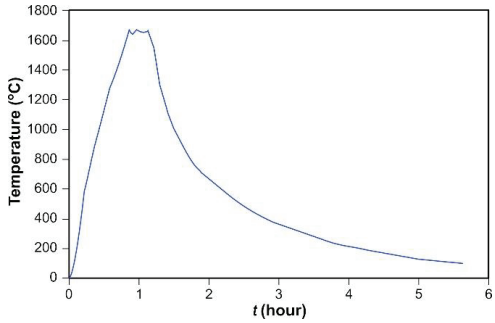

Fig. 3. The smelting temperature (°C) as a function of *t* (hour) from the slagmaking experiment.

2.2 Characterization techniques

High-resolution imaging, Energy Dispersive Spectroscopy (EDS) analysis, and X-ray element mapping of slags were carried out using Hitachi SU6600™ Scanning Electron Microscope (SEM). A high resolution Electron Probe Micro-Analyzer (EPMA) JXA-8500F™, supported by Wavelength Dispersive Spectroscopy (WDS), also used to get high accuracy on quantitative analysis of elements in selected phases of the slags. Phase identification of the slags and residues were undertaken with a Bruker D8 A25 DaVinci™ X-ray Diffraction (XRD) machine with CuKα radiation, between 10 - 75° diffraction angle, 0.01° step size, and 2.5° for both primary and secondary soller slit. The identification and qualitative phase analysis of the obtained XRD peaks were done by using DIFFRAC.EVA™.

For thermal analysis, a Thermogravimetry (TG) and Differential Thermal Analysis (DTA) NETZSCH STA 449C™, combined with mass spectrometry QMS 403C™ was used. Alumina crucible was used and exposed in synthetic air that flows at 30 mL/min and was heated at a ramp of 10 °C/min up to 1500 °C. Thus, after 30 min it was cooled down to room temperature at 10 °C/min. Furthermore, High Temperature Raman spectrometer Jobin Y'von LabRAM HR Evolution™ was used to determine the Raman spectra of the slags. It uses a visible pulse laser with a wavelength of 532 nm. The laser output power, slid width, scanning wavenumber range are 100 mW, 200 μm, 200 – 1200 cm^{-1}, respectively. A platinum crucible with 5 mm of diameter and 2 mm of depth was used when experimenting the measurement. The heating rate from room temperature to 1000 °C was 500 °C/min, in which the spectrum was measured after holding at 500, 800, and 1000 °C for 10 min. Furthermore, from 1000 – 1485 °C, the heating rate was 200 °C/min, in which the spectrum was measured after 10 min at 1200, 1300, 1400, 1450, 1485 °C. The measurements were carried out under an ambient pressure.

3. Results

3.1. The appearance of slags

After cooling down the slag samples to room temperature, then we cut half of the crucible of Slags 3(c), 3(d), 4(c), 4(d), and re-melted $C_{12}A_7$ and took an image of the cross-section as shown in Fig. 4. The colors of the slags from the reducing atmosphere are dark-grey, while slags from the oxidizing atmosphere are dominant in white, and the slag from the re-melting of Slag 3(a) at reducing atmosphere is dark-green. The appearance result agrees with the literature [15,19] as it is said that a slag containing CA and C_3A phase is likely to have grey color, whereas a slag that is produced from a smelting process using a carbon crucible that contains $C_{12}A_7$ phase has a dark green color.

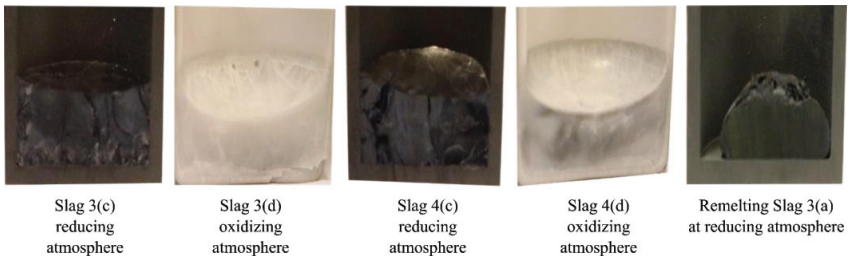

Fig. 4. A cross-section view of Slags 3(c), 3(d), 4(c), 4(d), and the remelted Slag 3(a).

3.2. Phase analysis

The XRD patterns of Slags 3(b), (c), and (d) are shown in Fig. 5. The patterns indicate the effect of atmospheric conditions on the slag phases. The order of phases from the strongest to the weakest intensities on Slag 3(b) is C_5A_3, CA, and C_3A. On Slag 3(c), the order of phases is C_3A, CA, and C_5A_3. While on Slag 3(d), the order is CA and C_3A.

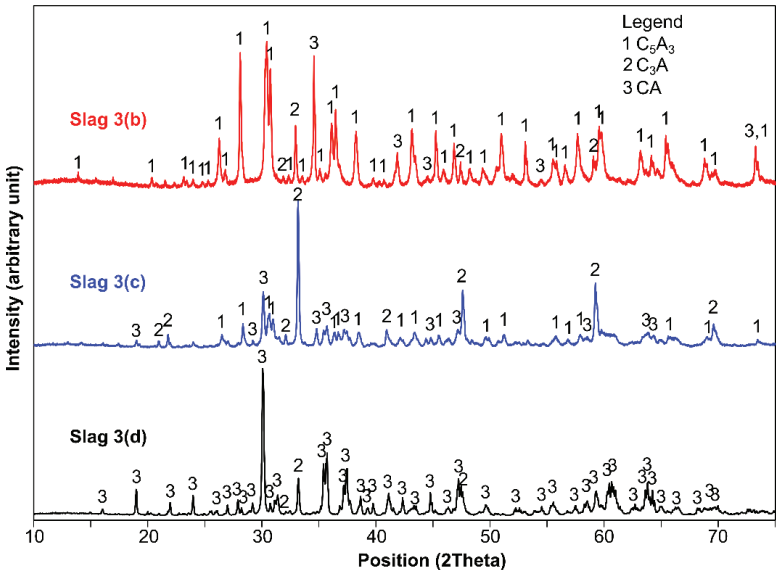

Fig. 5. XRD patterns of Slags 3(b), (c), and (d), produced from pure mixtures in reducing with O_2 presence, reducing, and oxidizing conditions, respectively.

The XRD patterns of Slags 3(a) and (b) is shown in Fig. 6. The patterns show the comparison of the phases of the slags produced from different purities. The strongest peak observed on Slag 3(a) that was produced from a less pure mixture is the $C_{12}A_7$ phase. On the other hand, as mentioned earlier, Slag 3(b) that was produced from the highly pure mixture consists of C_5A_3, C_3A, and CA phases.

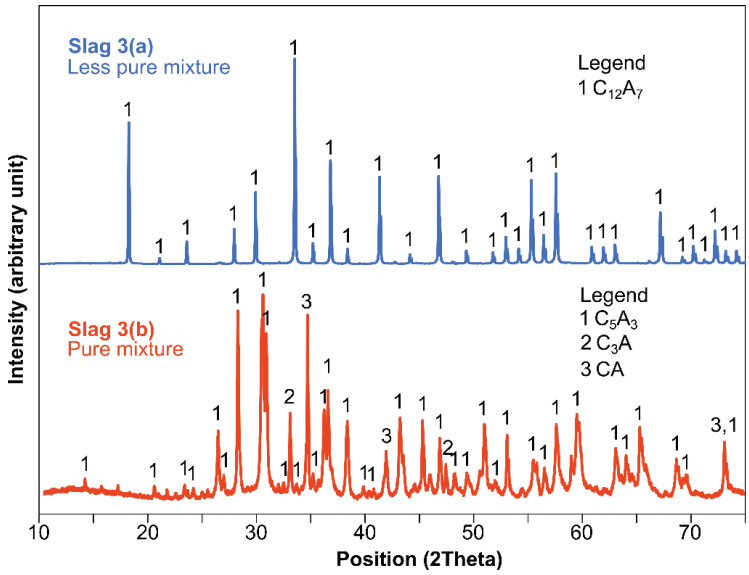

Fig. 6. XRD patterns of Slags 3(a) and (b).

XRD results of Slag 3(a) and Slag 3(a)-remelted at reducing condition are compared in Fig. 7. A Powder Diffraction File (PDF) database number 01-078-2975 that refers to $C_{12}A_7$ phase also included in the figure. As seen, the congruent $C_{12}A_7$ phase is still stable at room temperature even after the Slag 3(a) was re-melted. There are weak peaks at 17.5, 26.5, and 32 degree both in Slag 3(a) and in re-melted Slag 3(a) XRD patterns, in which later we find that the peak may belong to a Ca-Al-Si-O containing phase on the slags.

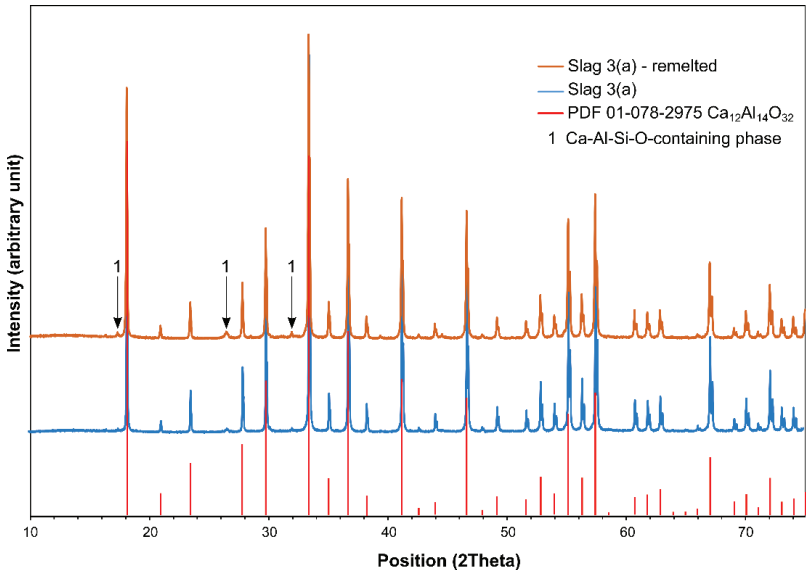

Fig. 7. XRD patterns of Slag 3(a) and Slag 3(a)-remelted.

The XRD patterns of Slags 4(b), (c), and (d) are shown in Fig. 8. The results show that under reducing condition with O_2 presence, C_5A_3 and C_3A are the observable phases on Slag 4 that was produced from pure mixtures. Meanwhile, C_5A_3 does not exist on Slags 4(c) and (d), which are both reducing and oxidizing conditions. The existing phases on Slags 4(c) and (d) are C_3A and CA.

The effect of mixtures purity on the phase equilibrium of Slag 4 is shown on XRD patterns in Fig. 9. As seen, the slag that was produced from less pure mixture has $C_{12}A_7$ and C_3A in equilibrium at room temperature. Meantime, the slag that was produced from pure mixture has C_5A_3 and C_3A phase. Both Slags 4(a) and (b) were exposed to reducing condition with O_2 presence during the smelting treatment.

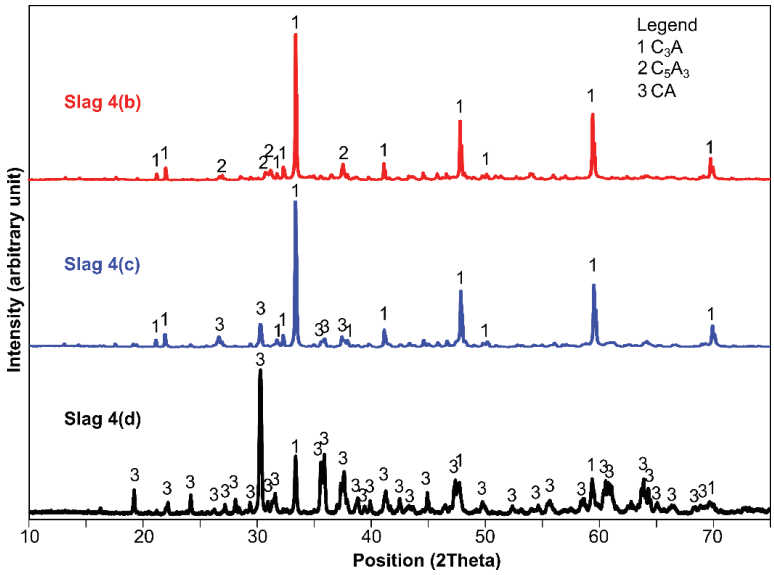

Fig. 8. XRD patterns of Slags 4(b), (c), and (d), produced from pure mixtures in reducing with O_2 presence, reducing, and oxidizing conditions, respectively.

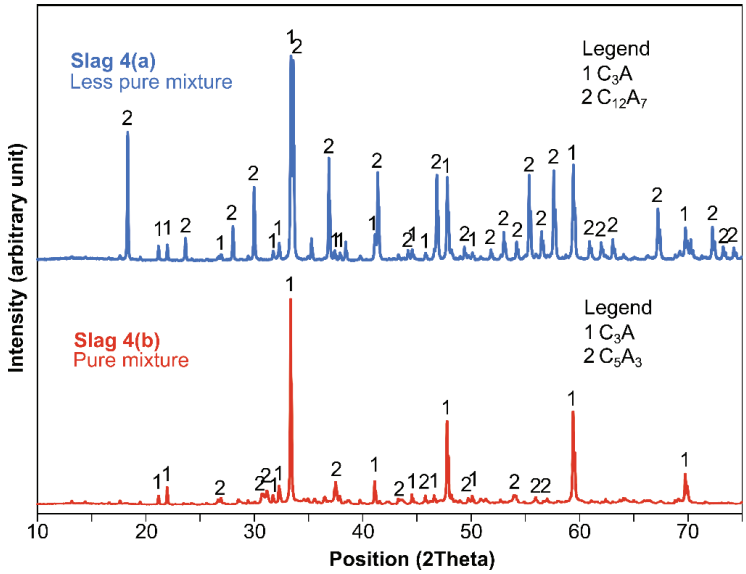

Fig. 9. XRD patterns of Slags 4(a) and (b).

3.3. Microstructural analysis

X-ray mapping of elements were performed for Slags 3(a) and 3(b) as typical results are shown in Figs. 10 and 11, respectively. As shown earlier from the XRD results, Slag 3(a) consists of a single $C_{12}A_7$ phase, meanwhile Slag 3(b) consists of C_5A_3, CA, and C_3A phases. The result of X-ray mapping elements for Slag 3(a) shows that in addition to $C_{12}A_7$, the slag also has another phase that is visually distinct due to its irregular shape and brighter contrast compared to the matrix. The phase has a higher concentration of calcium and silicon compared to the matrix (hereafter named Ca-Al-Si-O containing phase).

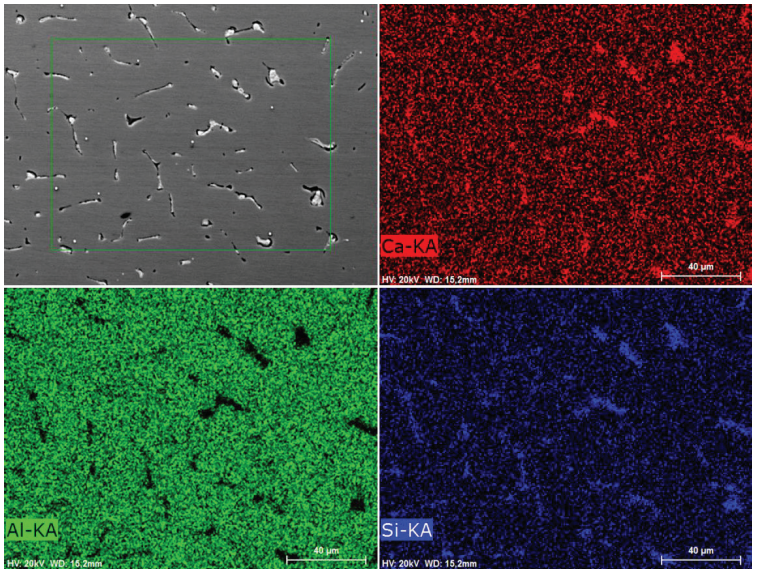

Fig. 10. X-ray mapping element of Slag 3(a) that shows different concentrations of Ca, Al, and Si.

Furthermore, the X-ray mapping of elements in Slag 3(b) in Fig. 11 shows that there are two phases exist in the slag; a matrix and bright phase. It seems that the bright phase, which is present between the matrix boundaries, has a slightly higher concentration of calcium than the matrix. Also, it is shown that a relatively low silicon concentration is concentrated within the grain boundaries.

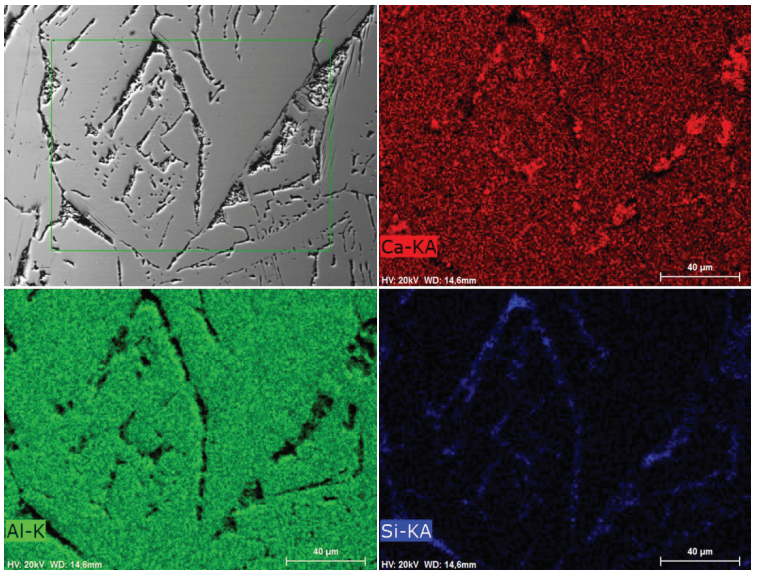

Fig. 11. X-ray mapping element of Slag 3(b) that shows different concentrations of Ca, Al, and Si.

In Fig. 12, a BSE image of Slag 3(a) is shown. The EDS points number 825 to 831 and 832 to 839 measures the elemental composition of Ca-Al-Si-O containing phase and matrix, respectively. The Ca-Al-Si-O containing phase consists of 43.27 wt.%Ca, 27.81 wt.%Al, 2.32 wt.%Si, 0.82 wt.%Mg, and 25.78 wt.%O, on average (Table 2). However, a portion of the detected Ca, Al, and O may be from the matrix as this phase is small. Meantime, the matrix consists of 37.94 wt.%Ca, 34.84 wt.%, and 27.23 wt.%O, on average. (Table 2). The mass ratio of Ca/(Al+Si) on the Ca-Al-Si-O containing phase and matrix is 1.44 and 1.09, respectively.

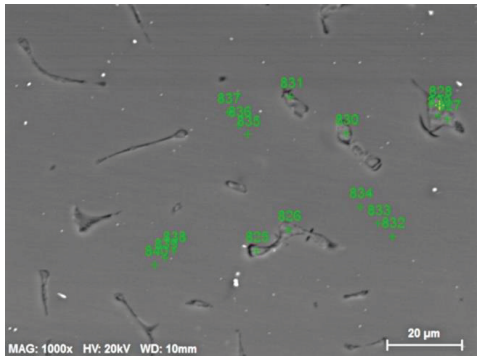

Fig. 12. SEM-BSE image of Slag 3(a) with EDS point on the Ca-Al-Si-O containing phase, which is number 825 to 831, and the matrix, which is number 832 to 839.

Table 2. EDS results of different phases on the Slag 3(a) in point illustrated in Fig. 12.

BSE	EDS point	Element (wt.%)					Mass
		Ca	Al	Si	Mg	O	Ca/(Al+Si)
Ca-Al-Si-O containing phase	825	41.90	30.22	2.24	0.80	24.83	1.29
	826	45.00	27.49	2.09	0.75	24.68	1.52
	827	43.32	26.47	2.49	0.83	26.88	1.50
	828	44.28	26.95	2.41	0.86	25.50	1.51
	829	44.93	26.78	2.58	0.85	24.86	1.53
	830	41.81	27.53	2.59	0.85	27.22	1.39
	831	41.64	29.25	1.82	0.80	26.49	1.34
	Ave	43.27	27.81	2.32	0.82	25.78	1.44
Matrix	832	37.92	34.75	0.00	0.00	27.33	1.09
	833	37.97	34.73	0.00	0.00	27.30	1.09
	834	37.94	34.80	0.00	0.00	27.26	1.09
	835	38.83	34.10	0.00	0.00	27.07	1.14
	836	37.50	35.21	0.00	0.00	27.29	1.07
	837	37.91	34.91	0.00	0.00	27.18	1.09
	838	37.35	35.42	0.00	0.00	27.23	1.05
	839	38.10	34.76	0.00	0.00	27.14	1.10
	Ave	37.94	34.84	0.00	0.00	27.23	1.09

Typical SEM-BSE images of the Slag 3(b) are shown in Fig. 13 which includes the EDS measurement points on both the bright phase and matrix, and the EDS results are given in Table 3. On average, the bright phase consists of 45.29 wt.%Ca, 25.15 wt.%Al, 0.09 wt.%Si, and 29.47 wt.%O. Meanwhile, the matrix consists of an average composition of 42.03 wt.%Ca, 31.51 wt.%Al, and 26.46 wt.%O.

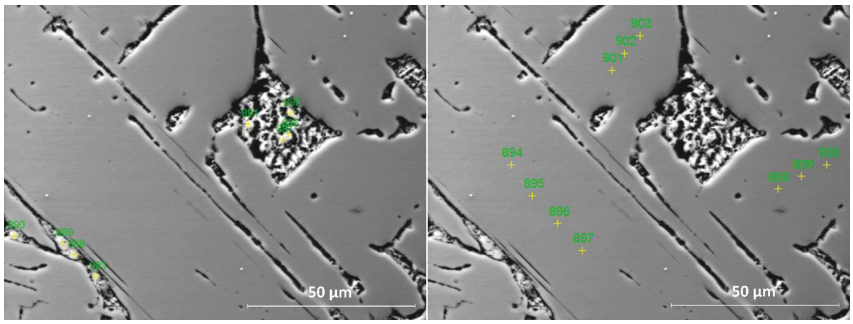

Fig. 13. SEM-BSE images of Slag 3(b) with EDS point on bright phase, which is 886 to 893, and the matrix, which is number 894 to 903.

Table 3. EDS result of different phases on the Slag 3(b).

BSE	EDS point	Element (wt.%)					Mass
		Ca	Al	Si	Mg	O	Ca/(Al+Si)
Bright phase	886	37.72	31.86	0.00	0.00	30.42	1.18
	887	48.20	27.59	0.00	0.00	24.21	1.75
	888	50.36	24.02	0.00	0.00	25.62	2.10
	889	49.81	22.13	0.00	0.00	28.06	2.25
	890	50.82	24.01	0.00	0.00	25.17	2.12
	891	41.89	23.77	0.00	0.00	34.34	1.76
	892	35.29	23.83	0.75	0.00	40.13	1.44
	893	48.24	23.95	0.00	0.00	27.81	2.01
	Ave	45.29	25.15	0.09	0.00	29.47	1.83
Matrix	894	42.38	31.00	0.00	0.00	26.61	1.37
	895	41.31	32.49	0.00	0.00	26.20	1.27
	896	42.22	31.29	0.00	0.00	26.48	1.35
	897	41.42	32.13	0.00	0.00	26.45	1.29
	898	41.78	31.68	0.00	0.00	26.54	1.32
	899	41.20	32.15	0.00	0.00	26.64	1.28
	900	42.52	31.15	0.00	0.00	26.33	1.37
	901	42.94	30.63	0.00	0.00	26.43	1.40
	902	42.00	31.56	0.00	0.00	26.44	1.33
	903	42.50	31.05	0.00	0.00	26.45	1.37
	Ave	42.03	31.51	0.00	0.00	26.46	1.33

BSE images of Slags 3(a) and 3(b) are shown in Fig. 14, and Fig. 15. The images were taken by EPMA. The BSE image of Slag 3(a) confirms the equilibrium of the Ca-Al-Si-O containing phase and $C_{12}A_7$ on the slag. Moreover, the WDS result of randomly selected points on the phases of the slags is presented in Table 4. The mass ratios of $CaO/(Al_2O_3+SiO_2)$ of the matrix and Ca-Al-Si-O containing phase on Slag 3(a) are 0.89 and 1.49, respectively. Meantime, the mass ratio of $CaO/(Al_2O_3+SiO_2)$ on the matrix of Slag 3(b) is 0.86.

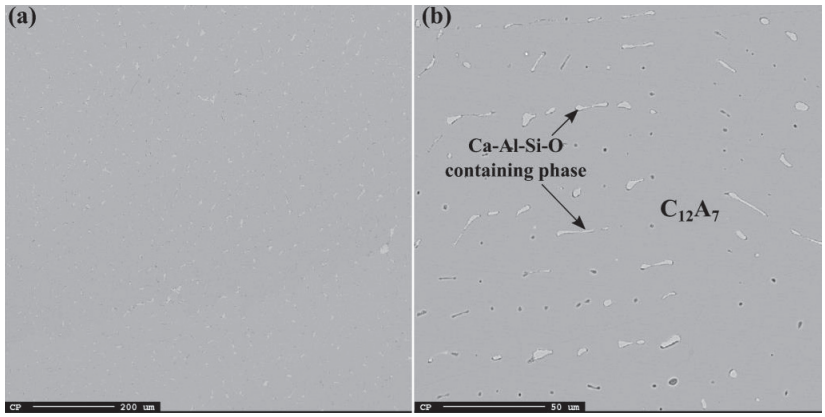

Fig. 14. BSE images of Slag 3(a) taken by EPMA instrument that shows the matrix ($C_{12}A_7$) and the Ca-Al-Si-O containing phase in different magnifications.

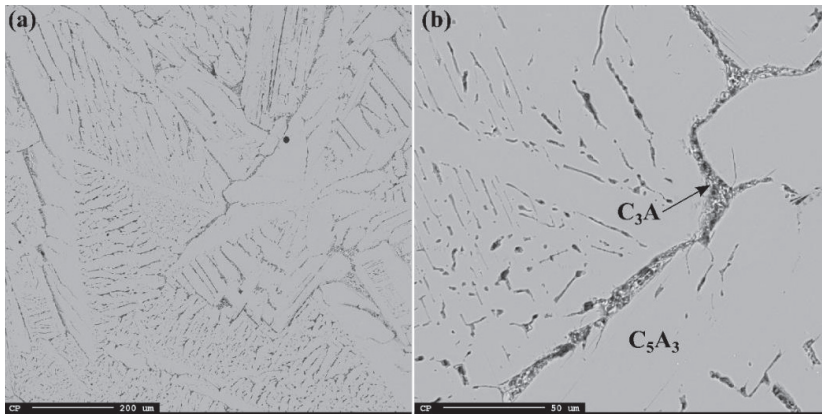

Fig. 15. BSE images of Slag 3(b) taken by EPMA instrument that shows the matrix (C_5A_3) and bright phase (C_3A) in different magnifications.

Table 4. A WDS result of Slags 3(a) and (b) from random points, on average.

Sample	Points	Constituent (wt.%)								Mass
		CaO	Al_2O_3	SiO_2	TiO_2	MgO	MnO	FeO	P_2O_5	$CaO/(Al_2O_3+SiO_2)$
Slag 3(a)	Matrix	47.02	52.62	0.08	0.03	0.19	0.03	0.03	0.02	0.89
	Ca-Al-Si-O-containing phase	59.43	37.33	2.67	0.02	0.40	0.11	0.01	0.03	1.49
Slag 3(b)	Matrix	46.23	53.60	0.12	0.00	0.01	0.01	0.00	0.02	0.86

3.4. Raman spectroscopy

A Raman spectra measurement of Slags 3(a) and (b) at room temperature is shown in Fig. 16. The strongest band of $C_{12}A_7$ in the present study is detected at 521 cm^{-1}, meanwhile other moderate intensities are seen at 312, 772, 880 cm^{-1}. The measured bands are in agreement with literature [33]. The band of bright phase on Slag 3(a) that was observed in Fig. 14 cannot be detected due to noises and its low quantity. On the other hand, the Raman measurement of Slag 3(b) shows that the C_5A_3 bands at 790, 601, 441, 345, and 300 cm^{-1} are relatively in fair agreement with the C_5A_3 bands in literature [34]. Meanwhile, the C_3A and CA bands are seen at 758 and 519 cm^{-1} that are also in good agreement with the literature [33].

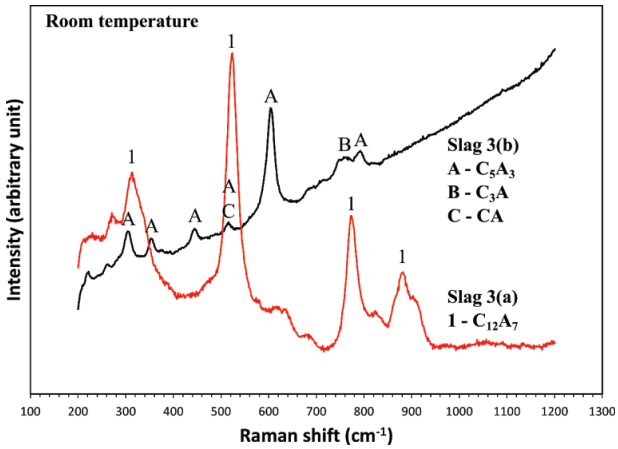

Fig. 16. Raman spectra of Slags 3(a) and (b) at room temperature.

In addition to room temperature, the in-situ Raman measurements of Slags 3(a) and 3(b) at 500, 800, 1000, 1200, 1400, 1450, and 1485 °C are shown in Fig. 17 and 18, respectively. In Fig. 17, the $C_{12}A_7$ band intensity at 490 ± 10 cm^{-1} decrease as the temperature increases. It is worth noting that the Raman band can be shifted from room to elevated temperatures due to the structural changes of the material from crystal to amorphous phase, as reported in the literature [35]. Therefore, as shown in Fig. 16 and 17 the $C_{12}A_7$ band shifts as the temperature increases. Furthermore, the respected band is undetected at temperature ≥ 1450 °C, which indicates that the $C_{12}A_7$ phase does not exist at these temperatures.

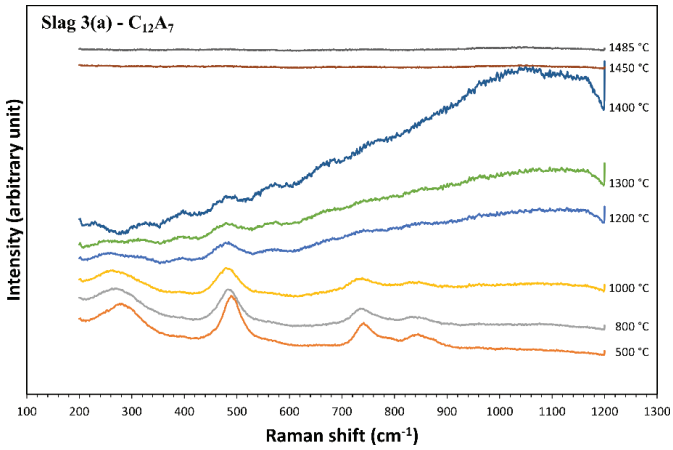

Fig. 17. In-situ Raman spectroscopy result of Slag 3(a) at 500, 800, 1000, 1200, 1300, 1400, 1450, and 1485 °C.

Moreover, the Raman measurement of Slag 3(b) at elevated temperatures shows that up to 1000 °C, the C_5A_3, C_3A, and CA phases are stable. At 1200 °C, however, the C_5A_3 bands are not detected. While, a strong band that is located at the same location as the $C_{12}A_7$ band is observed. This band is undetected at temperature ≥ 1450 °C, as observed for slag 3(a). The Raman measurement at 1450 and 1485 °C show that one or several phases co-exist in the heated slag as some weak bands are observed at these temperatures. However, it is very difficult to identify them due to the noises and their low intensity.

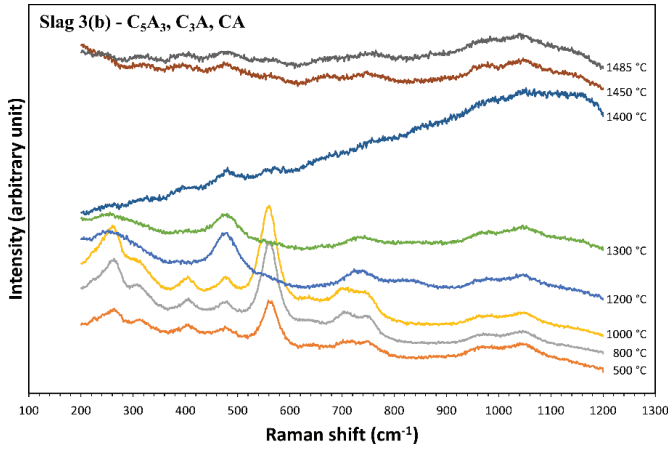

Fig. 18. In-situ Raman spectroscopy analysis of Slag 3(b) at 500, 800, 1000, 1200, 1300, 1400, 1450, and 1485 °C.

3.5. TG-DTA analysis

Fig. 19 shows the TG-DTA graphs of Slags 3(a) from room temperature to 1500 °C that was performed in a furnace that was exposed to synthetic air, using alumina crucible. In Fig. 19(a), the significant mass loss in the beginning of the measurement shall not be taken into consideration as it may be resulted from the error of weight calibration. Moreover, as seen, the sample gained mass up to 0.8 wt.% starting from 250 to 770 °C. Then it started to lose mass about 2 wt.% from 770 to 1390 °C. Therefore, in total the sample mass was lost up to 1.2 wt.% compared to the original weight during the heat treatment. In Fig. 19(b), several peaks of endothermic reactions during the heating step can be seen at 1270, 1340, and 1450 °C. Meanwhile, the peaks of exothermic reactions during the cooling step can be seen at 671 and 1180 °C. Fig. 19(c) shows the overall TG-DTA result as a function of time.

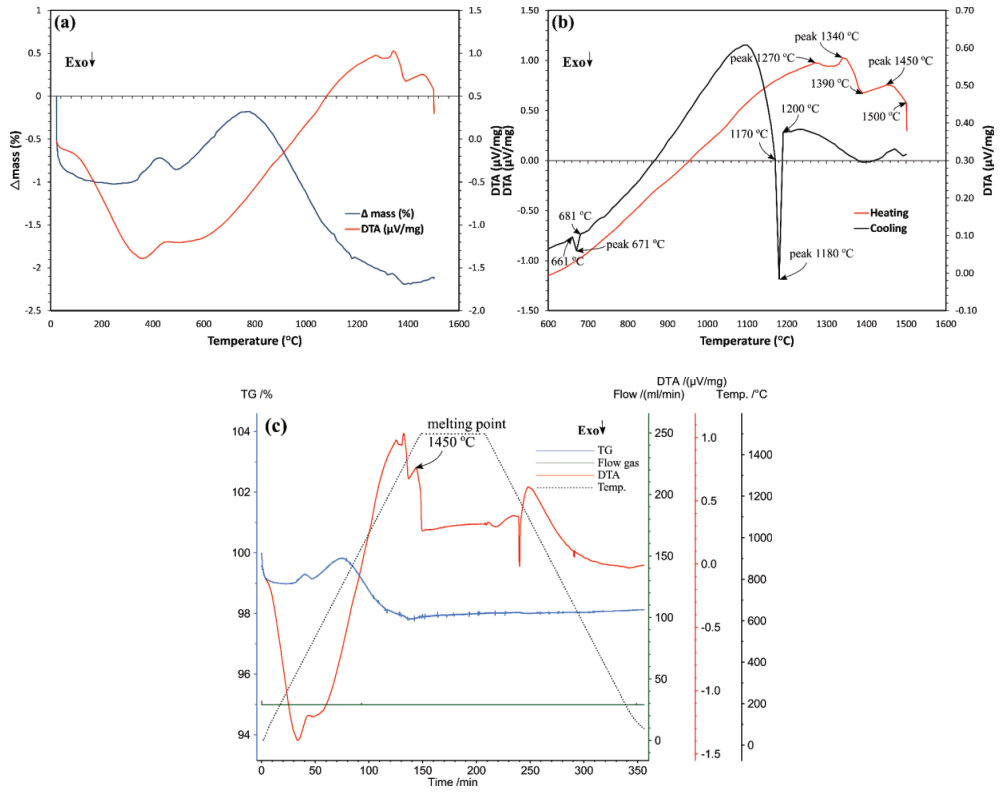

Fig. 19. TG-DTA graph of Slag 3(a) that shows: (a) the change of mass percentage (%) and DTA curve (μV/mg) as a function of temperature, (b) the differential of energy during heating and cooling steps at 600 – 1500 °C, and (c) TG-DTA as a function of time.

Furthermore, Fig. 20 shows the TG-DTA graph of Slags 3(b) from room temperature to 1500 °C that was performed in the same atmospheric condition and crucible as for the Slag 3(a). Similar to the previous result from Slag 3(a), the immediate mass loss in the beginning of the measurement shall not be taken into consideration due to the weight calibration. The sample lost mass 0.01 wt.% from 76 to 380 °C. Then, it gained mass 0.05 wt.% when the heating continued up to 470 °C. It lost mass gradually about 0.5 wt.% from 470 to 1310 °C. Thus, from 1310 to 1500 °C the sample loss its mass significantly up to 1.7 wt.%. Therefore, the total mass loss is 2.1 wt.% during the heat treatment. Moreover, the several peaks of endothermic reactions during the heating step are seen at 1310, 1350, and later at 1500 °C after it was holding for ca. 3 min. On the other hand, the peaks of exothermic reactions during the cooling step are seen at 750 and 1220 °C.

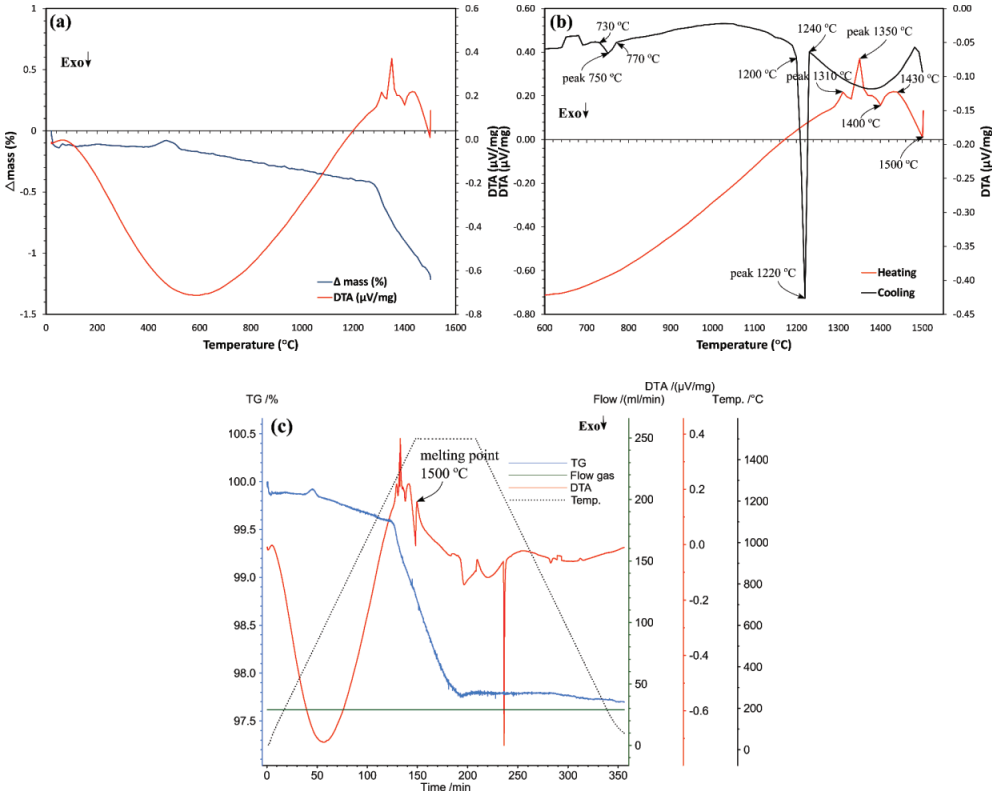

Fig. 20. TG-DTA graph of Slag 3(b) that shows: (a) the change of mass percentage (%) and DTA curve (μV/mg) as a function of temperature, (b) the differential of energy during heating and cooling steps at 600 – 1500 °C, (c) TG-DTA as a function of time.

4. Discussion

Based on the XRD, EDS, WDS and metallography observations, the effect of both atmospheric conditions and materials purity on the stability of $C_{12}A_7$ and C_5A_3 are discussed. Also, the evolution of phases of Slags 3(a) and 3(b) from Raman spectra and TG-DTA measurements are discussed.

4.1. The effect of atmospheric conditions and materials purity on $C_{12}A_7$ stability

As shown in the schematic of the melting setup in Fig. 2, the partial pressure of O_2 or $CO_{2\,(g)}$ was conditioned by the use of different crucibles and the use of lid to limit the contact of the melts with the surrounding air. The typical setup has been reported in the literature [15,36], in which using a graphite crucible to synthesize $C_{12}A_7$ phase at elevated temperatures. The $O_{2\,(g)}$ partial pressure at 1600 °C is 4.4×10^{-16} atm as calculated using the FactSage™. The calculation is in agreement with the research [15] stated that heating a closed-lid graphite crucible at 1600 °C created a strongly reducing atmosphere as low as $pO_2 = 10^{-16}$ atm inside of the crucible. The pressure is substantially lower than the pressure used by Imlach [8] that was managed to synthesize a stable $C_{12}A_7$ at elevated temperatures with $pO_2 = 10^{-8}$ atm.

Based on the XRD results of Slags 3(a) and 3(a)-remelted, the congruent $C_{12}A_7$ phase is stable either at reducing atmosphere or at a low partial pressure of $O_{2\,(g)}$. As of XRD results of Slags 3(b) and 3(c), the C_5A_3 phase exists with C_3A and CA phases at similar atmospheric conditions. It is important to note here that $C_{12}A_7$ does not co-exist with C_5A_3 phase in any given atmospheric conditions. We do not observe both $C_{12}A_7$ and C_5A_3 phases from Slags 3(d) and 4(d) that were produced from oxidizing atmosphere. We can confirm that the intensity of C_5A_3 peaks are decreased as the partial pressure of O_2 is decreased, which is shown by comparing the XRD results between Slags 3(b) and (c), and between Slags 4(b) and (c), where the graphite crucibles were exposed to air or closed using the lid, respectively. On the other hand, the lower intensity of the peaks due to the change of $O_{2\,(g)}$ partial pressure are not seen on $C_{12}A_7$ phase. We did not proceed smelting series of Slag 4(a) that contains $C_{12}A_7$ in equilibrium with C_3A phase at different atmospheric conditions. However, the re-melting of Slag 3(a) at reducing condition only produces a congruent $C_{12}A_7$ phase. Therefore, the intensity of $C_{12}A_7$ peaks on Slag 3(a)-remelted sample cannot be compared with the original Slag 3(a).

4.1.1 The silicon effects

According to the EDS and WDS results on the matrix and Ca-Al-Si-O containing phase of Slag 3(a), the major impurity in the $CaO\text{-}Al_2O_3$ slag impurities is SiO_2, which is 2.75 wt.%, on average. The other contaminants, i.e., TiO_2, MgO, MnO, FeO, and P_2O_5, accumulatively constitute for less than 1 wt.% of the slag. Therefore, it is more interesting to investigate the effect of silicon element (or SiO_2) on the stability of $C_{12}A_7$ phase than the other impurities.

Based on the phase and microstructure observations, it is evident that SiO_2 acts as one of the essential factors on the stabilization of $C_{12}A_7$ at room temperature, as the phase occurs only at slags that were produced from less pure mixtures. On Slag 3(a), SiO_2 exists as either in the matrix ($C_{12}A_7$) in a solute component in the $C_{12}A_7$ lattice, or in the Ca-Al-Si-O containing phase. We propose two of most likely explanations on how silicon or SiO_2 in both matrix and solid solution phase can stabilize $C_{12}A_7$:

(1) In the $C_{12}A_7$ matrix, the silicon cations may stabilize the extra framework O^{2-} anions in $C_{12}A_7$ unit cell that prevent the anions leave the cages in reducing conditions. Hence, this prevents the $C_{12}A_7$ to decompose to either C_5A_3 and C_3A [37], or C_3A and CA phases [5,8,15]. The $C_{12}A_7$ lattice might be slightly changed due to the Si-O bond in the matrix.

(2) In the Ca-Al-Si-O secondary phase, SiO_2 may act as a "supporting-phase" that helps $C_{12}A_7$ retains its structure at elevated temperatures and a very low $O_{2\,(g)}$ partial pressure. The Ca-Al-Si-O containing phase consists of oxides that may become the primary donor of O^{2-} ions to the $C_{12}A_7$ unit cell at elevated temperatures in reducing atmospheres.

*4.1.2 **The carbon effects***

In addition to silicon, another impurity that contributes to the stability of $C_{12}A_7$ is C_2^{2-} anions that can substitute O^{2-} anions in reducing conditions. The C_2^{2-} anions are originated from graphite crucible. It was claimed by Kim et al. [36] that the C_2^{2-} ions dissolve into the melt from the graphite crucible to compensate the oxygen deficiency in $C_{12}A_7$, which makes the $C_{12}A_7$ phase stable in reducing atmosphere. The C_2^{2-} and O^{2-} have close anion sizes, which are 1.2 and 1.4 Å, respectively. Thus, the C_2^{2-} ions may act as a template instead of the extra framework O^{2-} in the cages. In the current work, all $C_{12}A_7$-containing slags, i.e., Slags 3(a), remelted-3(a), and 4(a), were produced from reducing atmosphere by using graphite crucibles, which are in agreement with the result from Kim et al. However, as seen in the XRD patterns of Slags 3(b), 3(c), 4(b), and 4(c), these slags were melted using graphite crucible as well, yet no $C_{12}A_7$ phase was detected on the slags. Instead of $C_{12}A_7$, the C_5A_3, C_3A and CA phases are in equilibrium in these slags. Therefore, we suggest that the decomposition of $C_{12}A_7$ to C_5A_3, C_3A and CA follows a path as shown in reaction (1):

$$2(12CaO \cdot 7Al_2O_3) \rightarrow 4(5CaO \cdot 3Al_2O_3) + 3CaO \cdot Al_2O_3 + CaO \cdot Al_2O_3 \qquad (1)$$

The decomposition of $C_{12}A_7$ to three different phases may seem a complex solid-state phase transformation, which is dependent to the kinetics rate of crystallization. This is supported by a study done by Zhmoidin and Chatterjee [38]. They reported the removal of stabilizing additives (gases or anion template) from $C_{12}A_7$ or its melt leads to the densification of the structure with the formation of C_5A_3, or a mixture of C_5A_3, C_3A, and CA.

Based on the XRD results of Slags 3(b), 3(c), 4(b), and 4(c), we suggest that the role of C_2^{2-} ions on the stabilization of $C_{12}A_7$ is not significant in a one-stage melting treatment. The result is in agreement with the study from Kim et al. [19], in which they needed a two-stage melting treatment at 1600 °C to produce a stable $C_{12}A_7$ at room temperature using a graphite crucible. As we successfully synthesized a stable $C_{12}A_7$ only in a one-stage melting treatment (Slag 3(a)), we may conclude that the silicon or SiO_2 impurity in the mixture gives more significant factor than that of C_2^{2-} ions on the stabilization of the $C_{12}A_7$ phase.

4.2. The evolution of $C_{12}A_7$ and C_5A_3 phases at elevated temperatures

Table 5 shows the evolution of $C_{12}A_7$ phase in Slag 3(a) at elevated temperatures based on TG-DTA measurement. It is important to consider that the TG-DTA measurement was performed under oxidizing atmosphere. It was exposed to synthetic air with a flow rate of 30 mL/min in alumina crucible.

Table 5. The evolution of $C_{12}A_7$ at elevated temperatures in oxidizing condition.

Step	Temperature (°C)	TG-DTA remarks (endo/exothermic)	Description
Heating	250 – 770	Mass increases 0.8 wt.% (endothermic reaction)	The $C_{12}A_7$ phase uptakes water from the ambient atmosphere due to its zeolitic behavior. According to the literature [6,39], upon heating or cooling in ambient atmosphere, water is adsorbed at temperatures ≤ 1050 °C without significant change of the crystal structural parameters, as in following reaction (2) [20,40]: $(Ca_{12}Al_{14}O_{32})^{2+} \cdot O^{2-} + H_2O = (Ca_{12}Al_{14}O_{32})^{2+} \cdot 2(OH)^-$ (2) According to Hayashi et al. [40], the water uptake process follows these steps: (1) outward diffusion of an extra framework O^{2-} ion to the surface, (2) reaction of an O^{2-} ion with an H_2O molecule in the atmosphere at the surface to form a pair of OH^- ions, and (3) inward diffusion of OH^- ions.
	770 – 1390	Mass loss 2 wt.% (endothermic reaction)	Dehydration occurs and causing mass loss. Hayashi et al. [41] confirmed through the use of Thermogravimetry-Evolved Gas Analysis (TG-EGA) that H_2O desorption occurs at about 1200 °C. Also, it has been reported that the complete dehydration occurs at 1350 °C and results in a weight loss of 1.28 wt% [40]. The current results are in agreement with the literature, as the peak of endothermic reaction for dehydration occurs at 1340 °C and the mass loss is 1.2 wt.% compared to the original sample weight.
	1450	Melting point (endothermic reaction)	The peak of endothermic reaction at 1450 °C indicates the melting point of the phase, as it is also confirmed with in-situ Raman spectra at 1450 °C, which shows no $C_{12}A_7$

			bands are detected at the respected temperature. The result is in good agreement with Hallstedt [10] optimization study.
Cooling	1180	Decomposition (exothermic reaction)	Palacios et al. [37] reported that $C_{12}A_7$ may decompose to C_5A_3 and C_3A phases at 1100 °C under reducing conditions as shown in reaction (3). $4(12CaO \cdot 7Al_2O_3)=9(5CaO \cdot 3Al_2O_3)+3CaO \cdot Al_2O_3$ (3) Otherwise, it may crystallize to C_3A and CA when it was melted at 1600 °C under oxidizing and moisture-free condition, as suggested by Kim et al. [15] in reaction (4). $12CaO \cdot 7Al_2O_3=2.5(3CaO \cdot Al_2O_3)+4.5(CaO \cdot Al_2O_3)$ $\Delta H^{o}_{1180^{o}C} = -34.39 kJ/mol 12CaO \cdot 7Al_2O_3$ (4) The loss of O^{2-} ions template in oxidizing condition may occur as the melt was kept for a long time in the temperature range above 1500 °C, which leads to the decomposition of $C_{12}A_7$ to C_3A and CA, according to the literature [15]. Based on the TG-DTA result, we can confirm that the reaction (4) does not occur during the solidification; however, the decomposition happens during the cooling at 1180 °C.
	671	Unknown reaction (Exothermic reaction)	There is a relatively small heat generation from an exothermic reaction occurs at 671 °C. However, the chemical reaction cannot be confirmed as the established CaO-Al_2O_3 phase diagram at low temperatures is still unclear (< 1000 °C).

Table 6 shows the evolution of C_5A_3 phase on Slag 3(b) at elevated temperatures based on the TG-DTA measurement.

Table 6. The phase evolution of C_5A_3 at elevated temperatures in oxidizing condition.

Step	Temperature (°C)	TG-DTA remarks (endo/exothermic)	Description
Heating	470 – 1310	Mass loss gradually up to 0.5 wt.% (endothermic reaction)	The mass loss occurs most likely due to the dehydration.
	1310 – 1500	Mass loss significantly 1.7 wt.% (endothermic reaction)	It is evident that upon heating at this range of temperature several endothermic reactions occur, notably at 1310 and 1350 °C. The reactions are of similar to what occurs on Slag 3(a). Further observations using TG-EG may be necessary to investigate the evolution of O_2 and H_2O species on the slag at the respected temperatures.

	1500	Melting point of the slag (endothermic reaction)	The peak of endothermic reaction at 1500 °C after ca. 3 min of holding time indicates the melting point of the slag. However, we cannot confirm that it is the melting point of C_5A_3 as no literature has clearly reported it before. Rankin and Wright [3] reported that the phase has neither a definite melting point nor any temperature range of real stability.
Cooling	1220	Decomposition (exothermic reaction)	There has been no report on the crystallization of C_5A_3 from a melt. Thus, two different hypotheses concerning the exothermic reaction at this temperature can be constructed as follows: The decomposition reaction may involve either $C_{12}A_7$ or C_5A_3 phase. If the $C_{12}A_7$ firstly crystallized on the slag as the temperature is at solidus line, then after it completely solidified the decomposition reaction follows reaction (4). However, if the crystal C_5A_3 formed when the slag starts to solidify, then the decomposition of C_5A_3 to C_3A and CA phases in oxidizing condition follows reaction (5). $5CaO \cdot 3Al_2O_3 = 3CaO \cdot Al_2O_3 + 2(CaO \cdot Al_2O_3)$ (5) Either way, the decomposition of the matrix to C_3A and CA is evident, as we do not observe the existence of either $C_{12}A_7$ or C_5A_3 on Slags 3(d) or 4(d). Slags 3(d) and 4(d) were solidified from the melts made of the pure mixture at the oxidizing condition.
	750	Unknown reaction (Exothermic reaction)	Similar to the Slag 3(a), there is an exothermic reaction occurring at 750 °C. However, the chemical reaction cannot be confirmed as the established $CaO\text{-}Al_2O_3$ phase diagram at low temperatures has not been reported yet (< 1000 °C).

In addition to the TG-DTA result of C_5A_3 described above, it was found that the C_5A_3 phase is unstable in oxidizing condition when it is heated at temperatures above 1100 °C as seen in the in-situ Raman spectra measurement in Fig. 18. At these temperatures, the C_5A_3 bands disappears and at the same time, the $C_{12}A_7$ phase occurs in the slag. Hence, we suggest that the slag absorbs necessary O_2 gas or O^{2-} anions from the atmosphere to constitute a stable $C_{12}A_7$ at elevated temperatures.

Based on the experimental results obtained in the current study and the supportive literature data [5,15,37], a box-chart showing the stability of $C_{12}A_7$ phase formed from liquid state in different atmospheric conditions and purity is presented in Fig. 21. Explanations regarding the figure are as following:

1. A slag that is made from smelting a pure mixture of CaO and Al_2O_3 in a reducing atmosphere is unlikely to have the $C_{12}A_7$ phase according to the authors' result in the current study and literature [6,16]. An exception was a report after Kim *et al.* [15], in which they smelted the mixture two times before they had obtained $C_{12}A_7$ phase.

2. In an oxidizing condition using pure mixture, Nurse *et al.* [5] stated that the $C_{12}A_7$ phase can be obtained when a certain level of moisture is accessible. This agrees with authors' current results, where C_3A and CA are produced from the liquid slag instead of $C_{12}A_7$ phase.

3. We suggest that a stable $C_{12}A_7$ phase can be obtained from a calcium-aluminate melt with proper composition that contains impurities that is exposed either in a reducing or in an oxidizing atmosphere by using an inert crucible. A suitable crucible to contain the melt during the treatment is deemed necessary to produce a stable $C_{12}A_7$ at room temperature. Alumina crucible is not suitable to produce $C_{12}A_7$, as no $C_{12}A_7$ phase was obtained at room temperature using an alumina crucible. The reason is due to the dissolution of the alumina crucible into the melt upon treatment that destabilize the $C_{12}A_7$ phase.

4. The effect of less-pure materials and the use of inert crucible on the stability of $C_{12}A_7$ have never been reported earlier. Therefore, the current results can be useful for further research, or industrial use in manufacturing $C_{12}A_7$ in a relatively simple method.

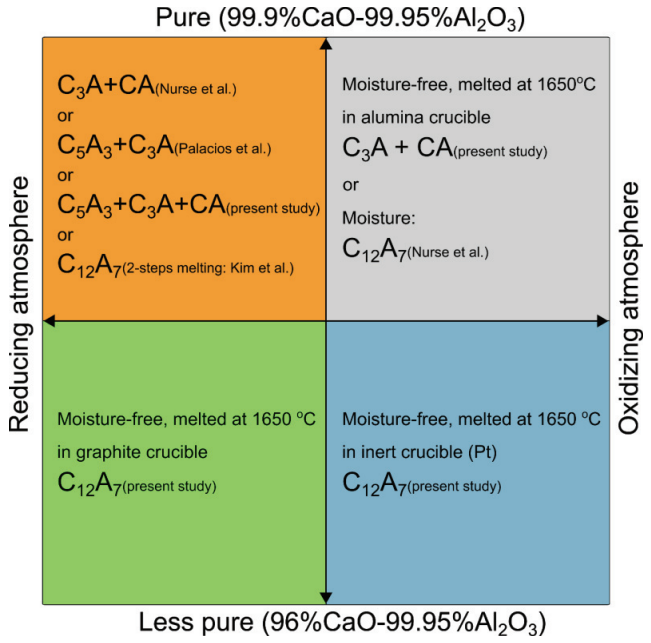

Fig. 21. Box-chart of the stability of $C_{12}A_7$ phase in different atmospheric conditions and purity of the mixtures.

4.3. Updating the $CaO-Al_2O_3-SiO_2$ phase diagram at low SiO_2 concentrations

The updated $CaO-Al_2O_3-SiO_2$ phase diagram at low SiO_2 mass fraction that includes $C_{12}A_7$ phase is shown in Fig. 22, which is constructed using FactSage™ with considering the obtained results of this work. The maximum solubility of SiO_2 in $C_{12}A_7$ phase is calculated as the following equation:

$$SiO_2 max\left(wt.\%\right)=7.482-0.0682\times Al_2O_3\left(wt.\%\right) \quad (6)$$

The maximum SiO_2 solubility in the $C_{12}A_7$ phase is a mathematical equation of curve a-b in the diagram in Fig. 22, which is valid for Al_2O_3 concentrations between 41 and 45 wt%. The $C_{12}A_7$ phase is called mayenite in literature, and as it was proved that it is stabilized by silicon component, it is logical to be called Si-mayenite here. The introduction of small amount of SiO_2 to the stoichiometric $C_{12}A_7$ causes its crystal structure stability to a significantly wider compositional range in which the ratio of C/(A+S) is almost fixed, while C/A is changed to larger numbers than the stoichiometric molar ratios in $C_{12}A_7$ in the Si-mayenite. It is worth noting that the introduction of Ti into the calcium-aluminate slags may also stabilize the mayenite formation, and correspondingly we may have a Ti-mayenite. The provided phase diagram data in Fig. 22 shows that the Si-Mayenite can dissolve a maximum amount of around 4.7 wt%SiO_2. However, the amount of silica in Si-mayenite is depending on the total silica in the system and also the Ca/Al ratio.

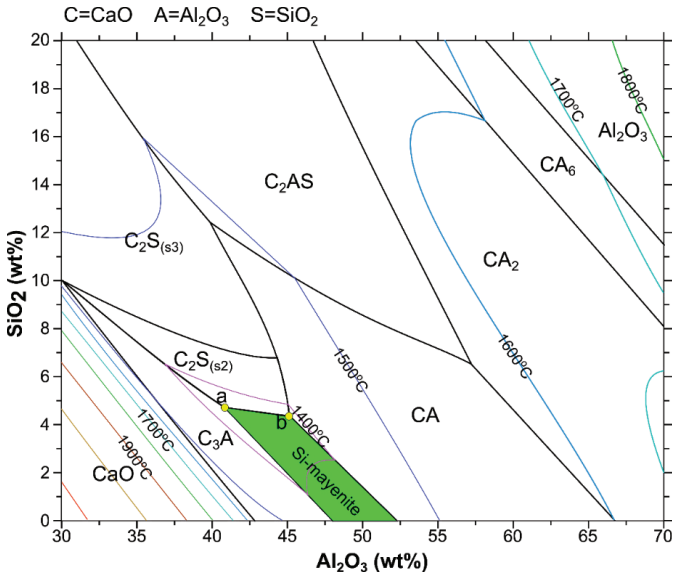

Fig. 22. Part of ternary $CaO-Al_2O_3-SiO_2$ phase diagram at low SiO_2 mass fraction, which shows curve a-b as the maximum solubility of SiO_2 in Si-mayenite phase.

5. Concluding remarks

The stability of $12CaO{\cdot}7Al_2O_3$ and $5CaO{\cdot}3Al_2O_3$ phases at room temperature produced from melts that are exposed to different atmospheric conditions and various raw materials purity was investigated. The main conclusions of this work are summarized as:

- The dehydration of $12CaO{\cdot}7Al_2O_3$ phase takes place at 770 – 1390 °C upon heating, before it melts congruently at 1450 °C.
- Stable $12CaO{\cdot}7Al_2O_3$ phase at room temperature is evident that is enforced by impurities, i.e., SiO_2, which play a significant role in maintaining the $12CaO{\cdot}7Al_2O_3$ structure with good reproducibility.
- As the silicon stabilizes the $12CaO{\cdot}7Al_2O_3$ phase (Si-mayenite), then it is possible to produce a stable phase in either reducing or oxidizing atmosphere by using a single smelting process.
- The $5CaO{\cdot}3Al_2O_3$ phase is an unstable/intermediate phase in the ternary $CaO\text{-}Al_2O_3\text{-}SiO_2$ system. It is decomposed to $12CaO{\cdot}7Al_2O_3$ above 1100 °C. However, in the current study, it exists only at room temperature when the $12CaO{\cdot}7Al_2O_3$ dissociates to a mixture of $5CaO{\cdot}3Al_2O_3$, $3CaO{\cdot}Al_2O_3$, and $CaO{\cdot}Al_2O_3$ phases during the cooling of the slag at 1180 ± 20 °C in a reducing atmosphere and is made from a pure 99.9 %CaO – 99.95 %Al_2O_3 mixture.

Acknowledgement

This research has been partially funded by NTNU in association with the Research Domain 5-Materials and the Society in SFI Metal Production (Project no. 237738), and co-funded by the ENSUREAL EU project (grant agreement no. 767533). The support from the both projects is acknowledged.

Conflict of interests

The authors declare that they have no known competing financial interests or personal relationships that could have appeared to influence the work reported in this paper.

6. Reference

[1] E.S. Shepherd, G.A. Rankin, F.E. Wrigth, The Binary Systems of Alumina with Silica,Lime and Magnesia.pdf, Am. J. Sci. 28 (1909) 293–333.

[2] E.S. Shepherd, G.A. Rankin, Preliminary Report on the Ternary System CaO–Al2O3–SiO2. A Study of the Constitution of Portland Cement Clinker., J. Ind. Eng. Chem. 3 (1911) 211–227. doi:10.1021/ie50028a005.

[3] G.A. Rankin, F.E. Wright, The Ternary System CaO-Al2O3-SiO2, Am. J. Sci. 39 (1915).

[4] W.. Büssem, A. Eitel, Die Struktur des Pentacalciumtrialuminats, Zeitschrift Für Krist. - Cryst.

Mater. 95 (1936). doi:10.1524/zkri.1936.95.1.175.

[5] R.W. Nurse, J.H. Welch, A.J. Majumdar, The CaO-Al2O3 System in a Moisture-free Atmosphere, Trans. Br. Ceram. Soc. 64 (1965) 409–418.

[6] R.W. Nurse, J.H. Welch, A.J. Majumdar, The 12CaO.7Al2O3 Phase in the CaO-Al2O3 System, Trans. Br. Ceram. Soc. (1965) 323–332.

[7] D.M. Roy, R. Roy, Crystalline Solubility and Zeolitic Behavior in Garnet Phases in the System CaO-Al2O3-SiO2, 4th Int. Congr. Chem. Cem. Vol.1. (1960) 307–314.

[8] J.A. Imlach, L.S.D. Glasser, F.P. Glasser, Excess Oxygen and the Stability of 12CaO.7Al2O3, Cem. Concr. Res. 1 (1971) 57–61.

[9] J.. Jeevaratnam, L.S.D.. Glasser, F.P. Glasser, Structure of Calcium Aluminate, 12CaO.7Al2O3, Nature. 194 (1962) 764–765. doi:10.1038/140607a0.

[10] B. Hallstedt, Assessment of the CaO-Al2O3 System, J. Am. Ceram. Soc. 73 (1990) 15–23. doi:10.1111/j.1151-2916.1990.tb05083.x.

[11] A.K. Chatterjee, G.I. Zhmoidin, The phase equilibrium diagram of the system CaO-Al2O3-CaF2, J. Mater. Sci. 7 (1972) 93–97. doi:10.1007/BF00549555.

[12] D.. Jerebtsov, G.. Mikhailov, Phase diagram of CaO–Al2O3 system, Ceram. Int. 27 (2001) 25–28. doi:10.1016/S0272-8842(00)00037-7.

[13] G. Eriksson, A.D. Pelton, Critical evaluation and optimization of the thermodynamic properties and phase diagrams of the CaO-Al2O3, Al2O3-SiO2, and CaO-Al2O3-SiO2 systems, Metall. Trans. B. 24 (1993) 807–816. doi:10.1007/BF02663141.

[14] E. Haccuria, T. Crivits, P.C. Hayes, E. Jak, Selected Phase Equilibria Studies in the Al2O3-CaO-SiO2 System, J. Am. Ceram. Soc. 99 (2016) 691–704. doi:10.1111/jace.13991.

[15] S.W. Kim, Y. Toda, K. Hayashi, M. Hirano, H. Hosono, Synthesis of a Room Temperature Stable 12CaO·7Al 2 O 3 Electride from the Melt and Its Application as an Electron Field Emitter, Chem. Mater. 18 (2006) 1938–1944. doi:10.1021/cm052367e.

[16] L. Palacios, A. Cabeza, S. Bruque, S. García-Granda, M.A.G. Aranda, Structure and Electrons in Mayenite Electrides, Inorg. Chem. 47 (2008) 2661–2667. doi:10.1021/ic7021193.

[17] D. Jiang, Z. Zhao, S. Mu, V. Phaneuf, J. Tong, Simple and Efficient Fabrication of Mayenite Electrides from a Solution-Derived Precursor, Inorg. Chem. 56 (2017) 11702–11709. doi:10.1021/acs.inorgchem.7b01655.

[18] A. Schmidt, M. Lerch, J.-P. Eufinger, J. Janek, R. Dolle, H.-D. Wiemhöfer, I. Tranca, M.M.

Islam, T. Bredow, H. Boysen, M. Hoelzel, CN-mayenite Ca12Al14O32(CN)2: Replacing mobile oxygen ions by cyanide ions, Solid State Sci. 38 (2014) 69–78. doi:10.1016/j.solidstatesciences.2014.09.017.

[19] S. Kim, M. Miyakawa, K. Hayashi, T. Sakai, M. Hirano, H. Hosono, Simple and Efficient Fabrication of Room Temperature Stable Electride: Melt-Solidification and Glass Ceramics, J. Am. Chem. Soc. 127 (2005) 1370–1371. doi:10.1021/ja043990n.

[20] R. Strandbakke, C. Kongshaug, R. Haugsrud, T. Norby, High-Temperature Hydration and Conductivity of Mayenite, Ca 12 Al 14 O 33, J. Phys. Chem. C. 113 (2009) 8938–8944. doi:10.1021/jp9009299.

[21] F.I. Azof, Y. Yang, D. Panias, L. Kolbeinsen, J. Safarian, Leaching characteristics and mechanism of the synthetic calcium-aluminate slags for alumina recovery, Hydrometallurgy. 185 (2019) 273–290. doi:10.1016/j.hydromet.2019.03.006.

[22] F.I. Azof, L. Kolbeinsen, J. Safarian, The Leachability of Calcium Aluminate Phases in Slags for the Extraction of Alumina, in: Trav. 46, Proc. 35th Int. ICSOBA Conf., ICSOBA, Hamburg, 2017: pp. 243–253. https://icsoba.org/sites/default/files/2017papers/Alumina Papers/AA13 - The Leachability of Calcium Aluminate Phases in Slags for the Extraction of Alumina.pdf (accessed February 25, 2018).

[23] A. Lazou, C. Van Der Eijk, E. Balomenos, J. Safarian, Smelting Reduction of Bauxite Residue and Beneficiation By-product in View of a Leachable Slag and Pig Iron Production, in: EMC 2019, 2019: pp. 17–34.

[24] F.I. Azof, L. Kolbeinsen, J. Safarian, Characteristics of Calcium-Aluminate Slags and Pig Iron Produced from Smelting-Reduction of Low-Grade Bauxites, Metall. Mater. Trans. B Process Metall. Mater. Process. Sci. 49 (2018) 2400–2420. doi:10.1007/s11663-018-1353-1.

[25] M. Vafeias, D. Marinos, D. Panias, J. Safarian, C. van Der Eijk, E. Solhem, Ingeborg; Balomenos, M. Ksiazek, P. Davris, From Red To Grey: Revisiting the Pedersen Process To Achieve Holistic Bauxite Ore Utilisation, in: Proc. 2nd Int. Bauxite Residue Valoris. Best Pract. Conf., 2018: pp. 111–117.

[26] F.I. Azof, L. Kolbeinsen, J. Safarian, Kinetics of the Leaching of Alumina-containing Slag for Alumina Recovery, in: Proc. EMC 2019, 2019: pp. 511–526. www.ensureal.com.

[27] J. Safarian, L. Kolbeinsen, Smelting-reduction of Bauxite for Sustainable Alumina Production, in: Sustain. Ind. Process. Summit, 2016: pp. 149–158.

[28] J. Safarian, L. Kolbeinsen, Sustainability in Alumina Production from Bauxite, in: Sustain. Ind.

Process. Summit, 2016: pp. 75–82.

[29] F.I. Azof, M. Vafeias, D. Panias, J. Safarian, The leachability of a ternary CaO-Al2O3-SiO2 slag produced from smelting-reduction of low-grade bauxite for alumina recovery, Hydrometallurgy. 191 (2020). doi:10.1016/j.hydromet.2019.105184.

[30] O.C. Fursman, H.E. Blake Jr., J.E. Mauser, Recovery of Alumina and Iron from Pacific Northwest Bauxites by the Pedersen Process, Albany, 1968.

[31] H.E. Blake, O.C. Fursman, A.D. Fugate, L.H. Banning, Adaptation of the Pedersen Process to the Ferruginous Bauxites of the Pacific Northwest, 1966.

[32] W. Bo, Z. Jianxin, Z. Shufeng, S. Huilan, Effect of Calcium/Aluminium Ratio on Crystal Structure and Al 2 O 3 Leaching Property of 12CaO-7Al 2 O 3, in: Light Met. 2014, John Wiley & Sons, Inc., Hoboken, NJ, USA, 2014: pp. 87–90. doi:10.1002/9781118888438.ch15.

[33] P. McMillan, B. Piriou, Raman spectroscopy of calcium aluminate glasses and crystals, J. Non. Cryst. Solids. 55 (1983) 221–242. doi:10.1016/0022-3093(83)90672-5.

[34] A.G. Kokhman, G.I. Zhmoidin, Vibrational Spectra of 12CaO.7Al2O3 and 5CaO.3Al2O3 Crystals, Zhurnal Prikl. Spektrosk. 35 (1981) 1322–1326. doi:0021-9037/81/3506-1322.

[35] P. Gillet, Raman spectroscopy at high pressure and high temperature. Phase transitions and thermodynamic properties of minerals, Phys. Chem. Miner. 23 (1996) 263–275. doi:10.1007/BF00207767.

[36] S. Kim, M. Miyakawa, K. Hayashi, T. Sakai, M. Hirano, H. Hosono, Simple and Efficient Fabrication of Room Temperature Stable Electride: Melt-Solidification and Glass Ceramics, J. Am. Chem. Soc. 127 (2005) 1370–1371. doi:10.1021/ja043990n.

[37] L. Palacios, Á.G. De La Torre, S. Bruque, J.L. García-Muñoz, S. García-Granda, D. Sheptyakov, M.A.G. Aranda, Crystal structures and in-situ formation study of mayenite electrides, Inorg. Chem. 46 (2007) 4167–4176. doi:10.1021/ic0700497.

[38] G.I. Zhmoidin, A.K. Chatterjee, Conditions and Mechanism of Interconvertibility of Compounds 12CaO.7Al2O3 and 5CaO.3Al2O3, Cem. Concr. Res. 14 (1984) 386–396. doi:10.1016/0008-8846(84)90057-7.

[39] D.M. Roy, R. Roy, Crystalline solubility and zeolitic behavior in garnet phases in the system CaO-Al2O3-SiO2-H2O, in: Fourth Int. Symp. Chem. Cem., Washington D.C., 1960: pp. 307–314.

[40] K. Hayashi, M. Hirano, H. Hosono, Thermodynamics and Kinetics of Hydroxide Ion Formation

in 12CaO·7Al2O3, J. Phys. Chem. B. 109 (2005) 11900–11906. doi:10.1021/jp050807j.

[41] K. Hayashi, M. Hirano, H. Hosono, Excess Oxygen in 12CaO·7Al 2 O 3 Studied by Thermogravimetric Analysis, Chem. Lett. 34 (2005) 586–587. doi:10.1246/cl.2005.586.

Paper 2

Characteristics of Calcium-Aluminate Slags and Pig Iron Produced from Smelting-Reduction of Low-Grade Bauxites

FABIAN IMANASA AZOF, LEIV KOLBEINSEN, and JAFAR SAFARIAN

Low-grade bauxite ores are not favorable in the conventional Bayer process for alumina production, as they are producing more bauxite residue (red mud) and accompanying lower alumina yield than high-grade ores. In the current study, the thermodynamics and characterization of calcium-aluminate slags and pig iron produced from smelting reduction of high iron- and silica-containing bauxites are studied. Coke and limestone are used to reduce the iron oxide and adjust the basicity of slag during smelting. There is evidence that complete iron separation from bauxite is feasible through smelting-reduction process, and up to 99.9 pct of iron can be eliminated. Moreover, it is shown that the partial separation of silicon, titanium, and other elements from the Al_2O_3-containing slag occurs. The phase compositions and the distribution of elements between the metal and slag phases provide information about the high-temperature behavior of the bauxite components during smelting reduction. Employing electron microscopy analysis, it is indicated that the morphologies of $CaO{\cdot}Al_2O_3$, $12CaO{\cdot}7Al_2O_3$, $2CaO{\cdot}Al_2O_3{\cdot}SiO_2$, and $CaO{\cdot}Al_2O_3{\cdot}SiO_2$ phases in the slag, as well as the complex oxides of Ca-Al-Si-Ti in the slag behave differently as the mass ratio of $Al_2O_3/(Fe_2O_3 + SiO_2)$ in the bauxite changes. It is also shown that the phases of slag produced from smelting-reduction below 5 K s^{-1} of cooling rate are proper for further leaching process.

https://doi.org/10.1007/s11663-018-1353-1

I. BACKGROUND

DATA from alumina processing industry show an estimated global average production of bauxite residue (red mud) to be 1 to 1.5 ton per ton of alumina, or about 150 million ton of red mud is produced annually.[1] A large number of efforts have been made to valorize this most-abundant industrial byproduct in the world in building materials,[2] using it as the rare earth element's source,[3] producing green direct-reduced iron (DRI),[4] consuming inorganic polymers and pozzolanic material,[5] and so on. However, none of these fields has moved to a large-scale commercial production due to economic reasons and particular challenges in processing the red mud. Thus, this caustic material is a prominent environmental issue and is a major concern on most of alumina refineries in the world, and obviously, increasingly lower grade of bauxite (high iron and silica content) makes the situation even more challenging. In the Bayer process, the iron present in the ore is the main component involved in the production of red mud, while silica causes loss of caustic soda to the solvent due to the high reactivity of the compound. The compositions of the bauxite are important in determining the amount of lime that should be added in the mixtures and, eventually, the ratios of CaO/Al_2O_3 (C/A) in the slags.

In 1927, Harald Pedersen[6] patented a method to extract alumina from bauxite without yielding any red mud; an overall illustration of the process is shown in Figure 1. This process was run commercially in Høyanger, Norway, during 1928 to 1969 with 17,000 ton of annual production before closing down.[7] During that period, other researchers had adapted the patent for utilizing ferruginous bauxite in Albany,[8] and a pilot-plant of alumina production from non-bauxitic source (clay) in Tennessee.[9] Years later, Miller and Irgens[10] also made preliminary studies on alumina refinery plant with 200,000 tons of annual production, based on the same process. The Pedersen process shows a promising potential for the prevention of red mud production, however, as per to date this process has been abandoned more than four decades. Lack of

FABIAN IMANASA AZOF, LEIV KOLBEINSEN, and JAFAR SAFARIAN are with the Department of Materials Science and Engineering, Norwegian University of Science and Technology (NTNU), 7491, Trondheim, Norway. Contact e-mail: fabian.i.azof@ntnu.no

Manuscript submitted February 12, 2018.
Article published online July 25, 2018.

literature and scientific evidence, especially in smelting-reduction part, has led the current authors to investigate the process thoroughly.

II. EXPERIMENTAL PROCEDURE

This section describes the applied experimental activities about the pyrometallurgical part of the Pedersen process for treating selected low-grade bauxites. Sequentially, the procedure consists of materials preparation and characterization, and the details of smelting-reduction treatment.

A. *Materials Preparation and Characterization*

Mixture comprises bauxite ore, lime, and coke was prepared in laboratory scale. Three low grade of bauxite ores, named B-, G-, and I-Bauxites were used in different mixtures. The characteristics of lime and coke based on the provided information are listed in Table I. The amounts of lime and coke used were based on the characteristics of the bauxites, and the lime/bauxite ratios for B-, G-, and I- are 0.55, 0.8, and 0.44, respectively.

Pig iron and slag are the products of the smelting-reduction treatment. For the targeted slag compositions, the CaO/Al_2O_3 (C/A) mass ratios were in the range of 0.65 to 0.75. This C/A ratio range is appropriate to obtain slag phases that has good leaching properties, as was reported in the literature.[11,12] The amounts of coke in the current study are 1.5 times larger than the stoichiometric needs to assure the complete reduction of iron oxides. Coke was dried in an oven at 373 K (100 °C) for 12 hours before use to remove any free-moisture content.

Parts of the ores and products were ground by ring mill into powder size for phase identification using Bruker D8 A25 DaVinci^{TM} X-ray Diffraction (XRD) with CuKα radiation, 10 to 75 deg diffraction angle, 0.01 deg step size, and 2.5 deg for both primary and secondary soller slits. The slag and pig iron samples were mounted in epoxy, polished, and carbon coated before employing Hitachi SU6600^{TM} Scanning Electron Microscope (SEM) to capture the secondary electron (SE) and backscattered electron (BSE) images, X-ray element mapping, and use of Energy Dispersive Spectroscopy (EDS). X-ray Fluorescence (XRF) analysis was used to identify the overall composition of the ores and pig iron and slag products. Moreover, a JXA-8500F^{TM} Electron Probe Micro-Analyzer (EPMA), supported by Wavelength Dispersive Spectroscopy (WDS), was applied for achieving high accuracy on quantitative analysis of elements in selected phases of the products.

B. *Smelting-Reduction Treatment*

The mixture of starting materials was set into an open graphite crucible with inner diameter of 115 mm. The crucible was placed in a 75-kVA induction furnace and heated slowly at the rate of 5 K s^{-1} until it reached 1923 K (1650 °C). The partial pressure of gas (O_2, N_2, CO, CO_2, *etc.*) inside of the crucible was not measured during the smelting trial. However, an oxidizing atmosphere during smelting reduction process can be considered to exist because the experiments were in the open furnace. The smelting-reduction duration was one hour at 1923 K (1650 °C), while the top of crucible was partially closed by refractories to minimize dissipation of the heat. However, the top was opened at intervals to crush the sintered materials or a solidified foamy-slag, while stirring of the melts was proper due to the induction in pig iron and gas bubbles movements in the slag. To compensate the heat loss, the mixture was heated up to 2023 K (1750 °C) during the last ten minutes of the treatment. Consequently, the means and standard deviations of B-, G-, and I-Bauxite smelting temperatures are 1937 ± 44 K, 1935 ± 54 K, and 1910 ± 38 K, respectively.

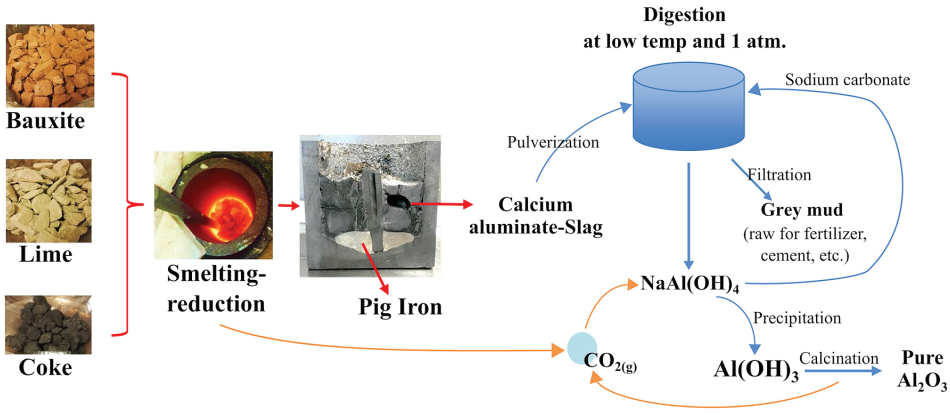

Fig. 1—An overview of Pedersen process.

The crucible was then cooled to the room temperature inside the furnace, while the power was off. To measure the temperature during the treatment, a tungsten/rhenium thermocouple (type C) inside a graphite rod, and an encapsulating alumina insulation tube were used. About two-thirds of the materials smelted in the first one hour of treatment, and after it cooled down to room temperature, the rest of materials were added, and another one hour of treatment was performed. For further analysis, the solidified materials and the crucible were crushed to separate slag and metal from the crucible.

Table I. Characteristics of Lime and Coke as Received

Composition	Lime (Weight Percent)	Coke (Weight Percent)
Al_2O_3	0.3	2.8
Fe	NA	0.6
Fe_2O_3	NA	0.9
SiO_2	1.0	5.6
TiO_2	NA	0.1
CaO	54.0	0.4
MgO	1.0	0.2
Mn	NA	0.03
MnO	NA	0.04
K_2O	0.1	0.2
C-Fix	NA	87.7
CO_2 (as Carbonate)	47.5	NA
P	10 ppm	0.1
S	110 ppm	0.4
H_2O	1.0	15.5
Volatile Matter	NA	1.53
Trace Elements	100 − sum	100 − sum

III. RESULTS

Results comprise four major parts: analysis of bauxites, smelting-reduction treatment, overall chemical compositions, and phase analysis in products.

A. *Characteristics of Bauxites*

An XRD analysis of the bauxites is presented in Figure 2. The mineralogy of B-Bauxite comprises kaolinite, gibbsite, cristobalite, goethite, anatase, and magnetite. The first three are shown as the dominant phases. G-Bauxite predominant phases are diaspore, boehmite, calcite, and hematite. It also has anatase as one of the gangue mineral. I-Bauxite is high in kaolinite and hematite, with relatively low amounts of diaspore and boehmite compared with G-Bauxite. It is worth noting that I-Bauxite has the highest intensity of anatase peaks compared with the other two.

Table II shows the normalized XRF analysis results of B-, G-, and I-Bauxites. Three major elements that contribute to the bauxite leaching extent are aluminum, iron, and silicon. These elements formed as either a hydroxide or oxide in bauxite as seen in XRD analysis presented above. The Loss of Ignition (LOI) content may decompose to air during smelting trial.

Prior to smelting, bauxite is obviously calcined at lower temperatures. Al_2O_3 and SiO_2 in calcined B- and I-Bauxite are formed as $Al_2O_3{\cdot}2SiO_2$ which is known as meta-kaolinite or aluminosilicate—a decomposed phase of kaolinite at high temperature. According to Kyriakogona *et al.*,[13] the degree of decomposition (dehydroxylation) is up to 98 pct when the calcination occurs at 1123 K (850 °C) in 60 minutes. Table III shows the normalized XRF analysis of the calcined bauxites, determined based on both XRF and XRD results.

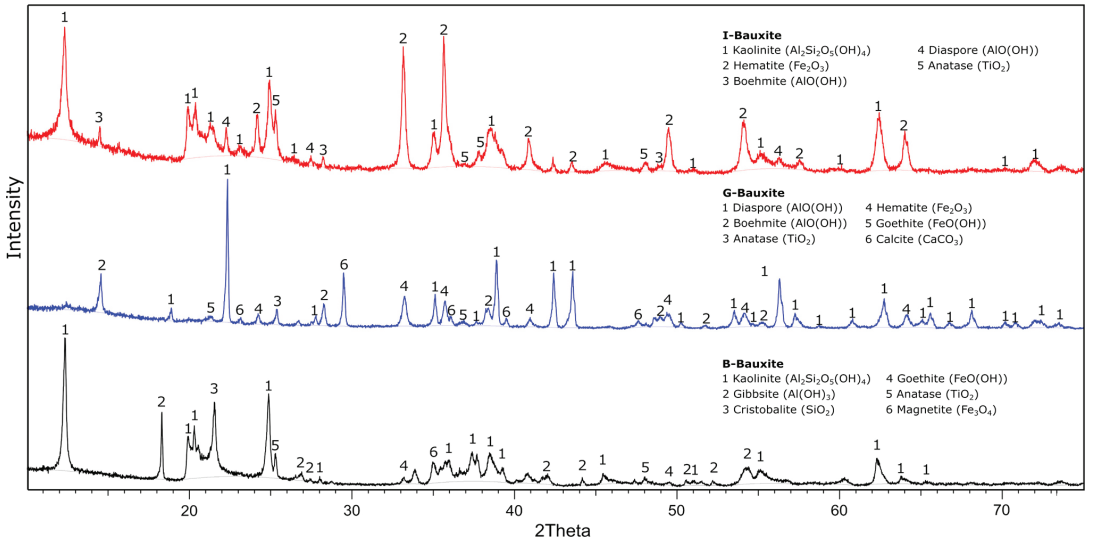

Fig. 2—XRD analysis of B-, G-, and I-Bauxites.

Table II. XRF Analysis of Different Bauxite Ores

Element	Bauxite Ore		
	B (Weight Percent)	G (Weight Percent)	I (Weight Percent)
Al	18.4	31.0	14.7
Fe	8.3	14.2	14.3
Si	22.2	3.4	23.9
Ti	3.3	3.4	4.3
Mg	0.1	0.3	0.2
Ca	NA	5.6	0.1
K	130 ppm	433 ppm	0.1
Mn	0.1	323 ppm	273 ppm
P	0.0	91 ppm	346 ppm
O*	100 − sum	100 − sum	100 − sum
LOI	~ 16.1	~ 14.6	~ 10.9

*Oxygen presents as oxides.

Table III. Normalized XRF Analysis of the Calcined Bauxites to the Corresponding Stable Oxides

Phase	Calcined Bauxite		
	B (Weight Percent)	G (Weight Percent)	I (Weight Percent)
Al_2O_3	44.2	65.4	35.7
Fe_2O_3	15.2	22.7	26.2
SiO_2	36.2	4.1	32.8
TiO_2	4.2	3.2	4.6
MgO	0.1	0.2	0.2
CaO	NA	4.4	0.1
K_2O	NA	NA	0.2
MnO	0.1	NA	NA

B. *Smelting-Reduction Behavior*

The measurement of cooling rate was carried out ranging from 1873 K to 1573 K (1600 °C to 1300 °C). As seen later in the $CaO\text{-}Al_2O_3\text{-}SiO_2$ ternary phase diagram, the latter temperature corresponds with the solidus line, which as expected means no solidification occurs upon cooling to this temperature. The mean measured cooling rates are 4.9, 4.8, and 5 K s^{-1} for B-, G-, and I-Bauxite, respectively. These cooling rates are well correlated with the masses (slag + iron) in the crucible where higher total mass shows slower cooling rate under similar conditions.

The cross-sectional views of the solidified slag and pig iron in crucible after smelting-reduction trials are displayed in Figure 3. The unreacted coke remaining on top of the slag is also illustrated. The separation of slag and iron produced from B-, G-, and I-Bauxites due to density differences is clearly seen. Obviously, coke particles are floating over the molten slag phase at elevated temperatures and thereafter. The different color appearances of the slags are mostly related to their different compositions. The volume pct values of slag and pig iron produced from different bauxites also were roughly estimated by visual observation. As mentioned

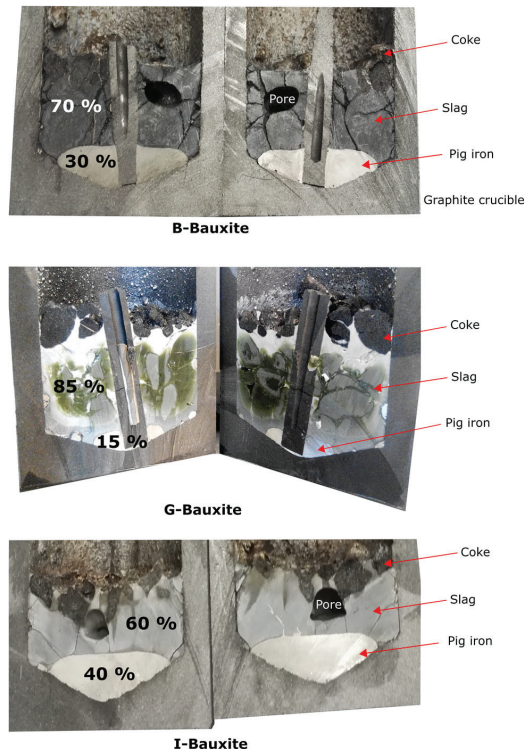

Fig. 3—Cross-sectional view of the solidified slag and pig iron produced from B-, G-, and I-Bauxite.

in the experimental setup, the order of lime/bauxite mass ratio from the lowest to the highest is as follows: I-Slag, B-Slag, and G-Slag. It appears that the pct of slag increases and that of pig iron decreases considerably with the increasing lime/bauxite mass ratio.

In large-scale experiments, a useful performance indicator will be masses of slag and metal (pig iron) produced from a given mass and composition of raw materials. Mass change characteristics, including the correlation between losses of mass with the extent of smelting-reduction reaction, are accordingly of great importance as a reference to large-scale experiments. Table IV shows the changes of mass in different setups after smelting trial. Total mass loss pct values for B-, G-, and I-Setup are 16.3, 15.4, and 6.1 pct, respectively. AQHowever, it becomes more interesting to see only the mass losses of starting materials occurring during reaction and not the losses from both graphite crucible and the rod. As can be seen, the estimated mass losses of materials after smelting trials are considerably high: 41.5, 39.4, and 21.2 pct for B-, G-, and I-Bauxite setups, respectively. Materials' mass losses after the experiment might be caused by their LOI property, solid–gas transformation, *i.e.*, $C \rightarrow CO_{(g)}$ or $CO_{2(g)}$, $CaCO_3 \rightarrow CaO + CO_{2(g)}$, and oxide-phase reduction, *i.e.*, $Fe_xO_y + yC \rightarrow xFe + yCO_{(g)}$, $SiO_y + yC \rightarrow Si + yCO_{(g)}$, and $TiO_2 + 2C \rightarrow Ti + 2CO_{(g)}$.

Table IV. Mass Changes of B-, G-, and I-Bauxite Setups After Smelting Trial

Condition	B-Bauxite (kg)	G-Bauxite (kg)	I-Bauxite (kg)
Crucible and Materials, Before Smelting[(a)]	8.76	9.26	7.74
Crucible and Materials, After Smelting[(b)]	7.34	7.84	7.27
Total Mass Loss: *(a) − (b)*	1.42 (16.3 pct)	1.42 (15.4 pct)	0.47 (6.1 pct)
Materials Before Smelting[(c)]	2.80	3.26	1.71
Materials After Smelting[(d)]: *(b)* − graphite crucible mass loss*	1.64	1.98	1.24
Measured Materials Mass Loss: *(c) − (d)*	1.16 (41.5 pct)	1.28 (39.4 pct)	0.47 (21.2 pct)

*The mass loss pct of the graphite crucible and graphite rod after 1 h of smelting trial are 2.2 ± 0.5 and 4 pct, respectively.

Table V. Normalized XRF Analysis of the Obtained Slags in Smelting-Reduction

	Slag		
Phase	B (Weight Percent)	G (Weight Percent)	I (Weight Percent)
Al_2O_3	47.5	46.1	36.7
SiO_2	11.2	2.3	30.3
TiO_2	0.9	1.8	2.8
MgO	0.4	0.5	0.5
CaO	36.8	48.1	28.0
K_2O	NA	NA	0.5
MnO	NA	NA	0.1
FeO	0.01	0.44	1.4
Trace Elements	NA	NA	NA

Table VI. XRF Analysis Results of Pig Iron Samples After Smelting-Reduction Treatment

	Pig Iron		
Element	B (Weight Percent)	G (Weight Percent)	I (Weight Percent)
Fe	89.9	92.0	92.7
C_{sat}	4.6	5.3	4.9
Si	4.0	0.2	1.2
Mn	0.5	0.2	0.4
Ti	0.6	0.9	0.2
V	0.1	0.2	0.1
Cr	0.1	0.5	0.1
P	450 ppm	950 ppm	0.1
S	NA	70 ppm	70 ppm
Trace Elements	100 − sum	100 − sum	100 − sum

C. *Chemical Compositions of Products*

The results of XRF analysis of the produced slags in Table V show the mass balance and smelting of mixtures was done properly as the C/A ratio on each slag is in the expected range, as mentioned in the experimental procedure. It is worth noting here of the low FeO_x content in the slag, which agrees with our previous result.[14] AQMost of the iron oxide becomes reduced to metal that saturated with carbon to form pig iron. As seen in Table VI, the B-, G-, and I-Pig iron materials contain 89.9 to 92.7 wt pct Fe and are saturated in carbon, and contain 0.2 to 4.0 wt pct Si, and low traces of titanium and minor elements, *i.e.*, V, Cr, P, and S, are also observed. Most of the minor elements are derived from coke and lime. The saturated carbon content is estimated here based on the silicon content and the reliable solubility data for carbon in Fe-Si-C melts.[15]

D. *Phase and Microstructural Analysis of the Products*

Phase identification of the slags resultng from XRD analysis is shown in Figure 4. B-Slag consists of $2CaO{\cdot}Al_2O_3{\cdot}SiO_2$ (C_2AS) and $CaO{\cdot}Al_2O_3$ (CA) as the primary and secondary phases, respectively. However, the latter phase seems to have another polymorph that bonds SiO_2 and MgO as is precisely identified later on BSE image. XRD analysis of G-Slag shows that the primary and secondary phases of the slag are composed of $12CaO{\cdot}7Al_2O_3$ ($C_{12}A_7$), CA and $5CaO{\cdot}3Al_2O_3$ (C_5A_3), respectively. The latter phase is considered as an unstable phase that may be reformed to $C_{12}A_7$ phase at high temperature.[16,17] In I-Slag, CAS phase appears as the dominant phase, followed by a small fraction of silica phase.

The X-ray elemental mappings of B-, G-, and I-Slag are shown in Figures 5 through 7, respectively. These figures show clearly the concentration extents of several elements in every structure that coexists in slag. In B-Slag, calcium and silicon are more concentrated in the bright structure, which is later shown to be C_2AS phase. Aluminum is more concentrated in the dark area within the lamellar structure. However, titanium and magnesium are dispersed uniformly. In G-Slag, the main structure ($C_{12}A_7$ phase) has more concentration of aluminum than other structures. Silicon and titanium are densely populated between large $C_{12}A_7$ grains. As seen in the figure, there are structures that have complex oxides between Ca-Si-Ti elements. In contrast with B-Slag, magnesium is concentrated in spots. The X-ray elemental mapping of I-Slag shows that titanium, aluminum, and magnesium are highly concentrated in the dark structure. Obviously, bright structure has more concentrations of calcium and silicon than the dark one. Two phases coexist between the $C_{12}A_7$ particles in G-Slag. Therefore, it is necessary to examine the structures in higher magnification and analyze the composition by means of SEM and EDS as the obtained results by these techniques are shown in Figure 8. It shows that the area with bright and dark structures has more concentration of titanium than other structures in slag.

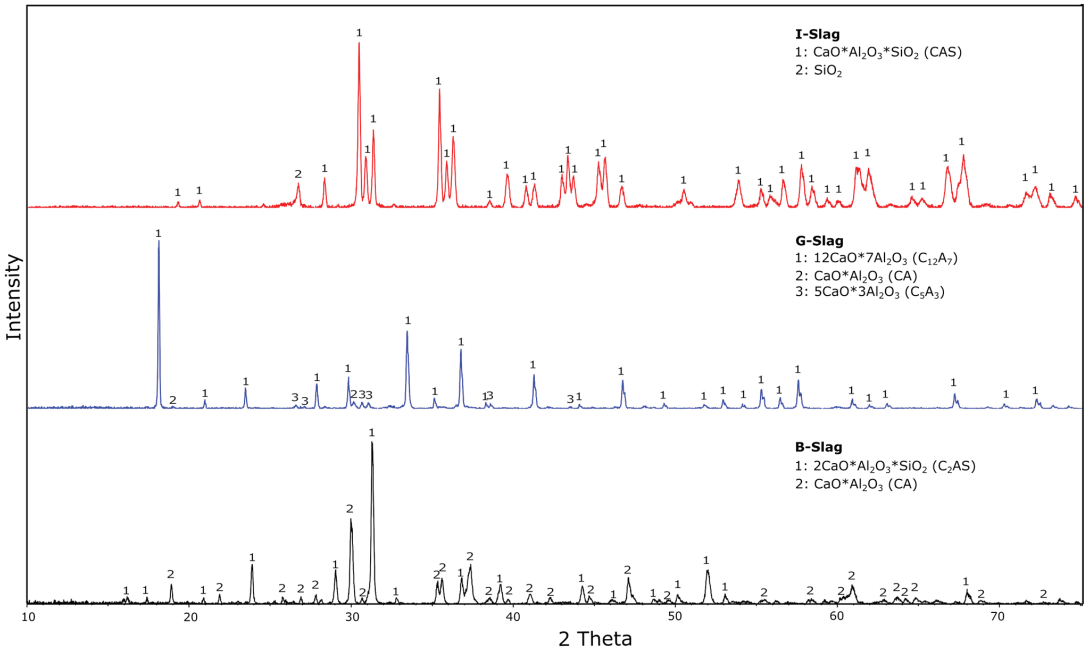

Fig. 4—XRD analysis results on B-, G-, and I-Slag.

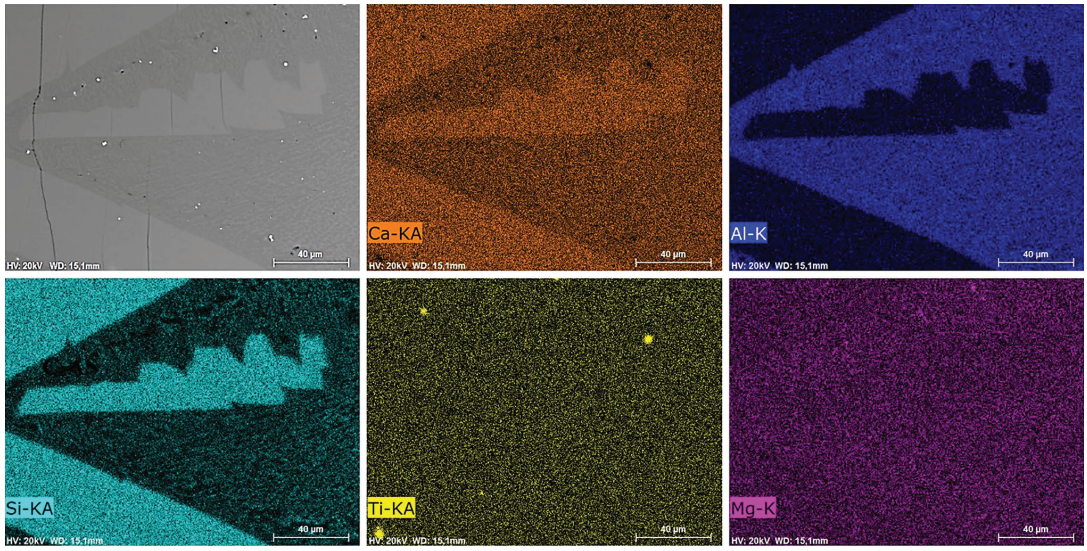

Fig. 5—X-ray element mapping of B-Slag.

Figures 9(a) through (c) show the BSE images of B-, G-, and I-Slag, respectively. As seen in the figure, three structures coexist in the B-Slag and the two main structures are seen in each G- and I-Slags. Composition of each structure was measured by WDS analysis at 2 to 3 locations shown in Figure 9. Table VII presents the WDS analysis of the observed phases in Figure 9. On average, concentrations of CaO, Al_2O_3, SiO_2 constitute more than 95 wt pct of the slags. On the other hand, FeO content is low in all structures of slags, averaging around 300 ppm, which is in agreement with the low measured FeO concentrations by XRF (Table V).

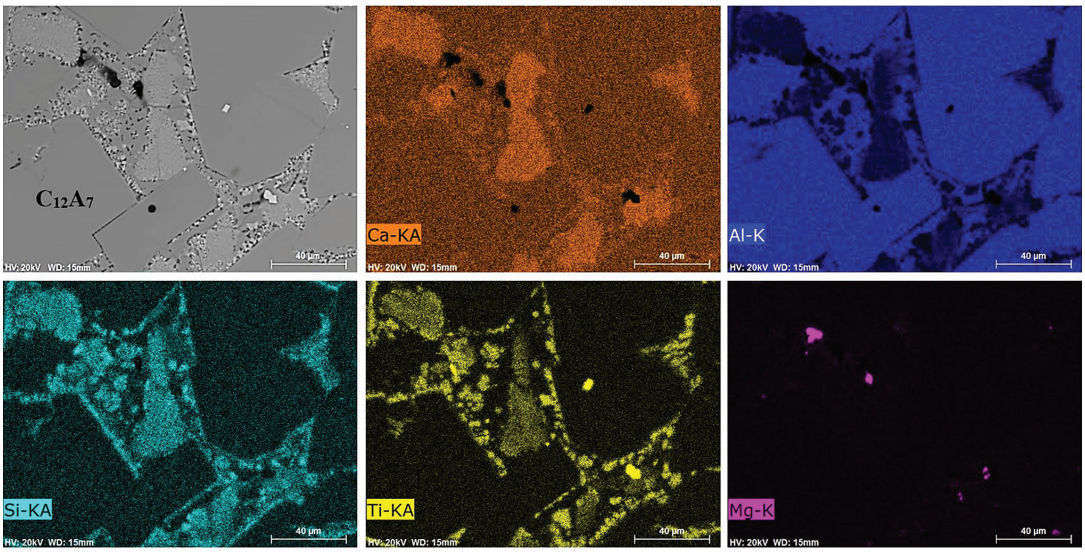

Fig. 6—X-ray element mapping of G-Slag.

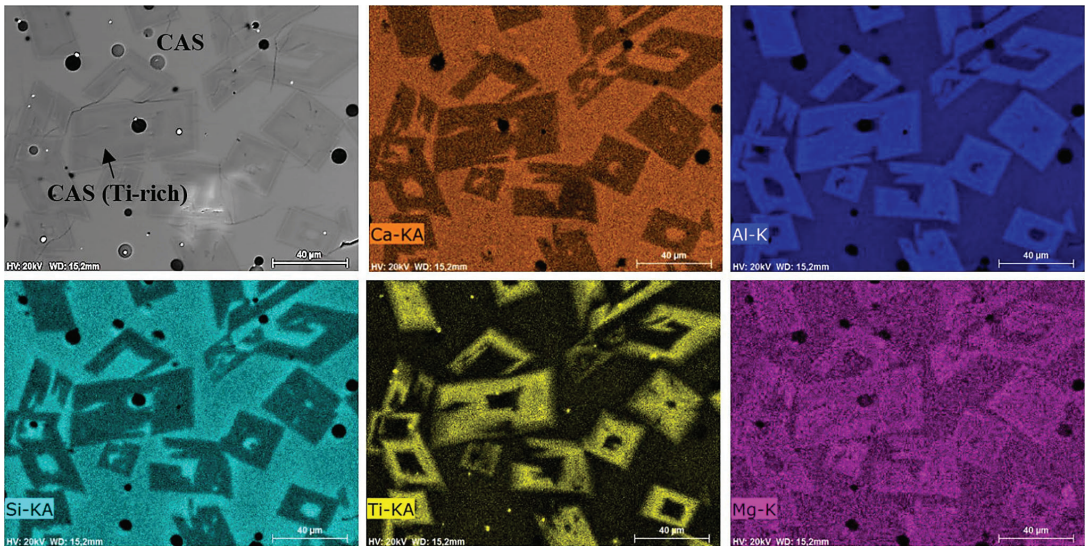

Fig. 7—X-ray element mapping of I-Slag.

Numbers (a)1-3, (a)4-6, and (a)7-9, are WDS results for the dark, fine lamellar, and bright structure that are present in B-Slag (Figure 9(a)), respectively. Dark structure is composed of 43 wt pct CaO, 35 wt pct Al_2O_3, and 22 wt pct SiO_2 on average. Fine lamellar has similar composition as the dark structure has, which is 43 wt pct CaO, 35 wt pct Al_2O_3, and 21 wt pct SiO_2 on average, while bright structure is predominantly composed of 55 wt pct CaO and 31 wt pct TiO_2 on average. Numbers (b)1-3 and (b)4-6 denote respectively, the compositions of the bright-coarse grain and smaller grain which are adjacent to a darker structure that is shown in G-Slag (Figure 9(b)). The first structure has 50 wt pct CaO and 49 wt pct Al_2O_3 on average. The

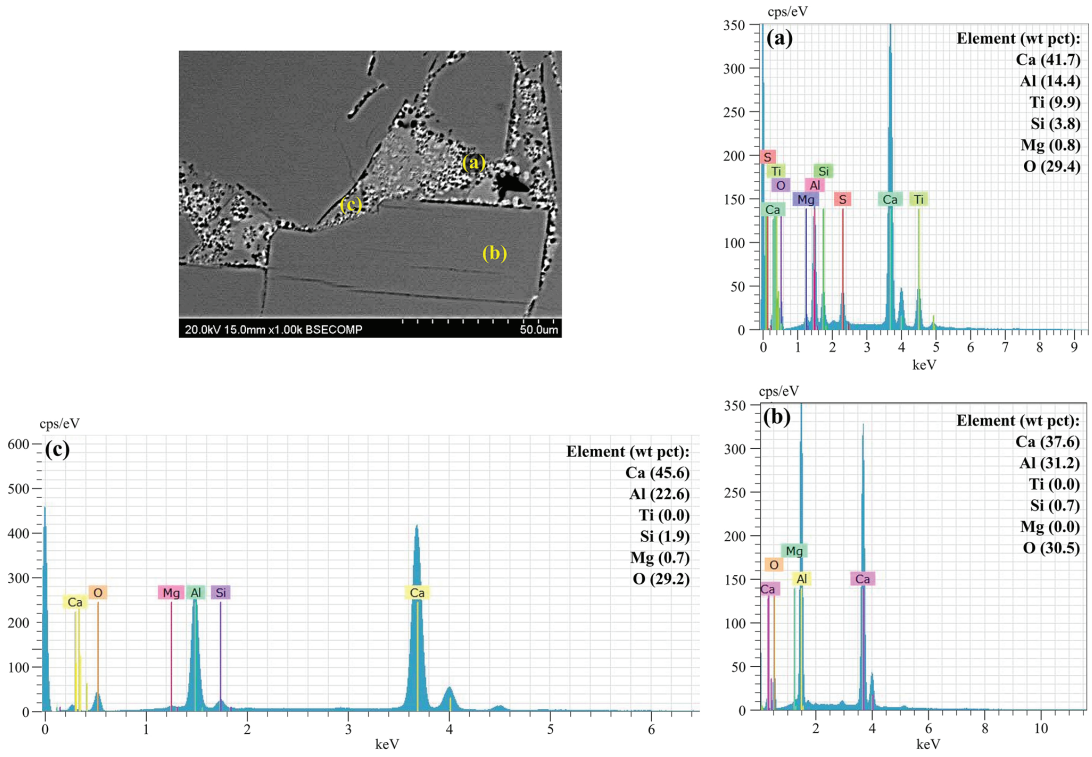

Fig. 8—BSE image of G-Slag with the corresponding EDS quantified analysis at (*a*) through (*c*) area.

latter one comprises 49 wt pct CaO, 43 wt pct Al_2O_3, 3 wt pct SiO_2, and 4 wt pct TiO_2. Numbers (c)1-3 and (c)4-6 show the bright and dark structures in I-Slag (Figure 9(c)), respectively. On average, the bright structure is composed of 31 wt pct CaO, 32 wt pct Al_2O_3, 34 wt pct SiO_2, and 1 wt pct TiO_2. The dark structure shows that it has less CaO and more TiO_2 than the bright one has: 28 wt pct CaO, 34 wt pct Al_2O_3, 33 wt pct SiO_2, and 3 wt pct TiO_2. BSE in I-Slag indicates it has significant number of pores, which are not observed in the B- and G-Slags.

BSE image in Figure 10 shows the cross-sectional views of B-Slag and adjacent B-Pig iron. The light phase shows the Fe-metal of pig iron, while the gray and dark one show carbide and graphite phases, respectively. Table VIII shows the WDS analysis results on the pointed phases. High concentration of titanium is found in carbide phase. Vanadium, as one of the carbide-forming elements, is concentrated in carbide phase, which is shown in points 3 and 4 of Figure 10. Phosphorus and manganese are detected in Fe-metal matrix with 0.2 and 1.1 wt pct on average. Most of the manganese oxide is reduced to pig iron as it has low presence in slags, which is 800 ppm on average. Other trace elements shown in table are recognized as potassium and calcium. In addition, the lower-magnification BSE image in Figure 11 shows the metal matrix and the coexisting phases in the produced metals.

IV. DISCUSSION

In this section, mass changes before and after of experiment, thermochemistry of the reactions, distribution of elements in slag and pig iron, and slag characteristics are discussed.

A. *Mass Balance*

From the LOI data of each bauxite presented in Table II, we can calculate the mass losses in B-, G-, and I-Bauxites due to the ignition, which are 0.28, 0.25, and 0.12 kg for the amounts used, respectively. The LOI data for lime due to the decomposition of lime into $CO_{2(g)}$ can be calculated based on the carbonate amounts in the same table, which are 0.45, 0.66, and 0.23 kg for B-, G-, and I-Bauxite setups, respectively. While the moisture content of coke is removed after preheating in the oven before use, the LOI of coke is 1.53 wt pct as shown in Table I, which gives loss as much as that of 2.10^{-3} kg.

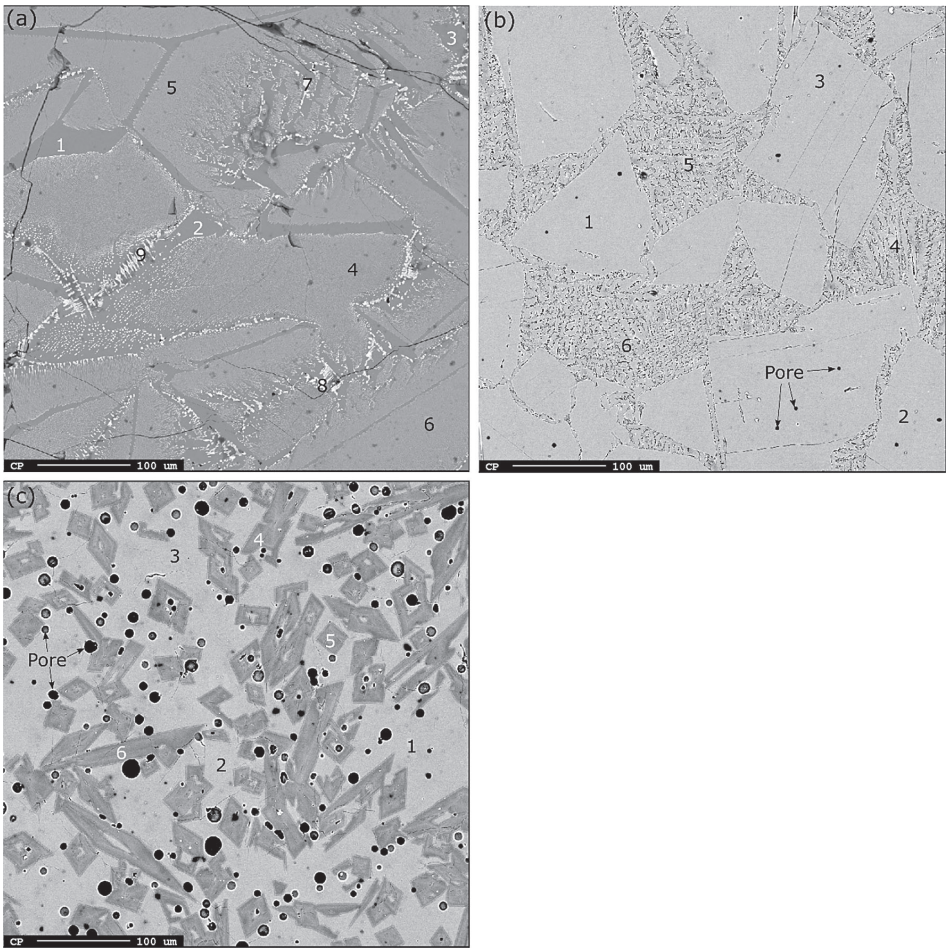

Fig. 9—BSE images of (*a*) B-Slag, (*b*) G-Slag, and (*c*) I-Slag.

Total losses due to transformation of C to $CO_{(g)}$ and oxide phase reduction can be calculated and given as 0.16, 0.21, and 0.16 kg for B-, G-, and I-Bauxites, respectively. This gives the theoretical mass losses for B-, G-, and I-Bauxites, respectively, as 0.9, 1.13, and 0.52 kg. As seen in Table IX, the theoretical mass loss with the measured one shows proper correlation, in particular for G- and I-Bauxites. The difference between theoretical and measured mass losses in B-Bauxite might be due to the losses of $SiO_{(g)}$. Details of this explanation will be discussed in Section IV–D.

B. *Smelting-Reduction Thermochemistry*

Based on the XRD results in shown in Figure 2, B- and I-Bauxites are constructed mainly from kaolinite. This phase is found in either bauxite or non-bauxitic source, clay. Many works have been carried out to extract alumina from kaolinite with acid or alkaline solution.[18–20] In the Bayer process, this is a major problem as the kaolinite is dissolved by sodium hydroxide solution which leads to high loss of caustic soda according to the following reaction:

$$Al_2Si_2O_5(OH)_{4(s)} + 6NaOH_{(l)} = 2Na_2SiO_{3(l)} + 2NaAl(OH)_{4(l)} + H_2O_{(l)}. \quad [1]$$

Furthermore, precipitation of the desilication products, *i.e.*, sodalite ($Na_8(Al_6Si_6O_{24})Cl_2$), cancrinite ($Na_6Ca_2((CO_3)_2Al_6Si_6O_{24})\cdot 2H_2O$), *etc.* occur at elevated temperatures that are energy consuming. Low-grade of bauxites are typically characterized by low Al_2O_3/SiO_2 mass ratio[18,21,22] and/or Al_2O_3/Fe_2O_3 mass ratio.[23] As both SiO_2 and Fe_2O_3 could be present in particular ore, we may classify the low-grade bauxites based on their low $Al_2O_3/(Fe_2O_3 + SiO_2)$ mass ratio. According to the concentrations of calcined bauxites in Table III, these ratios for B-, G-, and I-Bauxites are 0.8, 2.4,

Table VII. WDS Analysis of Phases Observed in B-, G-, and I-Slag Structures Shown in Fig. 9

Point No.	CaO (Weight Percent)	Al_2O_3 (Weight Percent)	SiO_2 (Weight Percent)	TiO_2 (Weight Percent)	MgO (Weight Percent)	FeO (Weight Percent)	V_2O_3 (Weight Percent)	MnO (Weight Percent)	P_2O_5 (Weight Percent)	K_2O (Weight Percent)
(a)1-3	42.66	35.05	21.62	0.33	0.29	NA	NA	0.01	0.03	NA
(a)4-6	42.99	34.72	21.41	0.61	0.23	0.01	0.01	0.01	0.01	0.01
(a)7-9	55.29	6.00	4.20	31.12	2.93	NA	0.26	0.19	NA	0.01
(b)1-3	49.58	48.99	0.79	0.32	0.24	0.01	0.01	0.03	0.03	NA
(b)4-6	48.94	42.66	2.73	4.35	1.12	0.04	0.05	0.07	0.04	NA
(c)1-3	30.81	32.35	33.95	1.36	0.41	0.10	0.03	0.12	0.02	0.85
(c)4-6	28.43	33.86	33.50	2.87	0.67	0.04	0.03	0.10	0.01	0.49

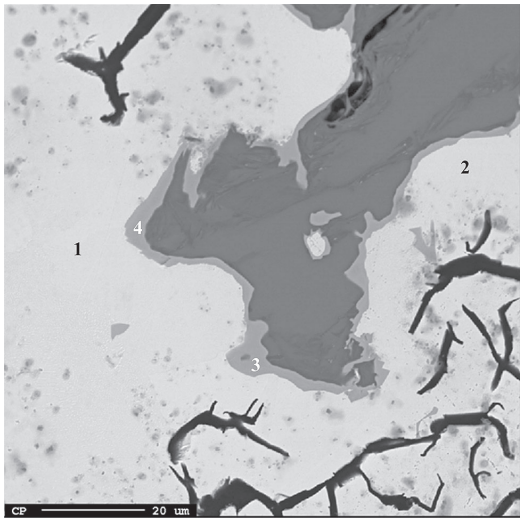

Fig. 10—BSE cross-sectional images of B-Slag and adjacent B-Pig iron.

and 0.6, respectively. These bauxites also have certain amount of TiO_2 that later in the slag phase might affect the slag chemistry, its self-disintegration, and leachability.[24] The effect of MgO content of slag on leachability has also been reported as it becomes the main impurity in blast furnaces' slag.[25] However, in the current study, the compositions of Mg and remaining elements are considered as trace elements, which have minimal effect on the slag properties. According to the obtained XRF results presented in Table V, 94.8 to 99.9 pct of Fe and Mn have been removed from the Al_2O_3-containing slag, together with parts of Si and Ti. Coke produces CO gas and dissolved carbon in molten iron, and carbon in both forms acts as the reductant for oxides in bauxite. In addition, the usage of graphite crucibles makes an additional carbon source for the carbothermic reduction. Based on the ores' characteristics, the main smelting-reduction reactions that may take place are as follows:

$$3Fe_2O_{3(s)} + C_{(s,\ dissolved)} = 2Fe_3O_{4(s)} + CO_{(g)}, \quad [2]$$

$$3Fe_2O_{3(s)} + CO_{(g)} = 2Fe_3O_{4(s)} + CO_{2(g)}, \quad [3]$$

$$Fe_3O_{4(s)} + C_{(s,\ dissolved)} = 3(FeO) + CO_{(g)}, \quad [4]$$

$$Fe_3O_{4(s)} + CO_{(g)} = 3(FeO) + CO_{2(g)}, \quad [5]$$

$$(FeO) + C_{(s,\ dissolved)} = Fe_{(l)} + CO_{(g)}, \quad [6]$$

$$(SiO_2) + 2\underline{C} = \underline{Si} + 2CO_{(g)}, \quad [7]$$

$$(SiO_2) + CO_{(g)} = SiO_{(g)} + CO_{2(g)}, \quad [8]$$

$$(SiO_2) + \underline{Si} = 2SiO_{(g)}, \quad [9]$$

$$SiO_{(g)} + \underline{C} = \underline{Si} + CO_{(g)}, \quad [10]$$

$$(TiO_2) + 2C_{(solid,\ dissolved)} = \underline{Ti} + 2CO_{(g)}, \quad [11]$$

$$(MnO) + \underline{C} = Mn + CO_{(g)}, \quad [12]$$

$$C_{(s)} = \underline{C}, \quad [13]$$

$$CO_{2(g)} + \underline{C} = 2CO_{(g)}. \quad [14]$$

The underline "_" and parenthesis "( )" notations denote the element or phase that is dissolved in the Fe-liquid solution and slag at known temperature, respectively. It is emphasized here that the reduction of Fe_2O_3 and Fe_3O_4 by $CO_{(g)}$ through reactions [3] and [5] is more feasible than reactions [2] and [4]. FeO and even Fe can be also formed in solid state; however, we here assume that Fe is mainly produced from FeO in the slag. Reactions [6] through [10] show the reduction mechanism of FeO and SiO_2 at slag/gas, gas/metal, and slag/metal interfaces as observed by Pomfret and Grieveson,[26] Teasdale and Hayes,[27] and Safarian *et al.*[28] A simple illustration can be given as in

Table VIII. WDS Analysis of Phases in B-Pig Iron Shown in Fig. 10

Point No.	Fe (Weight Percent)	C (Weight Percent)	Mn (Weight Percent)	Si (Weight Percent)	Ti (Weight Percent)	Mg (Weight Percent)	V (Weight Percent)	Al (Weight Percent)	P (Weight Percent)	Others (Weight Percent)
1	90.5	4.9	1.1	2.9	NA	0.1	0.3	NA	0.2	NA
2	90.5	4.6	1.1	3.1	0.1	0.1	0.3	NA	0.2	NA
3	2.8	13.1	NA	0.5	80.4	0.0	2.9	0.1	NA	0.2
4	2.3	15.0	NA	0.1	79.4	0.1	2.3	0.2	NA	0.6

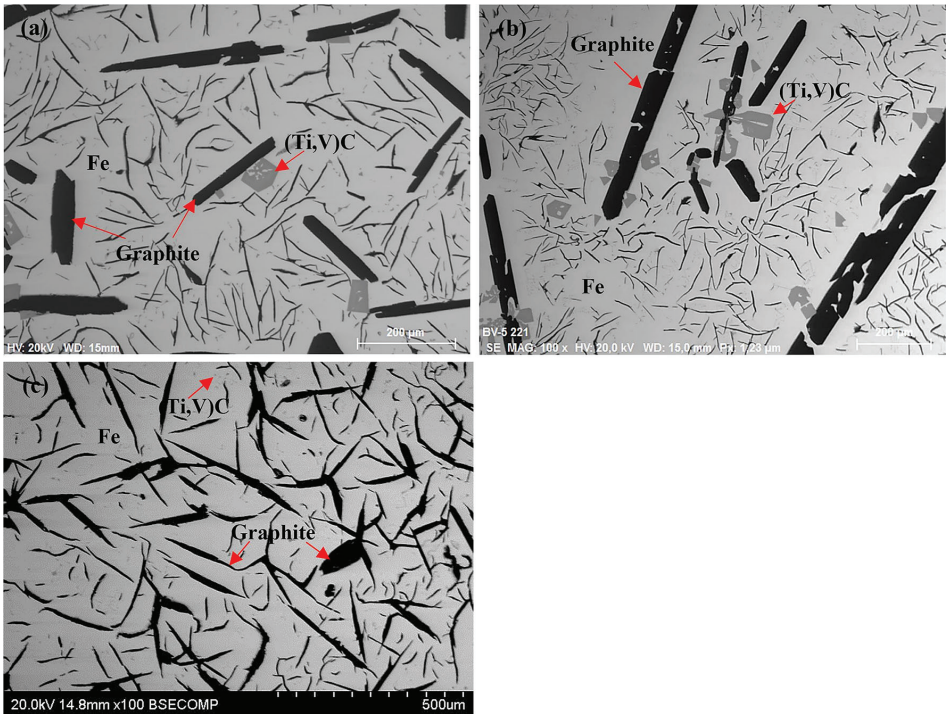

Fig. 11—BSE images showing the main coexisting phases in (*a*) B-, (*b*) G-, and (*c*) I-Pig iron samples.

Figure 12, where mass transports of the gaseous species (CO, CO_2, SiO) in gas bubbles at the slag/metal interface are very important.

As lime flux was used for slag making, the main reactions that occur in the process through high-temperature sintering and smelting can be expressed as in reactions [15] through [22]:

$$CaO_{(s)} + Al_2O_{3(s)} = (CaO \cdot Al_2O_3), \quad [15]$$

$$CaO_{(s)} + \frac{1}{3}Al_2O_{3(s)} = \frac{1}{3}(3CaO \cdot Al_2O_3), \quad [16]$$

$$CaO_{(s)} + \frac{7}{12}Al_2O_{3(s)} = \frac{1}{12}(12CaO \cdot 7Al_2O_3), \quad [17]$$

$$\frac{1}{3}(3CaO \cdot Al_2O_3) + \frac{1}{4}Al_2O_{3(s)} = \frac{1}{12}(12CaO \cdot 7Al_2O_3), \quad [18]$$

$$CaO_{(s)} + Al_2O_{3(s)} + SiO_{2(s)} = (CaO \cdot Al_2O_3 \cdot SiO_2), \quad [19]$$

$$CaO_{(s)} + Al_2O_{3(s)} + 2SiO_{2(s)} = (CaO \cdot Al_2O_3 \cdot 2SiO_2), \quad [20]$$

$$CaO_{(s)} + \frac{1}{2}Al_2O_{3(s)} + \frac{1}{2}SiO_{2(s)} = (2CaO \cdot Al_2O_3 \cdot SiO_2), \quad [21]$$

Table IX. Correlation Between Starting Materials' Mass Losses with Their Causes

Materials Mass Loss Causes	B-Bauxite Setup (kg)	G-Bauxite Setup (kg)	I-Bauxite Setup (kg)
Total Materials Mass Loss as Measured(1)	1.16	1.28	0.47
LOI of Bauxite[a]	0.28	0.25	0.12
LOI of Lime[b]	0.45	0.66	0.23
LOI of Coke[c]	2.10^{-3}	2.10^{-3}	2.10^{-3}
Total Loss Due to LOI(2): $a + b + c$	0.74	0.92	0.36
Mass Loss Due to Reduction(3)	0.16	0.21	0.16
Theoretical Mass Loss/Measured Mass Loss: (3)/(1)	0.77	0.87	1.10

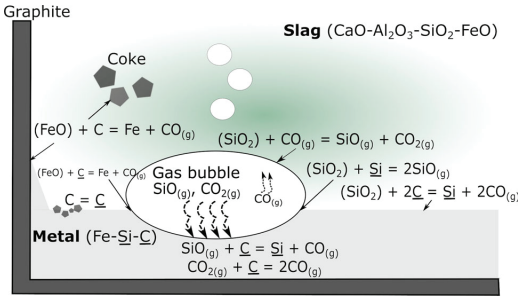

Fig. 12—Illustration of FeO and SiO_2 reduction by carbothermic reaction at slag/gas, gas/metal, and slag/metal interfaces.

$$CaO_{(s)} + TiO_{2(s)} = (CaTiO_3). \quad [22]$$

Here, we do not consider the FeO-containing phases in the slag, as we do not have much of it left in the final slag. For the sake of simplicity, the compounds that the slag is composed of are denoted as follows: CaO = C, Al_2O_3 = A, and SiO_2 = S. In thermodynamic perspective, the above reactions of pig iron and slag formation and their competition behaviors are dependent on the Gibbs energy changes at particular temperature. The Gibbs energy changes of the formation of the metal and slag components in pure state are calculated using HSC™ software. The reduction of pure iron oxides may occur below 1273 K (1000 °C), while silica and titania are phases that could be reduced by carbon at relatively high temperature, which means the separation of these two phases out of bauxites consumes more energy than iron. Moreover, the reduction of silica by $CO_{(g)}$ is unlikely to occur, as the Gibbs energy changes are positive at any given temperature. The slag-making reactions (reactions [15] through [22]) are viable at low temperature, and there is a large driving force for slag formation upon the heating of bauxite + lime to elevated temperatures. The WDS results in both slag and pig iron (Tables VII and VIII) show that the main phases are in solid solution form with certain solubility, instead of being in the pure forms. However, HSC™ calculations are made for pure substances, and the real Gibbs energy changes for the slag-making reactions may be even more negative than that the calculations indicate.

The equilibrium phases in different mixtures that coexist during and after the smelting-reduction can be calculated using thermodynamic software, FactSage™, at temperatures between 1273 K and 2073 K (1000 °C and 1800 °C) with an increment of 283 K (10 °C) and 0.70 ± 0.05 of C/A ratios. As the calculation results in Figure 13 indicate, the Fe-fcc phase coexists with the solidified forms of B-, G-, and I-Slags in the temperature range of 1273 K to 1663 K (1000 °C to 1390 °C). The lattice changes to Fe-bcc phase in the range from 1663 K to 1803 K (1390 °C to 1530 °C) before it starts to melt. In the meantime, liquid slag phase appears at around 1473 K (1200 °C), and its amount increases significantly at the range of 1673 K to 1773 K (1400 °C to 1500 °C). B- and I-Slags should have similar solid slag phases that are stable at temperatures below 1573 K (1300 °C) as seen in Figure 13. The sequential order from the highest to the lowest fraction of phase is $CAS_2 > C_2AS > CaTiO_3 > CaMg_2Al_{16}O_{27} > Ca_2Mg_2Al_{28}O_{46} >$ spinel. In addition, B-Slag has $CaAl_{12}O_{19}$ phase as well at 1673 K (1400 °C). The calculation results of the coexisting equilibrium phases in B- and I-Slag are not in agreement with the XRD results presented in Section III. The reason of the disagreement might be related to the element's distribution during smelting-reduction trial that will be discussed in Section IV–E.

G-Slag has CA phase that constitutes about 70 wt pct of the slag phase, followed by low amounts of C_2AS, $Ca_3MgAl_4O_{10}$, Ca_2SiO_4, $Ca_3Ti_2O_7$, spinel, and $KAlO_2$. FactSage™ does not recognize $C_{12}A_7$ phase in its database, and it is the reason that this phase is absent in the equilibrium phases of G-Slag. Apart from $C_{12}A_7$ phase, the presence of CA phase is in agreement with the XRD result of G-Slag. It is worthy to note that the amounts of TiO_2 and MgO of all obtained slags as in Table V are considerably low, which causes to not observe $CaTiO_3$, $CaMg_2Al_{16}O_{27}$, *etc.* in XRD analysis. However, the thermodynamic calculations here show that such phases may coexist with the main recognized phases in the slags.

C. *Effect of Slag Viscosity on Porosity*

The significant number of pores that appear in I-Slag in Figure 9(c) give strong indication of the gas formation during the oxides' reduction by the mechanism illustrated in Figure 12. The pores have been formed from the trapped gas that might emerge from the reduction reactions at the slag/metal interface. I-Slag has the highest amount of SiO_2 compared to others, and the basicity based on CaO/SiO_2 (C/S) mass ratio is 0.9, which is relatively acidic. This slag forms networking oxides in melts, which increase the viscosity and hinder the gas movement. In order to clarify this, FactSage™

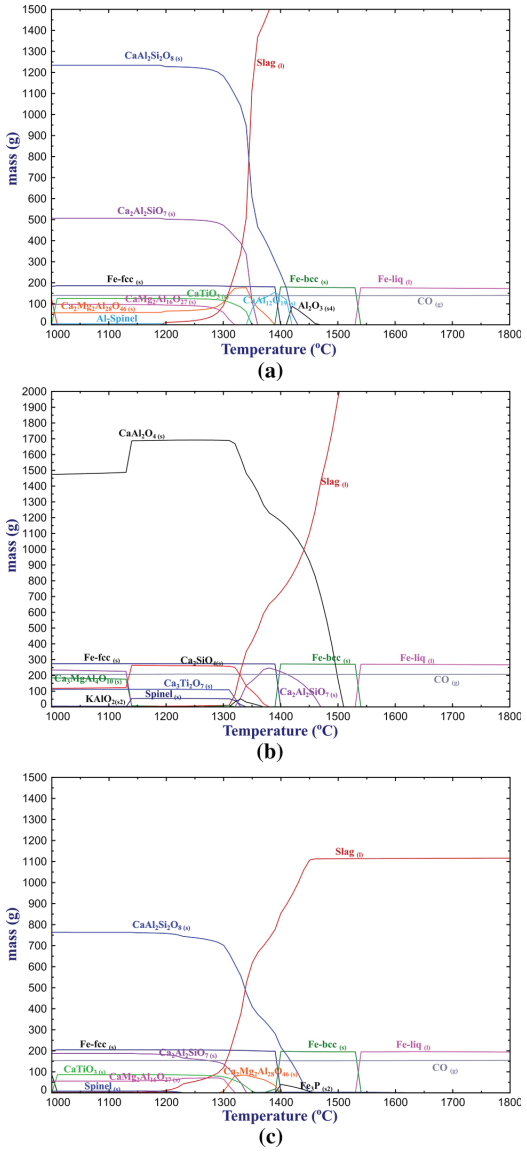

Fig. 13—The calculated phases in equilibria at different temperatures for (*a*) B-Bauxite, (*b*) G-Bauxite, and (*c*) I-Bauxite setups.

was applied to calculate the viscosities of the obtained B-, G-, and I-Slags produced at 1923 K (1650 °C) and viscosities of 0.17, 0.10, and 0.48 Pa s were, respectively, obtained as shown in Figure 14. The figure shows the correlation between different C/S mass ratios with the viscosities at 1723 K, 1823 K, and 1923 K (1450 °C, 1550 °C, and 1650 °C), where C/A mass ratio is equal to 1. It can be seen that by decreasing the temperature, the viscosity is significantly increased especially at the C/S mass ratio of less than 3. That is to say, the gas bubbles forming and leaving the slag/metal interface have more difficulties to rise in I-Slag than in the others as the I-Slag has more gas storage capacity. It is worth mentioning that during the smelting-reduction experiments more foaming of the I-Slag was observed than for the others, which is supporting the viscosity effect.

D. *Silica Losses from Slags*

The theoretical and measured mass loss differences in G- and I-Bauxites are relatively minor, whereas B-Bauxite shows otherwise (Table IX). This indicates that another factor has contributed to the loss of mass in B-Bauxite that might be elaborated as follows.

According to the XRF analysis of bauxite, B- and I-Bauxites have identical concentration of SiO_2. It is worthy to note that both have kaolinite as their main phase. Based on material balance calculation, total amounts of silicon either in starting materials and the products produced from B- and I-Bauxites should be 0.29 and 0.17 kg, respectively. In fact, both of the bauxites show nonequivalent amounts of silicon in their input–output balance. The estimated losses of silicon in B- and I-Slags are 72.7 and 17.6 pct, respectively.

Silicon could be lost as a gas phase $SiO_{(g)}$, which is produced from reaction between SiO_2 in slag with carbon in the metal, as in reaction [23]. Then, it is exiting from the slag when the gas bubble rises to the surface.

$$(SiO_2) + \underline{C} = SiO_{(g)} + CO_{(g)}. \qquad [23]$$

The Gibbs energy change of formation in reaction [23] at 2023 K (1750 °C) is − 2.2 kJ, which shows that high temperature is an important factor in the silica gas production from the slag. As mentioned in the experimental procedure, the mean smelting temperature of B-Bauxite is higher than that of I-Bauxite. Silica loss could explain one of the reasons why the concentration of silica in B-Slag is lower compared with I-Slag, although the mixture setup before the smelting trial has identical C/(A + S) mass ratios, that is, 0.36 and 0.34 for B- and I-Bauxites, respectively.

E. *The Distribution of Elements Between Slag and Pig Iron*

Based on equilibrium calculations in Figure 13, the main phases of B- and I-slags at low temperature should be CAS_2 and C_2AS phase, respectively. In contrast, the XRD results in Figure 4 show the main phases for B- and I-Slags to be C_2AS and CAS, respectively. This result is supported by XRF analysis of the products, which shows different compositions in slag and pig iron produced from B- and I-Bauxites, regardless of the similar phase and C/A ratio that the bauxite mixtures have before. This gives indication that during smelting-reduction and solidification of the melt, the elemental distribution may act as a decisive factor on the final phases in slag.

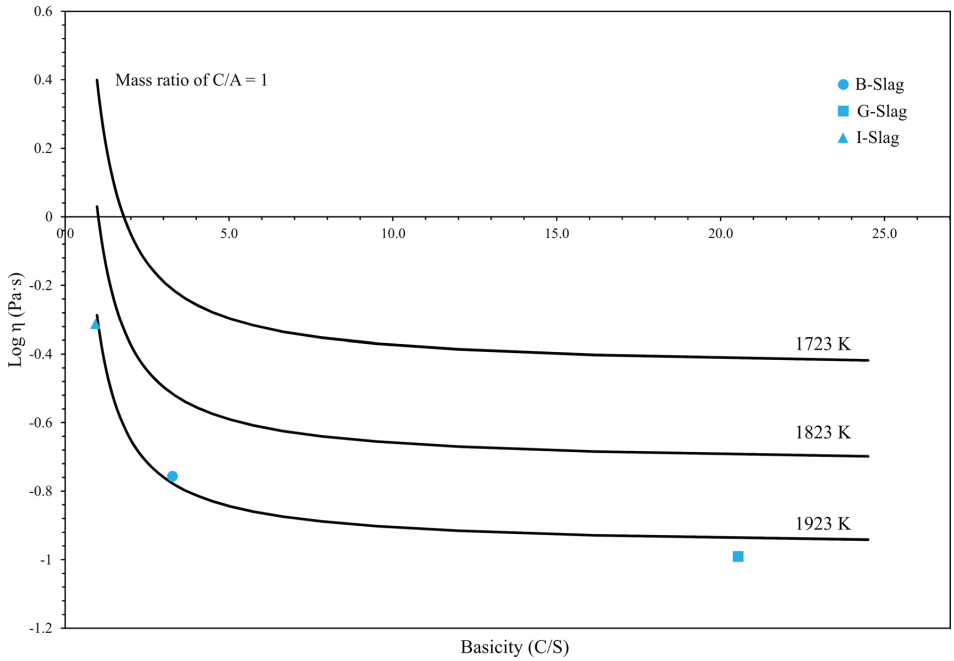

Fig. 14—Correlation between basicity (C/S) and viscosity in different C-A-S slags at different temperatures.

Figure 15 shows the distribution of phases in calcined bauxite ores and the corresponding slags after smelting-reduction according to the XRF results. The weight fractions of Al_2O_3 and SiO_2 phases remain the same before and after the treatment, which indicates that the two phases are not easily reduced during the smelting-reduction treatment. The significant decrease in the quantity of SiO_2 phase in B-Slag has already been discussed in Section IV–D. The CaO wt pct in G-Slag is higher than that in other slags because of the high amount of lime used to maintain the required C/A ratio to achieve the leachable calcium-aluminate phase.

The reduction extent of each phase can be calculated by simple mathematical expression:

$$\text{Reduction extent (pct)} = \left[\frac{W}{W^\circ}\right] \times 100 \text{ pct}, \qquad [24]$$

where W° is mass of the amount of metal based on the stoichiometry, as if 100 pct was reduced from an oxide and W is the actual amount of that metal present in the metal phase based on the XRF result of the pig iron. To simplify the mass loss based on the stoichiometry principle, we assume the iron reduction is 100 pct as the average WDS results of FeO content in all slags are low (see Table VII). Therefore, the SiO_2 reduction extents in B-, G-, and I-slag are 2.8, 1.3, and 1.6 pct, respectively. Higher SiO_2 reduction in B-Bauxite might be due to the higher smelting temperature of this trial compared with G- and I-Bauxites as discussed above. According to HSC data, reaction [8] transposes to the right side at temperature more than 1938 K (1665 °C), and based on the smelting temperature setup described in Section II–B, B-Bauxite was exposed to this temperature relatively longer than others. From kinetics point of view, carbothermic reduction of SiO_2 from slag is much slower than that of FeO. The other partially reduced phase was TiO_2. The TiO_2 reduction extents are 2.8, 8.4, 1.5 pct for B-, G-, and I-Bauxites, respectively. This calculation is in agreement with the amount of TiC that is observed in BSE image of the pig iron shown in Figure 11. The reduction of TiO_2 in reaction [11] proceeds at around 2023 K (1750 °C) when pure substances are involved. However, as the activity of titanium in the molten iron is low, the reduction of TiO_2 may occur at the lower process temperature to some extent, yielding dissolved titanium in iron. Under carbon-saturated condition, the dissolved titanium has high possibility to make bond with the existing carbon and forms TiC during solidification of pig iron (reaction [25]). This is further enhanced due to the low solubility of titanium in Fe-$C_{saturated}$-Ti system.[29]

$$\underline{\text{Ti}} + \text{C} = \text{TiC} \qquad \Delta G^\circ_{298\text{ K}} = -180.8 \text{ kJ/mole Ti} \qquad [25]$$

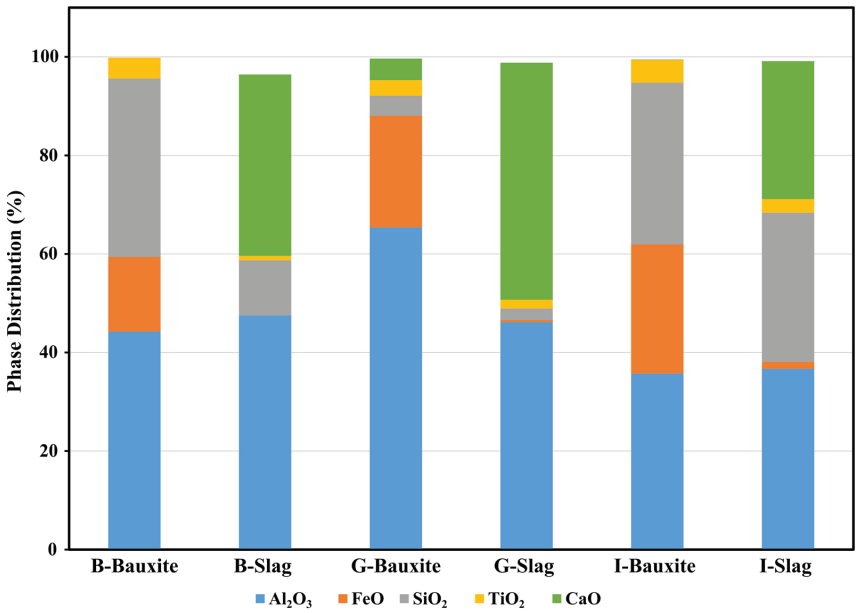

Fig. 15—Distribution of phases in bauxite ores and slags after smelting-reduction.

Another mechanism for the formation of TiC particles can be the direct reaction of the dissolved carbon in the melt with TiO_2 in the slag at slag/metal interface, as in reaction [26].

$$3C + (TiO_2) = TiC + 2CO_{(g)} \qquad \Delta G^{\circ}_{1873\,K} = -104.0\ \text{kJ/mole Ti} \qquad [26]$$

The thermodynamic activities given in reactions [11] and [26] are performed under standard conditions with the titanium activity being unity. Therefore, we need to evaluate the reactions under non-standard conditions, where we have a low titanium activity in the melt. For reactions [11] and [26], the expression of Gibbs energy changes can be written as

$$\Delta G_{11} = \Delta G^{\circ}_{11} + RT\ln\frac{a_{Ti}\cdot pCO^2}{a_{TiO_2}\cdot aC^2} \qquad [27]$$

$$\Delta G_{26} = \Delta G^{\circ}_{26} + RT\ln\frac{a_{TiC}\cdot pCO^2}{a_{TiO_2}\cdot aC^3} \qquad [28]$$

where $\Delta G_{11}{}^{\circ}$ and $\Delta G_{26}{}^{\circ}$ are the standard Gibbs energy changes of reactions [11] and [26], respectively. The activities of C and TiO_2 in the melt is unity and unknown, respectively. The partial pressure of $CO_{(g)}$ for both reactions is the same, thus Eqs. [27] and [28] can be rearranged to

$$\Delta G^{\circ}_{11} + RT\ln a_{Ti} = \Delta G_{11} - RT\ln\frac{pCO^2}{a_{TiO_2}\cdot aC^2} = \delta G_{11} \qquad [29]$$

$$\Delta G^{\circ}_{26} + RT\ln a_{TiC} = \Delta G_{26} - RT\ln\frac{pCO^2}{a_{TiO_2}\cdot aC^3} = \delta G_{26} \qquad [30]$$

Since activity of TiC is unity, then Eq. [30] becomes

$$\Delta G^{\circ}_{26} = \Delta G_{26} - RT\ln\frac{pCO^2}{a_{TiO_2}\cdot aC^3} = \delta G_{26} \qquad [31]$$

By comparing δG_{11} and δG_{26} values, we may predict which reaction is more favorable to occur at a particular temperature. We determine the activity of titanium in Fe-$C_{saturated}$-Ti system at 1873 K (1600 °C) from FactSage™ database and calculate the δG_{11} and δG_{26} in the melt, as seen in Figure 16.

Figure 16 shows that if the amount of titanium in the melt is less than about 0.01 mol pct, the reaction [11] is more favorable than reaction [26], which means the TiO_2 is reduced and yields the dissolved titanium in the metal. On the contrary, if the titanium content is larger than about 0.01 mol pct, then reaction [26] is more favorable than that of reaction [11], which means TiC formation at slag/metal interface is likely to occur.

As seen in WDS analysis of pig iron in Table VIII, silicon content on numbers 1 and 2 of B-Pig iron show higher amounts compared with that of silicon content in I-Pig iron (Table VI). This confirms the result in XRF analysis, and demonstrate the reduction mechanism of silica in bauxite during smelting-reduction. The WDS results of point numbers 3 and 4 shown in Table VIII confirmed the formation of (Ti,V)C in metal as was

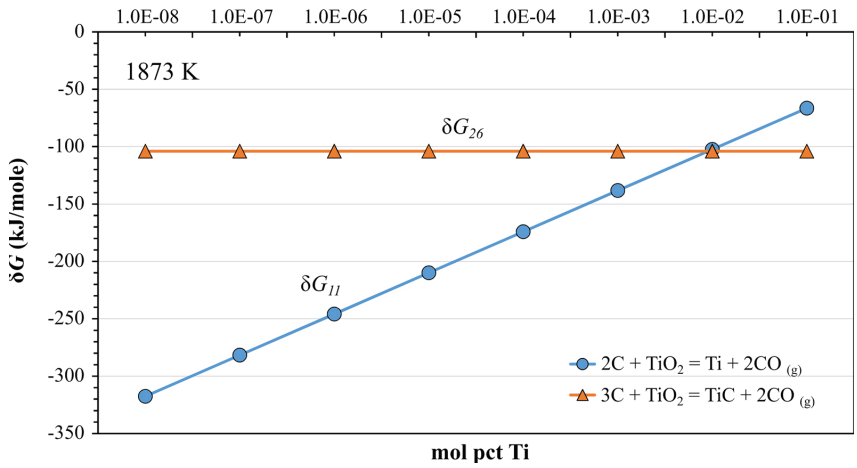

Fig. 16—The changes of δG_{11} and δG_{26} at 1873 K in different mol pct Ti.

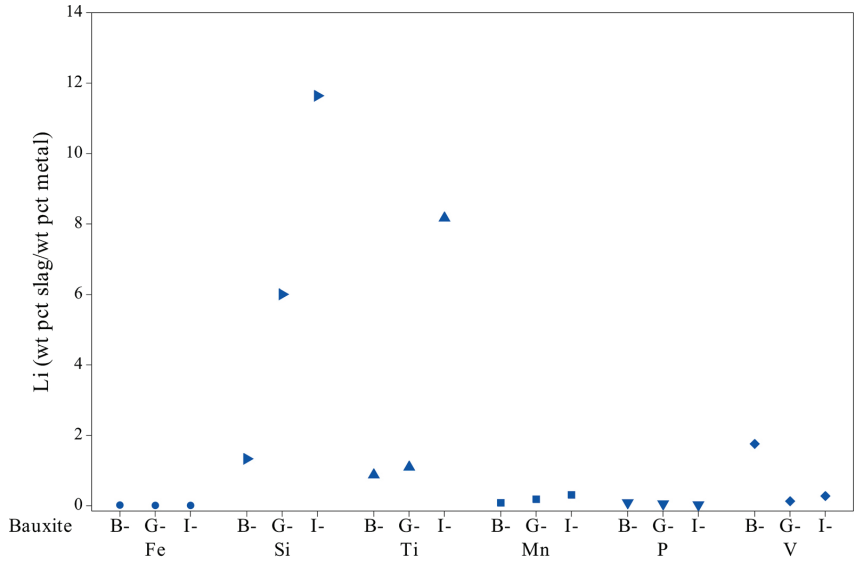

Fig. 17—Distribution coefficients of several elements in different bauxites.

reported from the literature.[7] As the solidus temperature of metal is lower than that of slag, the solute titanium in pig iron may segregate to the boundaries of metal and slag, and forms carbide.

Another important parameter in studying the slag-metal systems is the distribution of the dissolved elements between the slag and metal phases, and a distribution coefficient as L_i is defined, which is expressed as

$$L_i = \frac{(\text{wt pct } i)}{[\text{wt pct } i]}, \qquad [32]$$

where (wt pct i) and [wt pct i] represent the mass pct of element i in the slag and metal phases, respectively. The distribution coefficients of Fe, Si, Ti, Mn, P, and V in the current work are shown in Figure 17. Fe, Mn, P, and V have relatively low L_{Fe}, L_{Mn}, L_P, and

L_V values (0 to 1.7), which indicates that these elements are stable in pig iron and shows that iron was 99.9 pct reduced. On the other hand, the L_{Si} and L_{Ti} values vary depending on the type of bauxite and so the slag compositions, which are 1.3 to 11.6 and 0.8 to 8.2 for L_{Si} and L_{Ti}, respectively. More experiments are necessary to obtain better understanding on the elemental distribution in slag and pig iron produced from smelted bauxite.

F. *Stable Phases in the Slag System*

Even though the mixtures were set up with particular ratio of C/A, the other compounds, *i.e.*, SiO_2 and TiO_2 affect the construction of phases in the slag system. AQAs seen in Table V, the main slag compounds are CaO, Al_2O_3, and SiO_2, while TiO_2 content is negligible (< 3 wt pct) and is not forming any new phase in the system.[24] Therefore, the slag is regarded here as a ternary CaO-Al_2O_3-SiO_2 system. Employing FactSage™ phase diagram module, the projection of isothermal sections from 1573 K to 1873 K (1300 °C to 1600 °C) in CaO-Al_2O_3-SiO_2 system can be made as shown in Figure 18. Due to the limitation of compound database in FactSage, $C_{12}A_7$ phase is not shown in the projection. However, we draw the area of $C_{12}A_7$ phase manually into the ternary system (colored in pink) based on the provided information in the literature.[17,30]

The calculated ternary phase diagram corresponds with the XRD result of B-Slag in Figure 4. The direction of crystallization path proceeds toward the peritectic temperature and shows that C_2AS, CA, and β-C_2S phases are in equilibrium as condensed phases after solidification. However, neither β-C_2S nor γ-C_2S phases can be traced in the diagram. The absence of C_2S may be the reason why self-disintegration did not happen during cooling, as we observed. The self-disintegration of slag occurs due to the volume expansion by 12 pct as the crystalline phase transforms from β-C_2S to γ-C_2S.[24,31] In calcium-aluminate-containing-slag produced from blast furnace, it is reported that when the cooling rate is lower than 4.8 K s^{-1}, then the major phases of the slag are $C_{12}A_7$, γ-C_2S, and CA.[32] On the other hand, if the cooling rate is considerably high, that is, 4.8 to 5.4 K s^{-1}, the formation of C_2AS occurs. In the current study, the cooling rate averages were above 4.8 K s^{-1}. Another possible explanation would be related to the low presence of β-C_2S in B-Slag (< 5 pct), as calculated in Section IV–G, which is confirmed by no observation of the corresponding peaks in XRD spectra (Figure 4).

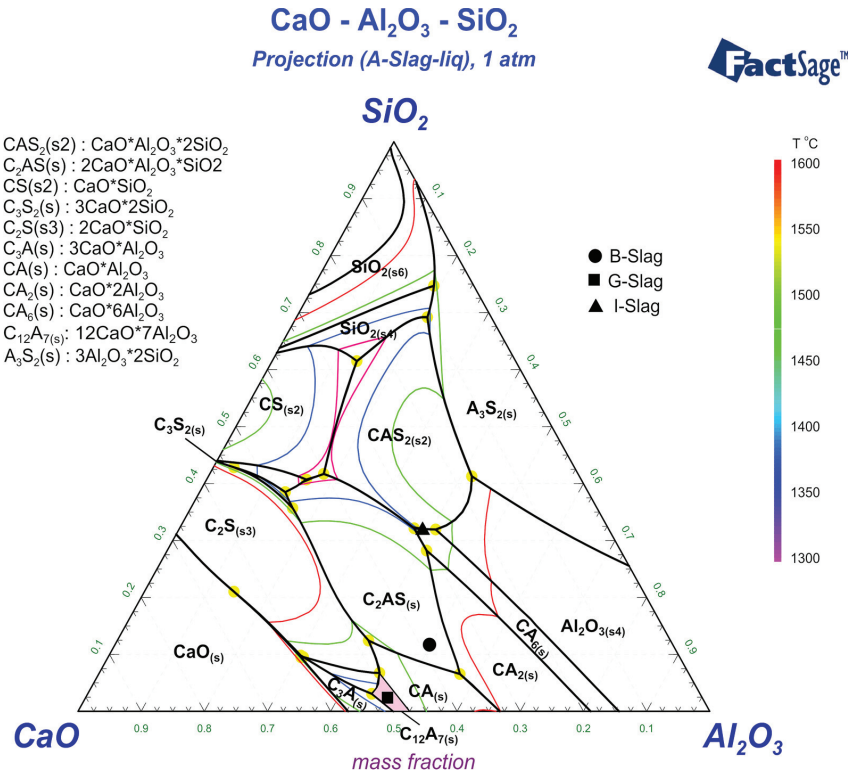

Fig. 18—Isothermal projection of ternary CaO-Al_2O_3-SiO_2 system.

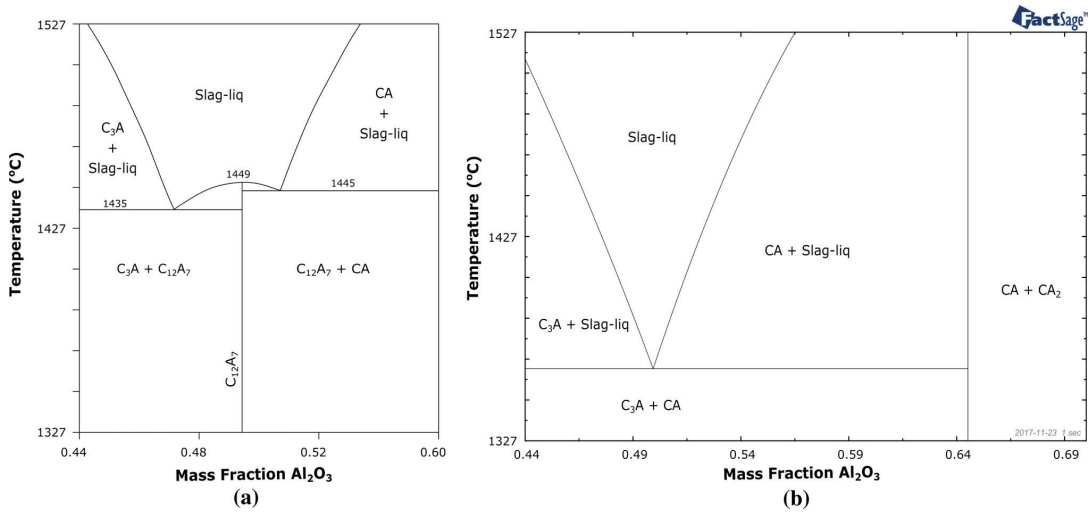

Fig. 19—Part of CaO-Al_2O_3 binary system where (*a*) the $C_{12}A_7$ phase is included and (*b*) a moisture-free without formation of $C_{12}A_7$ phase, as simulated by FactSage™.

Based on the XRD results, G-Slag has $C_{12}A_7$, CA, and a low fraction of C_5A_3 phase. The $C_{12}A_7$ phase was first observed by Rankin and Wright[33] in 1915 and has been discussed several times ever since. In 1965, Nurse *et al.*[34] observed that $C_{12}A_7$ phase is unstable in anhydrous or moist-free CaO-Al_2O_3 system, as it is in equilibrium with H_2O above 1223 K (950 °C) and forms $Ca_{12}Al_{14}O_{32}(OH)_2$ when is fully saturated: the water is present as hydroxyl ions in crystal structure. Later on, Haccuria *et al.*[35] showed that in a dry and high-purity (99.999 pct) argon atmosphere, the formation of $C_{12}A_7$ phase does not occur. Here in G-Slag, $C_{12}A_7$ phase is observed in its anhydrous form with the data given as follows: a = 11.99856 Å, V = 1727.38 $Å^3$, and density = 3.10^{-3} kg m^{-3}, in cubic I-43d (220) space group. The phase in the slag samples have been formed in an open furnace and oxidizing atmosphere, which subsequently is cooled to room temperature. The result is in agreement with Imlach *et al.*[36] who hypothesized that the $C_{12}A_7$ phase might be stable at high temperatures as it absorbs the excess of oxygen from any oxidizing atmosphere, even where pO_2 is as low as 10^{-3} Pa (10^{-8} bar). This finding is important to the study of calcium-aluminate slag making, as $C_{12}A_7$ phase is known as one of the leachable phases in CaO-Al_2O_3 system[8,11,17,37] and is, therefore, crucial to Pedersen process. Hallstedt[16] optimized the thermodynamic data of $C_{12}A_7$ phase and proposed that it melts congruently at 1449 °C. It has a eutectic with other phases C_3A and CA on each side, as shown in Figure 19(a). In our results, G-Slag consists mainly of 46.1 wt pct Al_2O_3 and 48.1 wt pct CaO, which means according to Figure 19(a) it may rather have C_3A and $C_{12}A_7$ than $C_{12}A_7$ and CA phases. AQHowever, Hallstedt considers only the binary system of CaO-Al_2O_3 and not the role of other constituents even if they were involved, such as silica, titania, *etc.* Moreover, C_3A phase is relatively unstable as it can be reacted with free-Al_2O_3 in the system to form $C_{12}A_7$ (see reaction [18]). In our previous study,[12] we did not observe the presence of $C_{12}A_7$ phase in a slag that was synthesized at high temperature and under oxidizing atmosphere. The composition was 38 wt pct and 62 wt pct of CaO and Al_2O_3, respectively. Instead of the occurrence of CA and $C_{12}A_7$ phase, the encountered phases were CA and C_3A, and this result agrees with a moisture-free binary diagram as shown in Figure 19(b).

The reason of this different phenomenon can be explained as follows:

1. In our previous study,[12] CA phase was the primary crystallized phase (91 wt pct by phase lever-rule), and when the cooling reached eutectic temperature, the remaining liquid may precipitate the $C_{12}A_7$ phase at grain boundaries. However, the amount of this phase was low (< 10 wt pct), and either it was dissolved in the adjacent CA phase or is dissociated to CA and C_3A phases at lower temperature as shown in reaction [33].

$$2C_{12}A_7 = 5C_3A + 9CA \qquad [33]$$

   As reported in the literature,[34] the Gibbs energy changes for reaction [33] are − 1.5, − 2.0, and − 3.5 kJ/mole CaO at 1700 K, 1600 K, and 1500 K (1427 °C, 1327 °C, and 1227 °C), respectively. Therefore, formation of C_3A and CA phases upon cooling was favorable.
2. In the current study, as indicated by the strongest intensity in XRD in Figure 4, the primary crystallized phase from G-Slag is $C_{12}A_7$. As it has significant

amount, it may absorb the required oxygen during precipitation and eventually become more stable. Based on this reasoning, we may hypothesize that unless the composition of the binary slag is on the range of its primary crystallization (about 46 to 51 wt pct Al_2O_3) or as the majority phase in the system, the $C_{12}A_7$ phase is likely to be unstable even in oxidizing atmosphere.

According to the XRD results in Figure 4, no CAS_2 phase in I-Slag is observed, which does not agree with the ternary system at 101.3 kPa (1 bar) shown in Figure 18. CAS that is observed is known as Calcium Tschermak's pyroxene (CATs) for geologists, which is one of the important constituent of the earth's upper mantle and of the natural aluminous pyroxenes. The crystallography pattern of CAS in the current study matched against the measurement of Okamura *et al.*[38]: $a = 9.609$ Å, $b = 8.652$ Å, $c = 5.274$ Å, $\beta = 106.06$ deg, $V = 421.35$ Å^3, in monoclinic $C2/c$ space group. The CAS phase is formed by a solid-state reaction as seen in reactions [34] and [35]. Okamura *et al.*[38] synthesized a single crystal of CAS from CAS_2, C_2AS, and Al_2O_3 after heating the mixture at 1573 K (1300 °C) within 24 hours in 18.10^5 kPa (18 kbar). On the other hand, Hariya and Kennedy[39] observed that CAS_2 decomposes to CAS and SiO_2 under high pressure and temperature.

$$CAS_2 + C_2AS + Al_2O_3 = 3CAS \quad [34]$$

$$CAS_2 = CAS + SiO_2 \quad [35]$$

Many studies concluded that CAS is a high-pressure and temperature phase.[38,40] In addition, Hays[41] reported that pure CAS is not stable below 1433 K (1160 °C), and the pressure field of stability is relatively narrow even at higher temperature. However, Ma *et al.*[42] stated that although synthetic CAS is a high-pressure phase, a natural CAS could be found in low-pressure atmosphere. Figure 9(c) shows that I-Slag does not have lamellar structure, which indicates the phases were not formed through a slow diffusion mechanism. Thus, in contrast to the conclusion that was given by some researchers above, we suggest that the reaction [35] may occur during the cooling of a congruently melted CAS_2 phase at ambient pressure. The coexisting phases of CAS and SiO_2 in XRD results of I-Slag are worth as the evidence in support of the argument. Nevertheless, this hypothesis needs further investigation.

G. *Phase Changes upon Slag Solidification and Cooling*

In Table VII, the WDS analysis of B-Slag on dark and bright structures is identical with the phases of C_2AS and $CaTiO_3$, respectively. The WDS results on fine lamellar phase indicate a C_2AS phase as it has similar composition with the dark phase, it only has more TiO_2. This may not be precise, as the lamellar is constructed with dark and less-bright phase. It is difficult to identify the composition of each layer as the thickness is as much as 2 μm. To understand the existing phases in lamellar structure, a crystallization path of B-Slag becomes necessary. Based on alkemade line and phase lever-rule we can describe it as follows:

1. Consider we have 100 g of slag with the composition of 50 wt pct Al_2O_3, 12 wt pct SiO_2, and 38 wt pct CaO, which is a normalized XRF data of B-Slag from Table V. At 1923 K (1650 °C), slag liquid phase exists, named liquid #1.
2. From 1923 K to 1783 K (1650 °C to 1510 °C), the primary crystallization of C_2AS occurs; liquid #1 $\rightarrow$ C_2AS + liquid #2. The slag consists 14 g of C_2AS phase (14 pct) and 86 g of liquid #2 phase (86 pct).
3. From 1783 K to 1623 K (1510 °C to 1350 °C), following reaction occurs: liquid #2 $\rightarrow$ C_2AS + CA + liquid (p). At this stage, lamellar structure coexists. The masses of C_2AS, CA, and liquid (p) phase are 30.1 (35 pct), 49 (57 pct), and 6.9 g (8 pct), respectively.
4. At 1623 K (1350 °C), liquid (p) + C_2AS $\rightarrow$ C_2S + CA, a peritectic reaction occurs. At the current stage, the remaining liquid is consumed, as well as the partial of C_2AS phase. The masses of liquid (p), C_2AS, C_2S, and CA phases are 6.9 g (66 pct), 3.55 (34 pct), 3.86 (37 pct), and 6.59 g (63 pct), respectively.
5. From 1623 K (1350 °C) to room temperature, at the solidus line, no liquids exist, and impurities may segregate and remain concentrated between the primary C_2AS grains. Total amount of condensed phases in B-Slag is

$$C_2AS = 14 \text{ g} + 30.1 \text{ g} - 3.55 \text{ g} = 40.55 \text{ g (40.6 pct)}$$

$$CA = 49 \text{ g} + 6.59 \text{ g} = 55.59 \text{ g (55.6 pct)}$$

$$C_2S = 3.86 \text{ g (3.8 pct)}$$

$$\text{Total} = 100 \text{ g (100 pct)}$$

On the other hand, coarse and small grain structures in G-Slag indicate the $C_{12}A_7$ phase. Grzymek *et al.*[43] observed that $C_{12}A_7$ has polymorphic transition phase, depending on the synthesizing temperature, condition of atmosphere (reducing or oxidizing), and the cooling rate when it was formed. AQGrzymek mentioned that when synthesis is carried out under an oxidizing atmosphere at 1770 K (1497 °C), and then slowly cooled, the structure is isotropic and grainy-ish with an anisotropic phase formed on grain boundaries, which is similar to the current result. The structure of CA phase in G-Slag is indistinguishable as the amount is considerably low.

In I-Slag, pointed WDS analysis on bright and dark structures correspond to CAS phase with insignificant difference on TiO_2 amount (1 to 2 wt pct). No lamellar structure is observed as it was in B-Slag. An X-ray elemental mapping on I-Slag in Figure 7 shows the dark structure has high concentration in titanium, and it has stronger bonding affinity to aluminum than that of calcium and silicon. Interestingly, these complex oxides do not behave similarly in G-Slag. The areas of the

phase that is rich in titanium have tendency to preferentially bond with calcium and silicon rather than aluminum, as shown in Figure 6, which is supported by SEM and EDS results for G-Slag in Figure 8. This gives valuable information for the leachability of the slag, as the titanium that bonded to the aluminum might hinder the alumina-leaching efficacy.

As we observed above, the slags B, G, and I contain different Al_2O_3-containing phases, and the leachability of them is important for extraction of alumina. The leaching behavior of $C_{12}A_7$ and CA phase has been studied in the literature, and the main point to be mentioned here is that both phases are soluble in sodium carbonate solution and therefore is favorable for the alumina recovery. Lundquist and Leitch[44] proposed the leaching reaction of CA phase where

$$CaO \cdot Al_2O_3 + Na_2CO_3 + 4H_2O = CaCO_3 + 2Na^+ + 2Al(OH)^{4-}, \quad [36]$$

while for $C_{12}A_7$ phase, the reaction may be described as follows[8]:

$$12CaO \cdot 7Al_2O_3 + 12Na_2CO_3 + 5H_2O = 7Na_2O \cdot Al_2O_3 + 12CaCO_3 + 10NaOH \quad [37]$$

However, no publication was found about the leachability behaviors of CAS, C_2AS, and C_5A_3 phases. This will be the subject of study of the current authors in the near future. Understanding the leaching behaviors of Al_2O_3-containing phases may pave the way to treat different metallurgical slags, which is quite important regarding the sustainable process development and circular economy.

V. CONCLUSION

The characteristics of calcium-aluminate-containing slags and pig iron produced from low-grade bauxite ores were studied. Using advance characterization techniques, the thermochemistry of oxides reduction, elemental distributions between the slag and metal products, and mechanisms of the formation of phases in them can be explained. The main conclusions drawn can be summarized as follows:

1. Iron from the ores is removed from 94.8 to 99.9 pct during smelting-reduction by carbon and yields the alumina-containing slag containing less than 1 wt pct Fe, dependent on the slag chemistry.
2. The partial separation of Mn, Si, Ti, V, and P oxides occurs through the smelting-reduction, where low distribution coefficients of L_{Mn}, L_P, and L_V are observed, while L_{Si} and L_{Ti} values are in ranges that are considerably wide depending on the characteristics of the produced slag.
3. The viscosity in calcium-aluminate slags with CaO/SiO_2 mass ratio less than three is higher compared with other compositions at elevated temperatures. It causes lower Fe-removal and yields more porous product.
4. Silicon loss from high SiO_2-containing bauxites may occur at elevated temperatures through the SiO gas formation.
5. The leachable slag phases ($CaO{\cdot}Al_2O_3$, $12CaO{\cdot}7Al_2O_3$), which are observed in G-Slag, are obtained after the smelting-reduction of bauxite that has $Al_2O_3/(Fe_2O_3 + SiO_2)$ mass ratio higher than two at cooling rate of up to 5 K s^{-1}.
6. The complex bonding between titanium and aluminum oxides in slag is not favorable for leaching process and is likely to occur in $CaO{\cdot}Al_2O_3{\cdot}SiO_2$ phase.

ACKNOWLEDGMENTS

The authors thank Hanne Sellæg for her valuable contribution in the laboratory experiments. The current research has been funded by the NTNU and cosponsored by the Research Domain 5–Materials and the Society in SFI Metal Production (a Norwegian Centre for Research-driven Innovation in metal production) under the Project Number 237738.

REFERENCES

1. K. Tsesmelis: *Proceedings of 35th International ICSOBA Conference*, 2017, vol. 42, p. 71.
2. D.J. Roth and J. Falter: *Proceedings of 35th International ICSOBA Conference*, 2017, vol. 42, pp. 539–45.
3. E. Ujaczki, P. Cusack, S. Clifford, T. Curtin, R. Courtney, and L. O'Donoghue: *Proceedings of 35th International ICSOBA Conference*, 2017, vol. 42, pp. 485–90.
4. B. Bhoi, P. Rajput, and C.R. Mishra: *Proceedings of 35th International ICSOBA Conference*, 2017, vol. 42, pp. 565–74.
5. T. Hertel, B. Blanpain, and Y. Pontikes: *Proceedings of 35th International ICSOBA Conference*, 2017, vol. 42, pp. 575–85.
6. H. Pedersen: *United States of America Patent*, 1927, 1618105.
7. J. Safarian and L. Kolbeinsen: *Sustainable Industrial Processing Summit*, 2016, pp. 149–58.
8. H.E. Blake Jr., O.C. Fursman, and A.D. Fugate: *US Bureau of Mines*, 1966, pp. 1–19.
9. T. Hignett: *Ind. Eng. Chem.*, 1947, vol. 39, pp. 1052–60.
10. J. Miller and A. Irgens: *Light Metals*, Springer, Cham, 1974, pp. 977–82.
11. R. Lundquist and H. Leitch: *US Bureau of Mines*, 1964, pp. 1–16.
12. F.I. Azof, L. Kolbeinsen, and J. Safarian: *Proceedings of 35th International ICSOBA Conference*, 2017, vol. 42, pp. 243–53.
13. K. Kyriakogona, I. Giannopoulou, and D. Panias: *Proceedings of the 3rd World Congress on Mechanical, Chemical, and Material Engineering*, 2017, pp. 1331–36.

14. H. Sellæg, L. Kolbeinsen, and J. Safarian: *Light Metals*, Springer, Cham, 2017, pp. 127–35.
15. S.H. Ahn, Y.H. Kim, J.P. Shin, and Y.E. Lee: *ISIJ Int.*, 2014, vol. 54, pp. 750–55.
16. B. Hallstedt: *J. Am. Ceram. Soc.*, 1990, vol. 73, pp. 15–23.
17. K.-S. Chou: *Retrospective theses and dissertations, Digital Repository of Iowa State University*, 1979, pp. 1–152.
18. A. Pehlivan, A.O. Aydin, and A. Alp: *Sakarya University Journal of Science*, 2012, pp. 92–98.
19. A.W.A. Al-Ajeel and S.I. Al-Sindy: *Iraqi Bull. Geol. Min.*, 2006, vol. 2, pp. 67–76.
20. J. Xiao, F. Li, Q. Zhong, H. Bao, B. Wang, J. Huang, and Y. Zhang: *Hydrometallurgy*, 2015, vol. 155, pp. 118–24.
21. P. Smith: *Hydrometallurgy*, 2009, vol. 98, pp. 162–76.
22. M. Jiayu, L. Zhibao, and X. Qinggui: *Am. Inst. Chem. Eng.*, 2012, vol. 58, pp. 2180–91.
23. H.E. Blake Jr., O.C. Fursman, A.D. Fugate, and L.H. Banning: *US Bureau of Mines*, 1968, pp. 1–19.
24. Z. Tong, Y. Li, and L. Lian: *Light Metals*, Springer, Cham, 2012, pp. 185–88.
25. B. Wang, H.-L. Sun, D. Guo, and S.-W. Bi: *Light Metals*, Springer, Cham, 2011, pp. 201–04.
26. R. Pomfret and P. Grieveson: *Can. Metall. Q.*, 1983, vol. 22, pp. 287–99.
27. S. Teasdale and P. Hayes: *ISIJ Int.*, 2005, vol. 45, pp. 634–41.
28. J. Safarian, L. Kolbeinsen, M. Tangstad, and G. Tranell: *Metall. Mater. Trans. B*, 2009, vol. 40**B**, pp. 929–39.
29. M. Sumito, N. Tsuchiya, and K. Okabe: *Trans. ISIJ*, 1981, vol. 21, pp. 414–21.
30. M. Kowalski, P. Spencer, and D. Neuschutz: *Slag atlas*, 2nd ed., Verlag Stahleisen GmbH, Dusseldorf, 1995.
31. H.-L. Sun, B. Wang, H.-Y. Yu, S.-W. Bi, and G.-F. Tu: *Light Metals*, Springer, Cham, 2010, pp. 29–32.
32. B. Wang, H.-L. Sun, X.-Z. Zhang, and S.-W. Bi: *Light Metals*, Springer, Cham, 2011, pp. 241–44.
33. G. Rankin and F. Wright: *Am. J. Sci.*, 1915, vol. 39, pp. 1–79.
34. R. Nurse, J. Welch, and A. Majumdar: *Trans. Br. Ceram. Soc.*, 1965, vol. 64, pp. 323–32.
35. E. Haccuria, T. Crivits, P.C. Hayes, and E. Jak: *Am. Ceram. Soc.*, 2015, vol. 99, pp. 691–704.
36. J. Imlach, L. Glasser, and F. Glasser: *Cem. Concr. Res.*, 1971, vol. 1, pp. 57–61.
37. H.-L. Sun, B. Wang, J.-X. Zhang, and S.-F. Zong: *Adv. Mater. Sci. Eng.*, 2014, pp. 1–6.
38. F.P. Okamura, S. Ghose, and H. Ohashi: *Am. Mineral.*, 1974, vol. 59, pp. 549–57.
39. Y. Hariya and G. Kennedy: *Am. J. Sci.*, 1968, vol. 266, pp. 193–203.
40. B.J. Wood: *Am. Mineral.*, 1976, vol. 61, pp. 599–602.
41. J.F. Hays: *Carnegie Institution Washington Year Book*, 1965, pp. 234–39.
42. C. Ma, S.B. Simon, G.R. Rossman, and L. Grossman: *Am. Mineral.*, 2009, vol. 94, pp. 1483–92.
43. J. Grzymek, A. Grzymek, Z. Konik, A. Stok, and M. Gawlicki: *Light Metals*, Springer, Cham, 1985, pp. 87–99.
44. R. V. Lundquist and H. Leitch: *US Bureau of Mines*, 1963, pp. 1–9.

Paper 3

The Leachability of Calcium Aluminate Phases in Slags for the Extraction of Alumina

Fabian Imanasa Azof[1], Leiv Kolbeinsen[2] and Jafar Safarian[3]
1. PhD student
2. Professor
3. Associate Professor
Norwegian University of Science and Technology (NTNU), Department of Materials Science and Engineering, Trondheim, Norway
Corresponding author: fabian.i.azof@ntnu.no

Abstract

Alumina is used primarily as feedstock for aluminum production. It occurs naturally in bauxite and clay and other minerals, and can be concentrated in industrial by-products such as coal gangue, fly ash, blast furnace slag, etc. The hydrometallurgical treatment of bauxite to recover alumina has been widely adopted industrially since the Bayer process was first employed commercially. However, the sustainability of alumina production by this means is less than ideal, due to the high production rate of poorly utilized and highly alkaline by-product that the process yields; bauxite residue or red mud. On the other hand, digestion of alumina-containing slags produced by reduction of bauxite results in no red mud production. In this work, the leachability of binary phases of CaO and Al_2O_3 in slags is studied under given conditions of temperature and time. Advanced characterization techniques are used to study the chemical composition, phases and microstructure of the slags and the digestion products. It is apparent that the leachability of a phase affects that of other phases. A less leachable phase could hinder the leachability of a more leachable phase. The experimental data shows that the leaching rate of slag from highest to the lowest is $CaO.Al_2O_3$, $3CaO.Al_2O_3$, and $CaO.2Al_2O_3$, respectively.

Keywords: Alumina, calcium oxide, slag, smelting reduction, leachability.

1. Introduction

Alumina (Al_2O_3) is found in different sources in nature, i.e. bauxite, nepheline, clay, and industrial by products such as coal gangue, fly ash, blast furnace slag, etc. However, metallurgical alumina produced from bauxite still dominates the world's alumina production due to the technical and economic feasibility of the Bayer process. A high-grade bauxite, with a mass ratio of Al_2O_3 to SiO_2 greater than 6.25 [1, 2], and/or high Al_2O_3 to Fe_2O_3 ratio [3], can be directly treated without much disruption along the sequential treatment steps of the Bayer process. However, regions that are far from the equatorial zone, who have more karst bauxite than lateritic deposits, generally need more rigorous (and costly) leaching conditions, or use a pyro-hydrometallurgical process to treat the bauxite. This is because in general, the mineralogical composition of laterite is $Al(OH)_3$ (gibbsite) and AlO(OH) (boehmite), while karst bauxite is AlO(OH) (boehmite) and AlO(OH) (diaspore), the latter being significantly more difficult to process [1].

An alternative method to beneficiate bauxite ore with high iron content is by smelting reduction as our recent studies in *research domain 5-Materials and Society* in SFI-metal production shows its feasibility in avoiding red mud production [4, 5]. It produces pig iron as a by-product, and a calcium aluminate slag as the source of alumina. This approach is the traditional Pedersen process [6]. Although there is no commercial production of alumina by this process, there has been research on hydrometallurgical treatment of calcium-aluminate slags. Lundquist and Leitch [7], Tong and Li [8], and Wang et al. [9] investigated the leachability of three calcium

aluminates ($12CaO.7Al_2O_3, 3CaO.Al_2O_3, 4CaO.Al_2O_3.Fe_2O_3$). These were produced from the lime-soda sinter process in a different solvent, calcium aluminate produced by smelting reduction of red mud with the addition of TiO_2, and MgO-containing calcium aluminate phases ($12CaO.7Al_2O_3$ and $\gamma - 2CaO.SiO_2$), and from blast furnace slag with the addition of Na_2O, respectively. Other researchers showed the synergistic effect of $12CaO.7Al_2O_3$ and $CaO.Al_2O_3$ on alumina leachability [10].

However, the leaching behavior of each calcium aluminate phase in the binary system is not yet clear. The leaching reaction of three calcium aluminate phases in alumina production are described below in Equations (1 – 3).

$$CaO.Al_2O_3 + Na_2CO_3 + 4H_2O = 2NaAl(OH)_4 + CaCO_3 \quad (1)$$

$$CaO.2Al_2O_3 + Na_2CO_3 + 2NaOH + 7H_2O = 4NaAl(OH)_4 + CaCO_3 \quad (2)$$

$$3CaO.Al_2O_3 + 3Na_2CO_3 + 12H_2O = 6NaAl(OH)_4 + 3CaCO_3 \quad (3)$$

To gain proper understanding about these slags' digestion, the leachability of CaO- and Al_2O_3-containing phases in the calcium aluminate slags produced from high purity oxides at elevated temperature is studied in this present work.

2. Experimental Procedure

The experimental procedure consisted mainly of materials preparation and characterization, leaching set up and results analysis. A procedural flow chart is presented in Figure 1.

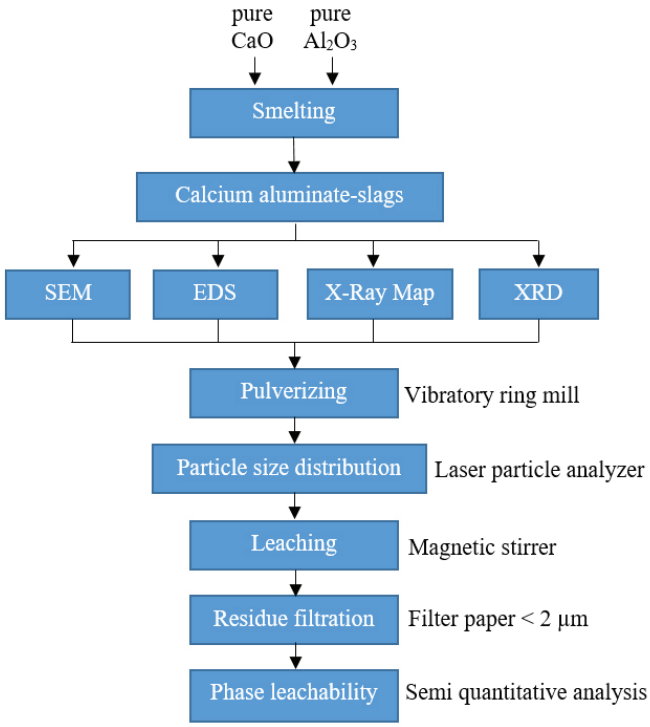

Figure 1. Flow chart of the experimental procedure.

2.1. Materials Preparation and Characterization

Two synthetic slags of $CaO–Al_2O_3$ system, named here Slag I and Slag II, were prepared by smelting the proportioned mixture of high purity CaO (96 wt.%) and Al_2O_3 (99.9 wt.%) powders inside graphite crucibles at 1650 ^oC for 1 hour by means of 75 kVA induction furnace. As can be seen in Figure 2, the target compositions of slag I and II were 33 wt.% CaO – 67 wt.% Al_2O_3 and 38 wt.% CaO – 62 wt.% Al_2O_3, respectively. The heating rate was kept slow at 15 ^oC/min up to 1000 ^oC to remove hydrates and moisture in the mixture, then 30 ^oC/min until reaching the targeted smelting temperature. The crucible was air cooled inside the furnace at 28 ^oC/min from 1650 ^oC to 1300 ^oC, and the rate decreased exponentially until it reached room temperature. A Tungsten/Rhenium alloy thermocouple with alumina insulating tube and wired with molybdenum alloy was inserted in a graphite thermo-well and fixed to the wall of the graphite crucible to measure the temperature inside of the crucible.

The crucible was crushed and the slags were collected and ground with a vibratory ring mill at 800 rpm for one minute. The size distribution was measured by laser particle analyzer, which gives 10 µm and 14 µm as the D_{50} value for slag I and II, respectively.

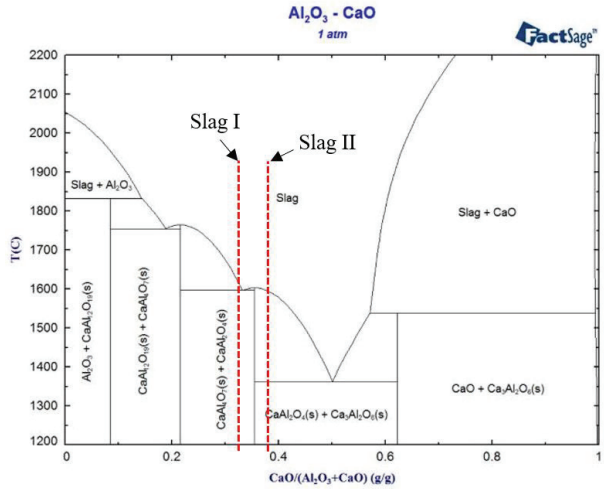

Figure 2. Target composition of slag I and slag II in $CaO–Al_2O_3$ phase diagram from FactSage database.

2.2. Leaching of Slags

The leaching experiments were done in a 50 mL glass beaker with a magnetic stirrer for agitation. The speed for the magnetic stirrer was 400 rpm. The glass beaker was partially submerged inside a water bath that was heated on top of a hot plate to minimise solution temperature variation. The solvent concentration was fixed at 120 g/L Na_2CO_3 and 7 g/L NaOH based on the literature [8, 9, 11]. To compensate for evaporation during leaching and ensure the proper reactions occurs, the amount of Na_2CO_3 used is 4 times the stoichiometry. The liquid to solid ratio is 20 and leaching temperature was 45 ^oC, 60 ^oC, and 75 ^oC with 30 minutes of holding time. The slag powder sample was added to the solvent after it reached the target temperature. After the leaching, all of the solution and remaining residue in the beaker was filtered using an ashless grade of quantitative filter paper with fine pores (< 2 µm). The residue

was washed with distilled water several times to ensure there is no alkali left, to avoid further reaction with the slag. It was then dried at 100 °C in an oven overnight, before being weighed and chemically analyzed by XRD with 5 – 75 degree diffraction angle and 0.01 degree step size.

3. Results and Discussion

3.1. Characteristics of Slags

The chemical and phase composition of slags as calculated by FactSage, Backscattered Electron (BSE) imaging, X-Ray elements map, and X-Ray Diffraction (XRD) are shown consecutively in Table 1, Figures 3 – 5.

It can be seen in Figure 3, which is confirmed by XRD results in Figure 5, that Slag I has $CaO.Al_2O_3$ (abbreviated as CA) and $CaO.2Al_2O_3$ (abbreviated as CA_2), while Slag II has CA and $3CaO.Al_2O_3$ (abbreviated as C_3A). This result agrees with the binary system of $CaO–Al_2O_3$ in literature [12, 13]. There is no $12CaO.7Al_2O_3$ observed in Slag II, as it is an unstable phase in anhydrous $CaO–Al_2O_3$ system as reported by Nurse et al. [14].

Table 1. Chemical composition of synthetic slags.

Sample name	CaO (wt.%)	Al_2O_3 (wt.%)	CA phase (wt.%)	CA_2 phase (wt.%)	C_3A phase (wt.%)
Slag I	33	67	84	16	-
Slag II	38	62	91	-	9

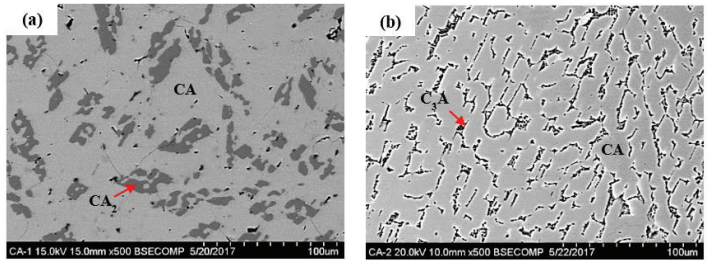

Figure 3. Backscattered electron image of two synthetic slags. (a) Slag I consists of $CaO.Al_2O_3$ (CA) and $CaO.2Al_2O_3$ (CA_2) phases. (b) Slag II consists of $CaO.Al_2O_3$ (CA) and $3CaO.Al_2O_3$ (C_3A) phases.

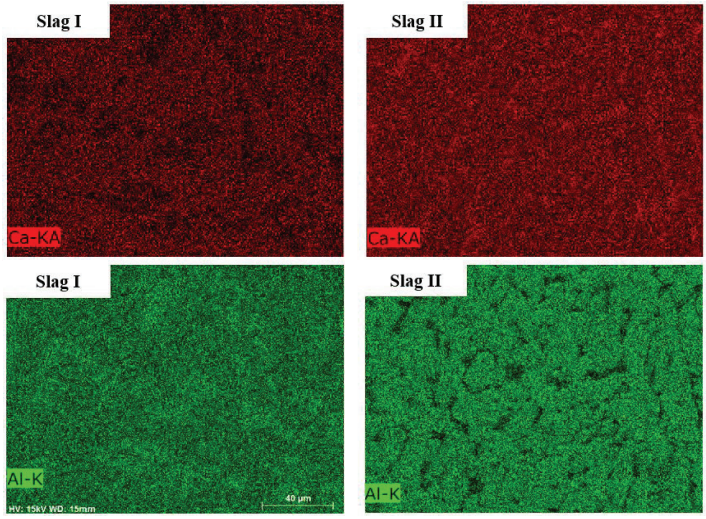

Figure 4. X-Ray element mapping of Slag I and II.

As shown in Figure 4, X-Ray element mapping of Slag I indicates that the matrix has both Calcium and Aluminum, and the secondary phase is rich in Aluminum. On the other hand, in Slag II the secondary phase is richer in Calcium than Aluminum.

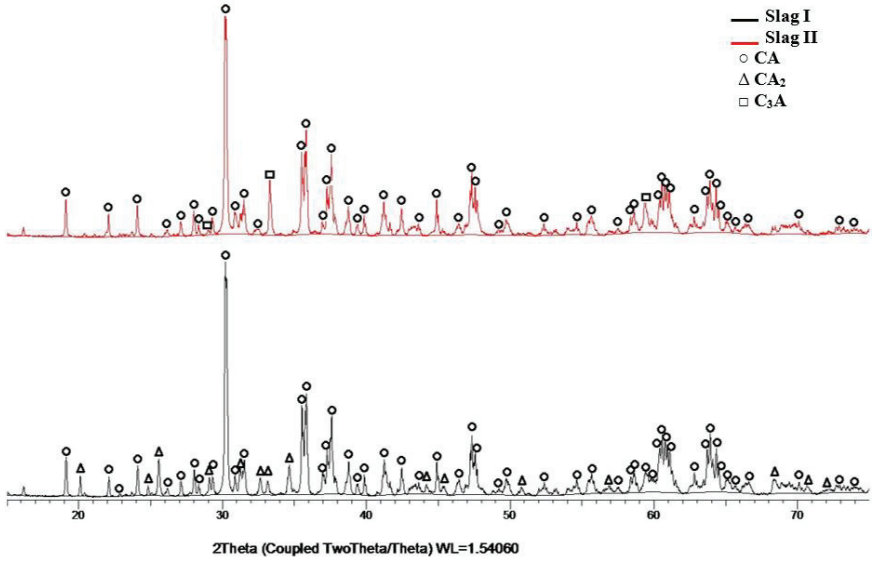

Figure 5. XRD pattern of Slag I and II.

3.2. Characterization of Leach Residue

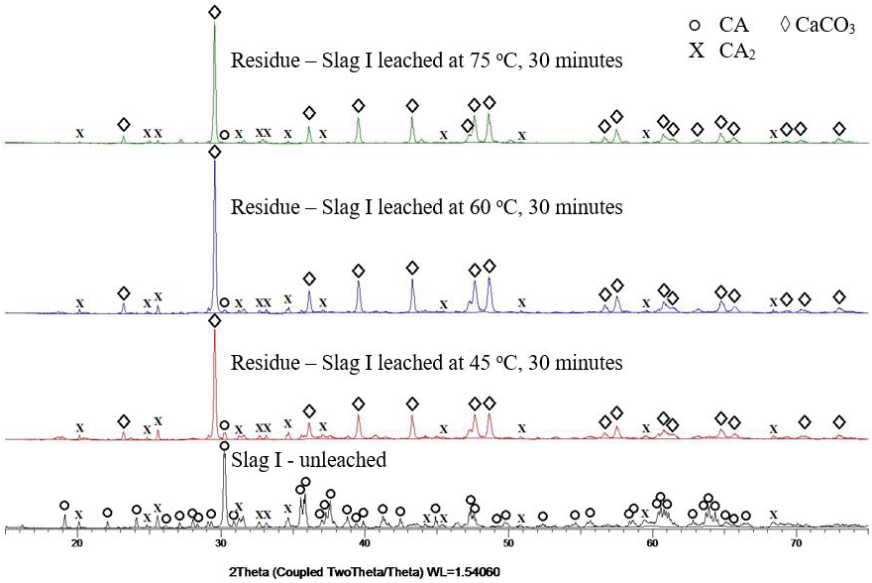

Figure 6. XRD pattern of Slag I residue after leaching at 45 °C, 60 °C, and 75 °C for 30 minutes.

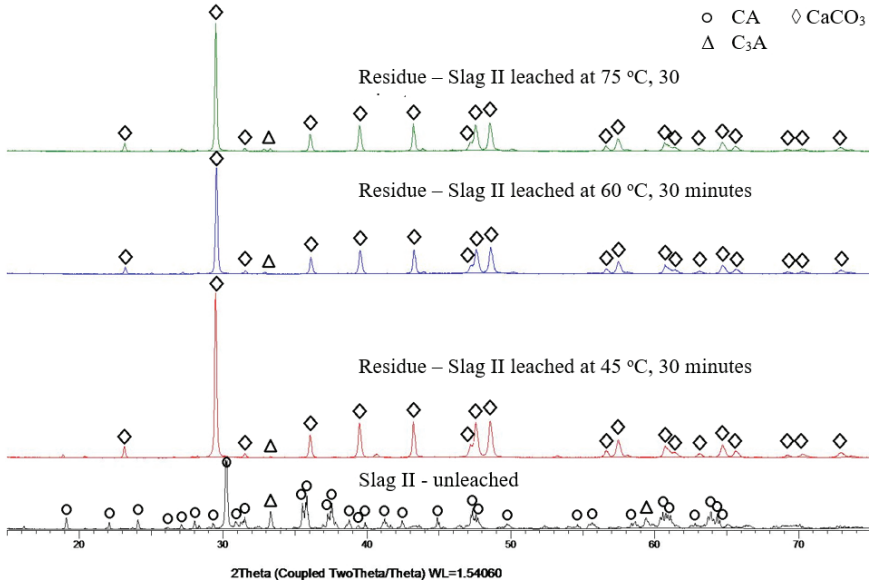

Figure 7. XRD pattern of Slag II residue after leaching at 45 °C, 60 °C, and 75 °C for 30 minutes.

After a series of leaches at different temperatures and times, the extent of CA, CA_2, and C_3A leaching was measured. Figures 6 and 7 show XRD patterns of leached Slag I and II at 45 °C,

60 °C, 75 °C after 30 minutes. It can be seen that the main phase of the residue is $CaCO_3$ and all three phases of calcium aluminate are leachable.

3.1. Effect of Temperature

The effect of temperature in digestion is significant as stated in previous studies [15 – 18]. In this work, slags are leached at relatively low temperature, i.e. 45 °C, 60 °C, and 75 °C, compared to the commercial Bayer process. Lower temperature means lower energy, which is favorable in regards to production cost in industry.

3.1.1. Leachability of CA Phase

The leaching extent of the calcium aluminate phase is calculated semi quantitatively by means of XRD analytical software then multiplied to the resulting mass of residue in the experiment. The calculation is described in Equation (4).

$$\eta_{leach} = \left(\frac{mass_{initial} - \left(wt.\%_{SQ} \times mass_{residue} \right)}{mass_{initial}} \right) \times 100\% \qquad (4)$$

where:

η_{leach}	Leachability of phase, %
$mass_{initial}$	Initial mass of phase, g
$wt.\%_{SQ}$	Semi quantitative weight fraction of phase, %
$mass_{residue}$	Mass of sample residue, g

The semi-quantitative leaching extent of the CA phase from Slag I and II can be seen in Figure 8. The leachability of CA in Slag I markedly increases from 79.2 %, 89.9 %, to 98.2 % by increasing the temperature from 45 °C, 60 °C, to 75 °C, respectively. While in Slag II, the leaching rate is quite stable at 94.5 % and 95.3 % at 45 °C and 60 °C respectively, increasing to 97 % at 75 °C. As observed here and mentioned in the literature [3, 20, 22, 23], CA is a soluble phase in sodium carbonate solutions. It is found here that CA_2 as the other phase present in Slag I hinders the leachability of CA. Further discussion on this observation, as well as CA_2 leachability is in section 3.1.2.

In principle, the leaching rate is associated with the reaction kinetics and their activation energies. The higher the activation energy of a reaction, the more sensitive the reaction to the temperature, and likely to be chemical rate controlling. It is worth noting that Abdel-Aal [15], Pereira et al. [16], and Yang et al. [17] showed that gibbsitic alumina digestion is chemical rate controlled. Until recently, Tong and Li [18] reported that calcium aluminate digestion is diffusion controlled, and temperature has less effect. It is obvious the different conclusions resulted from different composition and phases of alumina, experimental condition, etc. By using HSC 7.1 software, the change of enthalpy (ΔH) during digestion in different calcium aluminate phases can be calculated as shown in Figure 9.

The digestion of all three phases existing in the slags are through exothermic reactions. The order of energy release during reaction from the highest to the lowest is C_3A, CA_2, and CA. In other words, at a given leaching temperature, Slag I has two leachable phases that could accumulatively give more energy to the system than Slag II could have. However, since the CA_2 phase has low leachability, either advantageous or disadvantageous effects on the kinetic leaching rate is not clearly confirmed.

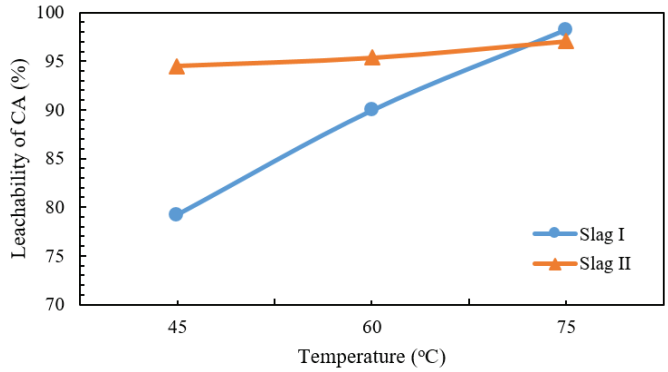

Figure 8. Leachability of CA phase on Slag I and Slag II at 45 °C, 60 °C, and 75 °C in 30 minutes.

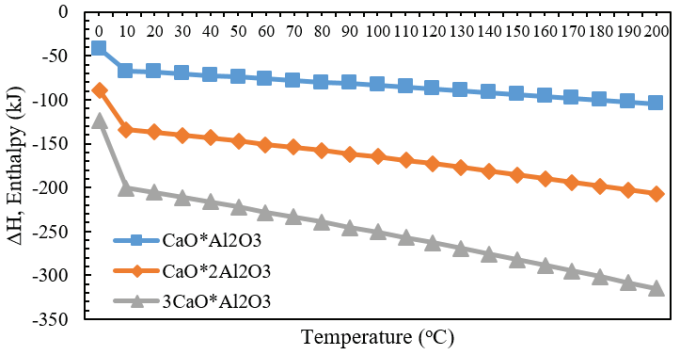

Figure 9. Change of enthalpy in digestion for different calcium aluminate phases.

3.1.2. Leachability of CA_2 Phase

As can be seen in Figure 10, the leachability of the CA_2 phase in Slag I after 30 minutes is 6.2 %, 15 %, and 69 % at 45 °C, 60 °C, and 75 °C , respectively. Below 45 °C, the CA_2 phase is practically insoluble. However, this leaching behavior is similar to that of the CA phase in Slag I (see Figure 8). Therefore, the hinder effect of CA_2 phase to CA leachability is apparent.

According to Equation (2), the leaching reaction of 1 mol of this phase needs 2 mol NaOH. In this work, the solvent concentration is fixed and sodium hydroxide concentration is relatively low; 2 times higher than the stoichiometry. However, this phase cannot be leached in a pure solution of sodium hydroxide due to CaO in the reduction slag reacting with NaOH to form $Ca(OH)_2$ which is followed by a reaction with $NaAl(OH)_4$ to form tricalcium hydro-aluminate ($3CaO.Al_2O_3.6H_2O$). This phenomenon gives lower yield to the alumina production, as reported by Wang et al. [19]. Therefore, it is of importance to ensure an adequate concentration of NaOH and Na_2CO_3 in the solvent to leach CA_2.

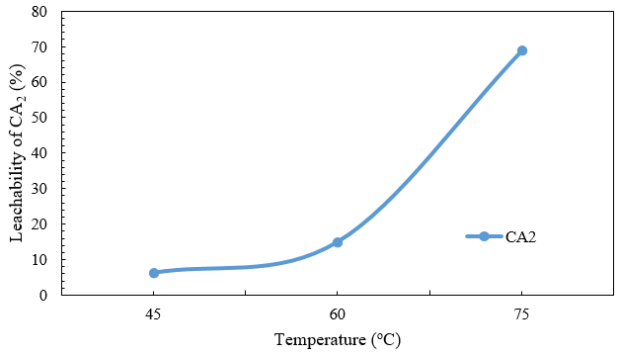

Figure 10. Leachability of CA_2 phase at 45 °C, 60 °C, and 75 °C after 30 minutes.

3.1.3. Leachability of C_3A Phase

It has been reported that the C_3A phase is difficult to leach and less than 50 % soluble in a 5 % solution of Na_2CO_3 [20, 21]. The present experimental results in Figure 11 show that the leachability of the C_3A phase at 45 °C, 60 °C, and 75 °C after 30 minutes of holding time are 46.7 %, 58.4 %, and 65 %, respectively. This indicates that the leachability of C_3A phase is higher than CA_2 at same given conditions.

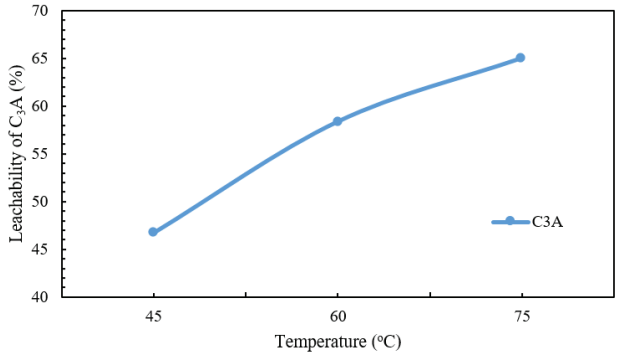

Figure 11. Leachability of C_3A phase in Slag II at 45 °C, 60 °C, and 75 °C after 30 minutes.

3.2. Effect of Leaching Duration

The leachability of CA and CA_2 phases in Slag I at different leaching times are shown in Figure 12. Consecutively, the CA leaching rate is 77.8 %, 79.2 %, and 95.4 % at 15, 30, and 60 minutes. While the CA_2 phase is leached to the extent of 0.2 %, 6.2 %, and 10.4 %.

It is worth noting that for the CA phase, leaching at 45 °C for 60 minutes could give a similar leaching rate as at 75 °C for 30 minutes. While for the CA_2 phase, the duration of leaching does not change dramatically the extent of leaching.

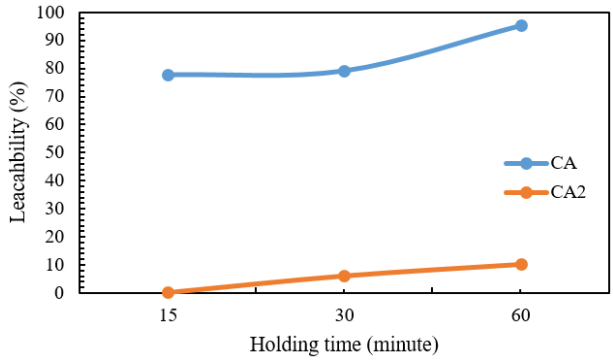

Figure 12. Extent of Leaching of CA and CA_2 phases in Slag I at 45 °C at different holding times.

4. Conclusions

Synthetic high purity calcium aluminate slags were prepared, pulverized, and subsequently leached by solutions containing Na_2CO_3 and NaOH at different temperatures and durations. The main results regarding the leachability of the slags can be summarized as:

1. Increased temperature significantly enhances the leachability. Moreover, the effect of temperature is dependent on the type and amount of phases in the slags.

2. The rate of leaching is fast and significant digestion occurs within relatively short reaction times. However, the extent of leaching in a given duration is dependent on the slag type.

3. In binary calcium aluminate slags, the leachability of one phase affects the leaching behavior of the other ones. The leachability of the $CaO.Al_2O_3$ phase in Slag I is hindered by the presence of the less leachable $CaO.2Al_2O_3$ phase.

4. The leachability of studied calcium aluminate phases in binary slags from highest to the lowest is $CaO.Al_2O_3$, $3CaO.Al_2O_3$ and $CaO.2Al_2O_3$.

Acknowledgement

The present research has been funded by NTNU and Research Domain 5–Materials and Society in SFI Metal Production (a Norwegian Centre for Research-driven Innovation in metal production).

References

1. Peter Smith, The processing of high silica bauxites – review of existing and potential processes, *Hydrometallurgy*, 2009, 162-176.
2. M. Jiayu, L. Zhibao, and X. Qinggui, A new process for Al_2O_3 production from low-grade diasporic bauxite based on reactive silica dissolution and stabilization in NaOH-$NaAl(OH)_4$ media, *American Institute of Chemical Engineers*, 2012, Vol. 58, No. 7, 2180-2191.
3. H.E. Blake Jr. et al., Adaptation of the Pedersen process to the ferruginous bauxites of the pacific northwest, *US Bureau of Mines Report Investigations*, No. 6939, 1968, 1-24.

4. Jafar Safarian and Leiv Kolbeinsen, Smelting-reduction of bauxite for sustainable alumina production, *Sustainable Industrial Processing Summit*, 2016, 1-8.
5. H. Sellæg, L. Kolbeinsen, and J. Safarian, Iron separation from bauxite through smelting-reduction process, *Light Metals* 2017, 127-135.
6. H. Pedersen, Process of manufacturing aluminum hydroxide, *US Patent Office*, No. 1618105, 1927.
7. R.V. Lundquist and H. Leitch, Aluminium extraction characteristics of three calcium aluminates in water, sodium hydroxide, and sodium carbonate solutions, *US Bureau of Mines Report Investigations*, Nevada, 1964, 1-16.
8. Z. Tong, Y. Li, L. Lian, Influence of titania on phase composition and self-powder and alumina leaching properties of calcium aluminate slag, *Light Metals* 2012, 185-188.
9. Wang et al., Effect of calcium/aluminium ratio on MgO containing calcium aluminate slags, *Light Metals* 2011, 201-204.
10. Wang et al., Synergistic effect of $C_{12}A_7$ and CA on alumina leaching property under low calcium/aluminum ratio, *Light Metals* 2015, 59-62.
11. Wang et al., Effect of Na_2O on alumina leaching property and phase transformation of MgO-containing calcium aluminate slags, *Transactions of Nonferrous Metals Society of China*, 2011, 2752-2757.
12. D.A. Jerebtsov and G.G. Mikhailov, Phase diagram of $CaO\text{-}Al_2O_3$ system, *Ceramics International*, 2001, 25-28.
13. Bengt Hallstedt, Assessment of the $CaO\text{-}Al_2O_3$ system, *Journal of the American Ceramic Society*, 1990, 15-23.
14. R.W. Nurse, J.H. Welch, and A.J. Majumdar, The $12CaO.7Al_2O_3$ phase in the CaO - Al_2O_3 system, *Transactions of the British Ceramic Society*, Vol. 64, 1965.
15. E.S.A. Abdel-Aal, Leaching kinetics of gibbsitic bauxite with sodium hydroxide, *E3S Web of Conferences* 8, 2016.
16. Pereira et al., The kinetics of gibbsite dissolution in NaOH, *Hydrometallurgy*, 2008.
17. Yang et al., Dissolution kinetics and mechanism of gibbsitic bauxite and pure gibbsite in sodium hydroxide solution under atmospheric pressure, *Transactions of Nonferrous Metals Society of China*, 2015.
18. Z. Tong and Y. Li, Leaching behavior of alumina from smelting reduction calcium aluminate slag with sodium carbonate solution, TMS, *Light Metals*, 2017.
19. Wang et al., Study on extracting aluminum hydroxide from reduction slag of magnesium smelting by vacuum aluminothermic reduction, *Light Metals* 2011, 205-209.
20. O.C. Fursman, H.E. Blake Jr., J.E. Mauser, Recovery of alumina and iron from pacific northwest bauxites by the Pedersen process, *US Bureau of Mines Report Investigations*, No. 7079, 1968, 1-22.
21. Wang et al., The effect of cooling rate on the leachability of calcium aluminate slags, *Light Metals* 2011, 241-244.
22. Jan Miller and Aake Irgens, Alumina production by the Pedersen process – history and future, *Light Metals* 1974, 977-982.
23. Jafar Safarian and Leiv Kolbeinsen, Sustainability in alumina production from bauxite, *Sustainable Industrial Processing Summit*, 2016.

Paper 4

Hydrometallurgy 185 (2019) 273–290

Contents lists available at ScienceDirect

Hydrometallurgy

journal homepage: www.elsevier.com/locate/hydromet

Leaching characteristics and mechanism of the synthetic calcium-aluminate slags for alumina recovery

Fabian Imanasa Azof[a,*], Yongxiang Yang[a,b], Dimitrios Panias[c], Leiv Kolbeinsen[a], Jafar Safarian[a]

[a] Department of Materials Science and Engineering, Norwegian University of Science and Technology (NTNU), Trondheim, Norway
[b] Department of Materials Science and Engineering, Delft University of Technology, Delft, the Netherlands
[c] School of Mining and Metallurgical Engineering, National Technical University of Athens (NTUA), Athens, Greece

ARTICLE INFO

Keywords:
Leaching characteristics
Leaching mechanism
Calcium-aluminate slags
Alumina
$CaO\text{-}Al_2O_3$ system

ABSTRACT

The leaching characteristics and mechanism of synthetic $CaO\text{-}Al_2O_3$ slags in alkaline solution at atmospheric pressure have been studied. The purpose of the study is to have a better understanding of the leaching part of the Pedersen process, as an alternative to the Bayer process for alumina production. The crystalline slags containing $CaAl_2O_4$, $Ca_3Al_2O_6$, $CaAl_4O_7$, and $Ca_{12}Al_{14}O_{33}$ phases, and leaching residues (predominantly $CaCO_3$) are characterized by X-ray Diffraction and semi-quantitative analysis. Of the leaching characteristics in a solution containing 120 g/L Na_2CO_3, the slag with the highest amount of $Ca_{12}Al_{14}O_{33}$ phase is the most leachable one in the $CaO\text{-}Al_2O_3$ system with about 95% of alumina extraction. The leaching extent is confirmed employing Inductively Coupled Plasma-High Resolution-Mass Spectrometer (ICP-HR-MS) analysis, and it decreases by 0.4% for every percent of the bayerite ($Al(OH)_3$) formation during the leaching. The less stable form of $CaCO_3$, i.e., vaterite, is formed over the leached slag particles that consist 33–49 wt% CaO, while $Ca_3Al_2(OH)_{12}$ (tricalcium alumina hydrate) precipitated at relatively low concentrations (< 6 wt%) in all residue. The non-bridging oxygen (NBO) over tetrahedral structure (T) index shows that the atomic structure may affect the leaching extent of the slags, the lower NBO/T index of the phase is the more difficult for the phase to leach or depolymerize. However, the $Ca_{12}Al_{14}O_{33}$ phase is an exception case where it has "free" O-ions at the center of the cage structure, which makes it easily depolymerize, therefore, the NBO/T index for the $Ca_{12}Al_{14}O_{33}$ phase becomes irrelevant. Furthermore, the morphology and size evolution of the obtained residue measured with laser particle analyzer indicates the agglomeration behavior of the residue particles during the leaching process.

1. Introduction

In alumina production by the Bayer process, the digestion of bauxite is one of the most energy consuming steps compared to the other parts (Gu et al., 2007; Mach, 2012). The digestion effectiveness of bauxite in this process mainly depends on its mineralogy (e.g., gibbsite, boehmite, or diaspore) knowing that different Al_2O_3-containing minerals require different digestion conditions (Meyer, 2004). Monohydrates (γ-AlOOH and α-AlOOH) are less reactive than the trihydrates (γ-$Al(OH)_3$), which needs a higher temperature and alkali concentration for their digestion (Alex et al., 2013). Nevertheless, all three minerals need considerably high pressure and temperature to yield the metallurgical grade of alumina. It is also known that the pre-desilication process at elevated temperature (Smith, 2009) and the bauxite residue (red mud) of this process have severe problems with the environment (Azof et al., 2018a; Safarian, 2018; Safarian and Kolbeinsen, 2016a, 2016b; Sellaeg et al., 2017), which need attentive regulation concerning its disposal and storage (Dentoni et al., 2014; World Aluminum, 2015).

Harald Pedersen (1927) had proven that it is viable to yield alumina at low pressure and temperature-leaching of calcium-aluminate slags that is produced from smelting-reduction of bauxite. The process does not produce red mud as the iron oxides of the bauxite is 99.9% reduced during the smelting (Azof et al., 2018b). Furthermore, the CO_2 gas produced from the smelting-reduction process can be utilized in its later process (precipitation), and the sodium carbonate used in the leaching treatment could be recovered from the leachate during the precipitation (see Fig. 1). Therefore, the Pedersen process can be a good alternative for alumina recovery with lower environmental impact than the Bayer process.

Some studies concerning the leachability of calcium aluminate

* Corresponding author at: Department of Materials Science and Engineering, Norwegian University of Science and Technology (NTNU), Bergbygget E-133, Trondheim N-7491, Norway.
E-mail addresses: fabian.i.azof@ntnu.no (F.I. Azof), y.yang@tudelft.nl (Y. Yang), panias@metal.ntua.gr (D. Panias), leiv.kolbeinsen@ntnu.no (L. Kolbeinsen), jafar.safarian@ntnu.no (J. Safarian).

https://doi.org/10.1016/j.hydromet.2019.03.006
Received 30 November 2018; Received in revised form 10 March 2019; Accepted 17 March 2019
Available online 19 March 2019

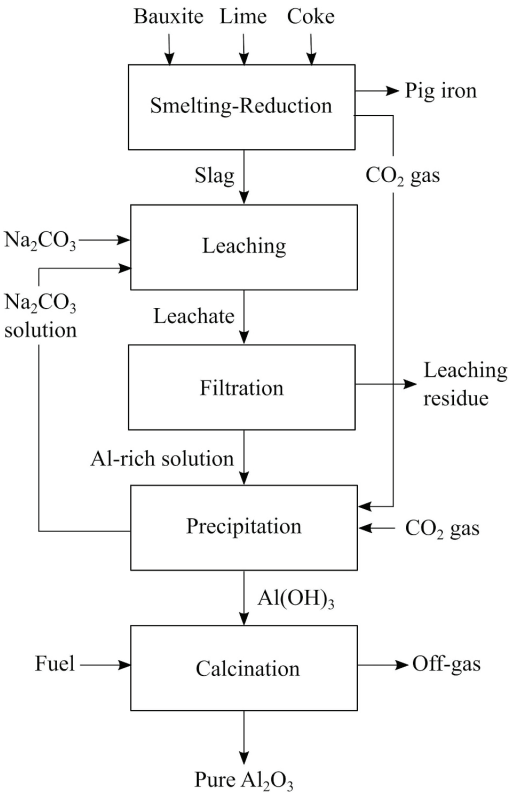

Fig. 1. Simplified flowsheet for material flow in the Pedersen Process.

phases in a $CaO-Al_2O_3$ binary system have been done in the past. Lundquist and Leitch (1963a), Lundquist and Leitch, 1963b, Lundquist and Leitch, 1964) studied the alumina leachability of $CaAl_2O_4$ (CA), $Ca_{12}Al_{14}O_{33}$ ($C_{12}A_7$) and $Ca_3Al_2O_6$ (C_3A) phases that was produced from the lime-soda sinter process in different solutions. According to their work, the alumina leaching extent up to 100% for CA phase was attained in a mixed NaOH + Na_2CO_3 solution containing 45 g/L Na_2O at 70 °C for 24 h, while $C_{12}A_7$ was optimally leached up to 100% in a solution containing 43–85 g/L Na_2CO_3 at 50–70 °C for 24 h. It is obvious that the leaching duration is depending on the amount of the reacted slags. Bo et al. (2015) showed the synergistic effect of $C_{12}A_7$ and CA mixtures on alumina leaching property, and Sun et al. (2014) investigated the leachability of $C_{12}A_7$ phase in NaOH and Na_2CO_3-containing solution (7 g/L and 120 g/L, respectively) at 75 °C for 30 min where the phase was synthesized at different holding time. In our previous study (Azof et al., 2017), we showed the effect of leaching temperature and duration on the leaching extent of three calcium aluminate phases: CA_2, CA, and C_3A. Also, it is shown that the less leachable calcium aluminate phase may affect the leachability of other phases, with the leachability order from high to the low order being CA, C_3A, and CA_2 phase.

Based on the literature, the $C_{12}A_7$ phase is known as one of the leachable phases in the $CaO-Al_2O_3$ system. This phase was reported as a metastable phase (Imlach et al., 1971; Nurse et al., 1965a, 1965b). Haccuria et al. (2016) claimed that the metastable $C_{12}A_7$ phase formation is not formed in a $CaO-Al_2O_3$ system under a dry-inert (99.999%Ar) atmosphere. However, the researchers who investigated the leachability of this phase have not mentioned about its instability (Blake et al., 1966; Bo et al., 2014; Bo et al., 2011; Fursman and Mauser, 1968; Sun et al., 2010; Yu et al., 2012; Zhang et al., 2016; Zhou et al., 2013). It is worth noting that these researchers could attain a stable $C_{12}A_7$ phase from lime-soda sintering or smelting-reduction process.

In the Pedersen leaching process, soluble calcium aluminate phases are imperative for successful alumina extraction with high yield. However, comprehensive information on the leaching behavior of synthetic calcium aluminate slags in caustic solution with different conditions, i.e., concentration, solution, temperature, leaching duration, have not been reported as the process was alive many years ago (1928–1969) and there were confidentiality concerns. Therefore, these have motivated us to study the stability of $C_{12}A_7$ and other calcium aluminate phases produced from $CaO-Al_2O_3$ slags, and their leaching behavior at specific conditions for alumina recovery.

2. Experimental procedure

The experimental studies were divided into (1) slag composition selection, (2) smelting and slag making, (3) leaching of the slags, and (4) characterization of the leaching products. They are described in details in the following.

2.1. Slag composition selection and preparation

In FactSage™ pure substances (FactPS) database of the $CaO-Al_2O_3$ system, the available condensed phases at room temperature and 1 atm are CaO, C_3A, CA, CA_2, $CaAl_{12}O_{19}$ (CA_6), and Al_2O_3. Whereas, $C_{12}A_7$ does not exist in the database, which is likely because of its metastable behavior as mentioned previously in section 1. However, as we want to assess the leachability of several calcium-aluminate phases in the $CaO-Al_2O_3$ system, including $C_{12}A_7$, we should have a phase diagram which includes this phase. By using the FactSage™ FactPS database and an additional thermochemistry data of $C_{12}A_7$ after Hallstedt (1990) we established a phase diagram of the $CaO-Al_2O_3$ system that includes $C_{12}A_7$ phase as seen in Fig. 2. Moreover, five different compositions of the slags were chosen in the range of 33–60 wt%CaO.

Pure CaO and $\alpha-Al_2O_3$ powders were used to make a mass of 50 g mixture thoroughly inside a mixing-jar with ceramic balls for each of the targeted slag composition, which is shown in Table 1. These slag compositions were chosen to produce different amounts of various calcium-aluminate phases in each slag, which are also given in Table 1, as calculated using the phase diagram of Fig. 2.

2.2. Slag production

The mixtures of powders were poured into graphite crucibles with about 30 mm and 50 mm of inner diameter and height. These crucibles were then put into a larger graphite crucible as illustrated schematically in Fig. 3, and it was put in an open 75-kVA induction furnace and heated slowly at the rate of 30 °C/min until it reached 1650 °C. The smelting duration was 30 min at this temperature and subsequently the furnace power was turned off, while the crucible was kept in the furnace to solidify and cool down the slags slowly to the room temperature. This was done in exposure to air, the cooling rate from 1650 to 1300 °C was about 34–37 °C/min. The thermocouple used in this study was tungsten/rhenium (C-type) which was encapsulated by alumina and graphite insulation tubes.

The obtained slags were pulverized employing vibratory ring mill Retsch RS-200 at 800 rpm for one minute. Size of the particles was then measured using laser particle analyzer Horiba LA-960 in a wet analysis (isopropanol with refractive index 1.378) based on volume distribution. Before the laser measurement, an ultrasound vibration was run 4 ± 1 min.

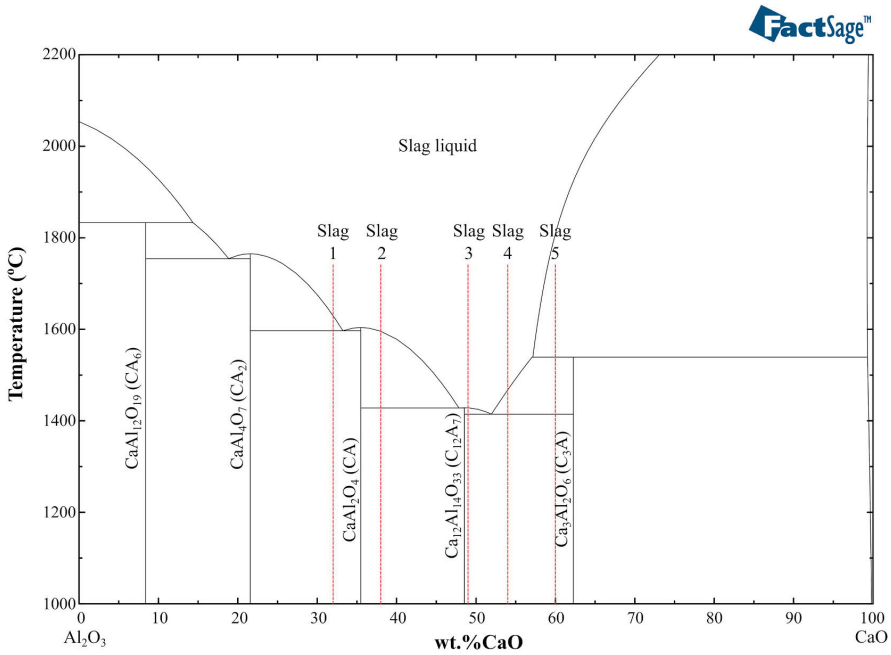

Fig. 2. Phase diagram of the CaO-Al_2O_3 system as constructed in FactSage™ for this study.

Table 1
Compositions of the slags and the estimated co-existing phases.

Sample name	Raw material ratio		Phase in equilibrium (based on phase lever-rule)
	CaO (wt %)	Al_2O_3 (wt %)	
Slag 1	33	67	82.2 wt%CA and 17.8 wt%CA_2
Slag 2	38	62	80.7 wt%CA and 19.3 wt%$C_{12}A_7$
Slag 3	49	51	96.6 wt%$C_{12}A_7$ and 3.4 wt%C_3A
Slag 4	54	46	60.2 wt%$C_{12}A_7$ and 39.8 wt%C_3A
Slag 5	60	40	83.5 wt%C_3A and 16.5 wt%$C_{12}A_7$

2.3. Leaching of the slag

A mass of 1 ± 0.05 g of slag for each of leaching experiments with 20 mL/g of liquid to solid ratio (L/S) was used. Pedersen (1927) stated that the alumina recovery from slags containing calcium aluminate phases could proceed in either sodium carbonate or sodium hydroxide solution as in the Bayer process. In the current study, two different solutions, which are Na_2CO_3 and Na_2CO_3 + NaOH, were used to observe the leaching mechanism and the alumina extraction extent in determined conditions. Our previous study in the leachability of CA and CA_2 phase (Azof et al., 2017) indicated a satisfactory alumina recovery of > 90% for CA phase. Therefore, we used the same parameters for the present study: 120 g/L of Na_2CO_3 and 7 g/L of NaOH for the leaching solutions, 45–75 °C for the leaching temperature, 10–120 min for the leaching duration, and 400 rpm for the stirring magnetic speed. The leaching experiment was performed inside an open beaker glass, which was heated on top of a hot plate as seen schematically in Fig. 4. The loss of solution due to the evaporation was neglected, and in order to minimize the loss, we contained the top of the beaker by using a plastic paraffin film. At the end of leaching, the leachate and the residue were filtered by an ashless grade of quantitative filter paper. The pregnant liquid solution (PLS) was stored in a vial, whereas, the residue was stored in a dryer at 100 °C for an overnight to remove the contained moisture.

2.4. Characterization of the slags and products

High-resolution imaging, Energy Dispersive Spectroscopy (EDS) analysis, and X-ray element mapping of slags and leaching residues were undertaken by using Hitachi SU6600™ Scanning Electron Microscope (SEM). Large slag particles were mounted by epoxy, polished, and carbon coated for SEM study, whereas slags powders were put on a particular carbon substrate for a morphology observation using the same SEM. Phase identification of the slags and residues were done by a Bruker D8 A25 DaVinci™ X-ray Diffraction (XRD) machine with CuKα radiation, between 10 and 75° diffraction angle, 0.01° step size, and 2.5° for both primary and secondary soller slit. The identification and quantitative phase analysis of the obtained XRD peaks were done by using DIFFRAC.EVA v.3 and TOPAS v.5 software based on the Rietveld method, respectively. Chipera and Bish (2013) claimed that the method is suitable for a quantitative phase analysis (QPA) as this method relies on the assumption that all phases in the sample are crystalline, which is relevant in the current study as later seen in the XRD results, where the slags do not contain amorphous phase. Literature (Guirado et al., 2000) showed that a QPA performed by Rietveld method in aluminous cement was somewhat in agreement with those performed by X-ray Fluorescence (XRF). Also, Inductively Coupled Plasma-High Resolution-Mass Spectrometer (ICP-HR-MS) Agilent 8800™ was used to analyze the compositions of the PLS.

3. Theoretical evaluation

In order to obtain a proper understanding of the leaching property of the slags and the effect of the reactions to the pH changes, we need to elaborate the leaching thermochemistry, and both pH and aluminum extraction yield calculations.

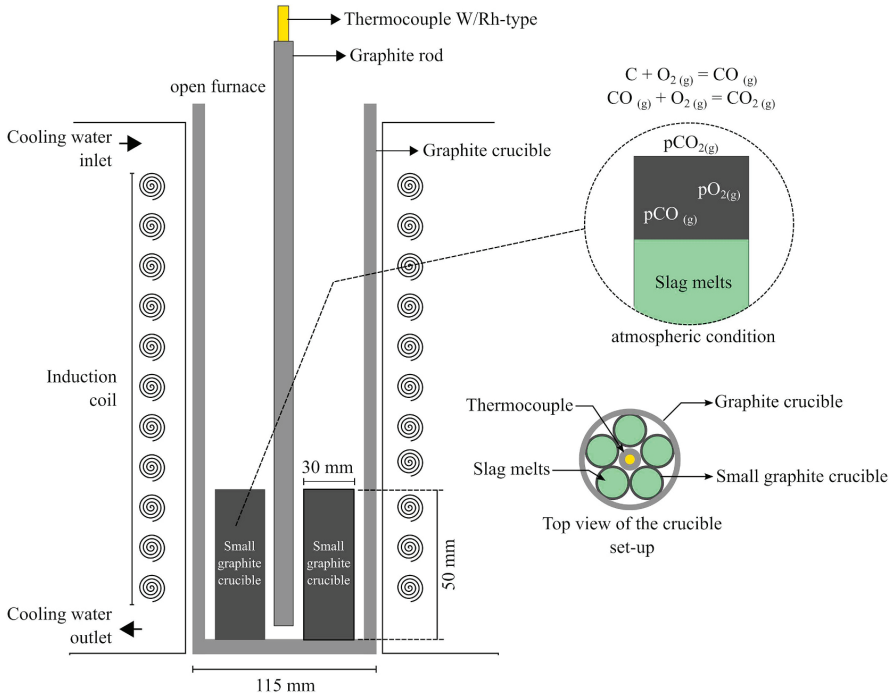

Fig. 3. A schematic of the slag making setup in induction furnace.

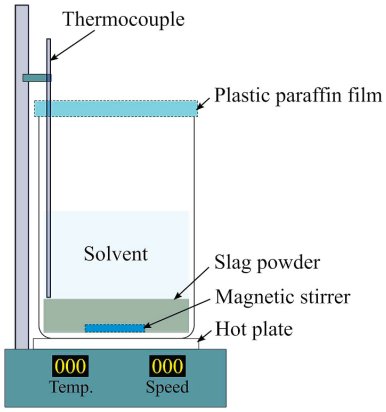

Fig. 4. A schematic of the leaching setup.

3.1. Leaching reactions

The leaching reactions between CA, CA_2, C_3A, and $C_{12}A_7$ phases and sodium carbonate solution can be written as shown in reactions (1)–(4), respectively (Azof et al., 2017; Blake et al., 1966). The Gibbs energy of reactions at 25 °C is calculated by using HSC Chemistry™, a thermodynamic software.

$$CaAl_2O_{4\,(s)} + Na_2CO_{3\,(aq)} = 2NaAlO_{2\,(aq)} + CaCO_{3\,(s)} \quad (1)$$

$$\Delta G^{\circ}{}_{25°C} = -58.2 \text{ kJ/mol } CaAl_2O_4.$$

$$CaAl_4O_{7\,(s)} + Na_2CO_{3\,(aq)} + 2NaOH_{(aq)} + 7H_2O_{(l)} = 4NaAl(OH)_{4\,(aq)} + CaCO_{3\,(s)} \quad (2)$$

$$\Delta G^{\circ}{}_{25°C} = -51.0 \text{ kJ/mol } CaAl_4O_7$$

$$Ca_3Al_2O_{6\,(s)} + 3Na_2CO_{3\,(aq)} + 2H_2O_{(l)} = 2NaAlO_{2\,(aq)} + 3CaCO_{3\,(s)} + 4NaOH_{(aq)} \quad (3)$$

$$\Delta G^{\circ}{}_{25°C} = -199.1 \text{ kJ/mol } Ca_3Al_2O_6$$

$$Ca_{12}Al_{14}O_{33\,(s)} + 12Na_2CO_{3\,(aq)} + 5H_2O_{(l)} = 14NaAlO_{2\,(aq)} + 12CaCO_{3\,(s)} + 10NaOH_{(aq)} \quad (4)$$

$$\Delta G^{\circ}{}_{25°C} = -745.2 \text{ kJ/mol } Ca_{12}Al_{14}O_{33}$$

As seen above, CA, C_3A, and $C_{12}A_7$ phase can be leached in a solution containing Na_2CO_3. The product of the reactions contains:

(1) Sodium aluminate in hydrated ($NaAl(OH)_4$) or un-hydrated ($NaAlO_2$) aqueous phase,
(2) NaOH $_{(aq)}$ such as in reactions (3) and (4), and.
(3) $CaCO_3$-containing residue (simply named as residue)

In reaction (2), to leach one mole of the CA_2 phase, we need one mole of $Na_2CO_{3\,(aq)}$ and two moles of NaOH $_{(aq)}$, while other calcium aluminates need no addition of NaOH $_{(aq)}$ in their leaching reactions. In Fig. 5, we can see the equilibrium amount of thermodynamic reaction (2) at temperature 25–100 °C in 1 atm as calculated using HSC Chemistry™ in Equilibrium Compositions module. The modeling is based on the Pitzer (1973) theory on calculating the activity coefficient of electrolytes. The input amount and output species that correspond to Fig. 5 is shown in Table 2. The input species and the amount used in the calculation are chosen as an attempt to indicate the experimental

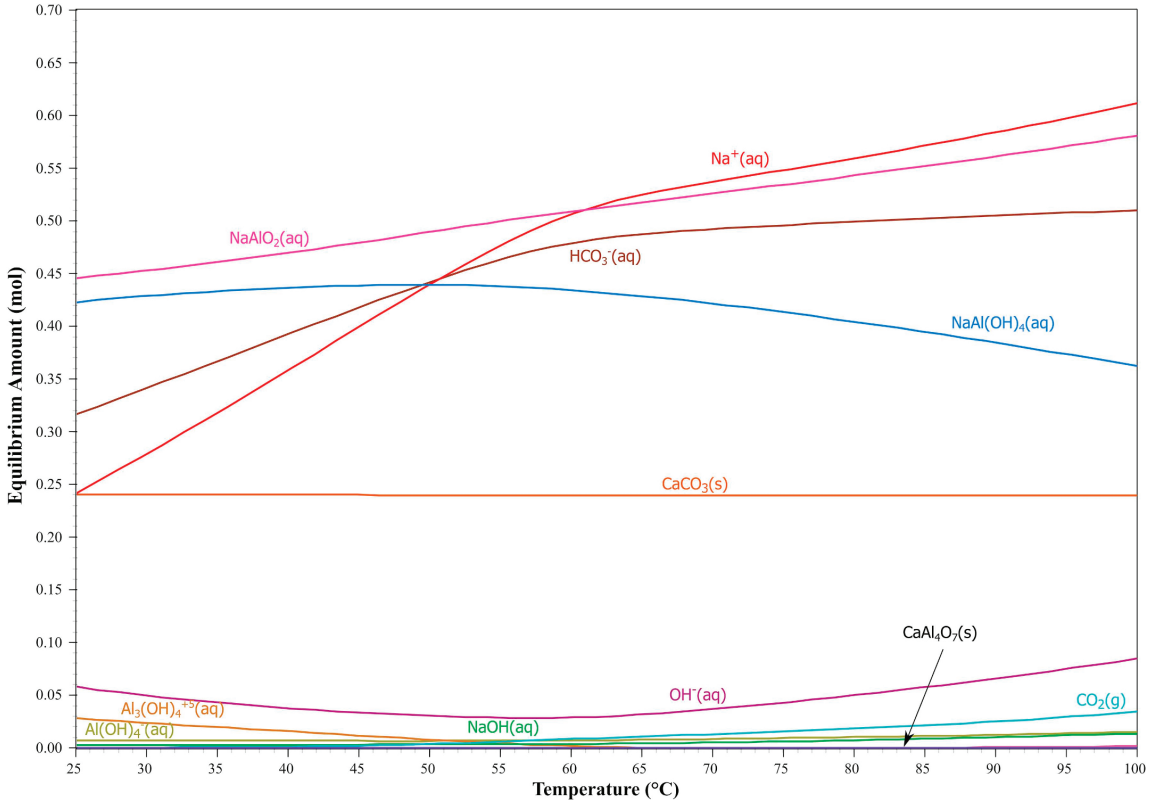

Fig. 5. The equilibrium amount of the leaching reaction of CA_2 phase at a temperature range of 25–100 °C.

Table 2
Input amount and output species that are used in the equilibrium calculation.

Input species	Phase	Mass (g)	Mass (mol)
H_2O	Liquid	1000	55.51
$CaAl_4O_7$	Solid	50	0.24
Na_2CO_3	Aqueous	120	1.13
OH^-	Aqueous	1.7×10^{-2}	1×10^{-3}
H^+	Aqueous	1×10^{-3}	1×10^{-3}
O_2	Gas	3.2×10^{-4}	1×10^{-5}
Output species			
$Al(OH)_{2(aq)}^+$	$Ca(OH)_{2(s)}$	$CH_2O_{2(g)}^+$	$NaOH_{(aq)}$
$Al(OH)_{3(aq)}$	$Ca_{(aq)}^{+2}$	$CH_2OH_{(g)}^+$	$NaAl(OH)_{4\ (aq)}$
$Al(OH)_{4(aq)}^-$	$Ca_3Al_2O_{6(s)}$	$CH_2OO_{(g)}^-$	$O_{2(aq)}^-$
$Al_{13}O_4(OH)_{24(aq)}^{+7}$	$CaAl_{12}O_{19(s)}$	$CH_3COO_{(aq)}^-$	$O_{2(g)}$
$Al_2(OH)_{2(aq)}^{+4}$	$CaAl_2O_{4(aq)}$	$CH_3O_{(g)}^-$	$O_{2(g)}^-$
$Al_2O_{(g)}^+$	$CaAl_2O_{4(s)}$	$CH_3O_{2(g)}^-$	$OH_{(aq)}^-$
$Al_2O_{2(g)}^+$	$CaAl_4O_{7(s)}$	$CH_3O_{2(g)}^+$	$OH_{(aq)}^-$
$Al_3(OH)_{4(aq)}^{+5}$	$CaC_2H_3O_{2(aq)}^+$	$CH_3OH_{(g)}^+$	$OH_{(g)}^-$
$AlO_{(g)}^-$	$CaC_2H_3O_{3(aq)}^+$	$CHO_{(g)}^+$	$OH_{(g)}^+$
$AlO_{(aq)}^+$	$CaCHO_{2(aq)}^+$	$CO_{(aq)}$	$H_2O_{(l)}$
$AlO_{(g)}^+$	$CaCO_{3(aq)}$	$CO_{(g)}$	$12CaO{\cdot}7Al_2O_{3(s)}$
$AlO_{2(g)}^-$	$CaCO_{3(s)}$	$CO_{2(aq)}$	$2CaO{\cdot}Al_2O_{3(s)}$
$AlOH_{(g)}^-$	$CaHCO_{3(aq)}^+$	$CO_{2(g)}$	$3CaO{\cdot}Al_2O_{3(s)}$
$AlOH_{(g)}^+$	$CaO{\cdot}2Al_2O_{3(s)}$	$H_{(aq)}^+$	$3CaO{\cdot}Al_2O_3{\cdot}10.2H_2O_{(s)}$
$AlOH_{(aq)}^{+2}$	$CaO{\cdot}Al_2O_{3(s)}$	$HC_2O4_{(aq)}^-$	$3CaO{\cdot}Al_2O_3{\cdot}11.6H_2O_{(s)}$
$C_2H_3O_{(g)}^+$	$CaOH_{(aq)}^+$	$HCO_{2(aq)}^-$	$3CaO{\cdot}Al_2O_3{\cdot}6H_2O_{(s)}$
$C_2H_3O_{3(aq)}^-$	$CaOH_{(g)}^+$	$HCO_{3(aq)}^-$	$3CaO{\cdot}Al_2O_3{\cdot}8H_2O_{(s)}$
$Ca(CHO_2)_{2(aq)}$	$CH_2O_{(g)}^+$	$Na_{(aq)}^+$	$3CaO{\cdot}Al_2O_3{\cdot}CaCO_3{\cdot}10.68H_2O_{(s)}$
$Ca(OH)_{2(aq)}$	$CH_2O_{2(g)}^-$	$NaAlO_{2(aq)}$	$4CaO{\cdot}Al_2O_3{\cdot}13H_2O_{(s)}$

leaching conditions, i.e., L/S = 20, 120 g/L Na_2CO_3, etc. The same amount of $H^+_{(aq)}$ and $OH^-_{(aq)}$ is introduced to maintain the electronic neutrality of the system. Also, a minor addition of $O_{2\ (g)}$ is necessary to help the Gibbs solver find the equilibrium composition.

In equilibrium, Fig. 5 indicates that the amount of CA_2 is considerably low compared to the sodium aluminate-containing aqueous phase at temperature 25–100 °C. This means that according to their thermodynamic properties the sodium aluminate-containing aqueous phase is more stable in the system than the slag. However, later we will see that the leaching property results based on the experiment show that side reactions could happen during the leaching and some calcium aluminate phases could be identified as the less leachable ones.

3.2. The pH calculation

The leaching agent was prepared by dissolving 120 g of Na_2CO_3 in 1 L of water (1.1 M Na_2CO_3). Therefore, the complete dissolution of Na_2CO_3 is shown by reaction (5).

$$Na_2CO_{3\,(aq)} = 2Na^+_{(aq)} + CO_3^{2-}{}_{(aq)} \quad (5)$$

The reaction of sodium cations and water yield a neutral solution. However, the carbonate anions act as weak alkali and can contribute to the pH of the solution as in reaction (6).

$$CO_3^{2-}{}_{(aq)} + H_2O_{(l)} = HCO_3^-{}_{(aq)} + OH^-{}_{(aq)} \quad (6)$$

As the initial concentration of CO_3^{2-} is known, we may set an initial, change, and equilibrium table for the above reaction as Table 3.

Table 3
Initial, change, and equilibrium condition of CO_3^{2-} reaction with water.

Condition	$[CO_3^{2-}]$	$[HCO_3^-]$	$[OH^-]$
Initial	1.1	0	0
Change	-x	+x	+x
Equilibrium	1.1 - x	x	x

Based on the HSC Chemistry™ database, the equilibrium constant (K_b) of reaction (6) is $2.049{\cdot}10^{-4}$, which gives Eq. (7).

$$Kb = \frac{a_{HCO_3^-} \cdot a_{OH^-}}{a_{CO_3^{2-}} \cdot a_{H_2O}} = 2.049{\cdot}10 - 4 \quad (7)$$

Where a_{HCO3-}, a_{OH-}, a_{CO32-}, a_{H2O} are the activities of HCO_3^-, OH^-, CO_3^{2-}, and H_2O in a solution, respectively. Assume the solution is an ideal mixture, then the activity is as same as the molar concentration. Consider the activity of water is unity and, thus, taking into account the equilibrium condition in Table 3, the Eq. (7) becomes Eq. (8).

$$2.049{\cdot}10 - 4 = \frac{x^2}{1.1 - x} \quad (8)$$

The x value is considerably small, thus neglecting x value in denominator gives $x = 0.015$. As $pOH = -\log [OH^-]$ and $pH = 14 - pOH$, then the theoretical pH in the leaching solution is 12.2.

Moreover, if we consider the slags leaching reactions (1)–(4) in the solution, the leaching product (i.e., $NaAlO_2$) can be hydrated with water and produce aluminate ion, whereas in a high pH solution it is in the form of $Al(OH)_4^-$ (Moolenaar et al., 1970), as seen in reaction (9). Furthermore, reaction (3) and (4) give NaOH as the leaching product, which is a strong alkali and can dissociate entirely in the solution as seen in reaction (10).

$$2NaAlO_{2\,(aq)} + 4H_2O_{(l)} = 2Na^+_{(aq)} + 2Al(OH)_4^-{}_{(aq)} \quad (9)$$

$$NaOH_{(aq)} = Na^+_{(aq)} + OH^-_{(aq)} \quad (10)$$

The $NaAlO_2$ aqueous solution could be considered as a weak alkali where the only fraction of it accepts protons from water, which means along with the dissociation of NaOH in reaction (10), both of these reactions most likely increase the pH extent of the leachate during the leaching.

3.3. Aluminum extraction yield

If we have a maximum aluminum leaching extent of each calcium aluminate phase and no materials loss during the experiment due to the evaporation and/or filtration, then based on the slags composition provided in Table 1, we may calculate the maximum extraction of aluminum in the leachate after the leaching treatment as shown in Table 4.

4. Results and discussion

The results obtained about the characteristics of the produced slags, their leaching behavior, and leaching products analysis are presented. Mechanisms related to the leaching of calcium aluminate phases will be discussed, supported by structural modeling of the phases.

Table 4
Maximum extraction of aluminum in the leachate.

Sample	Pulp concentration (g/L)	Aluminum in leachate (g/L)
Slag 1	50	17.7
Slag 2	50	16.4
Slag 3	50	13.5
Slag 4	50	12.2
Slag 5	50	10.6

4.1. Characteristics of the slags

The particle size distribution of each synthesized slag listed in Table 1 is shown in Fig. 6. Consecutively, the mean diameter of Slags 1, 2, 3, 4 and 5 is 7.8 ± 3.9, 7.1 ± 4.5, 26.6 ± 22.8, 5.4 ± 2.2, and 5.3 ± 2.3 μm. Slag 3 has the largest mean diameter of the particle as well as the standard deviation compared to the others as it has an agglomeration-type of particle and not easily disintegrated even though the ultrasound was applied for several minutes. We believe the agglomeration-tendency is caused by the high reactivity of $C_{12}A_7$ phase to the moisture as supported by literature:

(1) Jeevaratnam et al. (1964) and Nurse et al. (1965b) claimed the phase might contain up to 1.3 to 1.4 wt% H_2O at 1100 °C in an air of normal humidity,
(2) Roy and Roy (1960) claimed the $C_{12}A_7$ phase has zeolitic behavior, which means that the phase can absorb and desorb water as a function of temperature (with pH_2O fixed) without structural change,
(3) Thermogravimetric analysis by Hayashi et al. (2002) revealed that in a dry-oxygen environment the $C_{12}A_7$ phase losses its weight for about 1% when heated to 700 °C, and the loss was restored when cooled down to below 700 °C.

The XRD patterns of the obtained slags and the determined phases are presented in Fig. 7. Slag 1 has CA and CA_2 phases, Slag 2 has CA and C_3A phases, Slag 3 has a single $C_{12}A_7$ phase, Slag 4 has C_3A and $C_{12}A_7$ phases, and Slag 5 has C_3A and $Ca_5Al_6O_{14}$ (C_5A_3) phases. Most of the phases are well identified and formed in crystalline form, showing the applied cooling rates were proper for crystallization of the phases. A result of the relative fraction of the obtained phases is also shown in Fig. 7.

Based on the results in Fig. 7, three points are very important to note. First, the similarity of the Slags 1 and 3 compositions to the equilibrium ones as we have calculated based on lever-rule in Table 1. Second, the absence of $C_{12}A_7$ phase in Slags 2 and 5, which is discussed later. Third, the co-existence of C_5A_3 in Slag 5 that was "unrecognizable" in the phase diagram of CaO-Al_2O_3 in Fig. 2, however, it appears in the XRD spectrum.

As of today, $C_{12}A_7$ and C_5A_3 phases are not readily established in the CaO-Al_2O_3 system especially in certain atmospheric conditions as some literature omitted one or both phases in their assessment (Haccuria et al., 2016; Hallstedt, 1990; Jerebtsov and Mikhailov, 2001; Lutsyk et al., 2012; Mao et al., 2006). In our previous study (Azof et al., 2017), we also could not observe the presence of $C_{12}A_7$ phase in a slag produced from the same composition and condition, as we did observe again in this study for Slag 2. Knowing that CA is the dominant phase in Slag 2 (about 80 wt% based on phase lever-rule), and $C_{12}A_7$ is a metastable phase, then dissociation of the unstable $C_{12}A_7$ to C_3A and CA phase at low temperature proposed by Nurse et al. (1965a, 1965b), as shown in reaction (11) might be the reason.

$$2[Ca_{12}Al_{14}O_{33\,(s)}] = 5[Ca_3Al_2O_{6\,(s)}] + 9[CaAl_2O_{4\,(s)}] \quad (11)$$

The stable form of $C_{12}A_7$ phase in Slags 3 and 4 may be due to a relatively similar CaO: Al_2O_3 molar ratio of these slags to $C_{12}A_7$ phase. Also, the presence of "guest" anions, such as OH^- (Roy and Roy, 1960), halide ions, i.e., Cl^-, F^- (Jeevaratnam et al., 1964), and S^{2-} (Zhmoidin and Chatterjee, 1984), could favorably stabilize the phase. The latter suggestion needs further investigation to obtain more evidence on the stabilizing element that presents in the slags.

Concerning the C_5A_3 phase co-existence in Slag 5, Shepherd et al. (1909) were first among the researchers who reported the presence of the phase in the CaO-Al_2O_3 system. Subsequently, Rankin and Wright (1915) observed C_5A_3 phase with a composition of 47.8 wt%CaO and 52.2 wt%Al_2O_3 and said that it could form in either stable or unstable monotropic form. The stable form melts congruently at 1455 ± 5 °C,

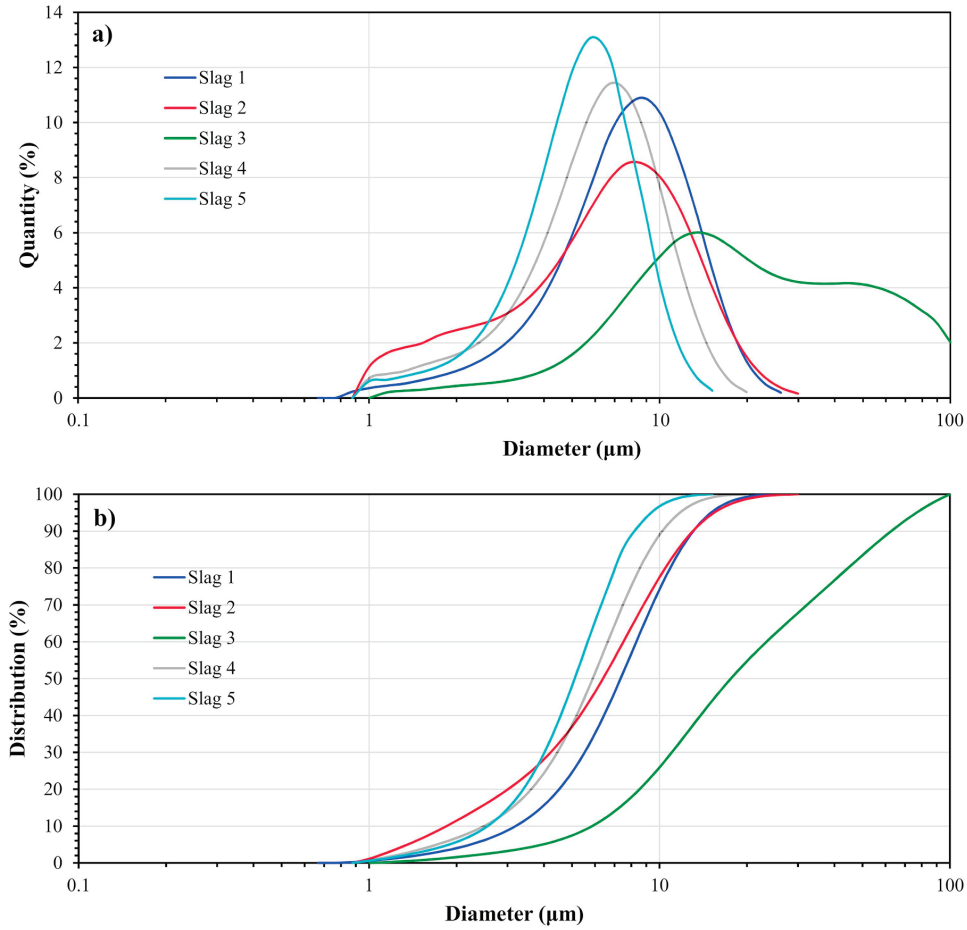

Fig. 6. Laser particle size measurement based on (a) differential and (b) accumulative type of the obtained slags.

and it could form a eutectic mixture with C_3A ($CaO:Al_2O_3$ mass ratio = 50:50) at 1395 ± 5 °C. This structure gave rise of some discussions and debate among scientists, Büssem (1936) said that the measured density of C_5A_3 phase does not agree with its chemical formula, and they proposed $C_{12}A_7$ formula instead of it. Thorvaldson and Schneider (1941) investigated the composition of the aluminate obtained by thermal decomposition of $3CaO{\cdot}Al_2O_3{\cdot}6H_2O$ ($Ca_3Al_2(OH)_{12}$) and showed that the free lime amount produced from $Ca_3Al_2(OH)_{12}$ dehydration suits with the composition of $C_{12}A_7$ than C_5A_3, correspondingly. In contrary, Aruja (1957) measured the density of two single-crystals of C_5A_3 and said that the orthorhombic C_5A_3 formula gives a better fit than $C_{12}A_7$, and the XRD pattern of both C_5A_3 and $C_{12}A_7$ showed that the compounds show no resemblance. Zhmoidin and Chatterjee (1984) stated that it is possible under conditions of deficit oxygen $C_{12}A_7$ is unstable, and C_5A_3 phase stabilizes with denser (3.03 g/cm^3) orthorhombic structure. Later on, Brisi et al. (1986) confirmed the possibility of making C_5A_3 from the $C_{12}A_7$ phase in solid-state reaction provided that low oxygen partial pressure and water vapor be preserved. In this study, the presence of reducing gas ($CO_{(g)}$) during smelting trials due to the use of graphite crucible could reduce the oxygen partial pressure and is believed to stimulate the stability of C_5A_3 in Slag 5.

4.2. Leaching behavior of the slags

The obtained leaching residue was analyzed to characterize the leaching behavior of the existing phases in the slags and the effect of dissolved slags on the pH of the leachate.

4.2.1. Phases of the leached residue

Fig. 8 shows the XRD patterns of each residue obtained after filtering the leachates. As expected, residue from each slag contains a considerably high amount of $CaCO_3$, which is in the form of calcite and vaterite, and some remaining undissolved phases. Also, $Al(OH)_3$ in bayerite form and $Ca_3Al_2(OH)_{12}$ phase are observed in some of the residues. The formation of solid $Al(OH)_3$ in this stage could be detrimental as it decreases the alumina yield in the leachate. While the latter phase is usually prepared in the Bayer process, which could assist the removal of impurities from the pregnant liquor (Whittington and Cardile, 1996). In this study, we may say that both $Al(OH)_3$ and $Ca_3Al_2(OH)_{12}$ can be formed due to the hydration of CA in water during the leaching treatment, which was proposed earlier by Lundquist and Leitch (1963a) as in reaction (12).

$$3[CaAl_2O_{4\,(s)}] + 12H_2O_{(l)} = Ca_3Al_2(OH)_{12\,(s)} + 4Al(OH)_{3\,(s)} \quad (12)$$

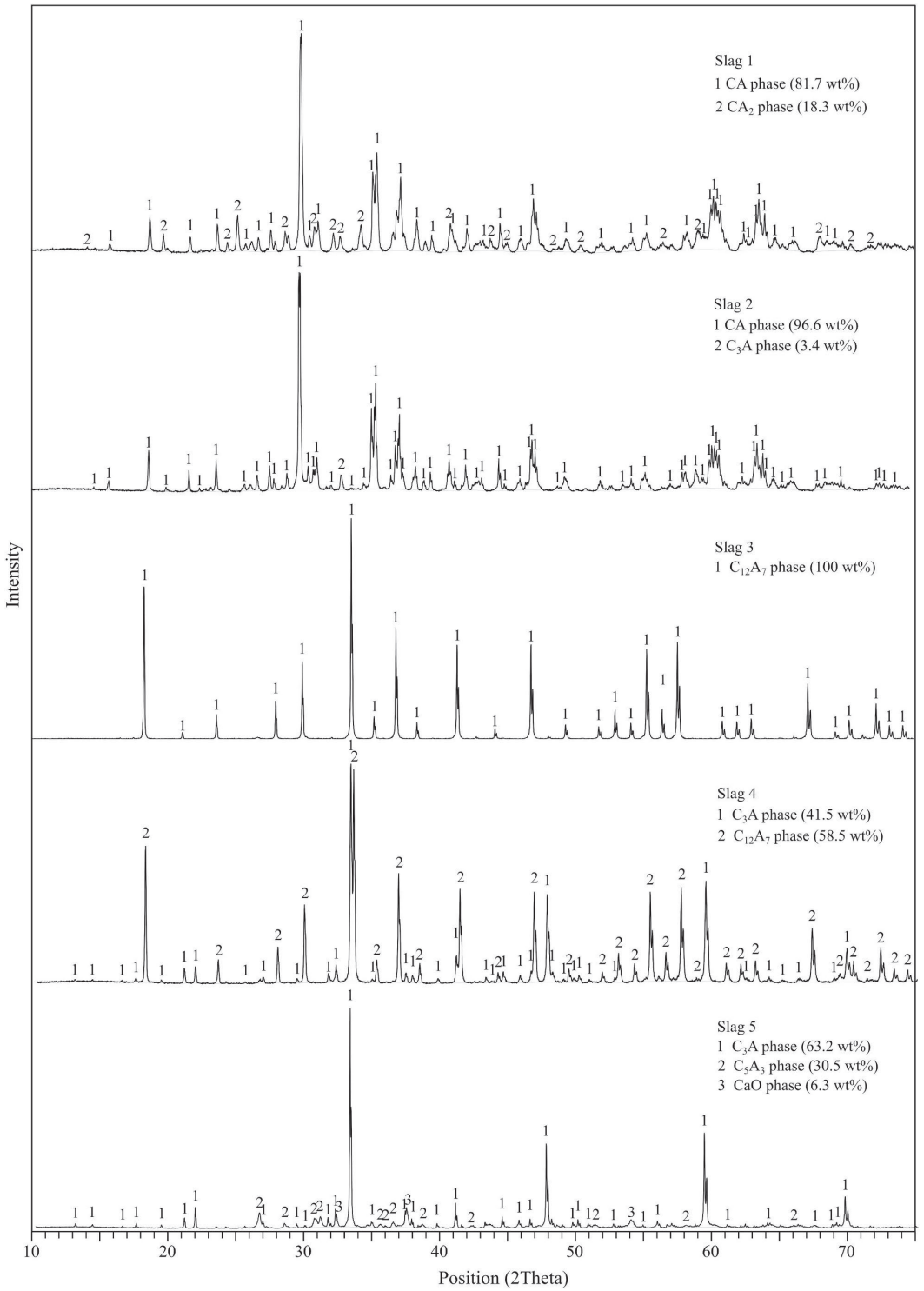

Fig. 7. XRD pattern of the obtained slags with the quantified compositions of the phases.

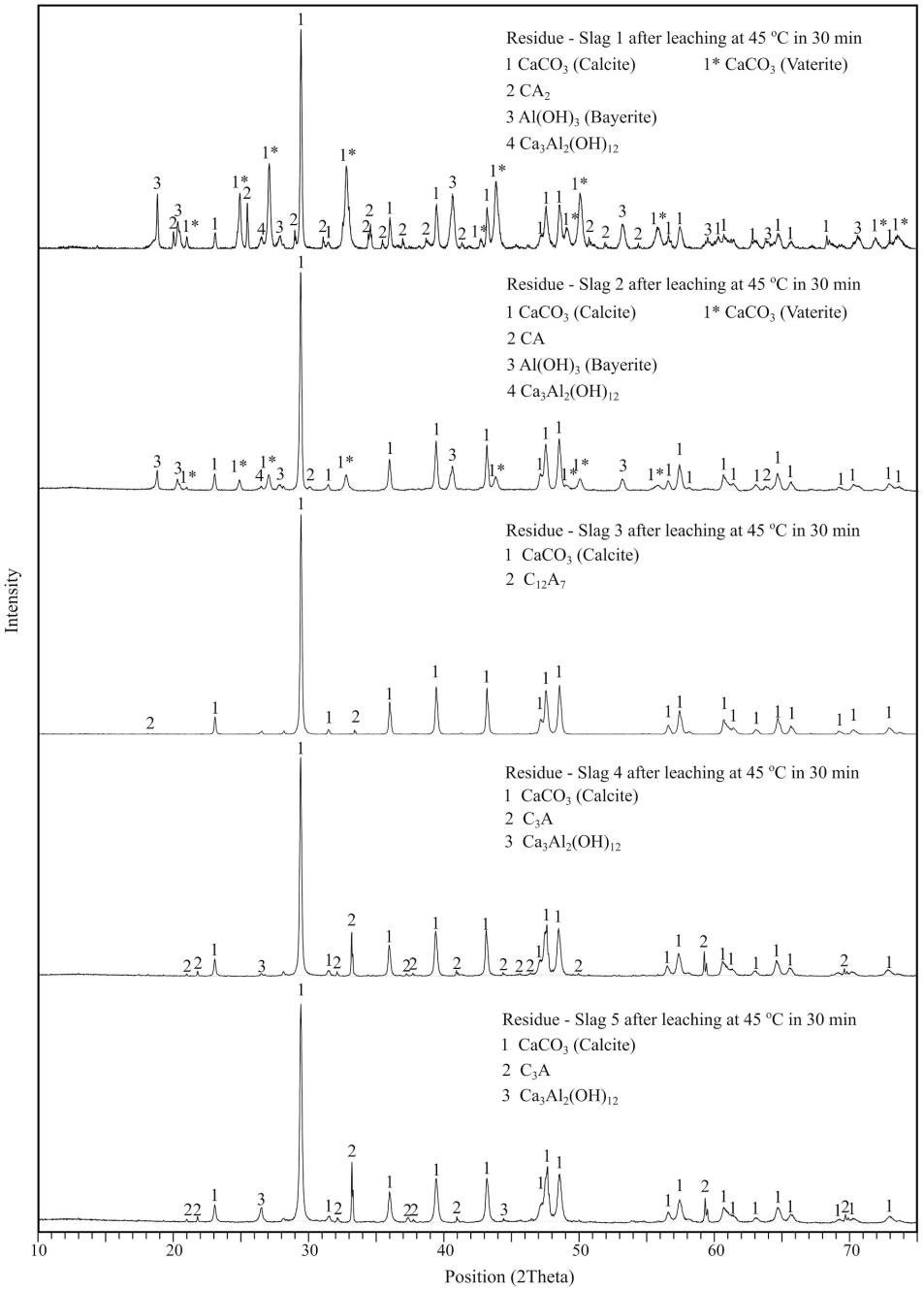

Fig. 8. XRD results of the residue of the slags after the leaching treatment at 45 °C in 30 min.

$\Delta G^{\circ}_{25°C} = -27.0$ kJ/mol $CaAl_2O_4$

The formation of $Ca_3Al_2(OH)_{12}$ in the residue of Slag 5 is not necessarily producing $Al(OH)_3$ as in the case of Slags 1 and 2. We suggest that the hydration of the C_3A phase in Slag 5 may produce $Ca_3Al_2(OH)_{12}$ as seen in reaction (13), which could explain the absence of $Al(OH)_3$ in the residue. Furthermore, the presence of free-CaO in Slag 5 could enhance the amount of $Ca_3Al_2(OH)_{12}$ after the leaching, as was proposed by Whittington et al. (1997) who claimed that the addition of CaO in sodium aluminate solution produces $Ca_3Al_2(OH)_{12}$ as we see in reaction (14).

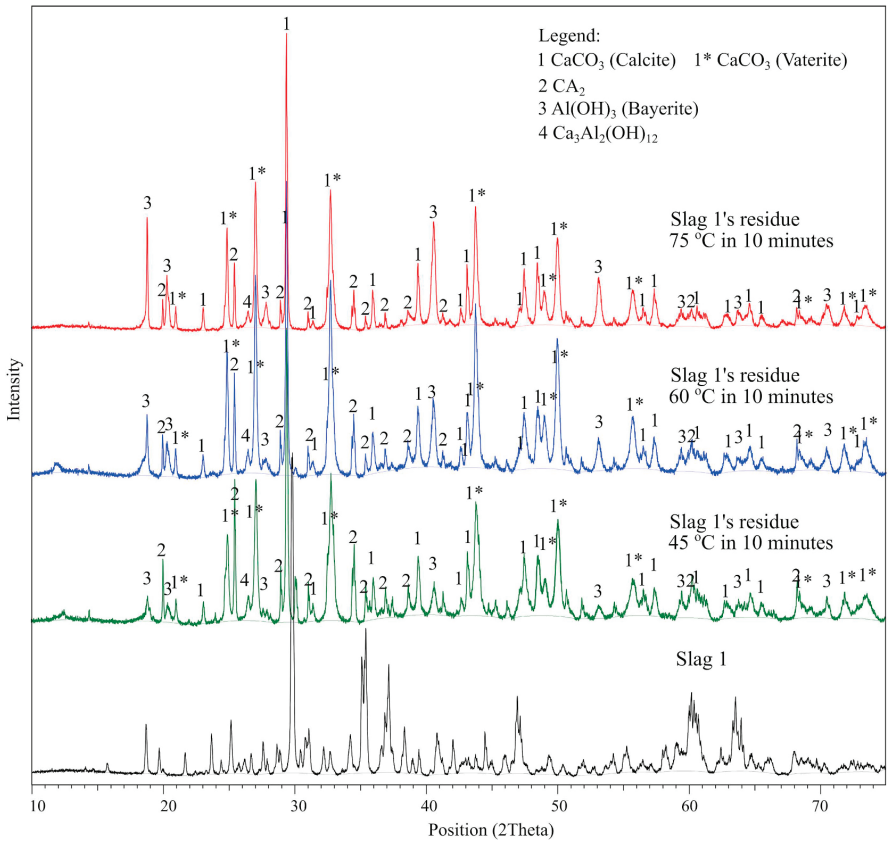

Fig. 9. XRD patterns of the residue obtained from Slag 1 after the leaching treatment in Na_2CO_3 solution at 45, 60, and 75 °C in 10 min.

$$Ca_3Al_2O_{6\,(s)} + 6H_2O_{(l)} = Ca_3Al_2(OH)_{12\,(s)} \quad (13)$$

$$\Delta G^{\circ}{}_{25°C} = -134.3\ \text{kJ/mol}\ Ca_3Al_2O_6$$

$$2NaAl(OH)_{4\,(aq)} + 3CaO_{(s)} + 3H_2O_{(l)} = Ca_3Al_2(OH)_{12\,(s)} + 2NaOH_{(aq)} \quad (14)$$

$$\Delta G^{\circ}{}_{25°C} = -49.9\ \text{kJ/mol CaO}.$$

4.2.2. Effect of temperature

Fig. 9 shows the XRD patterns of Slag 1 residue after being leached by Na_2CO_3 solution for 10 min at 45, 60, and 75 °C. The most distinct peaks observed from the three different temperatures are $Al(OH)_3$ and CA_2 peaks. It seems that by increasing temperature the intensities of Al $(OH)_3$ peaks become more apparent. Lundquist and Leitch (1963b) stated that the temperature gives modest effect to the precipitation of Al $(OH)_3$ when CA is leached in water. However, in principle, the formation of $Al(OH)_3$ in the Na_2CO_3 solution is as same as in the water, where it employs the hydration of CA (reaction (12)). We suggest that the undesirable precipitation may be accelerated by thermal energy.

On the other hand, by increasing the temperature, the CA_2 phase becomes more leachable as the intensity of its peaks decreases. This is supported by our former observation (Azof et al., 2017) that stated the leaching extent of CA_2 phase is markedly increased after about 60 °C. Therefore, it can be concluded here that the effect of leaching temperature on the alumina extraction extent is likely dependent on both the calcium aluminates composition and the solvent characteristics.

4.2.3. Effect of sodium hydroxide addition

In the original method of Pedersen (1927), "free sodium hydroxide" is used to prevent the dissolution of silica in pregnant solution, which is not of the interest in the current CaO-Al_2O_3 system. However, Pedersen claimed that if a larger proportion of "free sodium hydroxide" is used, the rate of alumina dissolution and the ratio of alumina to soda in the solution are decreased. As Pedersen did not mention specifically the amount of "free sodium hydroxide," we introduced NaOH in Na_2CO_3 solution about two times than the stoichiometry required in Slag 1 and 2 in our previous study (Azof et al., 2017), to validate Pedersen's statement.

Figs. 10 and 11 show the comparison of XRD patterns of the residues produced from Slags 1 and 2 in different solutions. As shown, the peaks intensity of $Al(OH)_3$ and $Ca_3Al_2(OH)_{12}$ in the two residues are noticeably low. The dissolution process of these phases in NaOH-containing solution is shown in reaction (15) and (16). The first one is a typical reaction in the pressure leaching of the Bayer process (Bayer, 1894; Safarian and Kolbeinsen, 2016a). While the latter is proposed by Alekseev (1982) that in NaOH solution (6–200 g/L) and at a certain temperature (25–90 °C) the $Ca_3Al_2(OH)_{12}$ may be unstable and dissociates to $Ca(OH)_2$ and NaAl(OH).

$$Al(OH)_{3\,(s)} + NaOH_{(aq)} = NaAl(OH)_{4\,(l)} \quad (15)$$

$$\Delta G^{\circ}{}_{25°C} = -7.0\ \text{kJ/mol}\ Al(OH)_3$$

$$Ca_3Al_2(OH)_{12\,(s)} + 2NaOH_{(aq)} = 2NaAl(OH)_{4\,(aq)} + 3Ca(OH)_{2\,(s)} \quad (16)$$

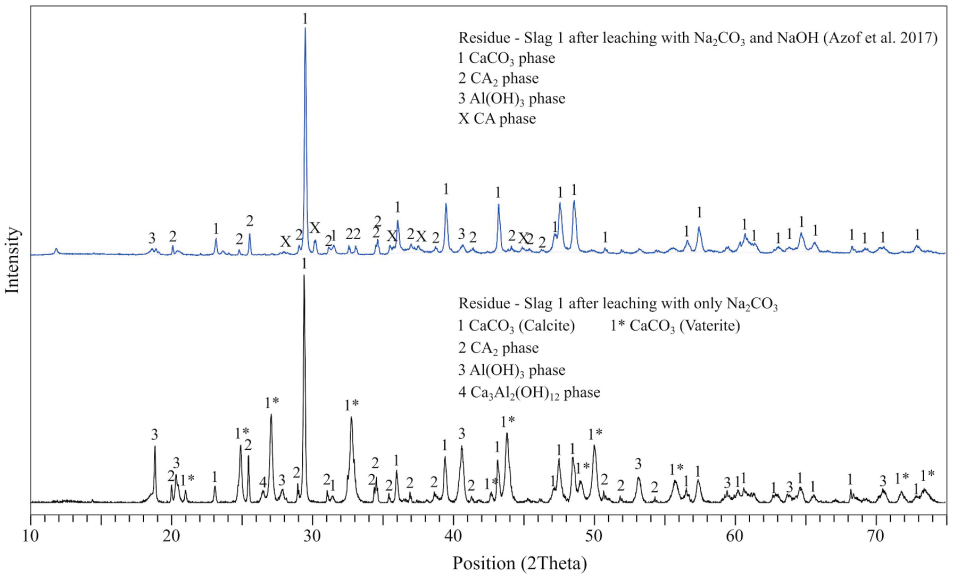

Fig. 10. XRD pattern of the obtained residues from Slag 1 after leaching in different solvents with the same temperature and duration.

$\Delta G^{\circ}_{25°C} = -22.9$ kJ/mol $Ca_3Al_2(OH)_{12}$

In reaction (12), we see that the CA phase can be hydrated in water and form $Ca_3Al_2(OH)_{12}$. However, it should be considered here that in a solution with some extent of NaOH concentration, the CA phase may also react with NaOH to form $Ca_3Al_2(OH)_{12}$ that leads to the alumina losses. Nevertheless, it gives sufficient OH^- ions to prevent $Al(OH)_3$ from precipitating (R.V. Lundquist and Leitch, 1963), as shown in reaction (17).

$$3[CaAl_2O_4]_{(s)} + 4NaOH_{(aq)} + 12H_2O_{(l)} = Ca_3Al_2(OH)_{12\,(s)} + 4NaAl(OH)_{4\,(aq)} \quad (17)$$

$\Delta G^{\circ}_{25°C} = -36.42$ kJ/mol $CaAl_2O_4$.

This means if we take into account the reaction of calcium aluminate in sodium carbonate and sodium hydroxide as in reactions (1) and (17), respectively, we can predict the equilibrium of the precipitated $CaCO_3$ and $Ca_3Al_2(OH)_{12}$ in residue based on the amount of NaOH and

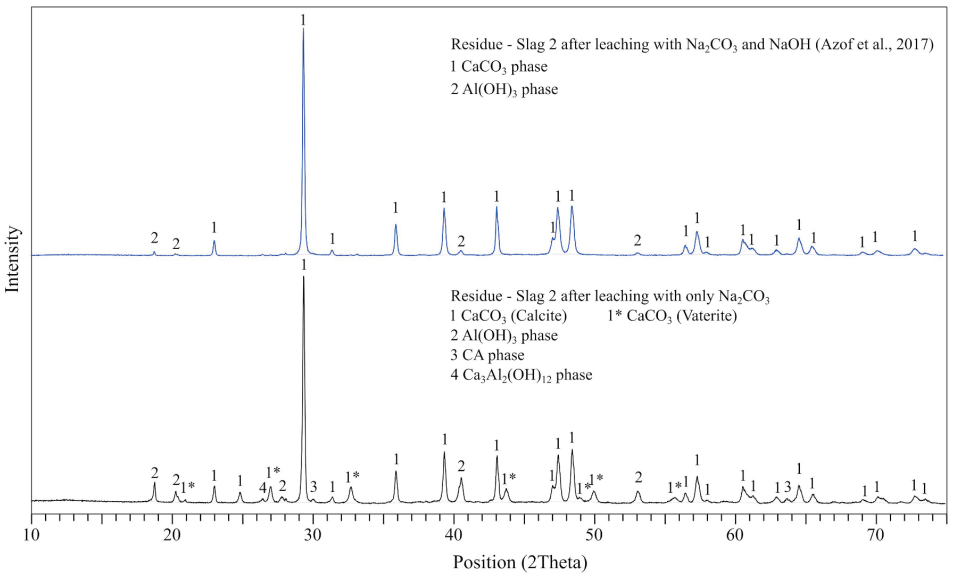

Fig. 11. XRD pattern of the obtained residues from Slag 2 after leaching in different solvents with the same temperature and duration.

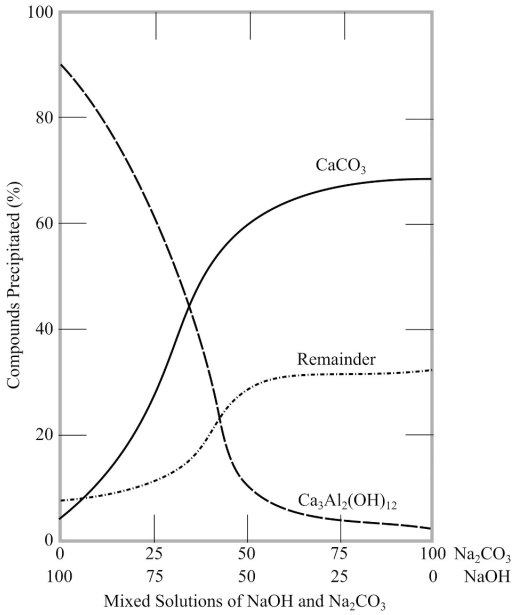

Fig. 12. Mixed solutions of NaOH and Na_2CO_3 in accordance with the precipitated compounds as reconstructed from Lundquist and Leitch (1963).

Na_2CO_3 in the mixed solution. Fig. 12 shows the relationship between the mixed solution ratio of NaOH:Na_2CO_3 to the number of precipitated compounds in the residue as reconstructed from Lundquist and Leitch (1963). The figure indicates that the carbonate anions in the solution are necessitated to the alumina loss prevention as it reacts with the calcium cations and replacing the hydroxyl ion, $Al_2(OH)_{12}^{2-}$, so that $CaCO_3$ precipitation is more favorable than the $Ca_3Al_2(OH)_{12}$ precipitation.

4.2.4. The solution pH and aluminum recovery

We measured the pH changes in the solution before and after the leaching of Slags 1–5 at certain temperatures. The pH meter was calibrated with buffer pH 4.0 and 7.0 before use. The pH was measured for the blank solution that consisted of 120 g/L Na_2CO_3 at 25 °C is 11.4 ± 0.1. Moreover, the pH range of the leachate is 12.5–12.9, which changes according to the leaching temperature and OH^- concentration. The aluminum amount in the leachates is then measured by ICP-HR-MS, and by comparing the result with the maximum aluminum recovery extent in Table 4, we may calculate the aluminum recovery extent as shown in Table 5.

The corresponding residues of the leaching experiments in Table 5 were washed and analyzed by XRD, and then semi-quantitatively calculated as shown in Fig. 13. The co-existing phases of the obtained residues are relatively similar to the residues that are leached at 45 °C after 30 min in Fig. 8. However, semi-quantitative calculations of the fraction of the phases of the residues may indicate that the calcite most likely precipitates in the increasing order of CaO:Al_2O_3 mass ratio, which is seen in the residues of Slags 1, 2, and 3, and then it starts decreasing in residue of Slags 4 and 5. Vaterite, the less stable form of $CaCO_3$, precipitates only in the residue of Slags 1 and 2, while it is unobservable in the residues of Slags 3, 4, and 5. More details on the vaterite phase formation are discussed later.

A relatively high amount of bayerite (21–39 wt%) is detected in the residue of Slags 1 and 2, while a low trace of it is seen in the residue of Slag 4. We may say that the precipitation of bayerite gives a significant contribution to the low extent of aluminum recovery, especially for Slags 1 and 2, as it consumes three-quarter moles of CA phase for one mole of bayerite, as seen in reaction (12). Based on the semi-quantitative result in Fig. 13, we suggest that the aluminum recovery decreases by 0.4% for every percent of bayerite precipitation. Furthermore, the $Ca_3Al_2(OH)_{12}$ phase is noticed at relatively low quantities (< 6 wt%) in all of the residues. We may conclude that the extent of alumina recovery in leaching is affected by the unleached slags and precipitation of unwanted compounds as in reaction (12)–(14); $Ca_3Al_2(OH)_{12}$ and bayerite.

4.3. Leaching mechanism

As discussed in previous part, not all calcium aluminates have the same leaching behavior and extent as we would have expected in the equilibrium condition in Fig. 5. This means that thermodynamic consideration is not the only factor that defines the leachability of the calcium aluminate phases if a specific leaching rate is expected. In this section, we discuss other factors that may also contribute to the leaching property. Moreover, the changes in particles morphology before and after the leaching process are shown and discussed.

4.3.1. The structure of calcium-aluminate phases

The previously determined crystal structures of CA (Ma et al., 2011), CA_2 (Baldock et al., 1970), C_3A (Mondal and Jeffery, 1975), and $C_{12}A_7$ (Boysen et al., 2007) were observed in the current study. We model the atomic arrangements in a unit cell of calcium aluminates that is shown in Fig. 14. The drawings produced by VESTA™ ver.3, which is a program for three-dimensional visualization and investigation of crystal structures (Momma and Izumi, 2011).

The CA and CA_2 phase have monoclinic (Baldock et al., 1970; Ma et al., 2011), while C_3A and $C_{12}A_7$ phase have cubic lattice system (Boysen et al., 2007; Mondal and Jeffery, 1975). Ca- and Al-atom shares six (octahedral) and four (tetrahedral) coordination number with O-atom, respectively. Calcium aluminate slag is an ionic compound in nature; consists of cations, i.e., Ca^{2+} and Al^{3+}, and anions, i.e. O^- and O^{2-}. However, the Al-tetrahedral sites are joined together in chains by bridging oxygen (BO), this results in a polymerized network structure, which is considered as a network former. In other words, we could say that the slag consists of both covalent (joined tetrahedrons) and ionic (cation-oxygen) bonds. The strength of the cation-oxygen bond could be presented by the field strength (z/r^2), where z is the charge and r is the radius of the cation (Mills et al., 2013). From the formula, we may

Table 5
The pH of leachates and aluminum recovery in several leaching conditions.

Sample	Leaching condition			pH in the leachate	Aluminum in the leachate (g/L)	Aluminum recovery (%)
	Solution	Temperature (°C)	Time (minute)			
Slag 1	120 g/L	75	10	12.5 ± 0.1	3.1 ± 0.05	17.5 ± 0.3
Slag 2	Na_2CO_3	60	10	12.9 ± 0.1	4.0 ± 0.03	24.4 ± 0.2
Slag 3		45	10	12.9 ± 0.1	12.6 ± 0.03	93.3 ± 0.2
Slag 4		45	10	12.9 ± 0.1	6.1 ± 0.05	50.0 ± 0.4
Slag 5		45	10	12.8 ± 0.1	4.9 ± 0.14	46.2 ± 1.3

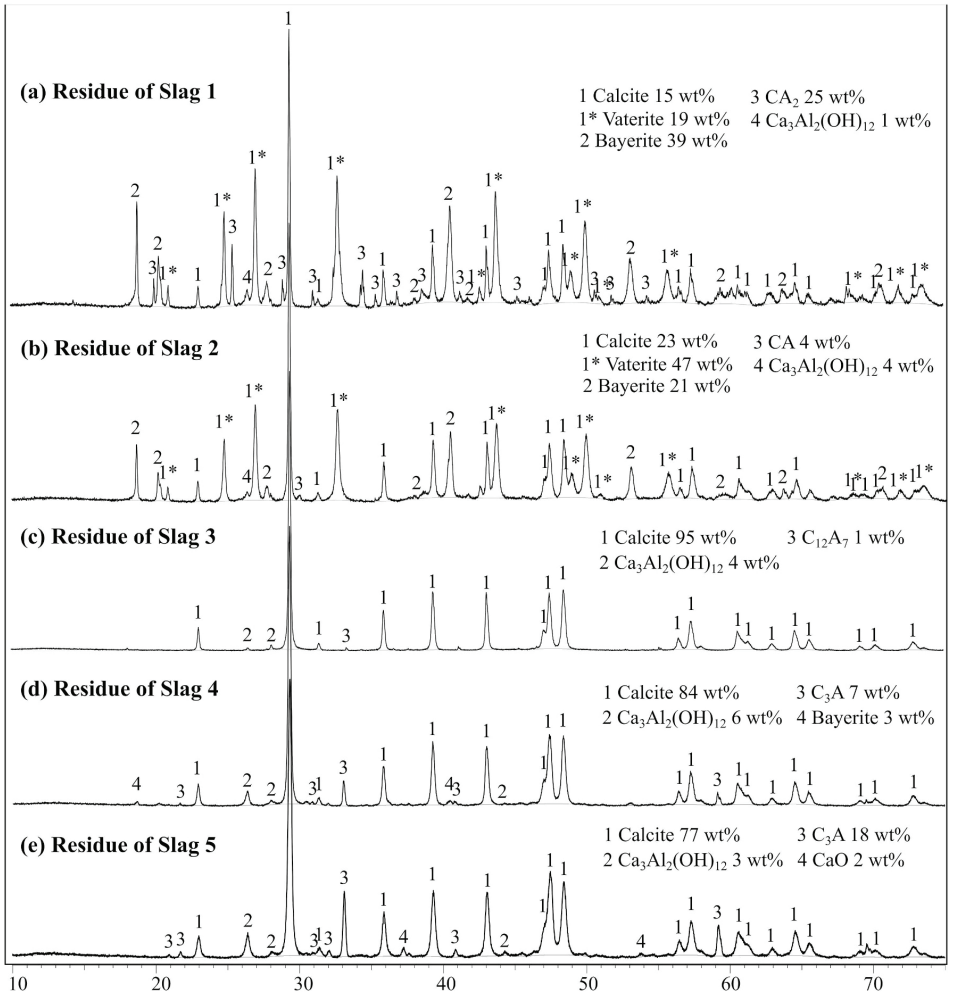

Fig. 13. XRD pattern of the obtained residues from the experiments carried out in conditions given in Table 5.

conclude that the field strength decreases with increasing cation size. Shannon (1976) stated that the Ca atomic radius is about two times larger than Al. Therefore, compared to the Al—O bond, the Ca—O bond is relatively weak.

Moreover, when Ca^{2+} and Na^{+} cations (in the form of Na_2O) co-exist in the structure, it tends to break the BO and form non-bridging oxygens (NBO). An NBO is oxygen that bridges from a tetrahedron to a neighboring, non-tetrahedral polyhedron (in this study, Ca-octahedral). The degree of polymerization of an aluminate compound is expressed as NBO/number of tetrahedral (T), whereas NBO/T = 0 shows a fully polymerized structure (Mysen, 1990; Mysen et al., 1985). In other words, by increasing the ratio of NBO/T then the structure is prone to depolymerize. Mills et al. (2013) proposed an equation of NBO/T as the ratio of the mole fraction of "available" network breaking oxides (where "available" means the total number of cations minus those on charge balancing duties) divided by the mole fraction of the network-forming oxides as in Eq. (18).

$$\mathrm{NBO/T} = 2(\sum X_{\mathrm{MO}} + \sum X_{\mathrm{M_2O}} - X_{\mathrm{Al_2O_3}})/(X_{\mathrm{SiO_2}} + 2X_{\mathrm{Al_2O_3}}) \quad (18)$$

Where X is the mole fraction and $X_{\mathrm{MO}} = X_{\mathrm{MgO}} + X_{\mathrm{CaO}} + X_{\mathrm{BaO}} + X_{\mathrm{FeO}} + X_{\mathrm{MnO}} + \ldots$ and $X_{\mathrm{M2O}} = X_{\mathrm{Li2O}} + X_{\mathrm{Na2O}} + X_{\mathrm{K2O}}$. The order of NBO/T for calcium aluminate phases in a typical leaching reaction (1)–(4) becomes $C_3A > C_{12}A_7 > CA > CA_2$. The index of the NBO/T of the Slags 1–5 and their leaching extent is shown in Table 6. It is noted here that the structure of $C_{12}A_7$ in Fig. 14 has a loose-bond of O-ions in the "cage," which may increase the depolymerize extent. Therefore, the NBO/T index for $C_{12}A_7$ becomes irrelevant. Nevertheless, the NBO/T order shows good agreement with the leachability of the calcium aluminate phases in literature (Azof et al., 2017; Fursman et al., 1968), where C_3A, $C_{12}A_7$, and CA are considered as the soluble phases in sodium carbonate solution, while CA_2 phase is the insoluble one. Also, Wells (1928) claimed that C_3A has a vigorous reaction towards the water, and the activity of the other aluminates (i.e., CA, C_5A_3) is distinctly less than that shown by C_3A. Thus it is obvious that the increasing degree of depolymerizing structure of calcium aluminates affecting the extent of its leaching property.

4.3.2. Morphology changes and size evolution

As mentioned in Section 4.2.1., the predominant phase of residue produced from the leaching reaction is $CaCO_3$. However, the formation

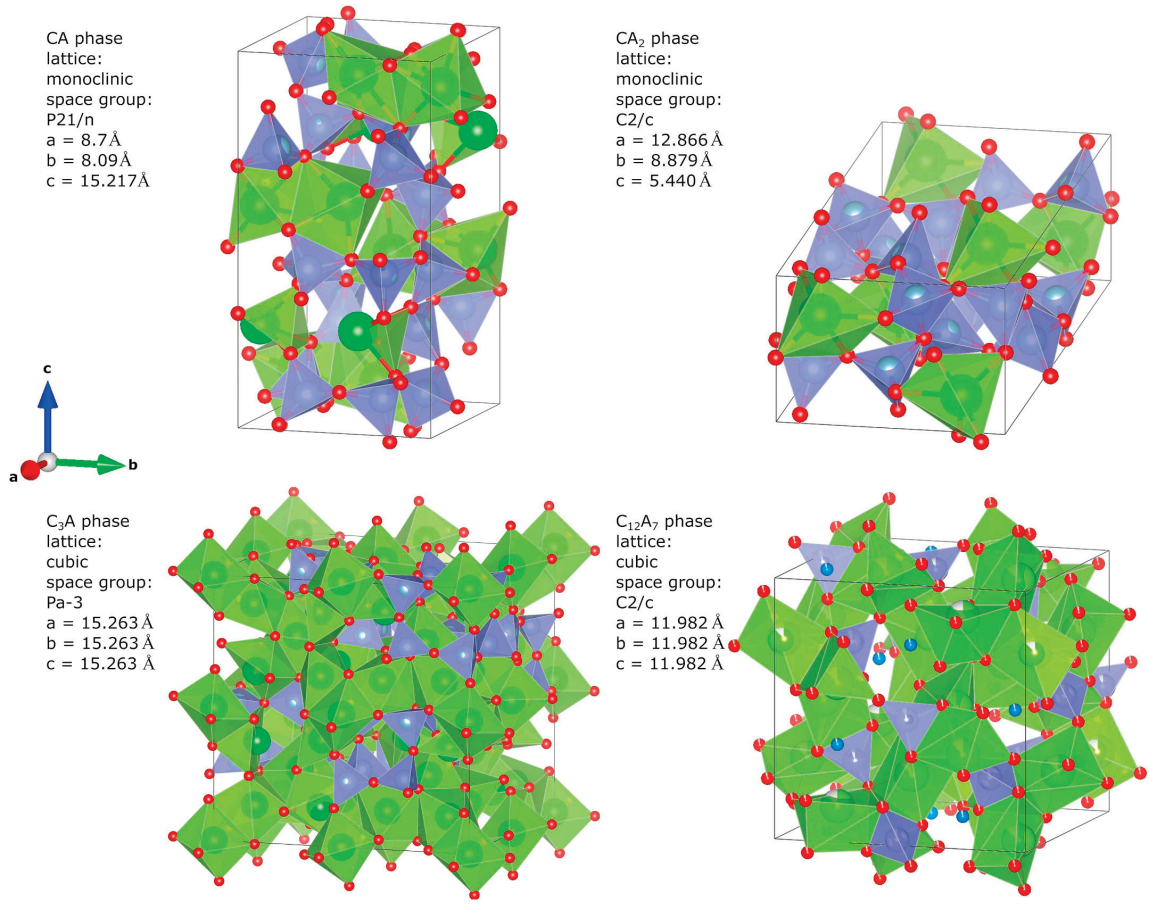

Fig. 14. Structure of CA, CA_2, C_3A, and $C_{12}A_7$ crystals. Green, light blue and red balls represent Ca, Al, and O atoms. AlO_4 tetrahedral and CaO_6 octahedral are shown by dark (purple) and light (green). The dark blue balls at the center of the $C_{12}A_7$ "cage" structure is the "free" O-ions in (1/4, 3/8, 0) position as proposed by Boysen et al. (2007). (For interpretation of the references to colour in this figure legend, the reader is referred to the web version of this article.)

Table 6
A relationship between NBO/T index of the slags and aluminum recovery.

Sample name	NBO/T index	Aluminum recovery* (%)
Slag 1	- 0.1	17.5 ± 0.3
Slag 2	0.1	24.4 ± 0.2
Slag 3**	N/A	93.3 ± 0.2
Slag 4	1.2	50.0 ± 0.4
Slag 5	1.4	46.2 ± 1.3

* Based on the ICP-HR-MS results in Table 5.

** Slag 3 consists of single $C_{12}A_7$ phase, which has "free" O-ions and easily depolymerize.

and morphology of residues produced from this typical reaction are still unclear. Fig. 15(a) shows the SEM image of solid Slag 1 before the leaching treatment, while Fig. 15(b), (c), and (d) show the residue with spherical and dendritic arm growth, agglomerated sphere particles with cauliflower-like in 3000×, and 5000× magnification, respectively. The SEM images of the residue are in agreement with the result of Hostomsky and Jones (1991) in their works on $CaCO_3$ precipitation from a supersaturated solution. They suggested that the agglomeration of an individual $CaCO_3$ particle is the dominant mechanism of increasing particle size compared to the primary crystal growth. This means that the agglomeration most likely causes changes in size.

Moreover, in Fig. 15(b) – (d) we see the morphology of the residue particles is in the small rounded particles clustered together, which is a typical morphology of vaterite (Söhnel and Mullin, 1982; Spanos and Koutsoukos, 1998). Vaterite is favorable to form at high pH (≥ 9.5) solution (Gómez-Morales et al., 1996; Hostomsky and Jones, 1991; Söhnel and Mullin, 1982). Also, vaterite is considered as a metastable phase and is gradually transformed into either calcite or aragonite, where calcite is the thermodynamically stable under normal conditions (Koutsoukos and Kontoyannis, 1984; Söhnel and Mullin, 1982). In the previous discussion in *4.2.4.*, and also shown in Fig. 13, the higher ratio of $CaO:Al_2O_3$ slags we have, the lower amount of vaterite would exist. However, it is difficult to distinguish the form of calcite and vaterite in Fig. 15 as it may not be separated clearly. Extensive works by Koutsoukos and Kontoyannis (1984) and Nancollas and Reddy (1971) showed that the temperature also plays an essential role in the precipitation rate of the vaterite's nuclei. However, it is relatively independent to the stirring speed (agitation).

According to the leaching mechanism that is discussed earlier in *4.3.1.*, depolymerization of solid calcium aluminates might take place in order to proceed with the leaching reactions. We suggest that the

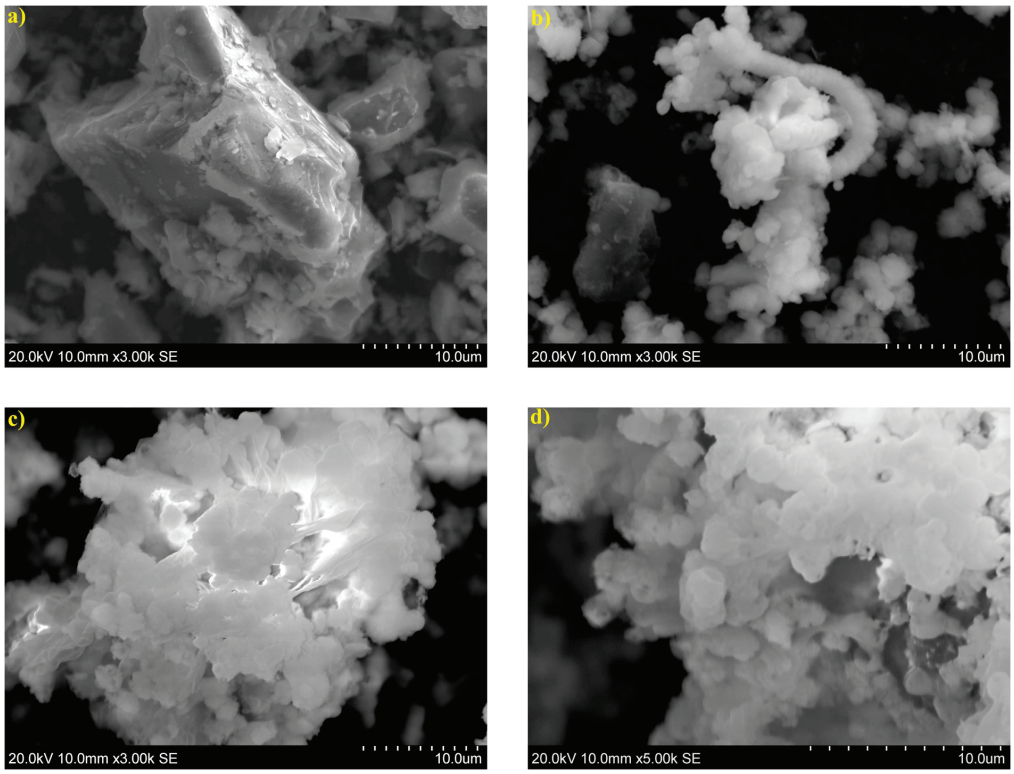

Fig. 15. SEM image of (a) the anisotropy and rock-like Slag 1, (b) spherical and dendritic arm growth of the residue, (c) and (d) agglomerated sphere particles with cauliflower-like in 3000× and 5000× magnification, respectively.

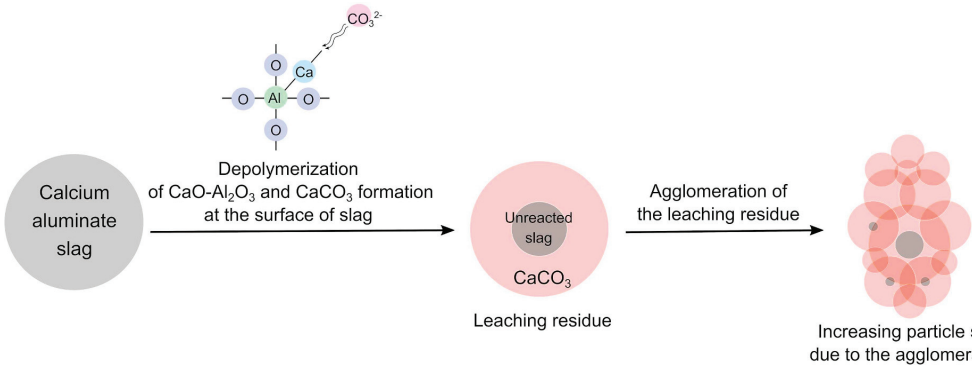

Fig. 16. Illustration of a leaching residue formation from a leachable calcium aluminate phase and increasing particle size of the $CaCO_3$-containing residue due to the agglomeration.

residue nucleation is taking place after the disintegration of solid slag in alkaline solution, which is caused by cations (Ca^{2+} and Na^{+}) depolymerization, and followed by strong ionic bonding between Ca^{2+}–CO_3^{2-}. In addition, we suggest that the primary nucleation is favorably taking place at the existing surface of particle (heterogeneous nucleation), in this case, the most suitable position is the surface of the reacting slag. Therefore, we may conclude here that the grown $CaCO_3$ layer at the surface of not completely reacted slag causes a slower conversion progress. Eventually, the more growth and then agglomeration of the $CaCO_3$-containing residue occur as illustrated in Fig. 16.

The evidence of agglomeration of $CaCO_3$-containing residue is shown by the particle size distribution of the obtained residue from Slags 1, 2, 3, and 4 in Fig. 17. It can be seen that the particle size could be classified into three different range; small (< 15 μm), moderate (30–40 μm), and large (100–170 μm). From Fig. 6 we know that the initial slags have an average of mean diameter < 15 μm. Considering

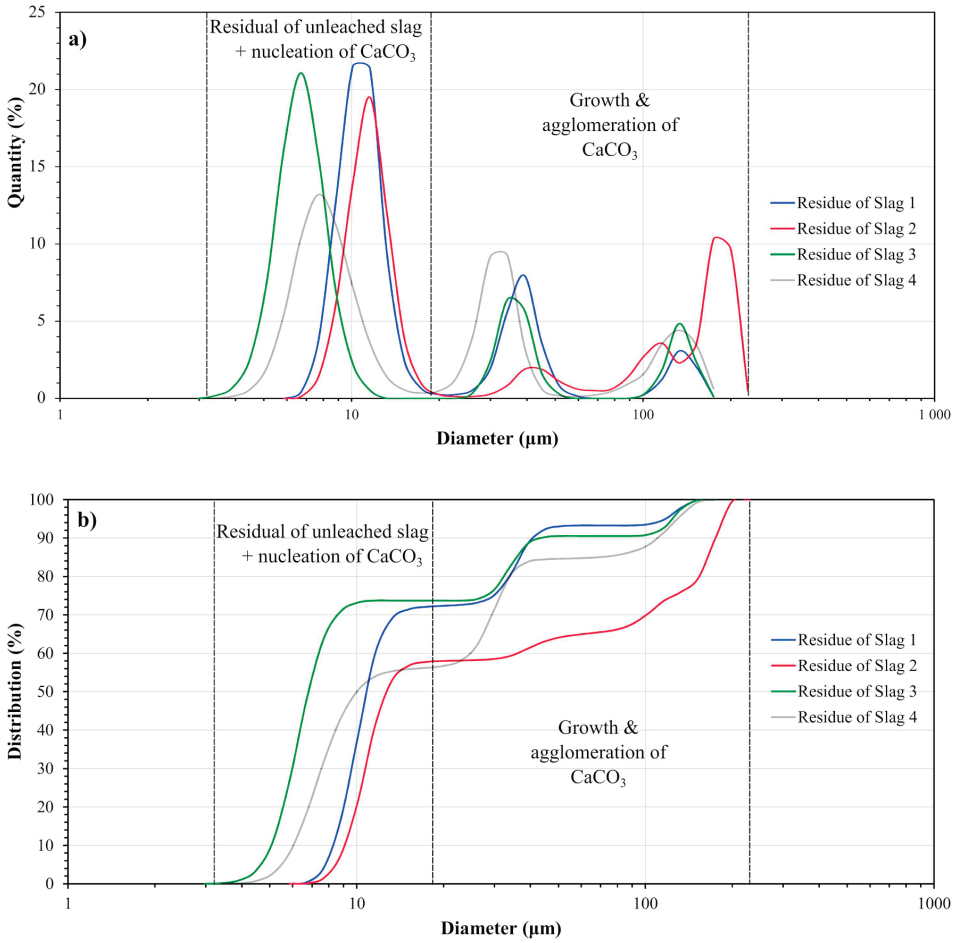

Fig. 17. Laser particle measurement based on (a) differential and (b) accumulative type of the obtained residues from Slags 1, 2, 3, and 4.

some slags were not reacted (or have low reactivity) with the Na_2CO_3 solution during the leaching treatment, the small range size of the residues is most likely a mixture of the residual of the unleached slag and primary nucleation of $CaCO_3$, while the moderate and large range sizes of the residues is composed mostly the $CaCO_3$ in vaterite and calcite forms. In general, the particle size range is relatively similar for all the obtained residues, which needs further investigation to see the factors that might influence the nucleation, growth, and agglomeration of the $CaCO_3$.

The use of the Scherrer equation (Langford and Wilson, 1978) to calculate the crystallite size through the full width at half maximum (FWHM) of each residue's XRD peak is not wise as the residue was finely grounded prior to the XRD observation, which, therefore, may give biased results on the precipitated and agglomerated residues.

The “humps” given by the laser particle measurement in Fig. 17(a) might give us doubt if the particle size was obtained without erroneous measures as the size classifications are so apparent and interestingly occur in each slag. Problems with the particle size measurement, in this case, employing laser diffraction, should be taken into account because the misrepresented data could lead us to an incorrect conclusion about the morphology and size evolution of the residues. Sabin (2011) described some issues related to the problems in measuring particle size employing the laser diffraction observation. Some of the problems are as follows:

(1) Broken particles that are caused by excessive ultrasonic energy,
(2) Bubble (artificial) peaks where the instrument cannot distinguish the particle and bubbles/gaseous objects, and.
(3) Opalescent/reflective particle artifact peaks where in some instances occurred when the particle is shiny, reflective, and opalescent.

Therefore, in an attempt to assure the results in Fig. 17, we have conducted SEM observation at low 100× and 500× magnification, which is shown in Fig. 18(a) and (b), respectively. By performing image analysis with ImageJ™, we can measure the size of the observed particles. Fine particle is excluded from the measurement as it is not easy to count small particles with an irregular shape. The result in Fig. 18(c) shows that the majority of coarse residues accounted for a moderate size diameter (30–40 µm), while the remainder is in tenth and hundredth-micrometer range, which support the measurement results in Fig. 17.

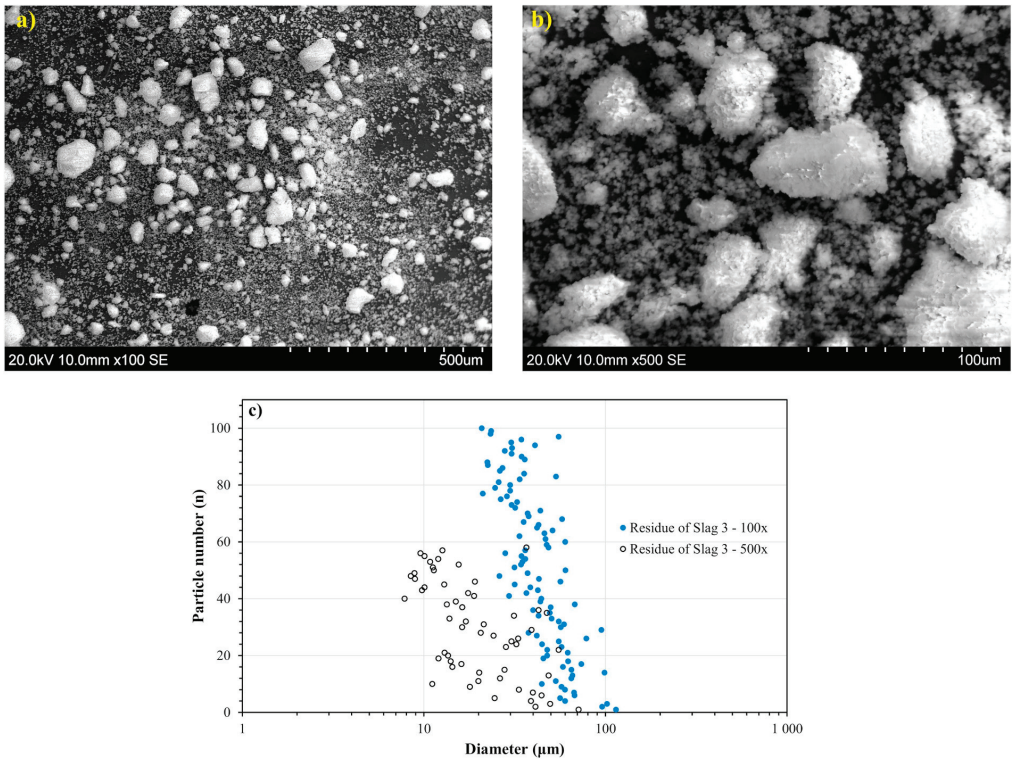

Fig. 18. SEM images of the residue of Slag 3 at (a) 100× and (b) 500× magnification, whereas, (c) the size distribution as calculated by ImageJ™ at coarse particles of $CaCO_3$ in (a) and (b).

5. Conclusions

A calcium aluminate slag which consists only $Ca_{12}Al_{14}O_{33}$ phase is seen as the most leachable slag in a sodium carbonate solution compared to the other slag compositions in the $CaO\text{-}Al_2O_3$ binary system. The leaching recovery may decrease with the precipitation of $Al(OH)_3$ in bayerite form, and $Ca_3Al_2(OH)_{12}$ phase. However, a "free-NaOH" can suppress the formation of those two compounds, accordingly. The less stable form of $CaCO_3$, vaterite, is likely formed in the residue from a relatively low calcium-containing slag (33–49 wt%), and the stable form, calcite, is optimally formed from slag which contains CaO > 49 wt%. The non-bridging oxygen (NBO) over tetrahedral structure (T) index shows that the atomic structure may affect the leaching extent of the slags, where in decreasing order the index of NBO/T of the calcium aluminate phases is $Ca_3Al_2O_6$ > $CaAl_2O_4$ > $CaAl_4O_7$. The $Ca_{12}Al_{14}O_{33}$ phase is an exception case where it has "free" O-ions at the center of the cage structure, which makes it easily depolymerize. The morphology and size changes of the obtained residues are apparent and clustered in the range of small (< 15 µm), moderate (30–40 µm), and large (100–170 µm), whereas the agglomeration of individual $CaCO_3$ particle might be the dominant mechanism of increasing particle size compared to the primary crystal growth.

Acknowledgement

Authors acknowledge Dr. Kai Tang (senior researcher at SINTEF Industry, Norway) for the contribution on the making of $CaO\text{-}Al_2O_3$ binary phase database in FactSage™ that includes $C_{12}Al_{14}O_{33}$ phase. The work was financed by NTNU [project number 237738], and supported by the Research Domain 5-Materials and Society in SFI Metal Production. The scientific support from ENSUREAL project (EU Horizon 2020) is also acknowledged.

References

Alekseev, A.I., 1982. Thermodynamic and experimental analysis of the system CaO-Al2O3-Na2O-H2O at 25-95 C. Zhurnal Prikl. Khimii 55, 2502–2506.
Alex, T.C., Kumar, R., Roy, S.K., Mehrotra, S.P., 2013. Leaching behaviour of high surface area synthetic Boehmite in NaOH solution. Hydrometallurgy. https://doi.org/10.1016/j.hydromet.2013.04.004.
Aluminum, World, 2015. Bauxite Residue Management: Best Practice.
Aruja, E., 1957. The unit cell of orthorhombic pentacalcium trialuminate, 5CaO.3Al203. Acta Crystallogr. 10, 337–339. https://doi.org/10.1107/S0365110X57000961.
Azof, F.I., Kolbeinsen, L., Safarian, J., 2017. The Leachability of calcium aluminate phases in slags for the extraction of alumina, in: Travaux 46. In: Proceedings of 35th International ICSOBA Conference. ICSOBA, Hamburg, pp. 243–253.
Azof, F.I., Kolbeinsen, L., Safarian, J., 2018a. Characteristics of calcium-aluminate slags and pig Iron produced from smelting-reduction of low-grade bauxites. Metall. Mater. Trans. B Process Metall. Mater. Process. Sci. 49, 2400–2420. https://doi.org/10.1007/s11663-018-1353-1.
Azof, F.I., Kolbeinsen, L., Safarian, J., 2018b. Characteristics of calcium-aluminate slags and pig Iron produced from smelting-reduction of low-grade bauxites. Metall. Mater. Trans. B Process Metall. Mater. Process. Sci. 49, 2400–2420. https://doi.org/10.1007/s11663-018-1353-1.
Baldock, P.J., Parker, A., Sladdin, I., 1970. X-ray powder diffraction data for calcium monoaluminate and calcium dialuminate. J. Appl. Crystallogr. 188–191.
Bayer, K.J., 1894. Process of Making Alumina. 515895.
Blake, H.E., Fursman, O.C., Fugate, A.D., Banning, L.H., 1966. Adaptation of the Pedersen process to the ferruginous bauxites of the Pacific Northwest. Bur. Mines US Dep. Inter. (6939), 1–21.
Bo, W., Hui-lan, S., Xue-zheng, Z., Shi-wen, B., 2011. The effect of cooling rate on the Leachability of calcium aluminate slags. In: Light Metals 2011. John Wiley & Sons, Inc., Hoboken, NJ, USA, pp. 241–244. https://doi.org/10.1002/9781118061992.ch43.

Bo, W., Jianxin, Z., Shufeng, Z., Huilan, S., 2014. Effect of Calcium/Aluminium Ratio on Crystal Structure and Al2O3 Leaching Property of 12CaO.7Al2O3. In: Light Metals 2014, pp. 87–90.
Bo, W., Jiajia, L., Huilan, S., Yubing, Z., Dongdong, L., 2015. Synergistic Effect of C12A7 and CA on Alumina Leaching Property under Low Calcium/Aluminum Ratio, in: Light Metals 2015. https://doi.org/10.1002/9781119093435.ch11.
Boysen, H., Lerch, M., Stys, A., Senyshyn, A., 2007. Structure and oxygen mobility in mayenite (Ca12Al14O33): a high-temperature neutron powder diffraction study. Acta Crystallogr. Sect. B Struct. Sci. 63, 675–682. https://doi.org/10.1107/S0108768107030005.
Brisi, C., Borlera, M.L., Montanaro, L., Negro, A., 1986. Hydration of 5CaO.3Al2O3. Cem. Concr. Res. 16, 156–160.
Büssem, W., 1936. Die Struktur des Pentacalciumtrialuminats. Zeitschrift für Krist. - Cryst. Mater. 95. https://doi.org/10.1524/zkri.1936.95.1.175.
Chipera, S.J., Bish, D.L., 2013. Fitting full X-ray diffraction patterns for quantitative analysis: a method for readily quantifying crystalline and disordered phases. Adv. Mater. Phys. Chem. 03, 47–53. https://doi.org/10.4236/ampc.2013.31A007.
Dentoni, V., Grosso, B., Massacci, G., 2014. Environmental sustainability of the alumina industry in Western Europe. Sustain. 6. https://doi.org/10.3390/su6129477.
Fursman, O.C., Blake Jr., H.E., Mauser, J.E., 1968. Recovery of Alumina and Iron from Pacific Northwest Bauxites by the Pedersen Process. Albany.
Gómez-Morales, J., Torrent-Burgués, J., Rodríguez-Clemente, R., 1996. Nucleation of calcium carbonate at different initial pH conditions. J. Cryst. Growth 169, 331–338. https://doi.org/10.1016/S0022-0248(96)00381-8.
Gu, Songqing, Qi, Lijuan, Zhonglin, Y., 2007. Energy Consumption in Bayer Process, in: Light Metals 2007. pp. 55–59.
Guirado, F., Galí, S., Chinchón, S., 2000. Quantitative Rietveld analysis of aluminous cement clinker phases. Cem. Concr. Res. 30, 1023–1029. https://doi.org/10.1016/S0008-8846(00)00289-1.
Haccuria, E., Crivits, T., Hayes, P.C., Jak, E., 2016. Selected phase Equilibria studies in the Al2O3-CaO-SiO2 system. J. Am. Ceram. Soc. 99, 691–704. https://doi.org/10.1111/jace.13991.
Hallstedt, B., 1990. Assessment of the CaO-Al2O3 system. J. Am. Ceram. Soc. 73, 15–23.
Hayashi, K., Hirano, M., Matsuishi, S., Hosono, H., 2002. Microporous crystal 12CaO·7Al 2 O 3 encaging abundant O - radicals. J. Am. Chem. Soc. 124, 738–739. https://doi.org/10.1021/ja016112n.
Hostomsky, J., Jones, A.G., 1991. Calcium carbonate crystallization, agglomeration and form during continuous precipitation from solution. J. Phys. D. Appl. Phys. 24, 165–170. https://doi.org/10.1088/0022-3727/24/2/012.
Imlach, J.A., Glasser, L.S.D., Glasser, F.P., 1971. Excess oxygen and the stability of 12CaO.7Al2O3. Cem. Concr. Res. (1), 57–61.
Jeevaratnam, J., Glasser, F.P., Glasser, L.S.D., 1964. Anion substitution and structure of 12CaO.7Al2O3. J. Am. Ceram. Soc. 47, 105–106. https://doi.org/10.1111/j.1151-2916.1964.tb15669.x.
Jerebtsov, D., Mikhailov, G., 2001. Phase diagram of CaO–Al2O3 system. Ceram. Int. 27, 25–28. https://doi.org/10.1016/S0272-8842(00)00037-7.
Koutsoukos, P.G., Kontoyannis, C.G., 1984. Precipitation of calcium carbonate in aqueous solutions. J. Chem. Soc. Faraday Trans. 1 Phys. Chem. Condens. Phases 80, 1181. https://doi.org/10.1039/f19848001181.
Langford, J.I., Wilson, A.J.C., 1978. Scherrer after sixty years: a survey and some new results in the determination of crystallite size. J. Appl. Crystallogr. 11, 102–113. https://doi.org/10.1107/S0021889878012844.
Lundquist, R.V., Leitch, H., 1963a. Solubility characteristics of monocalcium aluminate. US Dept. Inter. Bur. Mines 6294, 1–9.
Lundquist, R.V., Leitch, H., 1963b. Two Hydrated Calcium Aluminates Encountered in the Lime-Soda Sinter Process. US Dept. Inter. Bur. Mines, pp. 6335.
Lundquist, R.V., Leitch, H., 1964. Aluminum Extraction Characteristics of Three Calcium Aluminates in Water, Sodium Hydroxide, and Sodium Carbonate Solutions. Bureau of Mines, Boulder City.
Lutsyk, V.I., Zelenaya, A.E., Savinov, V.V., 2012. Phase trajectories in CaO-Al2O3-SiO2 melts. Crystallogr. Reports 57, 943–947. https://doi.org/10.1134/S1063774512070176.
Ma, C., Kampf, A.R., Connolly, H.C., Beckett, J.R., Rossman, G.R., Smith, S.A.S., Schrader, D.L., 2011. Krotite, CaAl2O4, a new refractory mineral from the NWA 1934 meteorite. Am. Mineral. 96, 709–715. https://doi.org/10.2138/am.2011.3693.
Mach, T., 2012. Energy Consumption in the Bayer Process. In: International Alumina Quality Workshop, pp. 375–378.
Mao, H., Hillert, M., Selleby, M., Sundman, B., 2006. Thermodynamic assessment of the CaO-Al2O3-SiO2 system. J. Am. Ceram. Soc. 89, 298–308. https://doi.org/10.1111/j.1551-2916.2005.00698.x.
Meyer, F.M., 2004. Availability of bauxite reserves. Nat. Resour. Res. 13, 161–172. https://doi.org/10.1023/B:NARR.0000046918.50121.2e.
Mills, K.C., Hayashi, M., Wang, L., Watanabe, T., 2013. The structure and properties of silicate slags. Treatise on Process Metallurgy. Elsevier Ltd. https://doi.org/10.1016/B978-0-08-096986-2.00008-4.
Momma, K., Izumi, F., 2011. VESTA 3 for three-dimensional visualization of crystal, volumetric and morphology data. J. Appl. Crystallogr. 44, 1272–1276. https://doi.org/10.1107/S0021889811038970.
Mondal, P., Jeffery, J.W., 1975. The crystal structure of tricalcium aluminate, Ca3Al2O6. Acta Crystallogr. B 31, 689–697. https://doi.org/10.1107/S0567740875003639.
Moolenaar, R.J., Evans, J.C., McKeever, L.D., 1970. The structure of the aluminate ion in solutions at high pH. J. Phys. Chem. 74, 3629–3636. https://doi.org/10.1021/j100714a014.
Mysen, B.O., 1990. Relationships between silicate melt structure and petrologic processes. Earth Sci. Rev. 27, 281–365. https://doi.org/10.1016/0012-8252(90)90055-Z.
Mysen, B.O., Virgo, D., Seifert, F.A., 1985. Relationships between properties and structure of aluminosilicate melts. Am. Mineral. 70, 88–105. https://doi.org/10.1007/BF00413348.
Nancollas, G., Reddy, M., 1971. The crystallization of calcium carbonate. II. Calcite growth mechanism. J. Colloid Interface Sci. 37, 824–830. https://doi.org/10.1016/0021-9797(71)90363-8.
Nurse, R.W., Welch, J.H., Majumdar, A.J., 1965a. The CaO-Al2O3 system in a moisture-free atmosphere. Trans. Br. Ceram. Soc. 64, 409–418.
Nurse, R.W., Welch, J.H., Majumdar, A.J., 1965b. The 12CaO.7Al2O3 Phase in the CaO-Al2O3 System. Trans. Br. Ceram. Soc 64, 323–332.
Pedersen, H., 1927. Process of Manufacturing Aluminum Hydroxide. 1618105.
Pitzer, K.S., 1973. Thermodynamics of electrolytes. I. Theoretical basis and general equations. J. Phys. Chem. 77, 268–277. https://doi.org/10.1021/j100621a026.
Rankin, G.A., Wright, F.E., 1915. The ternary system CaO-Al2O3-SiO2. Am. J. Sci. 39.
Roy, D.M., Roy, R., 1960. Crystalline solubility and zeolitic behavior in garnet phases in the system CaO-Al2O3-SiO2-H2O. In: Fourth international symposium on the chemistry of cement. Washington D.C, pp. 307–314.
Sabin, A., 2011. Problems in particle size: laser diffraction observations. Fine Part. Tecnol. 15, 35–43.
Safarian, J., 2018. Extraction of Iron and Ferrosilicon Alloys from Low-Grade Bauxite Ores, in: Extraction 2018, the Minerals. Metals & Materials Series. Springer International Publishing, Cham, pp. 825–837. https://doi.org/10.1007/978-3-319-95022-8_66.
Safarian, J., Kolbeinsen, L., 2016a. Sustainability in Alumina Production from Bauxite. In: Sustainable Industrial Processing Summit, pp. 75–82.
Safarian, J., Kolbeinsen, L., 2016b. Smelting-reduction of Bauxite for Sustainable Alumina Production. In: Sustainable Industrial Processing Summit, pp. 149–158.
Sellaeg, H., Kolbeinsen, L., Safarian, J., 2017. Iron Separation from Bauxite Through Smelting-Reduction Process. In: Minerals, Metals and Materials Series, pp. 127–135. https://doi.org/10.1007/978-3-319-51541-0_19.
Shannon, R.D., 1976. Revised effective ionic radii and systematic studies of interatomic distances in halides and chalcogenides. Acta Crystallogr. Sect. A 32, 751–767. https://doi.org/10.1107/S0567739476001551.
Shepherd, E.S., Rankin, G.A., Wrigth, F.E., 1909. The binary Systems of Alumina with silica, lime and magnesia.Pdf. Am. J. Sci. 28, 293–333.
Smith, P., 2009. The processing of high silica bauxites - review of existing and potential processes. Hydrometallurgy. https://doi.org/10.1016/j.hydromet.2009.04.015.
Söhnel, O., Mullin, J.W., 1982. Precipitation of calcium carbonate. J. Cryst. Growth 60, 239–250. https://doi.org/10.1016/0022-0248(82)90095-1.
Spanos, N., Koutsoukos, P.G., 1998. Kinetics of precipitation of calcium carbonate in alkaline pH at constant Supersaturation. Spontaneous and seeded growth. J. Phys. Chem. B 102, 6679–6684. https://doi.org/10.1021/jp981171h.
Sun, H., Wang, B., Yu, H., Bi, S., Tu, G.-F., 2010. Effect of Na2O on Alumina Leaching and Self-Disintegrating Property of Calcium Aluminate Slag. In: Light Metals 2010.
Sun, H.L., Wang, B., Zhang, J.X., Zong, S.F., 2014. Characterization and alumina leachability of 12CaO·7Al2O3 with different holding times. Adv. Mater. Sci. Eng. https://doi.org/10.1155/2014/730616.
Thorvaldson, T., Schneider, W.G., 1941. The composition of the "5:3" calcium aluminate. Can. J. Res. 19b, 109–115. https://doi.org/10.1139/cjr41b-015.
Wells, L.S., 1928. Reaction of water on calcium aluminates. Bur. Stand. J. Res. 1, 951. https://doi.org/10.6028/jres.001.034.
Whittington, B.I., Cardile, C.M., 1996. The chemistry of tricalcium aluminate hexahydrate relating to the Bayer industry. Int. J. Miner. Process. 48, 21–38. https://doi.org/10.1016/S0301-7516(96)00011-7.
Whittington, B.I., Fallows, T.M., Willing, M.J., 1997. Tricalcium aluminate hexahydrate (TCA) filter aid in the Bayer industry: factors affecting TCA preparation and morphology. Int. J. Miner. Process. 49, 1–29. https://doi.org/10.1016/S0301-7516(96)00035-X.
Yu, H., Pan, X., Wang, B., Zhang, W., Sun, H., Bi, S., 2012. Effect of Na2O on formation of calcium aluminates in CaO–Al2O3–SiO2 system. Trans. Nonferrous Met. Soc. China 22, 3108–3112. https://doi.org/10.1016/S1003-6326(11)61578-1.
Zhang, Y., Lü, W., Qi, Y., Zou, Z., 2016. Recovery of iron and calcium aluminate slag from high-ferrous bauxite by high-temperature reduction and smelting process. Int. J. Miner. Metall. Mater. 23, 881–890. https://doi.org/10.1007/s12613-016-1303-3.
Zhmoidin, G.I., Chatterjee, A.K., 1984. Conditions and mechanism of Interconvertibility of compounds 12CaO.7Al2O3 and 5CaO.3Al2O3. Cem. Concr. Res. 14, 386–396. https://doi.org/10.1016/0008-8846(84)90057-7.
Zhou, Y., Wu, L., Wang, J., Wang, H., Dong, Y., 2013. Alumina extraction from high-alumina ladle furnace refining slag. Hydrometallurgy. https://doi.org/10.1016/j.hydromet.2013.08.007.

Paper 5

Hydrometallurgy 191 (2020) 105184

Contents lists available at ScienceDirect

Hydrometallurgy

journal homepage: www.elsevier.com/locate/hydromet

The leachability of a ternary $CaO-Al_2O_3-SiO_2$ slag produced from smelting-reduction of low-grade bauxite for alumina recovery

Fabian Imanasa Azof[a,*], Michail Vafeias[b], Dimitrios Panias[b], Jafar Safarian[a]

[a] Norwegian University of Science and Technology (NTNU), Department of Materials Science and Engineering, Trondheim, Norway
[b] National Technical University of Athens (NTUA), School of Mining and Metallurgical Engineering, Athens, Greece

ARTICLE INFO

Keywords:
Low-grade bauxite
Smelting-reduction
Aluminate slag
Alumina
Leachability
Leaching residue

ABSTRACT

A combination of smelting-reduction of bauxite and leaching treatment of the produced slag for alumina recovery is known as the Pedersen process. The process is considered to be more sustainable for producing metallurgical-grade alumina than the Bayer process as it does not produce bauxite residue (red mud), which is one of the most abundant industrial byproducts in the world. In this work, the leachability of a ternary $CaO-Al_2O_3-SiO_2$ slag produced from smelting-reduction of low-grade bauxite has been studied. The obtained calcium aluminate-slag consists of $Ca_{12}Al_{14}O_{33}$ and $CaAl_2O_4$ phases with minor amounts of complex oxide phases. A leaching series have been carried out at different temperatures, $Na_2O_{(carbonate)}$:$Na_2O_{(caustic)}$ concentration ratios. The composition of solids and leaching liquors were analyzed for measuring the recovery of the aluminum and silicon. The results show that the highest aluminum extraction extent in the current study is 46.7%, which is achieved at a temperature of 75 °C, 1 atm, in 60 g/L $Na_2O_{(carbonate)}$ solution, in 30 min of leaching time. A passive calcium-containing layer at the slag's surface acts as a mass transfer barrier for the reactants and products of the leaching reactions, making their diffusion the rate-limiting step. A high concentration of $Na_2O_{(caustic)}$ may decrease the aluminum extraction of the slag as a result of insufficient carbonate anions in the system, where the dissolved aluminum reacts with the calcium cations and produce $3CaO{\cdot}Al_2O_3{\cdot}6H_2O$ phase.

1. Introduction

Excessive production of bauxite residue (red mud), which is estimated 150 million tonnes annually in 2017 (Tsesmelis, 2017) becomes one of the major concerns amongst alumina producers. The severe accidents on red mud dams occurred during the last decades (Norway's Norsk Hydro apologises for spills in Brazil river_2018.pdf WWW Document, 2018; Outrage as plant bosses acquitted over fatal toxic spill in Hungary WWW Document, 2016) boosted many research projects on red mud valorization worldwide. However, according to recent literature (Azof et al., 2018), none of them have been scaled up to commercial production due to economic reasons and particular challenges. In 1927, a Norwegian metallurgist named Harald Pedersen (1927) had patented a process for manufacturing aluminum hydroxide from ferruginous bauxite that was based on the combination of both pyro- and hydrometallurgical processes. The schematic flow sheet of the original Pedersen process is shown in Fig. 1. The process produces pig iron, metallurgical-grade alumina, and an inert leaching residue called grey mud, which can be used in the agriculture industry as a fertilizer or soil improver, and one of rare earth elements potential resource (Vafeias et al., 2018). Thus, the Pedersen process eliminates the red mud problem as encountered in the Bayer process.

The amount of the red mud produced in the Bayer process is positively related to the mass concentration of iron-bearing phases in the bauxite, which is evident as the composition of the red mud is dominated by iron oxide phases (Safarian and Kolbeinsen, 2016a). In alumina industries, bauxite with relatively low Al_2O_3/SiO_2 mass ratio is considered as low-grade bauxite. Meanwhile, bauxite with low Al_2O_3/Fe_2O_3 mass ratios can be regarded as low-grade bauxite as well (Blake et al., 1966). Although from a technical point of view bauxites with low Al_2O_3/Fe_2O_3 mass ratios can be treated with the Bayer process, however, from an economic point of view their treatment is unfavorably facing additionally the challenge of disposal of vast amounts of red mud produced as mentioned earlier. On the contrary, the Pedersen process seemed to be more advantageous for the treatment of low-grade bauxites. A relationship between the content of alumina and iron oxides in a typical bauxite and laterite deposit is reconstructed from Nielsen (1978) in Fig. 2, which shows that the Pedersen process is suitable for all grades of deposit in the particular compositions.

Furthermore, Smith (2009) states that bauxite with an Al_2O_3/SiO_2

* Corresponding author.
E-mail address: fabian.i.azof@ntnu.no (F.I. Azof).

https://doi.org/10.1016/j.hydromet.2019.105184
Received 20 April 2019; Received in revised form 20 September 2019; Accepted 17 October 2019
Available online 28 October 2019
0304-386X/

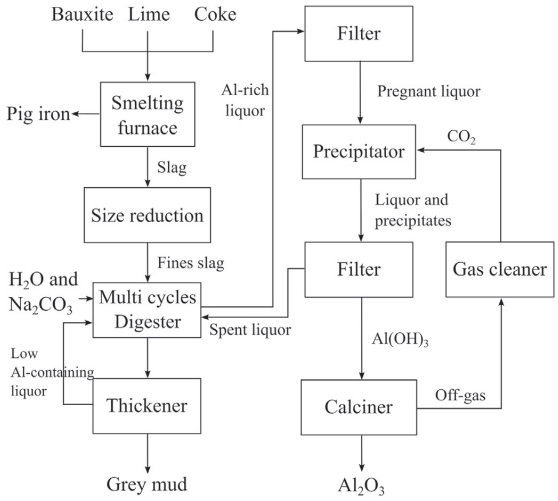

Fig. 1. A schematic flow sheet of the original Pedersen process.

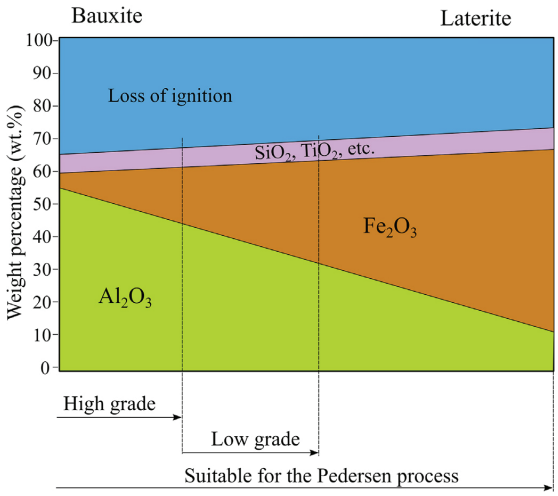

Fig. 2. The relationship between the content of alumina and iron oxide in a bauxite and laterite deposit, as was reconstructed after Nielsen (1978).

mass ratio < 6.25 or with a reactive silica content higher than 8 wt% is regarded as low-grade one, and is considered uneconomic for the Bayer process. This typical bauxite is not favorable for both the Bayer and the Pedersen process due to the silicon-bearing phases that may dilute into the solution during the digestion that needs a further desilication treatment. Table 1 shows the chemical composition of bauxites that were taken from several locations in the world.

Moreover, Fig. 3 shows the distribution of bauxites based on Al_2O_3/SiO_2 and Al_2O_3/Fe_2O_3 mass ratios that correspond to the bauxite ores in Table 1. In Fig. 3, we only consider the ratio between three major compounds, which are Al_2O_3, SiO_2, Fe_2O_3, and do not include TiO_2 as it has a relatively low concentration; < 4 wt%.

Norwegian University of Science and Technology (NTNU) through research domain 5-Materials and Society in SFI-metal production and National Technical University of Athens (NTUA) have initiated and started preliminary work on reviving the Pedersen process. The European Union under Horizon 2020 program also has launched ENSUREAL project (www.ensureal.com) that was based on the same process, where the two universities were also involved. Most of the authors' previous studies (Azof et al., 2018; Safarian, 2018a, 2018b; Safarian and Kolbeinsen, 2016a, 2016b; Sellaeg et al., 2017) focused on the pyro-metallurgical part, especially in the smelting-reduction process of low-grade bauxite ores. Our several studies (Azof et al., 2017, 2019a, 2019b) in the hydro-metallurgical part of the Pedersen process were mainly focused on the leaching characteristics of synthetic CaO-Al_2O_3 slags. In the meantime, there has been limited information provided from the literature regarding the leaching characteristics of ternary CaO-Al_2O_3-SiO_2 slag produced from the smelting-reduction of bauxite, as well as the physicochemical characteristics of residue (grey mud) generated from the leaching process. Therefore, in the current work, we study the leachability of a calcium aluminum silicate slag in different leaching conditions (e.g., temperature, Na_2CO_3-NaOH concentration of the leaching solution) for alumina recovery and investigate the chemical properties and morphology of grey mud.

2. Theoretical calculation

In the literature (Azof et al., 2018), the smelting-reduction process, which uses a mixture of lime, coke, and bauxite ore with CaO/Al_2O_3 molar ratios of 1.0–1.7 as the feed material, produces a calcium aluminate slag that contains leachable phases in a sodium carbonate solution. The known leachable phases are $CaAl_2O_4$ (denoted as CA) and $Ca_{12}Al_{14}O_{33}$ (denoted as $C_{12}A_7$) (Azof et al., 2017; Blake et al., 1966; Lundquist and Leitch, 1963a, 1963b). However, other calcium-aluminum-silicate phases, i.e., $CaAl_2SiO_6$ (denoted as CAS), $Ca_2Al_2SiO_7$ (denoted as C_2AS), may also coexist in the slag depending on the nature of silicon content of the bauxite ore.

The leaching reactions of CA and $C_{12}A_7$ phase in Na_2CO_3 solution and their Gibbs energy change values at room temperature can be written as follows (Azof et al., 2017; Blake et al., 1966; Lundquist and Leitch, 1963a, 1963b):

$$CaAl_2O_{4(s)} + Na_2CO_{3(aq)} = 2NaAlO_{2(aq)} + CaCO_{3(s)}$$
$$\Delta G°_{25°C} = -53.6\ kJ/molCaAl_2O_4 \quad (1)$$

$$Ca_{12}Al_{14}O_{33(s)} + 12Na_2CO_{3(aq)} + 5H_2O_{(l)} = 14NaAlO_{2(aq)} + 12CaCO_{3(s)} + 10NaOH_{(aq)}$$
$$\Delta G°_{25°C} = -745.2\ kJ/molCa_{12}Al_{14}O_{33} \quad (2)$$

Both Reactions (1) and (2) show that the formation of $NaAlO_2$ aqueous phase is favorable at room temperature. By using HSC™ v.9 equilibrium compositions module, we calculate the thermo-chemical equilibrium of CA and $C_{12}A_7$ leaching reactions at different temperatures. The result is shown in Fig. 4. The amount of input and list of output species used in the calculation are enclosed as a supplementary material of the article. The selection is based on the possible phases that may form in an aqueous solution that consists of Al–O–H–Ca–C–Na element according to the software's database.

As seen in Fig. 4, CA and $C_{12}A_7$ have a negligible amount in the equilibrium condition at the respected range of temperatures, which indicates that the phases are leachable in solution. The solid product of the leaching reactions in equilibrium, $CaCO_3$, has a constant amount regardless of the temperature.

3. Experimental

In this section, we describe the materials preparation, characterization of the samples, and leaching equipment and process parameters.

3.1. Slag preparation

The main material used in the current study is a slag that was produced by a smelting-reduction process of a mixture of bauxite, coke,

Table 1
Chemical composition of bauxites at several locations in the world.

No	Country, location	Reference	Composition (wt%)				
			Al_2O_3	SiO_2	Fe_2O_3	TiO_2	LOI
1	Greece, Parnassos-Ghiona	(Laskou et al., 2005)	62.5	2.1	19.5	2.9	13.0
2	Former Soviet Union, Severouraisk	(Hudson et al., 2000)	58.0	6.7	15.9	2.6	16.9
3	France, Southern Districts	(Hudson et al., 2000)	55.8	4.5	22.1	2.8	14.8
4	Former Yugoslavia, Mostar	(Hudson et al., 2000)	54.2	4.1	22.1	2.8	16.9
5	Indonesia, Bintan	(Hudson et al., 2000)	53.3	3.9	12.1	1.6	29.1
6	Iran, Sar-Faryab	(Zarasvandi et al., 2010)	52.5	6.4	19.7	3.3	18.1
7	Brazil, Trombetas	(Hudson et al., 2000)	51.8	5.1	13.9	1.2	28.0
8	Hungary, Halimba	(Hudson et al., 2000)	50.4	6.4	22.8	2.8	17.6
9	Guinea, Friguia	(Hudson et al., 2000)	49.5	6.2	14.3	1.6	28.4
10	Jamaica, Clarendon	(Hudson et al., 2000)	49.0	2.7	18.0	2.4	28.0
11	India, Orissa	(Hudson et al., 2000)	47.7	2.8	23.2	1.1	25.1
12	China, Guangxi	(Liu et al., 2009)	54.8	6.4	18.9	NA	NA
13	Guyana, Mackenzie	(Hudson et al., 2000)	59.2	4.9	2.9	2.4	30.5
14	Surinam, Onverdacht	(Hudson et al., 2000)	59.1	4.3	3.1	2.5	31.0
15	Australia, Weipa	(Hudson et al., 2000)	58.8	4.6	7.0	2.5	27.2
16	Guinea, Boke	(Hudson et al., 2000)	56.5	1.5	8.0	3.7	30.3
17	Surinam, Moengo	(Hudson et al., 2000)	53.8	4.2	10.4	2.8	28.8
18	China, Guizhou	(Liu et al., 2009)	65.7	9.0	5.5	NA	NA
19	China, Shanxi	(Liu et al., 2009)	62.3	11.6	5.8	NA	NA
20	China, Henan	(Liu et al., 2009)	65.3	11.8	3.4	NA	NA
21	China, Shandong	(Liu et al., 2009)	55.5	15.8	8.8	NA	NA
22	United States, Arkansas	(Hudson et al., 2000)	51.3	11.3	6.6	2.2	28.6
23	Australia, Darling Range	(Hudson et al., 2000)	36.9	26.4	16.4	1.1	19.2
24	Iran, Kanisheeteh	(Calagari and Abedini, 2007)	33.9	25.8	27.3	3.9	9.2
25	Indonesia low-grade, Bintan	(Kusrini et al., 2018)	35.5	33.7	29.7	1.1	NA

and lime from our previous study (Azof et al., 2018). The mixture was melted in an induction furnace at 1650 °C for one hour, then slowly cooled down to the room temperature. The iron oxide and other oxides in the bauxite were reduced to some extent and yield pig iron. On the other hand, the solidified oxides that mainly comprises of CaO–Al_2O_3–SiO_2 compound is the slag. The composition of bauxite and slag are presented in Table 2. The slag was pulverized by a RETSCH™ ring mill for 30 s in 700 rpm, which gives D_{50} 73.6 μm for the particle size, as measured by a laser particle analyzer after 2 min of ultrasound vibration.

3.2. Characterization of materials

3.2.1. Characterization of solids

We used non-destructive X-ray Fluorescence (XRF) SPECTRO XEPOS™ to measure the chemical composition of the grey mud produced from the leaching treatment. The Backscattered Electron (BSE) images and the multi-point Energy Dispersive Spectroscopy (EDS) of both the slag and grey mud were performed by using Hitachi SU6600™ Scanning Electron Microscope (SEM). Moreover, an X-ray elemental mapping of the grey mud's cross section was carried out using JEOL JXA- 8500F Electron Probe Micro Analyzer (EPMA) with Wavelength Dispersive X-ray Spectrometer (WDS). For mineralogy phase

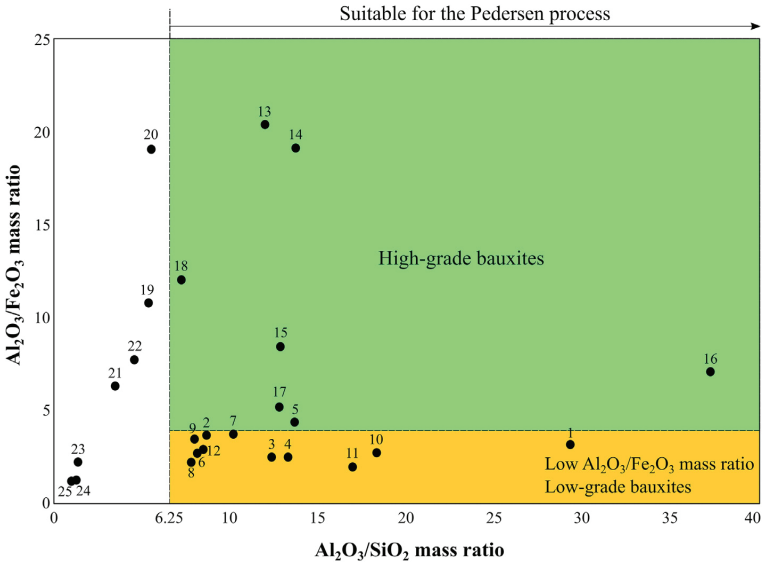

Fig. 3. Distribution of bauxite ores that is based on Al_2O_3/SiO_2 and Al_2O_3/Fe_2O_3 mass ratios. The ores in the green, gold, and white-colored areas indicate that they have relatively high Al_2O_3/SiO_2 and Al_2O_3/Fe_2O_3, low Al_2O_3/Fe_2O_3, and low Al_2O_3/SiO_2 mass ratios, respectively. (For interpretation of the references to colour in this figure legend, the reader is referred to the web version of this article.)

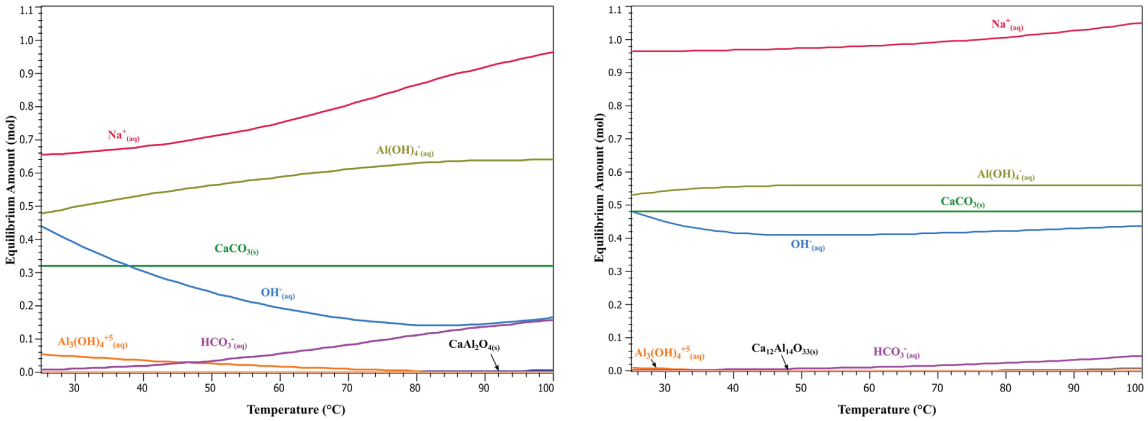

Fig. 4. The thermochemical simulation of the equilibrium amount of species in an aqueous solution at a temperature at 25–100 °C and 1 atm that corresponds to: (a) the leaching reaction of CA, (b) the leaching reaction of $C_{12}A_7$ phases.

Table 2
The composition of low-grade bauxite and slag.

Materials	Constituents (wt%)					
	Al_2O_3	CaO	SiO_2	TiO_2	Fe_2O_3	MgO
Bauxite	65.4	4.4	4.1	3.2	22.7	0.2
Slag	46.1	48.1	2.3	1.8	0.9	0.5

identification, we used Bruker D8 A25 DaVinci™ X-ray Diffractometer (XRD) with CuKα radiation, 10 to 75 deg. diffraction angle, 0.01 deg. step size, and 2.5 deg. for both primary and secondary soller slits.

3.2.2. Analysis of liquor samples

The liquor samples of the pregnant liquid solution (PLS) were taken after separating the solid and liquid by using an ashless grade of quantitative filter paper. Inductively Coupled Plasma Optical Emission Spectrometry (ICP-OES) was used to measure the concentration of aluminum and silicon of the PLS for observing the recovery of aluminum and silicon from the slag after the leaching treatment.

3.3. Leaching setup and process parameters

The leaching treatment was performed inside a Parr 4563 mini reactor, which is an Inconel alloys-based vessel with 600 mL capacity that is resistant to chemical attack. The reactor was heated through a conduction heating. It has a lid that is made of Teflon, which is fitted with a condenser for condensing the water vapors that allows the pressure inside of the reactor remained in ambient pressure, and at the same time keeps the liquid-solid (L/S) weight ratio of the system relatively constant. The temperature was measured with a Pt thermocouple and the stirring was performed through a mechanical stirrer. The thermocouple, stirrer, and heater were connected to Parr 4841, a Programmable Logic Controller (PLC), to set and measure the necessitate parameters during the leaching treatment. A schematic of the leaching setup is shown in Fig. 5.

The leaching solution used in this study has a constant concentration of 60 g/L Na_2O, which was made by mixing distilled water, Na_2CO_3 powder and NaOH pellet with 99.8 wt% and 99.0 wt% purity, respectively. The dissolved Na_2CO_3 and NaOH give an extent of Na_2O concentration of the solution that can be denoted as $Na_2O_{(carbonate)}$ and $Na_2O_{(caustic)}$, respectively. Moreover, the concentration mass ratio of $Na_2O_{(carbonate)}$ to $Na_2O_{(caustic)}$ in the solution was varied from 100:0, 85:15, 75:25, and 50:50. By this definition, a leaching solution with 0 wt%$Na_2O_{(caustic)}$ means that the solution contains 60 g/L of $Na_2O_{(carbonate)}$ (denoted as 100 wt% $Na_2O_{(carbonate)}$) and has no $Na_2O_{(caustic)}$. Also, using the same definition, a leaching solution with 50 wt%$Na_2O_{(caustic)}$ means that the solution consists of 30 g/L of $Na_2O_{(caustic)}$ and $Na_2O_{(carbonate)}$ each. The L/S mass ratio was kept at 20:1, and the leaching temperature variations, pressure, and leaching time were 45, 60, 75 °C, 1 atm, and 30 min, respectively.

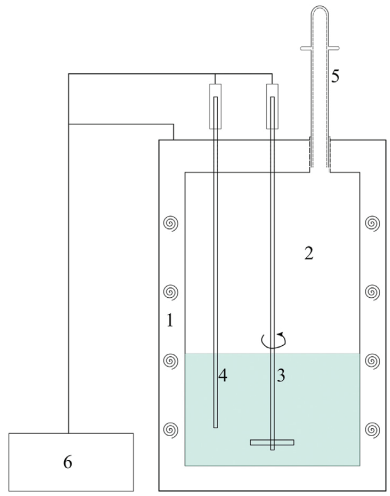

Fig. 5. A schematic of the leaching setup. Legend: 1. Heating element; 2. Inconel-based reactor; 3. Impeller; 4. Thermocouple; 5. Condenser; 6. Programmable Logic Controller (PLC).

4. Results and discussion

This section shows the results and discussion about the characterization of the slag before and after the leaching treatment, slag's leachability in different temperatures and concentration ratios of $Na_2O_{(carbonate)}$: $Na_2O_{(caustic)}$, and characteristics of the grey mud.

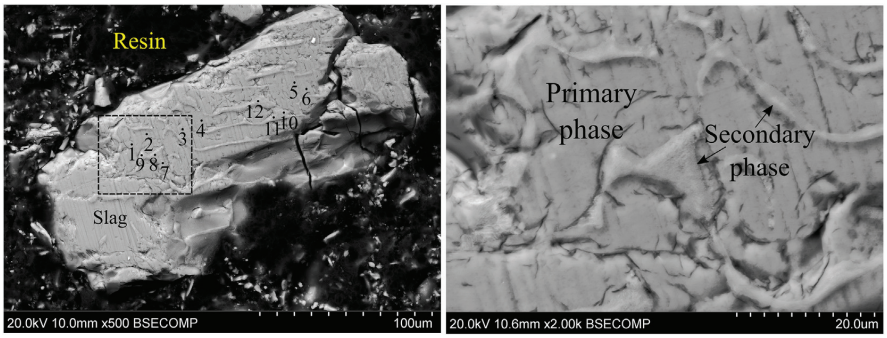

Fig. 6. BSE cross-sectional images of the slag in (a) 500× magnification and (b) 2000× magnification.

4.1. Characteristics of the slag

As seen previously in Table 2, the slag primarily consists of CaO, Al_2O_3, and relatively low concentration of SiO_2, TiO_2, and Fe_2O_3. Based on our previous X-ray Diffraction (XRD) analysis of the slag (Azof et al., 2018), the slag is dominated by $C_{12}A_7$ phase, while minor phases are CA and $Ca_5Al_6O_{14}$ (denoted as $5CaO{\cdot}3Al_2O_3$ or C_5A_3). Fig. 6(a) and (b) show the BSE cross-sectional image of the slag in 500× and 2000× magnification, respectively.

In Fig. 6(b), there are only two distinct phases that can be identified clearly, which can be denoted as a primary and secondary phase. The primary and secondary notations used in this study referring to their relative amount of each phase, which means that the primary phase is considered as a phase that has a higher amount compared to the secondary one. Moreover, Table 3 gives the EDS point analysis that corresponds to the numbers in Fig. 6(a). As seen, the primary phase consists of calcium and aluminum with 39.7 and 31.8 wt% on average, respectively, with no available result on Si and Ti element. However, later in a result of the WDS and X-ray mapping elements of the cross-section of grey mud using EPMA, we can see that Si and Ti also present in a low concentration on the primary phase. This small variance of elemental composition results may happen due to the different characterization techniques applied.

Furthermore, the secondary phase consists of 39.1 wt% Ca, 23.8 wt % Al, 3.7 wt% Si, and 3.4 wt% Ti, on average. The average of Ca/Al mass ratio of primary and secondary phase is 1.2 and 1.6, respectively. Based on the similarity of Ca/Al mass ratio between primary and $C_{12}A_7$ (Ca/Al mass = 1.3), we may conclude that the primary phase is the $C_{12}A_7$ phase. While the secondary phase is a calcium-alumina-silica-titanate bearing phase that was not detected on our previous XRD results, which is likely due to its low amount.

Table 3
The composition of the slag under different EDS points.

Phase	Location	Elements (wt%)					
		Ca	Al	Si	Ti	O	Ca/Al mass ratio
Primary	Point 1	43.1	28.1	NA	NA	28.8	1.5
	Point 2	38.1	31.5	NA	NA	30.4	1.2
	Point 3	39.4	32.9	NA	NA	27.7	1.2
	Point 4	39.0	32.1	NA	NA	28.9	1.2
	Point 5	39.8	33.3	NA	NA	26.9	1.2
	Point 6	38.6	32.9	NA	NA	28.5	1.2
	Average	39.7	31.8	NA	NA	28.5	1.2
Secondary	Point 7	36.6	25.1	3.7	3.4	31.2	1.5
	Point 8	39.6	22.6	4.1	3.6	30.1	1.8
	Point 9	37.9	24.2	3.8	3.6	30.5	1.6
	Point 10	41.4	21.8	4.2	3.6	29.0	1.9
	Point 11	39.4	23.4	3.7	3.6	29.9	1.7
	Point 12	39.9	25.8	2.7	2.3	29.3	1.5
	Average	39.1	23.8	3.7	3.4	30.0	1.6

4.2. Leachability of the slag

The subsection of leachability of the slag covers the aluminum and silicon recoveries based on the leaching series that was carried out. Also, it includes a thermodynamic perspective of the effect of different $Na_2O_{(carbonate)}$: $Na_2O_{(caustic)}$ concentration ratios to the aluminum recovery.

4.2.1. Aluminum and silicon extraction

A ternary CaO-Al_2O_3-SiO_2 phase diagram is shown in Fig. 7. It is shown the area of preferred slag compositions that are easily soluble in sodium carbonate solutions (green area) according to Blake et al. (1966). The calcium aluminate phases that are present in this area are only the CA as well as $C_{12}A_7$. Moreover, two red dotted lines have been drawn inside the green area representing the optimum slag compositions according to the Company, Norsk Aluminium (1944a,b). The line located closer to the CaO-SiO_2 axis represents a calcium aluminate slag with high silica content (> 10%) while the other represents a calcium aluminate slag with low silica content (< 10%). Finally, a yellow point shows the position of the studied slag in the ternary phase diagram after its normalization. For the normalization the lime reacted with TiO_2 was subtracted from the total CaO content of the slag assuming the formation of $CaO{\cdot}TiO_2$ phase.

As is seen, the composition of studied slag is located in the green area with the leachable slags and very close to the area of $C_{12}A_7$ phase, even though it is not located on one of the red lines showing the optimum compositions according to the Norsk Aluminium patent. An investigation about the optimum leach composition as claimed by the patent was reported elsewhere (Fursman et al., 1968).

Regarding the leachability of the slag, concentrations of Al and Si in the PLS after series of leaching are shown in Fig. 8. The results show that leaching solutions with 100 wt%$Na_2O_{(carbonate)}$ produce 5.4–5.7 g/L of aluminum in the PLS. Whereas, lower concentrations of aluminum between 2.3 and 4.1 g/L are produced from solutions with 50 wt% $Na_2O_{(caustic)}$ at any studied temperatures. Furthermore, silicon concentration in the PLS is ranging from 0.1–0.2 g/L. As shown in the figure, the higher aluminum concentration of the solution is, the higher concentration of silicon will be. It is also worth to note, the aluminum and silicon concentrations from solutions that were treated at 60 and 75 °C show similar results. We may suggest that for energy consumption and aluminum yield considerations in the current study, leaching at 60 °C is preferable than leaching at 75 °C.

In addition, the aluminum and silicon extraction of the slag after a

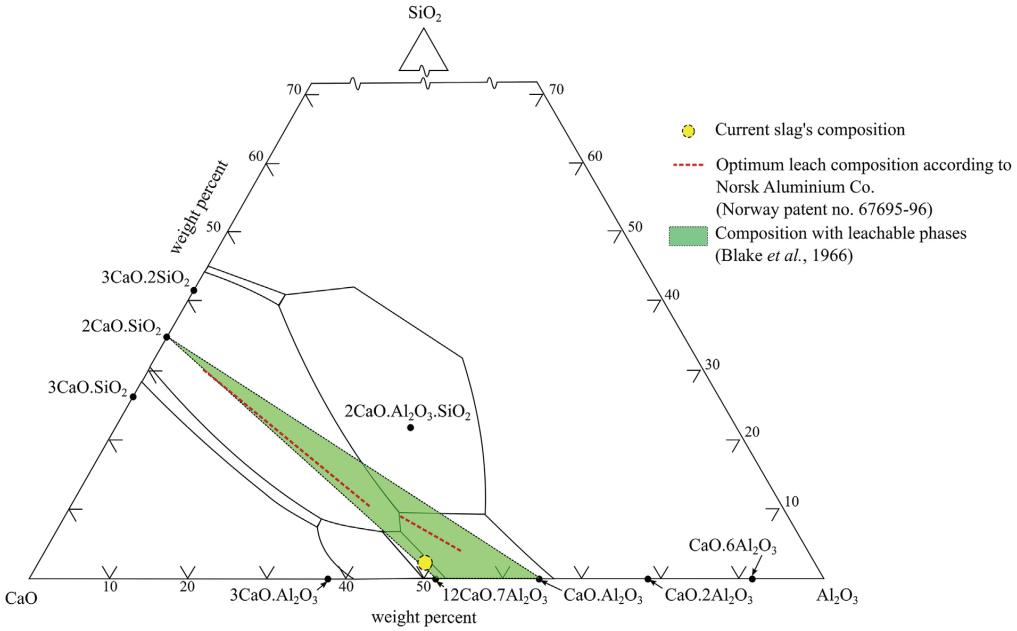

Fig. 7. A ternary $CaO\text{-}Al_2O_3\text{-}SiO_2$ phase diagram. A yellow dotted-circle indicating the composition of current slag, a red dash-line showing an optimum leach composition according to Norsk Aluminum Co. at low and high-silica content, and a light green area showing a composition that may form leachable phases. (For interpretation of the references to colour in this figure legend, the reader is referred to the web version of this article.)

series of leaching experiments is shown in Fig. 9(a) and (b), respectively. The highest aluminum extraction extent in the current study is 46.7%, which is achieved at a temperature of 75 °C and 1 atm in 100% $Na_2O_{(carbonate)}$ solution. While the lowest one is 18.9% that is attained at 45 °C in 50:50 of $Na_2O_{(carbonate)}$:$Na_2O_{(caustic)}$ concentration.

In Fig. 9(a), it is evident that the increasing of $Na_2O_{(caustic)}$ concentration ratio leads to the decreasing of aluminum extraction extent. The phenomena are apparent, as the increasing ratio of $Na_2O_{(caustic)}$ means that the available $Na_2O_{(carbonate)}$ in the solution is decreasing. The availability of $Na_2O_{(carbonate)}$ is necessary to proceed with the leaching reactions. Also, we find that the leaching at a high $Na_2O_{(caustic)}$ concentration generates grey mud that contains aluminum hydrated phase that results in loss of aluminum in the PLS, which will be discussed further in Section 4.3.2, which is on the phase of grey mud. Moreover, it seems that the differences in temperature give a mild effect on the extent of aluminum extraction. As the leaching time is

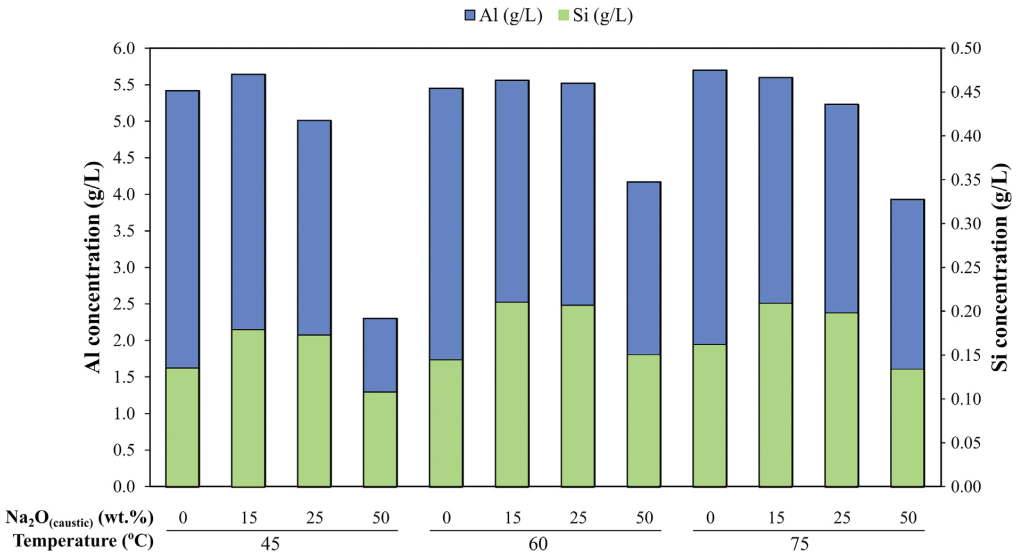

Fig. 8. Aluminum and silicon concentrations in the PLS obtained from different leaching conditions.

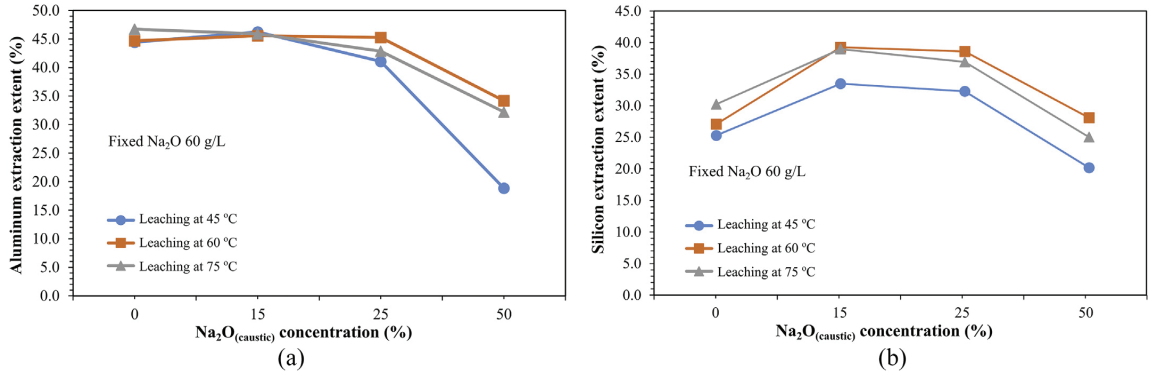

Fig. 9. (a) Aluminum and (b) silicon extraction extent of the leaching of slag. The leaching temperature and pressure are 45, 60, and 75 °C at 1 atm, and the leaching time is 30 min in 60 g/L Na_2O solution with different concentration of $Na_2O_{(caustic)}$.

considerably short (30 min), further experiments with varying more parameters (e.g., leaching time, stirring rate, particle size, L/S, etc.) are necessary to have a better understanding of the leaching kinetics of the slag.

On the other hand, as seen in Fig. 9(b), the silicon dissolution in the PLS substantially increases as the $Na_2O_{(caustic)}$ concentration ratio increases up to 25%, and then it decreases significantly together with the aluminum dissolution as the $Na_2O_{(carbonate)}$:$Na_2O_{(caustic)}$ concentration ratio is 50:50. It is confirmed in the literature (Fursman et al., 1968) that the excessiveness of $Na_2O_{(caustic)}$ concentration increases the silicon dissolution into the PLS, which is in agreement with the result at 15 and 25% of $Na_2O_{(caustic)}$ concentration. However, the mechanism of decreasing the extent of silicon dissolution at 50:50 $Na_2O_{(carbonate)}$:$Na_2O_{(caustic)}$ is unclear. We suggest that it is likely due to the decreasing rate of the main leaching reactions as the silicon in the PLS originates from the depolymerized slag that contains silicon impurity. The leaching mechanism is discussed later in Section 4.3.1.

Furthermore, similar to the aluminum extraction, we find that the leaching temperature gives a modest effect to the silicon dissolution as well. A low leaching temperature is more favorable than a high one to minimize the silicon dissolution in the PLS, which is in agreement with the original Pedersen patent where Pedersen used moderate temperatures for the digestion (Pedersen, 1927).

4.2.2. Effect of the sodium hydroxide concentration

In the original Pedersen (1927) process, it was stated that a "free sodium hydroxide" is needed to prevent the dissolution of silicon during the leaching, and if a larger proportion of "free sodium hydroxide" is used the alumina dissolution decreased. The latter claim is in agreement with the current results, considering the alumina dissolution decreases as the $Na_2O_{(caustic)}$ increases. However, in the current result, we could not observe the effect of "free sodium hydroxide" on the prevention or reduction of the silicon dissolution as the first sentence of the claim stated. Even though as small as 12 g/L of $Na_2O_{(caustic)}$ was added to the solution, the silicon extraction extent increases by approximately 10%, on average.

The discrepancy between the Pedersen patent and the current result might have resulted from the different digestion's concentration, the method applied, and the phase of calcium aluminate used, which can be described as following:

First, in the original Pedersen process, the aqueous solvent is a dilute solution that consists of 18–23 g/L $Na_2O_{(carbonate)}$ in which the amount of "free sodium hydroxide" is about 10 wt% of the amount of total carbonate. Whereas, in the current study, we use up to 60 g/L $Na_2O_{(carbonate)}$, and the addition of NaOH is larger than the Pedersen, which is amounted from 13 to 75 wt% of the total carbonate.

Second, the Pedersen original patent uses two or more countercurrent leaching steps, where an excess of slag is charged to the first leachate to lower the SiO_2 content in the final solution. Also, the filtrate from the CO_2 precipitation stage that contains a high concentration of Na_2CO_3 is charged to the second or final extraction stage, which allows the ratio of free Na_2CO_3 over the calcium aluminate is maintained. On the other hand, in the current study, we performed a single leaching stage experiment in a relatively shorter leaching time compared to the original patent.

Third, according to Fursman et al. (1968), the $Na_2O_{(caustic)}$ concentration of the leachate shall be controlled as if it excessive then the silicon dissolution increases, and when it is too low, the $Al_2O_3{\cdot}H_2O$ precipitates and become lost in the grey mud. They claimed that introducing CO_2 gas during the leaching would be necessitated to control the $Na_2O_{(caustic)}$ or $OH^-_{(aq)}$ level, as shown in the Reaction (3).

$$CO_{2(g)} + 2OH^-_{(aq)} = CO_3^{2-}{}_{(aq)} + H_2O_{(l)}$$
$$\Delta G^o_{25^oC} = -55.9\ \text{kJ/mol}CO_2 \quad (3)$$

The leaching reaction between $C_{12}A_7$ in the slag with Na_2CO_3 generates NaOH. Therefore, they control the $Na_2O_{(caustic)}$ concentration during the leaching so that the $Na_2O_{(caustic)}$ of the solution is within the prescribed "limit" and, subsequently, use the produced $CO^{2-}_{3(aq)}$ to react with the remaining $C_{12}A_7$ phase. Fursman et al. used a leaching solution that consists of 26 g/L of $Na_2O_{(carbonate)}$. On the contrary, we did not introduce CO_2 gas into the solution during the leaching as we used Na_2CO_3 concentration three times higher than they did. As seen in the Reaction (3), the use of CO_2 gas generates $CO^{2-}_{3(aq)}$ in the solution, which means more of free-Na_2CO_3 is available in the system and may accelerate the production of $CaCO_3$-layer at the surface of slag. The $CaCO_3$ layer at the slag's surface is not beneficial to the aluminum extraction extent that is later will be discussed in Section 4.3.

The effect of sodium hydroxide concentration on the alumina dissolution can be explained from a thermodynamic perspective. The Gibbs energy change of Reaction (2) can be written as in Eq. (4).

$$\Delta G_2 = \Delta G_2^\circ + RT \times \ln K_{eq} \quad (4)$$

where $\triangle G_2$ and $\triangle G^\circ{}_2$ are the change of Gibbs energy in Reaction (2) at non–standard and standard condition, respectively. R, T, and K_{eq} are the gas constant, temperature, and equilibrium constant, respectively. The equilibrium constant can be defined by the molar activities (a) ratio between product and reactant of the coexisting phases, which is shown in Eq. (5).

$$K_{eq} = \frac{(a_{NaAlO_2})^{14} \times (a_{NaOH})^{10}}{(a_{Na_2CO_3})^{12} \times (a_{H_2O})^5} \quad (5)$$

If K_{eq} were higher than one, then the $\triangle G_2$ tends to positive values and reaction would move favorably to the left. Likewise, if K_{eq} were lower than one, then the $\triangle G_2$ tends to negative values and reaction would move to the right. The molar activity of an aqueous species is a function of the molar activity coefficient and concentration of the species in the system. Moreover, according to the Le Chatelier principle, if any system at equilibrium is disturbed by changing a parameter affecting it (e.g., concentration) the position of equilibrium moves to counteract the change. In other words, the position of equilibrium would be changed by manipulating the concentration of, for instance, the $Na_2O_{(caustic)}$. The addition of $Na_2O_{(caustic)}$ concentration in the system would shift the equilibrium to the left side of reaction as the K_{eq} value increases, and then decrease the dissolution of alumina to some extent. Another result and discussion on the high $Na_2O_{(caustic)}$ concentration effects on the aluminum extraction based on the phases obtained on the grey mud will be discussed in the Section 4.3.2.

4.3. Characteristics of the grey mud

Results of the BSE cross-section, phase identification, and morphology of the grey mud are presented and discussed in the current section.

4.3.1. Cross-section analysis of the grey mud

The BSE cross-sectional image of the grey mud obtained after the leaching treatment of the slag with 100% $Na_2O_{(carbonate)}$ solution at 45 °C is shown in Fig. 10(a). Next to the figure, an X-ray mapping of several elements of the slag is shown. Subsequently, a normalized WDS point analysis is presented in Table 4. As seen, the grey mud consists of an unreacted slag and a layer that is relatively uniform covering the unreacted slag's surface. Similar to the unleached slag in Fig. 6, the unreacted slag also consists of the primary and secondary phases. The primary phase is indicated as the $C_{12}A_7$ phase, and consists of 46.9 wt% CaO and 52.0 wt% Al_2O_3, on average, with a small number of impurities, i.e., SiO_2, MgO, TiO_2. Meanwhile, the secondary phase consists of 44.1 wt% CaO, 41.0 wt% Al_2O_3, 9.4 wt% SiO_2, 4.9 wt% TiO_2, on average. Moreover, the calcium-containing layer has 50.4 wt% CaO on average, and relatively low Al_2O_3, SiO_2, TiO_2, which is 0.5, 0.2, and 0.4 wt% on average, respectively.

Furthermore, the X-ray mapping element in Fig. 10(b) shows that the formed layer has a higher concentration of Ca and C than that of the unreacted slag. This indicates the layer is a calcium carbonate-containing phase. Also, a small fraction of silicon, titanium, and magnesium elements are detected on the layer as supported by the WDS result in Table 4. It is important to note here that the area of the secondary phase, which is noticeable on the figure from its high concentration of silicon, titanium, and magnesium, also co-exists with the calcium carbonate on the formed layer. This suggests that the secondary phase is a non-leachable phase that remains in its solid phase after the leaching, in which eventually in equilibrium with the calcium carbonate produced from the leaching reaction.

According to the observations above, we propose a leaching mechanism of a calcium aluminate slag that has both leachable and non-leachable phases, which is shown schematically in Fig. 11.

The leaching mechanism can be divided to three main stages:

(a) The initial stage. The slag consists of a leachable $C_{12}A_7$ phase (shown as number 1) and non-leachable Ca-Al-Si-Ti bearing phase (shown as number 2). At this stage, the leaching reactions occur at the surface of slag particles between the leachable phase and the sodium carbonate solution. In a solid/liquid reaction, a boundary layer is created between the interfaces of the surface with the bulk fluid. The boundary layer is the layer of medium that is not very mobile due to solvent molecules are bound to the surface, and layers of solvent molecules near the surface tend to associate with surface and near-surface molecules (Free, 2013). That is to say, it is essential for the leaching reactions to start by transporting the ionic species (CO_3^{2-}, Na^+) through the bulk fluid towards to adjacent of the surface of the slag and subsequently followed by diffusing the ions through the boundary layer. Furthermore, the products of the leaching reaction are $CaCO_3$ (shown as number 3), $NaAlO_2$, and NaOH. As shown in the WDS result in Table 4, it is confirmed that the $C_{12}A_7$ phase contains small impurities, e.g., SiO_2. We suggest that the impurities are small (submicron) intrusions of the secondary phase in the primary one that is difficult to observe by SEM. Also, we propose that as the leachable phases digested, the impurities are "liberated" from the phase, and therefore, dissolved in the pregnant liquid solution as aqueous phases.

(b) The $CaCO_3$ growth stage. According to the leaching Reactions (1) and (2), the $CaCO_3$ is the only solid product produced from the

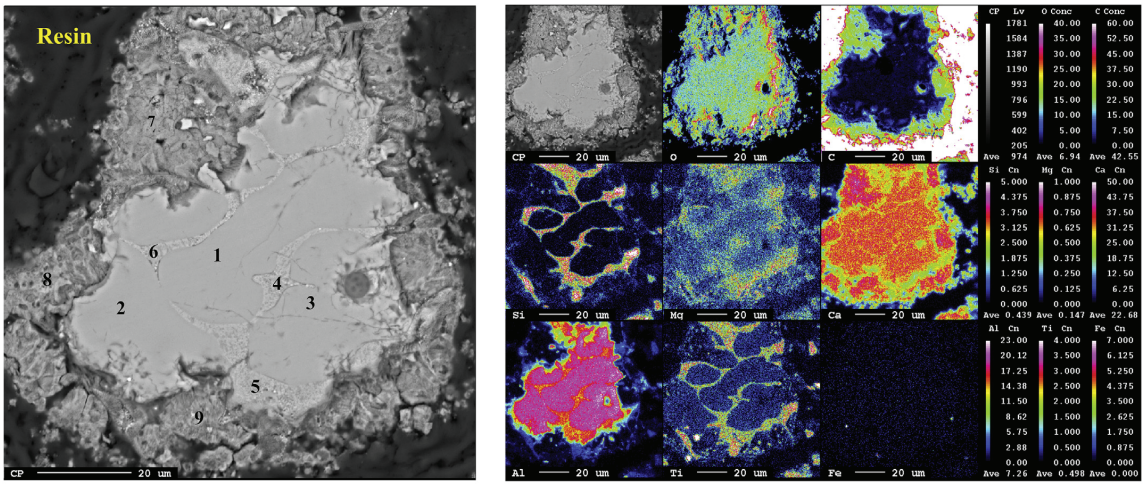

Fig. 10. Image of the cross-section of grey mud obtained: (a) BSE of grey mud, and (b) X-ray mapping of several elements after the leaching treatment of the slag in 100%$Na_2O_{(carbonate)}$ solution, at 45 °C and 1 atm in 30 min.

Table 4
A normalized WDS point analysis.

Points	CaO (wt%)	Al_2O_3 (wt%)	SiO_2 (wt%)	MgO (wt%)	P_2O_5 (wt%)	TiO_2 (wt%)	MnO (wt%)	FeO (wt%)	CO_2[a](wt%)
1–3	46.9	52.0	0.2	0.2	2×10^{-2}	0.6	NA	2×10^{-2}	NA
4–6	44.1	41.0	9.4	0.5	1×10^{-2}	4.9	4×10^{-2}	3×10^{-2}	NA
7–9	50.4	0.5	NA	NA	NA	NA	NA	NA	48.3

[a] Where CO_2 in carbonate phase.

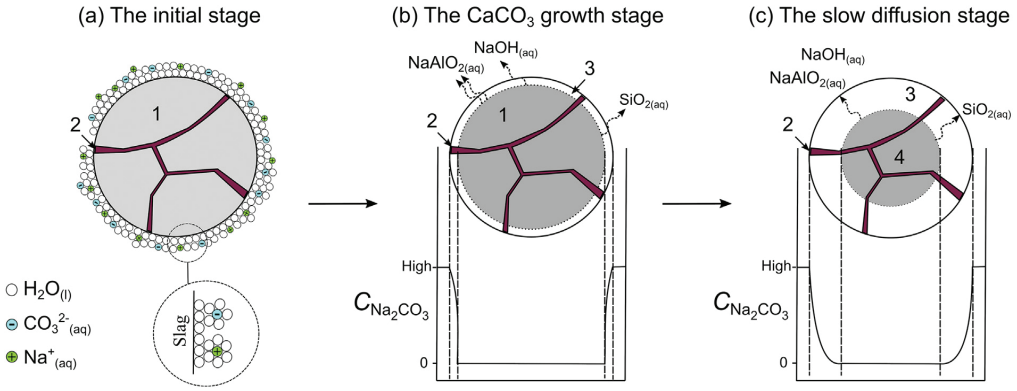

Fig. 11. The leaching mechanism of a slag that consists of three stages; the initial, the $CaCO_3$ growth, and the slow diffusion stages. Legend: 1. Leachable mayenite phase; 2. Unleachable Ca-Al-Si-Ti bearing phase; 3. $CaCO_3$; 4. Unreacted slag.

leaching. It nucleates and grows on a substrate, which is the surface of the slag. The $CaCO_3$ grows uniformly and forms a passive layer. Due to the formation of this passive layer, the Na_2CO_3 concentration may decrease gradually from the outer surface of the layer until the surface of the unreacted slag. On the other hand, the unleached phase remains in its solid phase, as the phase does not react with the Na_2CO_3.

(c) The slow diffusion stage. The Na_2CO_3 diffuses slowly through the layer, as the medium is relatively dense. However, we can see in Fig. 9 that the layer has some visible cracks that may allow the Na_2CO_3 propagate to the core. If there is no new crack-path nor pores formed during the leaching, thus, in the end, we may assume that there is a stage when Na_2CO_3 does not suffice for the leaching reaction on the surface of the unreacted slag (shown as number 4). When this stage happens then, the leaching extent progresses slowly, and the amount of mass transfer from the unreacted slag to the pregnant liquid solution is negligible.

4.3.2. Phases of the grey mud

The XRD results of the grey mud in Fig. 12 confirms the calcium-containing layer is the $CaCO_3$ phase that is either in the form of calcite or vaterite. We do not observe the peaks of vaterite on the grey mud obtained from $Na_2O_{(caustic)}$-addition solution. We suggest that the formation of vaterite or calcite are affected by the $Na_2O_{(caustic)}$ concentration of the system, i.e., pH., which is in agreement with the literature (Söhnel and Mullin, 1982). Moreover, the remaining peaks are $C_{12}A_7$ and C_5A_3 as the unleached slag. The formation of $CaCO_3$ on the slag's surface gives valuable information on the leaching behavior of the slag. The passive layer of $CaCO_3$ does not react with the leaching agent Na_2CO_3, which slows the leaching Reactions (1) and (2) to occur as mentioned in the previous section; hence we may say that the reaction is diffusion rate limiting.

Another interesting observation from the XRD result is the precipitation of $Ca_3Al_2(OH)_{12}$ (denoted as $3CaO{\cdot}Al_2O_3{\cdot}6H_2O$) phase in the residue obtained from the leaching solution that contains 25 to 50% $Na_2O_{(caustic)}$. The $3CaO{\cdot}Al_2O_3{\cdot}6H_2O$ phase is a hydrogarnet solid phase that theoretically consists of 26.9 wt% Al_2O_3. The precipitation of the phase causes loss of alumina during the leaching. The high content of $Na_2O_{(caustic)}$ appears to be the main reason why the hydrogarnet phase precipitates, which is in agreement with the result from literature (Lundquist and Leitch, 1963a, 1963b). The literature stated that as the carbonate ion concentration in the solution increased from 0 to 100%, the amount of $3CaO{\cdot}Al_2O_3{\cdot}6H_2O$ precipitated showed a corresponding decrease, and $CaCO_3$ was precipitated instead. In other words, if the leaching system has a high $Na_2O_{(carbonate)}$ concentration of the total alkali, wherein this study is higher than 85%, then the $CaCO_3$ is favorably precipitated instead of $3CaO{\cdot}Al_2O_3{\cdot}6H_2O$ phase. The carbonate anions in the solution react with the calcium cations from the depolymerization of the calcium aluminate slag. Likewise, if the number of carbonate anions is insufficient, then the dissolved aluminum species reacts with the calcium cations and produce $3CaO{\cdot}Al_2O_3{\cdot}6H_2O$.

Moreover, Table 5 shows the XRF analysis of the grey mud produced from 45, 60, and 75 °C leaching temperature in 100% $Na_2O_{(carbonate)}$ solution. The composition is shown after a loss on ignition (LOI) test by heating the grey mud inside a muffle furnace at 950 °C, air atmosphere, for about one hour. The tests resulted in 21.2 wt% of mass losses on average, which is due to the decomposition of $CaCO_3$ to CaO and $CO_{2(g)}$. The primary phase of the grey mud is CaO and then followed by a relatively low amount of Al_2O_3 (7 ± 1 wt%).

4.3.3. Morphology of the grey mud

The morphology of different grey muds has been investigated and is shown in Fig. 13. Fig. 13(a) and (b) show the morphology of grey mud (hereafter named GM-A) produced from 100% $Na_2O_{(carbonate)}$ solution at 45 °C and 1 atm in 1000× and 3000× magnification, respectively. Meanwhile, Fig. 12(c) and (d) are the morphology of other grey mud (hereafter named GM-B) produced from 50:50 concentration ratio of $Na_2O_{(carbonate)}$:$Na_2O_{(caustic)}$ solution in 1000× and 2000× magnification, respectively.

The GM-A consists of calcite and vaterite crystals. A calcite crystal has a cubical shape, whereas vaterite has a spherical one (Ni and Ratner, 2008; Wang et al., 2013). Vaterite is the least stable

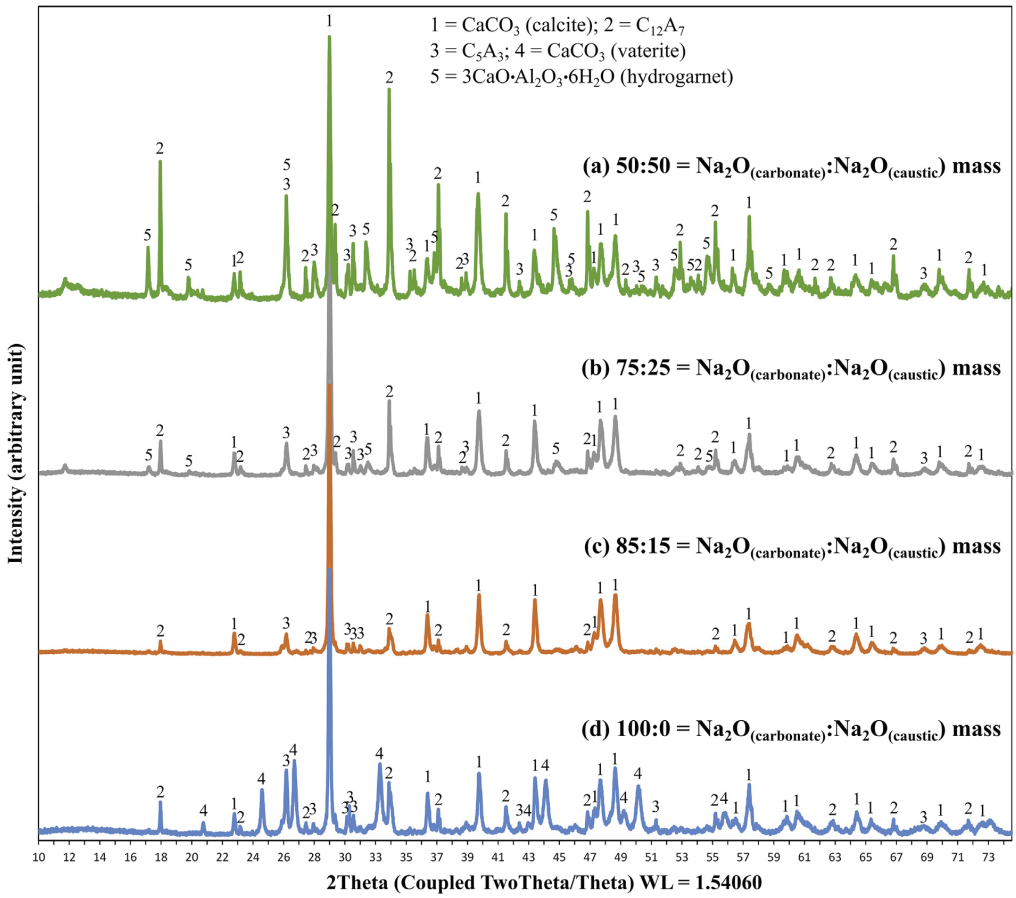

Fig. 12. XRD patterns of the grey muds obtained from the leaching treatment of the slag in 60 g/L Na_2O, at 45 °C, 1 atm, in 30 min under different concentration ratios of $Na_2O_{(carbonate)}$:$Na_2O_{(caustic)}$; (a) 50:50, (b) 75:25, (c) 85:15, (d) 100:0.

Table 5
The XRF analysis of grey mud after an LOI test.

Constituents	Leaching temperature		
	45 °C (wt%)	60 °C (wt%)	75 °C (wt%)
CaO	64.0	57.9	63.8
Al_2O_3	7.8	5.9	5.9
SiO_2	2.2	1.8	1.7
TiO_2	2.9	3.1	3.1
Na_2O	2.2	2.1	2.1
Fe_2O_3	1.0	1.3	1.5
MgO	0.6	0.5	0.5
P_2O_5	0.1	4.2×10^{-2}	1.1×10^{-2}
V_2O_5	4.3×10^{-2}	3.5×10^{-2}	3.3×10^{-2}
Cr_2O_3	5.9×10^{-2}	5.3×10^{-2}	5.9×10^{-2}
MnO	6.4×10^{-2}	6.5×10^{-2}	6.4×10^{-2}
LOI	17.7	25.9	19.9

thermodynamic form of $CaCO_3$ compared to other polymorphs (e.g., aragonite and calcite) (Ni and Ratner, 2008). However, the polymorphs could exist at the same time depending on the condition and kinetics of the transformation (Dickinson and McGrath, 2004). In an aqueous solution, vaterite can transform to aragonite in 60 min at 60 °C and to calcite in 24 h at room temperature as demonstrated by Ogino et al. (1987).

On the other hand, the GM-B consists of calcite, and a fibrous-like shape, which incorporates and forming a network structure to other grains. The fibrous-like shape does not resemble the morphology of any un-hydrated $CaCO_3$ polymorphs, i.e., vaterite, aragonite, and calcite. Also, the fibrous-like shape does not resemble a morphology of typical hydrogarnet crystal, which is an octahedral according to the literature (Kyritsis et al., 2009). However, an observation of the interaction between kaolinite ($Al_2Si_2O_5(OH)_4$) and portlandite ($Ca(OH)_2$) solution made by Donchev et al. (Donchev et al., 2010) showed that fine-needle and fibrous-like products could be interconnected with hydrogarnet crystals. They have assumed that the fibrous-like product is a mixture of primarily formed gehlenite hydrate ($2CaO{\cdot}Al_2O_3{\cdot}SiO_2{\cdot}8H_2O$), hydrogarnet, and calcium-silicate-hydrate gel. Thus, it is very likely that the fibrous-like shape of the GM-B in the current study is a calcium-silicate-hydrate phase that incorporates the hydrogarnet crystals.

5. Conclusion

The leaching treatment of a ternary $CaO\text{-}Al_2O_3\text{-}SiO_2$ slag produced from smelting-reduction of low-grade bauxite was carried out at 45, 60, and 75 °C and 1 atm in 30 min with different proportion $Na_2O_{(carbonate)}$ and $Na_2O_{(caustic)}$ with a fixed liquid-solid ratio 20 mL/g and

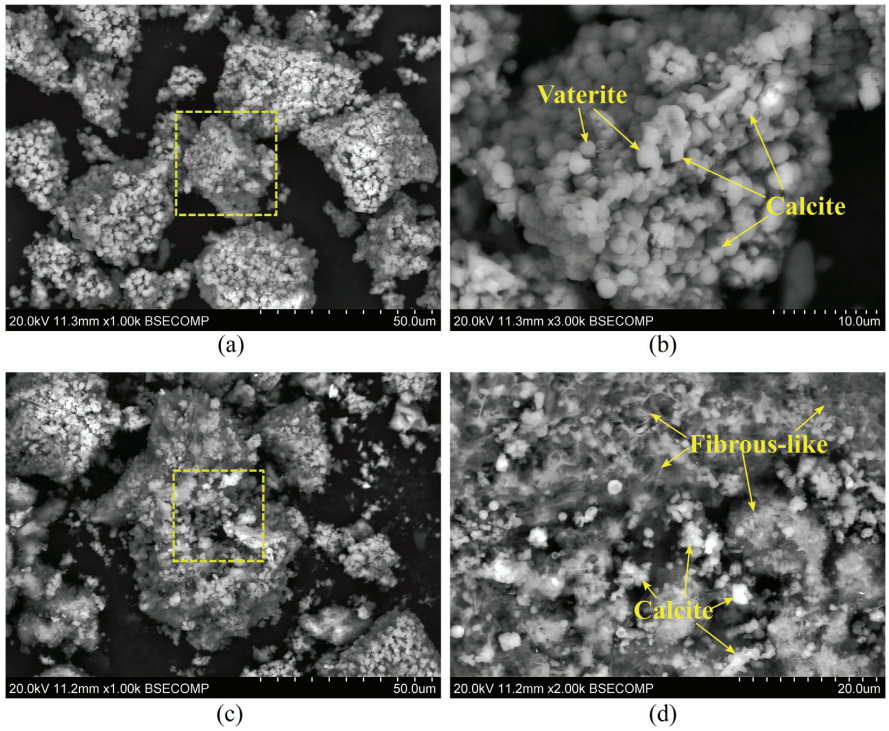

Fig. 13. BSE images of the morphology of the grey mud obtained after leaching of the slag in the 100% $Na_2O_{(carbonate)}$ solution at 45 °C in 30 min, in (a) 1000× and (b) 3000× magnification. Meanwhile, (c) and (d) are BSE images of grey mud obtained after leaching of the slag in the 50:50 $Na_2O_{(carbonate)}$:$Na_2O_{(caustic)}$ solution in 1000 and 2000× magnification, respectively.

concentration of 60 g/L Na_2O. The leaching characteristics can be summarized as follows:

(1) The leaching reaction of calcium-aluminate phases in a sodium carbonate solution is fast and temperature gives mild effect to the aluminum extraction in the first 30 min of the reaction.
(2) The addition of $Na_2O_{(caustic)}$ in the solution decreases the aluminum dissolution of the slag, while it increases the silicon dissolution into the pregnant liquid solution.
(3) The calcite-containing layer formed and distributed around the surface of the slag as the leaching reactions progress.
(4) The kinetics of leaching reaction appears to be diffusion rate limited as the passive calcium carbonate-containing layer formed at the unreacted surface of slag and may inhibit the progress of leaching reactions.

The results obtained from the current study may pave a new way to utilize $CaO\text{-}Al_2O_3\text{-}SiO_2$ slag more effectively. The slow diffusion of Na_2CO_3 to the unreacted $12CaO{\cdot}7Al_2O_3$ phase due to the formation of the calcite-containing layer at the surface of slag is suggested to be the reaction limiting. Therefore, leaching that employs a mechanochemical treatment such as wet grinding, or a sonochemical treatment using ultrasound, can be used to break the layer during the leaching. Such treatments may allow the Na_2CO_3 diffuse to and attack the unreacted $12CaO{\cdot}7Al_2O_3$, and achieve a high aluminum extraction extent.

Acknowledgement

The NTNU has funded the research and supported by the Research Domain 5 – Materials and the Society in SFI Metal Production (Project no. 237738). The School of Mining and Metallurgical Engineering, NTUA, is acknowledged for the use of leaching reactor, ICP-OES, and XRF analyzer. The scientific support from the ENSUREAL Horizon 2020 project is also acknowledged.

Appendix A. Supplementary data

Supplementary data to this article can be found online at https://doi.org/10.1016/j.hydromet.2019.105184.

References

Azof, F.I., Kolbeinsen, L., Safarian, J., 2017. The Leachability of Calcium Aluminate Phases in Slags for the Extraction of Alumina, in: Travaux 46, Proceedings of 35th International ICSOBA Conference. ICSOBA, Hamburg, pp. 243–253.
Azof, F.I., Kolbeinsen, L., Safarian, J., 2018. Characteristics of calcium-aluminate slags and pig Iron produced from smelting-reduction of low-grade bauxites. Metall. Mater. Trans. B Process Metall. Mater. Process. Sci. 49, 2400–2420. https://doi.org/10.1007/s11663-018-1353-1.
Azof, F.I., Kolbeinsen, L., Safarian, J., 2019a. Kinetics of the leaching of alumina-containing slag for alumina recovery. Proc. EMC 2019, 511–526.
Azof, F.I., Yang, Y., Panias, D., Kolbeinsen, L., Safarian, J., 2019b. Leaching characteristics and mechanism of the synthetic calcium-aluminate slags for alumina recovery. Hydrometallurgy 185, 273–290. https://doi.org/10.1016/j.hydromet.2019.03.006.
Blake, H.E., Fursman, O.C., Fugate, A.D., Banning, L.H., 1966. Adaptation of the Pedersen Process to the Ferruginous Bauxites of the Pacific Northwest. Bureau of Mines US Department of the Interior.
Calagari, A.A., Abedini, A., 2007. Geochemical investigations on Permo-Triassic bauxite horizon at Kanisheeteh, east of Bukan, West-Azarbaidjan, Iran. J. Geochem. Explor. 94, 1–18. https://doi.org/10.1016/j.gexplo.2007.04.003.
Company, Norsk Aluminium, 1944a. Process for the Production of Calcium Aluminate Slags Containing Less Than Approximately 10 Percent Silica. pp. 67696.
Company, Norsk Aluminum, 1944b. Process for the Production of Calcium Aluminate Slags Containing more Than 10 Percent Silica. pp. 67695.
Dickinson, S.R., McGrath, K.M., 2004. Aqueous precipitation of calcium carbonate

modified by hydroxyl-containing compounds. Cryst. Growth Des. 4, 1411–1418. https://doi.org/10.1021/cg049843i.
Donchev, I., Ninov, J., Doykov, I., Petrova, N., Dimova, L., 2010. On the formation of cement phases in the course of interaction of kaolinite with portlandite. J. Univ. Chem. Technol. Metall. 45, 391–396.
Free, M.L., 2013. Hydrometallurgy: Fundamentals and Applications. John Wiley & Sons, Inc, New Jersey.
Fursman, O.C., Blake Jr., H.E., Mauser, J.E., 1968. Recovery of Alumina and Iron from Pacific Northwest Bauxites by the Pedersen Process. (Albany).
Hudson, L.K., Misra, C., Perrotta, A.J., Wefers, K., Williams, F.S., 2000. Aluminum Oxide, in: Ullmann's Encyclopedia of Industrial Chemistry. Wiley-VCH Verlag GmbH & Co, KGaA, Weinheim, Germany. https://doi.org/10.1002/14356007.a01_557.
Kusrini, E., Harjanto, S., Herdino, F., Prasetyanto, E., Rahman, A., 2018. Effect of mechanochemical and roasting techniques for extraction of rare earth elements from Indonesian low-grade bauxite. IOP Conf. Ser. Mater. Sci. Eng. 316, 012025. https://doi.org/10.1088/1757-899X/316/1/012025.
Kyritsis, K., Meller, N., Hall, C., 2009. Chemistry and morphology of hydrogarnets formed in cement-based CASH hydroceramics cured at 200° to 350°C. J. Am. Ceram. Soc. 92, 1105–1111. https://doi.org/10.1111/j.1551-2916.2009.02958.x.
Laskou, M., Economou-Eliopoulos, M., Mitsis, I., 2005. Bauxite ore as an energy source for bacteria driving iron-leaching and bio-mineralization. Hell. J. Geosci. 45, 163–174.
Liu, W., Yang, J., Xiao, B., 2009. Review on treatment and utilization of bauxite residues in China. Int. J. Miner. Process. 93, 220–231. https://doi.org/10.1016/j.minpro.2009.08.005.
Lundquist, R.V., Leitch, H., 1963a. Solubility characteristics of monocalcium aluminate. US Dept. Inter. Bur. Mines 6294, 1–9.
Lundquist, R.V., Leitch, H., 1963b. Two hydrated calcium aluminates encountered in the lime-soda sinter process. US Dept. Inter. Bur. Mines 6335.
Ni, M., Ratner, B.D., 2008. Differentiating calcium carbonate polymorphs by surface analysis techniques-an XPS and TOF-SIMS study. Surf. Interface Anal. 40, 1356–1361. https://doi.org/10.1002/sia.2904.
Nielsen, K., 1978. The pedersen process - an old process in a new light. Erzmetall 31, 523–525.
Norway''s Norsk Hydro apologises for spills in Brazil river_2018.pdf WWW Document, 2018. The Local. URL. https://thelocal.no/20180319/norways-norsk-hydro-apologises-for-spills-in-brazil-river (accessed 8.14.18).
Ogino, T., Suzuki, T., Sawada, K., 1987. The formation and transformation mechanism of calcium carbonate in water. Geochim. Cosmochim. Acta 51, 2757–2767. https://doi.org/10.1016/0016-7037(87)90155-4.
Outrage as plant bosses acquitted over fatal toxic spill in Hungary WWW Document, 2016. Guard. URL. https://www.theguardian.com/world/2016/jan/28/outrage-plant-bosses-acquitted-fatal-toxic-spill-hungary (accessed 8.14.18).
Pedersen, H., 1927. Process of Manufacturing Aluminum Hydroxide. pp. 1618105.
Safarian, J., 2018a. Hydrometallurgical processes at NTNU for sustainable production of feedstock for aluminum and solar industries. In: 4th Hydrometallurgy Seminar, (Oslo).
Safarian, J., 2018b. Extraction of iron and ferrosilicon alloys from low-grade bauxite ores. In: Davis, B. (Ed.), Extraction. 2018. pp. 825–837. https://doi.org/10.1007/978-3-319-95022-8_66.
Safarian, J., Kolbeinsen, L., 2016a. Sustainability in alumina production from bauxite. In: Sustainable Industrial Processing Summit, pp. 75–82.
Safarian, J., Kolbeinsen, L., 2016b. Smelting-reduction of bauxite for sustainable alumina production. In: Sustainable Industrial Processing Summit, pp. 149–158.
Sellaeg, H., Kolbeinsen, L., Safarian, J., 2017. Iron separation from bauxite through smelting-reduction process. In: Minerals, Metals and Materials Series, pp. 127–135. https://doi.org/10.1007/978-3-319-51541-0_19.
Smith, P., 2009. The processing of high silica bauxites - review of existing and potential processes. Hydrometallurgy. https://doi.org/10.1016/j.hydromet.2009.04.015.
Söhnel, O., Mullin, J.W., 1982. Precipitation of calcium carbonate. J. Cryst. Growth 60, 239–250. https://doi.org/10.1016/0022-0248(82)90095-1.
Tsesmelis, K., 2017. Bauxite mine rehabilitation & bauxite residue management: a global perspective. In: Proceedings of 35th International ICSOBA Conference. ICSOBA, pp. 71.
Vafeias, M., Marinos, D., Panias, D., Safarian, J., van Der Eijk, C., Solhem, I., Balomenos, E., Ksiazek, M., Davris, P., 2018. From red to grey: revisiting the Pedersen process to achieve holistic bauxite ore utilisation. In: Proceedings of the 2nd International Bauxite Residue Valorisation and Best Practices Conference, pp. 111–117.
Wang, H., Alfredsson, V., Tropsch, J., Ettl, R., Nylander, T., 2013. Formation of CaCO3 deposits on hard surfaces—effect of bulk solution conditions and surface properties. ACS Appl. Mater. Interfaces 5, 4035–4045. https://doi.org/10.1021/am401348v.
Zarasvandi, A., Zamanian, H., Hejazi, E., 2010. Immobile elements and mass changes geochemistry at Sar-Faryab bauxite deposit, Zagros Mountains, Iran. J. Geochem. Explor. 107, 77–85. https://doi.org/10.1016/j.gexplo.2010.06.007.

Paper 6

Kinetics of the Leaching of Alumina-containing Slag for Alumina Recovery

Fabian Imanasa Azof, Leiv Kolbeinsen, Jafar Safarian

Norwegian University of Science and Technology (NTNU)
Department of Materials Science and Engineering
N-7491 Trondheim, Norway

Keywords: Bauxite, alumina, smelting, leaching, kinetics, alumina-containing slag.

Abstract

The leaching kinetics of an alumina-containing slag produced from the smelting-reduction of low-grade bauxite, which contained a significant amount of iron and low levels of SiO_2 and TiO_2, is studied. The leaching rates were evaluated by sampling the pregnant liquid solution at different periods using Inductively Coupled Plasma-High Resolution-Mass Spectrometer (ICP-HR-MS). In addition, the effect of temperature to the leaching extent was also studied at several temperatures. The leaching experiments were performed in a mixing reactor that was heated inside of an oven at atmospheric pressure. The conditions for the solvent concentration, liquid to solid ratio, and mixing speed were kept at 60 g/L Na_2O, 20, and 50 swings per minute, respectively. The leaching mechanism was studied by investigating the cross-section of the slag particles after the leaching with Scanning Electron Microscope (SEM). It was found that the particles in residue have agglomeration tendency during the leaching. Moreover, the $CaCO_3$ and $Ca_3Al_2(OH)_{12}$ produced from the leaching reactions may create a passive layer on the surface of the slag so that it makes the attack of fluid reactant to the unreacted slag become more delicate. It is shown that the slag leaching reactions could be defined as a solid layer diffusion rate limiting, as a good correlation between the fraction conversion and time and dependent on the temperature was observed. Although the solid-fluid reaction in the system is complex, it is indicated that both ash diffusion and "Ginstling and Brounshtein" models for shrinking core model show good correlation with results.

1 Introduction

For decades, alumina industries have been struggling to find the most efficient and comprehensive way to manage bauxite residue (red mud) as an inevitable excess of Bayer process. As of today, dry stacking of filter-pressed red mud is believed as one of the best available methods in alumina processing industries as it able to reduce significantly the risk of dam failure, decrease the total area required for red mud deposit in dry basis, and relatively easy on transporting [1]. However, we believe that this technique is only a temporary solution for the time being and could drift our focus away on what the real problem is; red mud.

Red mud contains primarily iron oxide that may not be dissolved in an alkaline solution to a certain extent. It is a by-product from the Bayer process, which occurs after the digestion of bauxite ore in caustic soda at relatively high temperatures (140 – 300 °C) and pressure (3.5 MPa) [2]. In 1927, an alternative process invented by Harald Pedersen [3], which is later known as Pedersen process, had successfully yielded alumina by employing the smelting-reduction treatment to the bauxite ore, and then subsequently leach the obtained slag in a sodium carbonate solution with small concentration of caustic soda at low temperature (40 – 80 °C) and atmospheric pressure for alumina recovery. The slag produced from the smelting-reduction treatment contains a high concentration of alumina and calcium oxide and relatively low amount of iron oxide. The iron oxide is almost completely reduced, while other elements in the bauxite, i.e. manganese, titanium, silicon, etc., are partially reduced from their oxides phase during the treatment [4]–[7]. The calcium aluminate-containing slag consists of several leachable $CaO–Al_2O_3$ phases that could produce soluble sodium aluminate from the leaching reaction with sodium carbonate solution, which then can be precipitated as the hydrated alumina ($Al(OH)_3$). Thus, the calcination of the precipitates yields pure alumina (Al_2O_3). In other words, the process does not produce red mud at any stages of it. And instead of the red mud, the process, which is known as Pedersen process, produces grey mud that majorly consists of calcium carbonate [8]. An overview and comparison between the Bayer and the Pedersen process in terms of the alumina production sustainability were studied previously [9]. Moreover, the European Union under Horizon 2020 programme has launched ENSUREAL project (www.ensureal.com) in 2017 that is based on the Pedersen process and one of the primary objectives is to make the aluminum industries in Europe becomes more sustainable, from the environment and economic point of view.

The leaching reactions of typical calcium aluminate slags in the sodium carbonate solution are reported in the literature [10], [11] as shown in reaction (1) and (2):

$$CaO{\cdot}Al_2O_{3\,(s)} + Na_2CO_{3\,(aq)} = 2NaAlO_{2\,(aq)} + CaCO_{3\,(s)} \quad (1)$$

$$\Delta G°_{25°C} = -53.6 \text{ kJ/mol } CaO{\cdot}Al_2O_3$$

$$12CaO{\cdot}7Al_2O_{3\,(s)} + 12Na_2CO_{3\,(aq)} + 5H_2O_{\,(l)} = 14NaAlO_{2\,(aq)} + 12CaCO_{3\,(s)} + 10NaOH_{\,(aq)} \quad (2)$$

$$\Delta G°_{25°C} = -745.2 \text{ kJ/mol } 12CaO{\cdot}7Al_2O_3$$

The Gibbs energy change of reactions (1) and (2) are calculated by using HSC™ thermochemistry software. In our previous study [10] we leached synthetic calcium aluminate slag, which predominantly consists of $CaO{\cdot}Al_2O_3$ phase, in a mixed 120 g/L Na_2CO_3 + 7 g/L NaOH solution after the leaching at 45 °C within 30 minutes and we attained a high leachability of the phase up to 93 %. In literature, Lundquist and Leitch [11] claimed that they could recover 100 % of alumina from $12CaO{\cdot}7Al_2O_3$ in 43 – 85 g/L Na_2CO_3 solution at 50 – 70 °C for 24 hours, which obviously the duration is depending on the amount of the slags and kinetics of the reactions. Therefore, these findings encourage authors to study the leaching mechanism as well as the kinetics of the reactions that occur during the leaching of the alumina-containing slag in sodium carbonate solution.

2 Experimental Procedure

The experiments carried out in this study were necessitated to observe the leaching kinetics of an alumina-containing slag produced from a low-grade bauxite ore through an integrated Pedersen process in lab scale. The flow chart of the experiments in the leaching part is presented in Figure 1.

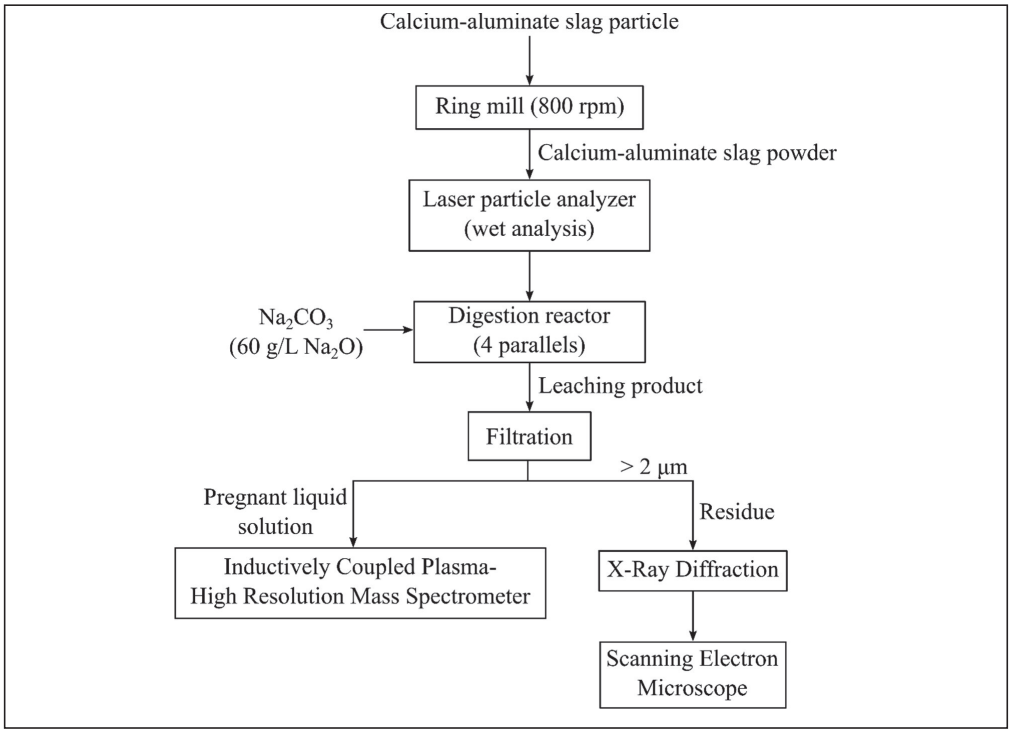

Figure 1: The experimental flow chart

2.1 Materials preparation and characterization

We have prepared the calcium-aluminate slag that was produced by the smelting-reduction treatment of a low-grade bauxite from the previous study [6]. The smelting-reduction treatment was carried out by smelting a proportional mixture of bauxite ore, lime, and coke in a mass ratio of lime/bauxite equals to 0.8 inside a graphite crucible at 1650 °C for one hour. From the smelting-reduction treatment, we have slag and pig iron as the main and by-product, respectively. After the separation, the slag then grounded with a ring mill for further leaching use. The chemical composition of the slag is given in Table 1. The composition was taken by means of Inductively Coupled Plasma-High Resolution Mass Spectrometer (ICP-HR-MS) and has been normalized to its oxide form. As we see, the slag predominantly consists of calcium oxide and alumina, which are 47.8 and 44.18 wt%, respectively. Whereas the remaining oxides are SiO_2, TiO_2, Fe_2O_3, etc. Moreover, in order to measure the particle size of the produced powder we use a laser particle analyser, which is Horiba LA-960, in a wet analysis (isopropanol with refractive index 1.378) based on volume distribution.

Table 1: Chemical composition of the slag in oxide phase as measured by ICP-HR-MS

Phase	**CaO**	**Al_2O_3**	**SiO_2**	**TiO_2**	**Fe_2O_3**	**MgO**	**MnO**	**P_2O_5**	**SO_3**	**V_2O_5**
wt.%	47.80	44.18	5.53	1.51	0.50	0.37	0.03	0.01	0.04	0.01

2.2 Leaching experiment

In the current study, we performed leaching where the reactants were the slag and sodium carbonate solution, as the solid substance and the solvent, respectively. The solvent concentration was fixed as 60 g/L Na_2O, where the leaching temperature was at 35 and 45 °C, and the liquid to solid ratio (mL/g) was 20. The solvent was stored in a digestion reactor, which was a Polytetrafluoroethylene (PTFE)-base with the capacity of 45 mL and covered with stainless steel as the outer body. It was placed on a holder that able to swing approximately 45 deg with 50 swings per minute (spm). The lid of the digestion reactor was partially open, which allows the pressure inside of it remained at 1 atm. Four parallels of the digestion reactor were heated in the oven at the same time as seen in Figure 2. After the display showed the targeted temperature, we poured the slags into the digestion reactors. Then at different periods, we took out one of the digestion reactors from the oven and did the filtration afterward using an ashless grade of filter paper (< 2 μm). By this method, we have an independent leaching treatment and prevent the sampling errors that resulted from taking multiple samples of the same solution at different periods.

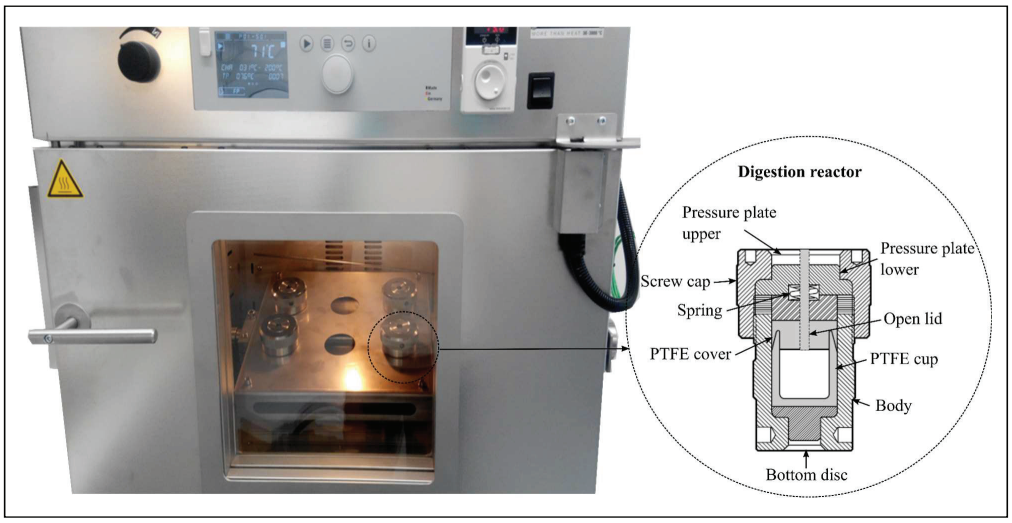

Figure 2: The digestion reactors were placed on the swinging holder inside of the oven

2.3 Characterization techniques

The quantitative analysis of the pregnant liquid solutions (PLS) obtained from the leaching trials were carried out by using ICP-HR-MS Agilent 8800™. On the other hand, the phases of the residue were characterized by X-Ray Diffraction (XRD) with CuKα radiation, 10 to 75 deg diffraction angle, 0.01 deg step size, and 2.5 deg for both primary and secondary soller slits. Whereas the microstructure of residue's cross-section observed by means of Hitachi SU6600™ Scanning Electron Microscope (SEM) with the feature of Backscattered Electron image (BSE), Energy Dispersive Spectroscopy (EDS), and X-ray mapping element.

3 Kinetics model consideration

Considering a non-porous solid particle that exposed in a fluid gives us solid-fluid heterogeneous reactions. Levenspiel [12] proposed two simple models, which are a progressive-conversion model (PCM) and shrinking-core model (SCM). The first model assumes that the reactant fluid reacts with the particle at all times at different rates and locations within the particles. In other words, the PCM model may work for solid-fluid reactions where the reactions occur at the solid interface continuously and progressively without whatsoever interference from the solid products. Whereas the SCM model was based on the work of Yagi and Kunii [13], they studied the combustion behaviour of carbon particles in flames and fluidized beds. Yagi and Kunii observed that the existing unreacted core after the combustion might be resulted from incomplete conversion due to different rate-limiting steps; gas

film and ash diffusions, or chemical reaction. The established kinetics equation in SCM [12] for ash diffusion and chemical reaction rate limiting can be described as in equation (3) and (4), respectively.

$$(k/r^2)t = 1 - 3(1-X)^{2/3} + 2(1-X) \quad (3)$$

$$(k/r)t = 1 - (1-X)^{1/3} \quad (4)$$

Where t is the ongoing conversion time, r is the radius of the reacting particle, X is the fraction of the particle's conversion, k is the apparent rate constant of the reaction. A few researchers [14], [15] studied the aluminum dissolution in Bayer process use the equation (4) against their kinetics experimental data. Moreover, Avrami [16] equation for solid-state phase transformations is shown in equation (5) for first-order reaction form and has also been used in literature for solid-liquid reactions.

$$kt = -\ln(1-X) \quad (5)$$

Avrami formulated the equation based on the nucleation and nuclei growth of the phases, where the kinetics reaction is fast at the beginning of the growth and as nuclei grow larger they eventually impinge on one another, which then slow and cease the growth. According to Tong and Li [17], the kinetics reaction behaviour of the nucleation and phase's grain growth are relatively similar with the leaching kinetics of a calcium-aluminate slag in alkaline solution, in which the reaction is fast in the beginning and then significantly slow after certain times. Another kinetics equation that can be used in the solid-fluid reaction is the solid-state equation proposed by Ginstling and Brounshtein [18], and Jander [19] for diffusion rate limiting reactions as seen in equation (6) and (7), respectively.

$$(k/r^2)t = 1 - (2X/3) - (1-X)^{2/3} \quad (6)$$

$$(k/r^2)t = (1 - (1-X)^{1/3})^2 \quad (7)$$

In the current study, we analyse the leaching mechanism of calcium-aluminum slag in solvent based on the experimental observation and by fitting the right-hand side of the equation (3) – (7) against the time. The apparent rate constant is not discussed in this paper to limit the scope of discussion.

4 Results and Discussion

The results presented in following section consist of the characteristics of the slag, the changes on the slag's morphology after the leaching treatment, the effect of the leaching time and temperature on the aluminum extraction extent, and some of the kinetic models on the leaching reactions.

4.1 Characteristics of the slag

As mentioned previously in section 2.1, the slag was grounded by means of the ring mill to fit in the digestion reactor and for the sake of leaching effectivity. The size distribution of the slag is shown in Figure 3. Whereas the D_{10}, D_{50}, and D_{90} of the slag is 4.2, 9.0, and 16.4 µm, respectively.

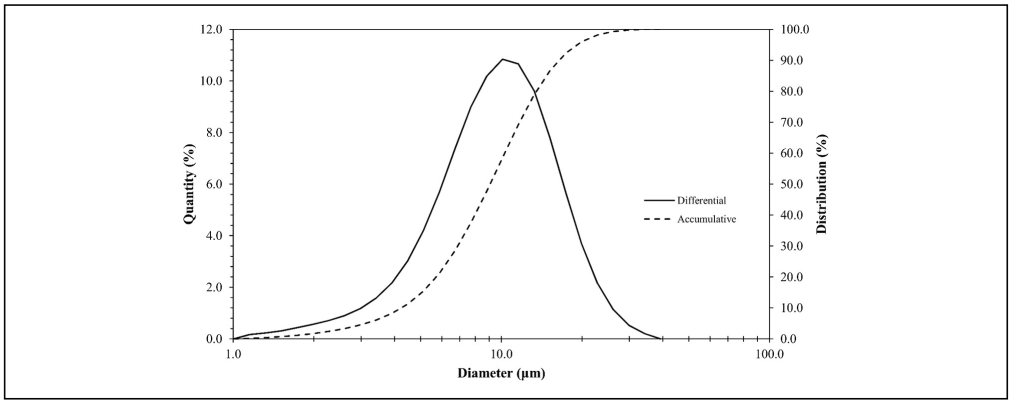

Figure 3: Size distribution of the slag

Moreover, the XRD analysis of the slag is seen in Figure 4, which shows $12CaO{\cdot}7Al_2O_3$ (denoted as $C_{12}A_7$) as the majority of the phase and followed by small amount of $CaO{\cdot}Al_2O_3$ (denoted as CA), and $5CaO{\cdot}Al_2O_3$ (denoted as C_5A_3). According to the reaction (1) and (2), $C_{12}A_7$ and CA phases are leachable in a Na_2CO_3 solution. However, the thermochemistry data of the reaction between C_5A_3 with Na_2CO_3 is unknown in HSC™ ver. 9.

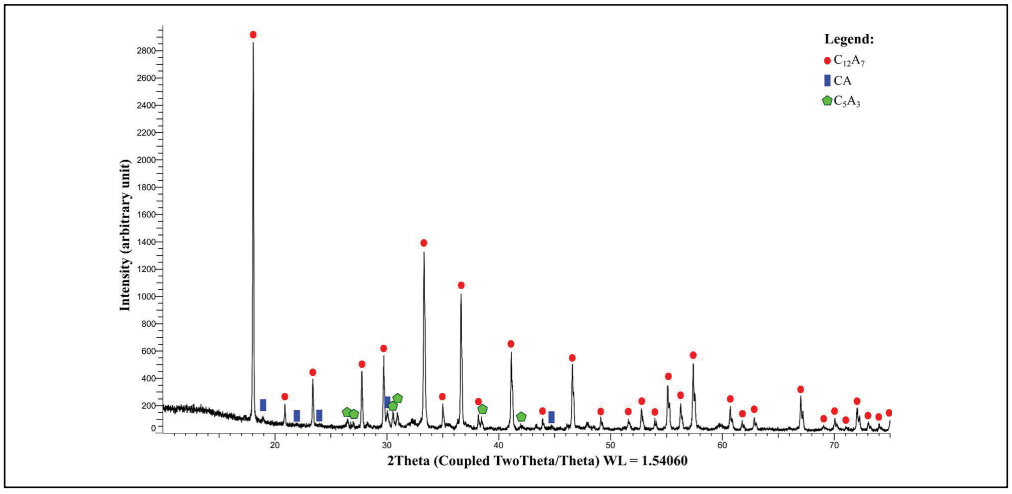

Figure 4: XRD spectrum of the slag

4.2 Aluminum extraction extent

A series of the leaching trial has been done, thus the quantitative measurement of the aluminum concentration of the pregnant leaching solution (PLS) has been performed by ICP-HR-MS. The name of the sample is PLS-35 and PLS-45 which indicates the sample is obtained from PLS that has been leached at 35 and 45 °C, respectively. The aluminum extraction extent can be calculated as in equation (8):

$$\text{Aluminum extraction extent (\%)} = \frac{W_{Al}^{PLS}}{W_{Al}^{Slag}} \times 100\ \% \quad (8)$$

Where W_{Al}^{PLS} and W_{Al}^{Slag} are the masses of aluminum in the PLS and slag, respectively. The aluminum extraction extent of the trials can be seen in Figure 5. The straight and dash line indicates the polynomial regression for aluminum extraction extent on PLS-35 and PLS-45, respectively. As we see, the extraction extent progresses as the leaching time increases and obviously, the rate and extent or leaching are relatively higher at a higher temperature. However, even though the retention time is 100 minutes at 45 °C, the extraction extent in PLS-45 is relatively low. Therefore, an investigation of the morphology and phases of the leaching product was further done to give us more information on the leaching mechanism.

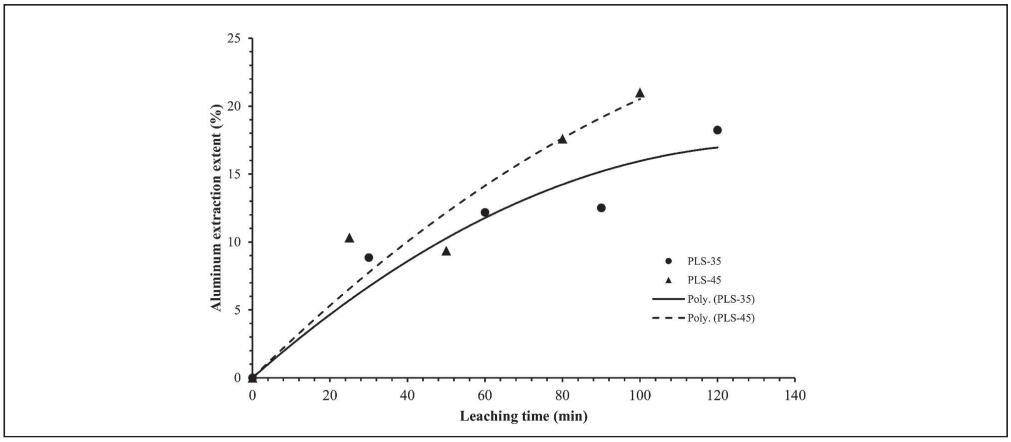

Figure 5: Aluminum extraction extent vs leaching time at different temperatures

4.3 The phases of the residue and morphology analysis

Figure 6 shows the XRD peaks of the residues that are obtained after the leaching treatment at 35 °C in different periods. The phases observed from the residues are $C_{12}A_7$, C_5A_3, $CaCO_3$, and a hydrogarnet phase ($Ca_3Al_2(OH)_{12}$). We notice that the phases obtained are similar for all of the leach residues in different periods. The $C_{12}A_7$ and C_5A_3 phases still co-exist in the residue, which indicates an incomplete leaching reaction. The $CaCO_3$ phase is the expected solid product produced from the

reaction (1) and (2). While $Ca_3Al_2(OH)_{12}$ phase may co-exist in the residue because of the side reactions of CA that occurred during the leaching. The formation of $Ca_3Al_2(OH)_{12}$ phase from the side reactions of CA may be described in reaction (9) and (10), as proposed by Lundquist and Leitch [20]. The Gibbs energy change of the reactions is calculated in HSC™ ver. 9.

$$3[CaO{\cdot}Al_2O_3]_{(s)} + 12H_2O_{(l)} = Ca_3Al_2(OH)_{12(s)} + 4Al(OH)_{3(s)} \quad (9)$$

$$\Delta G°_{25°C} = -27.0 \text{ kJ/mol } CaO{\cdot}Al_2O_3$$

$$3[CaO{\cdot}Al_2O_3]_{(s)} + 4NaOH_{(aq)} + 12H_2O_{(l)} = Ca_3Al_2(OH)_{12(s)} + 4NaAl(OH)_{4(aq)} \quad (10)$$

$$\Delta G°_{25°C} = -36.4 \text{ kJ/mol } CaO{\cdot}Al_2O_3$$

The existence of $Ca_3Al_2(OH)_{12}$ is an undesirable product in the leaching treatment as it decreases the yield of aluminum recovery from the slag. However, our previous study [10] showed that no $Ca_3Al_2(OH)_{12}$ was produced after the leaching of synthetic CA in a Na_2CO_3 solution with an addition of NaOH.

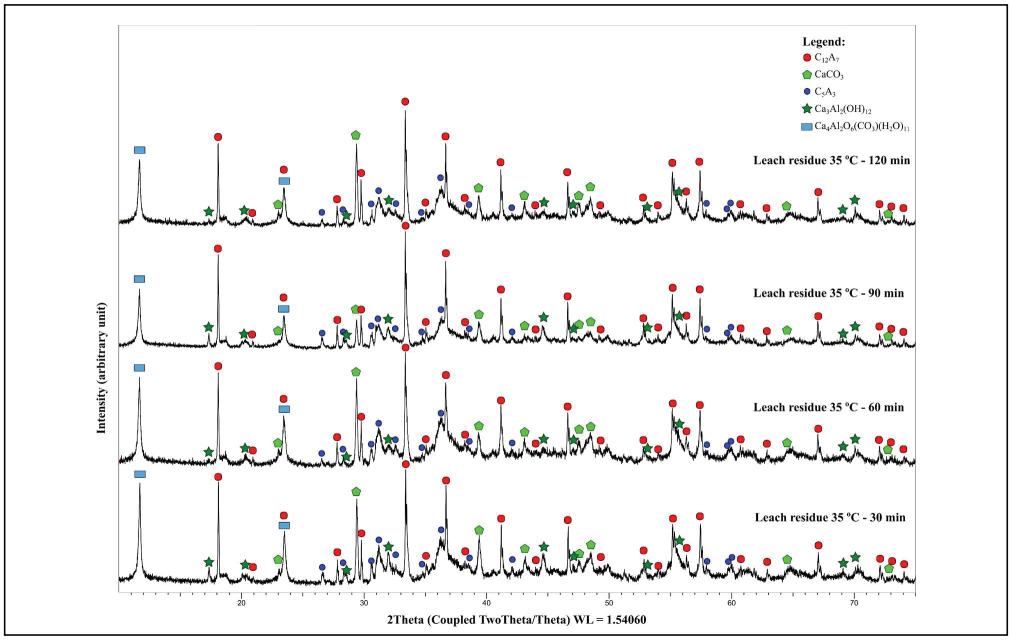

Figure 6: XRD peaks of the residue after the leaching treatment at 35 °C at different periods

The morphologies of the slag particles before and after the leaching trials are shown in BSE images in Figure 7(a) – (d). In Figure 7(a), we see that the slag has rock-alike and might be classified as a non-porous particle. Whereas Figure 7(b) – (d) show the different morphologies of the solid particles that exist as the residues. We suggest that the solid particles in Figure 7(b) and (c) are polymorphs of $CaCO_3$ that are produced from the leaching reactions (1) and (2). The needle-like shape in Figure 7(b)

resembles aragonite, which is one of the metastable forms of $CaCO_3$ [21], [22]. While the cubic shape in Figure 7(c) is similar to the morphology of calcite [22], which is reported as the most thermodynamically stable form of $CaCO_3$ [22], [23]. Concerning the different carbonate polymorphs that are formed during the leaching, Dickinson and McGrath [23] said that the kinetic factors that are relevant to the process of crystallization of $CaCO_3$ might influence the morphology and polymorph of the crystals. Moreover, in a heterogeneous system, both aragonite and calcite need a substrate to nucleate and grow. Thus, the surface of the calcium-aluminate slag that exposed to the solvent may act as the primary substrate for the nucleation of the $CaCO_3$ crystal. The amount of $CaCO_3$ increases as the mass transfer of the leaching reaction (1) and (2) progresses. If we see the similarity of the size of each individual particle in Figure 7(a) – (c), we may say that Figure 7(b) and (c) show the morphologies of the residue when the slag is fully converted, or in other words, the mass transfer of aluminum into the solution according to reactions (1) and (2) has been stopped. However, a lower magnification of the clustered residue in Figure 7(d) shows that the residue may be agglomerated and formed a significantly larger particle size compared to the slag, which indicates that other leaching mechanisms may occur in the system.

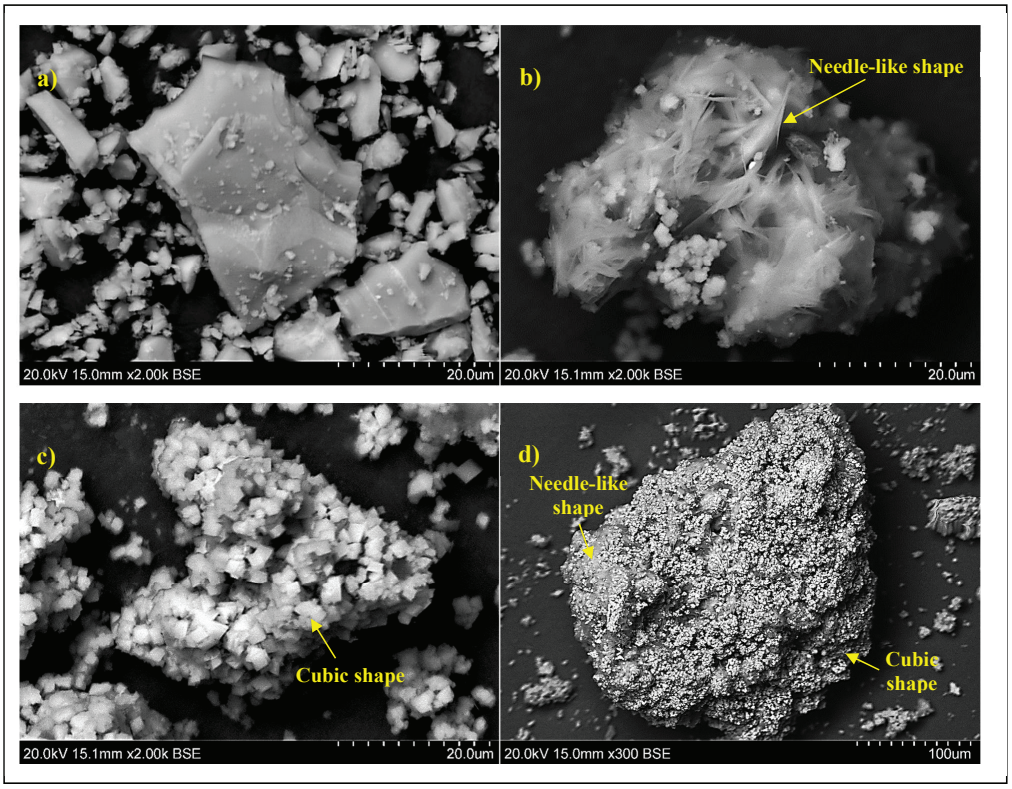

Figure 7: BSE image of the morphology of (a) the slag particle before the leaching treatment, whereas (b) – (d) are the residues that are covered with different polymorphs of $CaCO_3$

4.4. Cross-section analysis of the residue

We found that the particles in residue materials are agglomerated during the leaching process, thus, they have obtained larger particle size than that of the slag. The BSE image and X-ray mapping elements on the cross-section of the agglomerated residue are shown in Figure 8. Several notes can be taken from Figure 8:

1. The residue particles may have agglomerated during the leaching and the particle size increases significantly as indicated by the image's scale differences between Figure 7 and 8.
2. The crystalline bridges induced by the crystal growth of the solid leaching products may cause the agglomeration phenomena, which is also supported in the literature [24].
3. Agglomeration of the residue primarily consists of the unleached calcium-aluminate slag as the aluminum concentration inside of the agglomerate is high, which is indicated by green colour in X-ray mapping element.
4. The fluid reactant may need a long time to diffuse to the surface of the unreacted slag phases inside the relatively dense agglomerate.
5. The nucleation and initial growth of $CaCO_3$ crystals as well as $Ca_3Al_2(OH)_{12}$ phase at the surface of the slag particles create a passive layer that may slow down the leaching reactions.

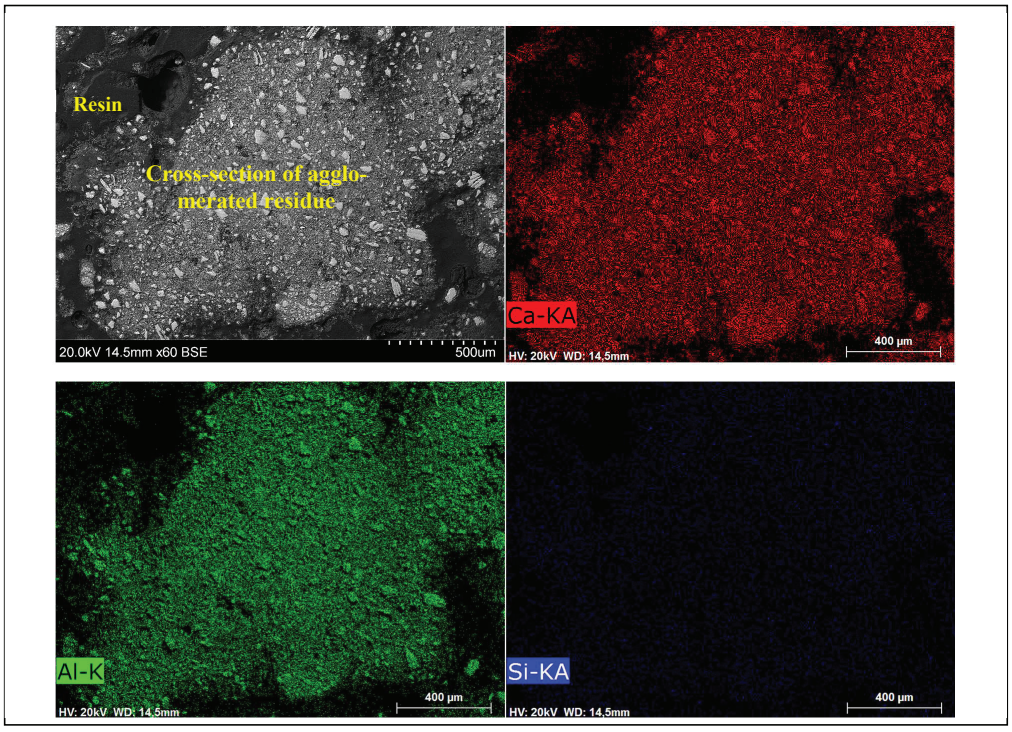

Figure 8: X-ray mapping element on the cross-section of the agglomerated residue

4.5 Kinetics of the aluminum dissolution

In the previous section, we observed that the leaching of the slag produces solid products, i.e. $CaCO_3$ and $Ca_3Al_2(OH)_{12}$, that may have accumulated at the surface of the slag (Figure 7(b) and (c)). On the other hand, the agglomeration tendency of the particles during the leaching may hinder the attack of the solvent to the unreacted slag's surface. Therefore, the topography of the residue in kinetics modelling point of view is relatively complex. Based on the kinetics equation (3) – (7) we may construct the correlation between the function of conversion, $f(X)$, with the leaching time as shown in Figure 9.

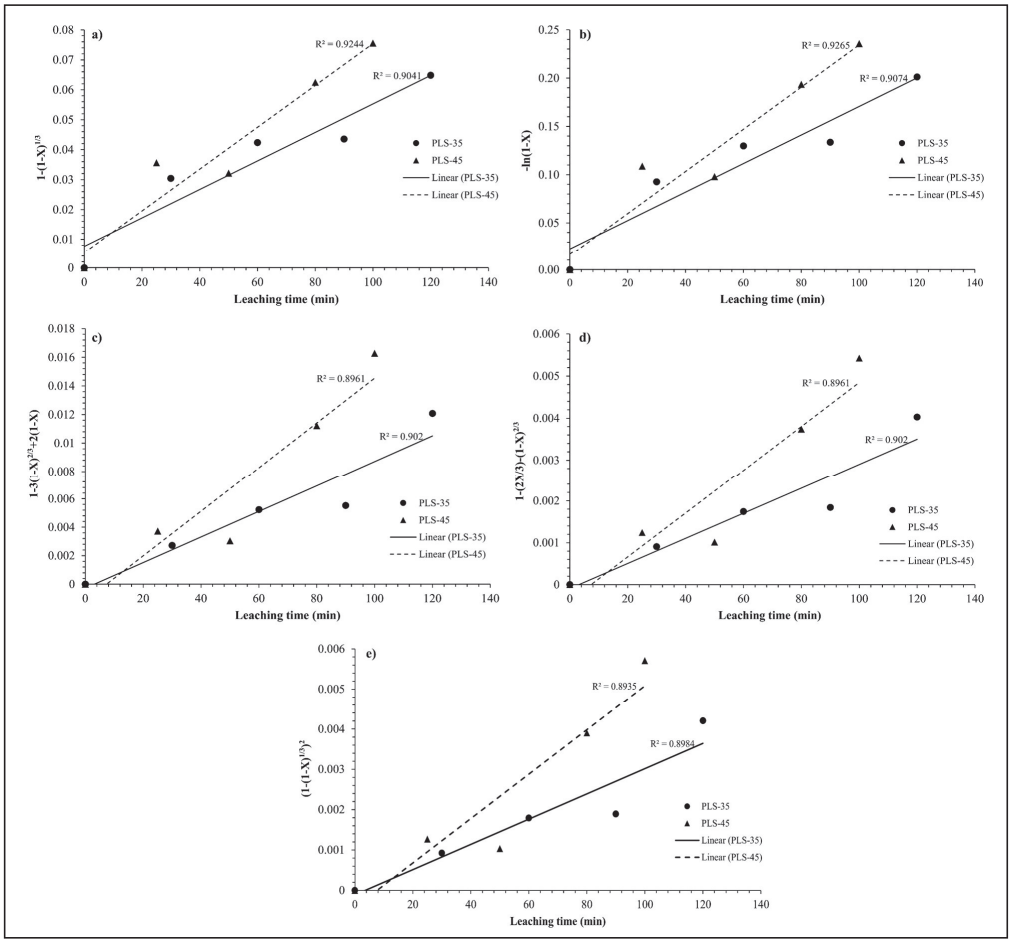

Figure 9: The kinetics rate modelling based on the experimental result using (a) chemical reaction rate limiting in SCM, (b) Avrami first-order reaction, (c) ash-diffusion rate limiting in SCM, (d) Ginstling and Brounshtein diffusion equation, (e) Jander diffusion equation

As we see in Figure 9(a) and (b), which are based on the chemical reaction rate limiting and Avrami's nucleation equations, they show similarity for the relationship between $f(X)$ and t. However, we may also see that the regression lines do not intercept with origin. On the other hand, Figure 9(c) – (e) show the relationship of $f(X)$ and t based on the diffusion rate-limiting equations, which are more acceptable than that of Figure 9(a) and (b), as the regression lines are fairly intercepted with zero. In the current study, equations from ash diffusion rate limiting in SCM and Ginstling and Brounshtein are suggested as the closer kinetics modelling approximation compared to the reality than that of Jander diffusion equation. We may agree that the accuracy of the kinetics modelling with the experimental data is essential if we want to use the model to predict our future leaching process. However, a relatively low least square (R^2) provided by the regression lines in Figure 9(c) – (e) indicates that other factors may have not been accommodated by the equations. The diffusion rate limiting kinetics equation (3), (6) and (7) assume that the reacting particle has a spherical shape with homogeneous size. Whereas, in the current study we have particles with no spherical shape with a size distribution (Figure 3). Moreover, the occurring of side reactions (section 4.3.) and agglomeration tendency of the residues (section 4.4.) causes the prediction of kinetics reaction rate became more challenging. However, by comparing the results of the established equations, we may have a conclusion that the rate-limiting for current leaching system is the diffusion of the leaching agents through a solid product layer. Nevertheless, it might be interesting to see the effect of agitation on the aluminum extraction extent and study the kinetics reaction rate in a homogeneous size.

5 Conclusion

The leaching kinetics of alumina-containing slag in sodium carbonate solution has been studied. The slag consisted of $CaO{\cdot}Al_2O_3$, $12CaO{\cdot}7Al_2O_3$, and $5CaO{\cdot}3Al_2O_3$ phases. The first two phases are leachable in sodium carbonate solution for aluminum recovery. The leached slag may have converted to $CaCO_3$ in different polymorphs depending on the kinetics of the crystallization of the phase. The cross-section analysis of the residue revealed that the slag has not been leached properly as the residue has agglomeration tendency and a calcium-containing passive layer is formed on the slag particles. Therefore, the solvent needs to diffuse through this dense layer to reach the surface of the leachable phases or unreacted slag portion in the particles. The regression between the well-known kinetic equations and the experimental results in the current study approved that the solid layer diffusion is the rate-limiting step.

6 Outlook

A further investigation on the effect of different agitation speed or type would be beneficial to understand the kinetics and mechanism of the leaching, as it might be the significant factor on the aluminum

extraction extent of the Pedersen process. Also, the effect of different polymorphs of $CaCO_3$ passive-layer on the diffusion behavior of the leaching reactant will be investigated in our near future works.

Acknowledgement

The research has been funded by the NTNU and supported by the Research Domain 5 – Materials and the Society in SFI Metal Production (a Norwegian Centre for Research-driven Innovation in metal production) under the Project Number 237738. The scientific support from the ENSUREAL EU Horizon 2020 project (Grant Agreement no. 767533) is acknowledged.

References

[1] Balomenos, E. (2018): Bauxite Residue Handling Practice and Valorisation Research in Aluminium of Greece, proceedings of The 2nd International Bauxite Residue Valorisation and Best Practices Conference, pp. 29–37.

[2] Balomenos, E., Panias, D., and Paspaliaris, I. (2011): Energy and Exergy Analysis of the Primary Aluminum Production Processes: A Review on Current and Future Sustainability, Mineral Processing and Extractive Metallurgy Review, vol. 32, no. 2, pp. 69–89.

[3] Pedersen, H. (1927): Process of Manufacturing Aluminum Hydroxide, US Patent 1618105.

[4] Sellaeg, H. Kolbeinsen, L., and Safarian, J. (2017): Iron Separation from Bauxite through Smelting-Reduction Process, proceedings of Light Metals 2017, pp. 127–135.

[5] Safarian, J. and Kolbeinsen, L. (2016): Smelting-reduction of Bauxite for Sustainable Alumina Production, proceedings of Sustainable Industrial Processing Summit 2016, pp. 1–8.

[6] Azof, F. I., Kolbeinsen, L., and Safarian, J. (2018): Characteristics of Calcium-Aluminate Slags and Pig Iron Produced from Smelting-Reduction of Low-Grade Bauxites, Metallurgical and Materials Transactions B, vol. 49, no. 5, pp. 2400–2420.

[7] Safarian, J. (2018): Extraction of Iron and Ferrosilicon Alloys from Low-Grade Bauxite Ores, proceedings of Extraction 2018, pp. 825–837.

[8] Vafeias, M., Marinos, D., Panias, D., Safarian, J., van Der Eijk, C., Solhem, I., Balomenos, E., Ksiazek, M., Davris, P. (2018): From Red To Grey: Revisiting the Pedersen Process To Achieve Holistic Bauxite Ore Utilisation, proceedings of The 2nd International Bauxite Residue Valorisation and Best Practices Conference, pp. 111–117.

[9] Safarian, J. and Kolbeinsen, L. (2016): Sustainability in Alumina Production from Bauxite, proceedings of Sustainable Industrial Processing Summit 2016, pp. 1–6.

[10] Azof, F. I., Kolbeinsen, L. and Safarian, J. (2017): The Leachability of Calcium Aluminate Phases in Slags for the Extraction of Alumina, proceedings of 35th International ICSOBA Conference, vol. 42, pp. 243–253.

[11] Lundquist, R. V. and Leitch, H. (1964): Aluminum Extraction Characteristics of Three Calcium Aluminates in Water, Sodium Hydroxide, and Sodium Carbonate Solutions, US Bureau of Mines, pp. 1 – 16.

[12] Levenspiel, O. (1999): Chemical Reaction Engineering-3rd edition, John Wiley & Sons, Inc.

[13] Yagi, S. and Kunii, D. (1955): Studies on combustion of carbon particles in flames and fluidized beds, Combustion of Solids, vol. 5, no. 1, pp. 231–244.

[14] Abdel-Aal, E.-S. A. (2016): Leaching Kinetics of Gibbsitic Bauxite with Sodium Hydroxide, E3S Web Conference, vol. 8, p. 01021.

[15] Yang, H., Pan, X., Yu, H., Tu, G., and Sun, J. (2015): Dissolution kinetics and mechanism of gibbsitic bauxite and pure gibbsite in sodium hydroxide solution under atmospheric pressure, Transactions of Nonferrous Metals Society of China, vol. 25, no. 12, pp. 4151–4159.

[16] Avrami, M. (1939): Kinetics of Phase Change. I General Theory, The Journal of Chemical Physics, vol. 7, no. 12, pp. 1103–1112.

[17] Tong, Z. and Li, Y. (2017): Leaching Behavior of Alumina from Smelting Reduction Calcium Aluminate Slag with Sodium Carbonate Solution, pp. 37–43.

[18] Sharp, J. H., Brindley, G. W., and Achar, B. N. N. (1966): Numerical Data for Some Commonly Used Solid State Reaction Equations, Journal of the American Ceramic Society, vol. 49, no. 7, p. 379.

[19] Jander, W. (1930): Reactions in the Solid State at High Temperatures, Zeitschrift für Anorganische und Allgemeine Chemie, vol. 190, no. 1, pp. 397–406.

[20] Lundquist, R. V. and Leitch, H. (1963): Solubility characteristics of monocalcium aluminate, US Department of Interior Bureau of Mines, vol. 6294, pp. 1–9.

[21] Ni, M. and Ratner, B. D. (2008): Differentiating calcium carbonate polymorphs by surface analysis techniques-an XPS and TOF-SIMS study, Surface and Interface Analysis, vol. 40, no. 10, pp. 1356–1361.

[22] Wang, H., Alfredsson, V., Tropsch, J., Ettl, R., and Nylander, T. (2013): Formation of $CaCO_3$ Deposits on Hard Surfaces—Effect of Bulk Solution Conditions and Surface Properties, ACS Applied Materials and Interfaces, vol. 5, no. 10, pp. 4035–4045.

[23] Dickinson, S. R. and McGrath, K. M. (2004): Aqueous Precipitation of Calcium Carbonate Modified by Hydroxyl-Containing Compounds, Crystal Growth and Design, vol. 4, no. 6, pp. 1411–1418.

[24] Schnebelen, M., Mozet, K., Jakob, A., Sy, D., Plasari, E., and Muhr, H. (2015): Agglomeration Mechanisms and Kinetics during the Carbonation of a Suspension of Lime in a Pilot Batch Reactor, Crystal Structure Theory and Applications, vol. 04, no. 03, pp. 35–46.

Paper 7

Leaching kinetics and mechanism of slag produced from smelting-reduction of bauxite for alumina recovery

Fabian Imanasa Azof, Jafar Safarian

Department of Materials Science and Engineering, Norwegian University of Science and Technology (NTNU), Trondheim, Norway.

Corresponding author (email): Fabian Imanasa Azof (fabian.i.azof@ntnu.no)

Abstract

In the present study, we investigate the kinetics and mechanism of the leaching of calcium aluminate slag in Na_2CO_3 solution for alumina recovery. The slag consists of leachable phases, e.g., $12CaO{\cdot}7Al_2O_3$, $CaO{\cdot}Al_2O_3$, $5CaO{\cdot}3Al_2O_3$, and a complex unleachable phase that contains Ca-Al-Si-Ti oxides. A series of leaching treatment is done at different temperatures, leaching times, stirring rates, Na_2CO_3 concentrations, and different setups which includes wet-grinding and shaking-digestion reactor. The highest alumina recovery up to 90.5 % is obtained after the slag is leached by 10 wt.% Na_2CO_3 solution, at low temperatures (30 – 45 °C) within 90 min. It is shown that the rate of alumina recovery is high at the beginning of leaching and is then slow down due to the calcite layer product nucleation and growth at the surface of slag. The wet-grinding leaching and vigorous stirring increase the possibility of the collision between both particles and the stirrer that breaks the calcite layer, yielding less residue agglomeration and better recovery compared to the slow and mild agitations. A surface observation of the slag using electron microscopy shows that the calcite starts to nucleate at the unleachable phase as the best deposition site which has the least mass transfer barrier in the system. The apparent activation energy of the leaching reaction is calculated as 10.8 – 19.9 kJ/mol which indicates the reaction is diffusion rate limited as revealed by the applied kinetic models.

Keywords: Kinetics; leaching mechanism; alumina recovery; calcium aluminate slag; smelting-reduction bauxite

1. Background

Alumina industry is deemed necessary to produce a metallurgical grade alumina that has a lower environmental footprint, as the renown Bayer process has been producing a less-utilized residue (red mud) abundantly as nearly as 150 million tons per year (Tsesmelis, 2017). Numerous environmental damage due to mismanaged on red mud disposal has been raised in media, and unfortunately, none of the research projects on red mud valorization have been scaled up to commercial production due to particular challenges. Also, due to a specific use of bauxite that can be treated effectively by the Bayer process, a high dependency of alumina industry on high-grade bauxite ores mined only from particular regions, i.e., near-equatorial zone, to get lateritic bauxite is favoured.

Exciting results from one of the alternative processes for a sustainable alumina recovery have been reported in the literature (Azof et al., 2018, 2017; Blake et al., 1966; Fursman et al., 1968; Miller and Irgens, 1974; Safarian and Kolbeinsen, 2016a, 2016b; Sellaeg et al., 2017). The process is based on a smelting-reduction of the bauxite with subsequent leaching of the obtained aluminate slag in a sodium carbonate solution. It was invented by Harald Pedersen, which was later called the Pedersen process, in 1927 (Pedersen, 1927). The process is proper for successful recovery of alumina and iron from the bauxite, while no red mud is produced. A schematic of the Pedersen process that is adapted from Nielsen (Nielsen, 1978) is shown in Fig. 1.

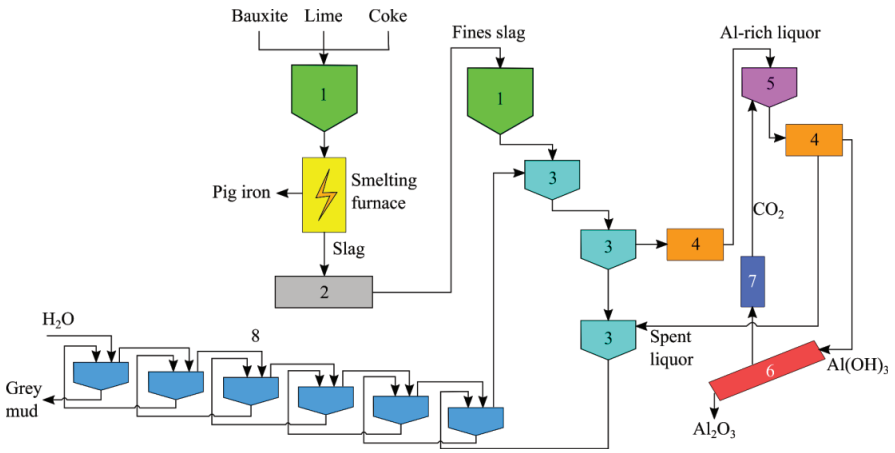

Fig. 1. A schematic of the Pedersen process that was adapted from the original Pedersen process' flowsheet. Legend: 1 = Silo; 2 = Crusher; 3 = Digester; 4 = Filter; 5 = Precipitator; 6 = Calciner; 7 = Gas cleaner; 8 = Thickener.

Authors' studies on the leaching characteristics of synthetic CaO-Al_2O_3 slags and a slag produced from the smelting-reduction of a commercial low-grade bauxite have been published earlier (Azof et al., 2020, 2019c). The kinetics behavior and the mechanisms of the leaching reactions in the Pedersen process are still unclear as the occurring solid-fluid reaction during the leaching is considerably complicated, and there is no significant published work in this area. Therefore, the present work is now focused on the experimental study of kinetics of the leaching of calcium aluminate slags. Innovative electron microscopy study on the samples is applied to discover the solid product growth during leaching. Moreover, different kinetic models are evaluated for the experimental results to determine the process rate limiting steps and outline the mechanism of leaching.

2. Leaching Reactions

Typical leaching reactions of the Pedersen process were stated in the literature (Azof et al., 2017; Blake et al., 1966) and are shown in Equations (1) and (2). The change of standard Gibbs energy is also presented after each equation as calculated from a thermochemistry software HSC™. In general, the reactions involve leachable calcium aluminate phases, such as $CaO{\cdot}Al_2O_3$ (denoted as CA), $12CaO{\cdot}7Al_2O_3$ (denoted as C12A7), and $5CaO{\cdot}3Al_2O_3$ (denoted as C5A3) phases, Na_2CO_3, and H_2O. Thus, the reactions produce:

(1) $NaAlO_2$ in an aqueous phase, which is an aluminum-rich soluble phase that is later precipitated by carbonation after the leaching process, and

(2) A leaching residue as the byproduct, which is also referred to as grey mud, and it predominantly consists of $CaCO_3$ and unreacted slag (Vafeias et al., 2018).

$$CaO{\cdot}Al_2O_{3(s)} + Na_2CO_{3(aq)} = NaAlO_{2(aq)} + CaCO_{3(s)} \quad (1)$$

$$(\Delta G^{\circ}_{25°C} = -53.6\ \text{kJ/mol}\ CaO{\cdot}Al_2O_3)$$

$$12CaO{\cdot}7Al_2O_{3(s)} + 12Na_2CO_{3(aq)} + 5H_2O_{(l)} = 14NaAlO_{2(aq)} + 12CaCO_{3(s)} + 10NaOH_{(aq)}$$

$$(\Delta G^{\circ}_{25°C} = -745.2\ \text{kJ/mol}\ 12CaO{\cdot}7Al_2O_3) \quad (2)$$

Based on authors' recent study on the morphology and cross-section analysis of the grey mud (Azof et al., 2019a), the polymorph of $CaCO_3$ (e.g., calcite, aragonite, vaterite) nucleated and covers the surface of the slag, meanwhile the unreacted slag remains inside of the core. Fig. 2 illustrates the depolymerization of a calcium aluminate slag in Na_2CO_3 solution and $CaCO_3$ formation from a cross-section view.

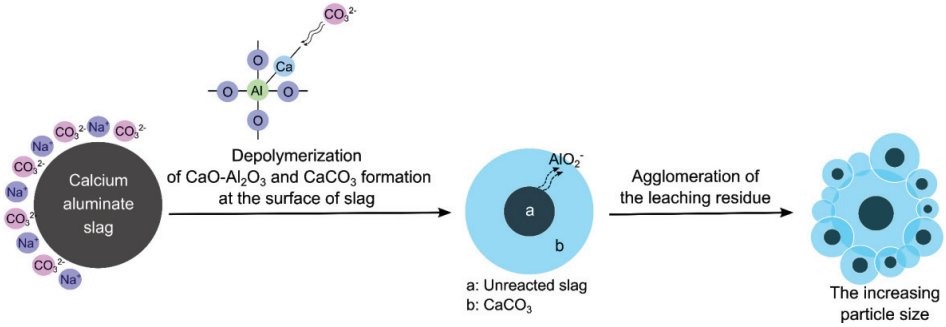

Fig. 2. An illustration of the depolymerization of calcium aluminate slag particle during the leaching in Na_2CO_3 solution and $CaCO_3$ formation from a cross-section view.

3. Solid-Fluid Kinetics Equation for Spherical Particles

The kinetics equation of solid-fluid reactions in a leaching process can be treated similar to the solid-gas reaction. The type of the heterogeneous reaction to be considered is the reaction of a solid and a liquid that yields solid and liquid products. Spherical reacting particle as one of the most practical models in kinetics equation also used in this study to make a simplification on the calculations. In the authors' recent work (Azof et al., 2019b), we have managed preliminary works about the kinetics behavior of a calcium-aluminate slag that was leached in a sodium carbonate solution. The data was reasonably in good agreement with Ginstling – Brounshtein's equation (Ginstling and Brounshtein, 1950) and "ash diffusion" equation in shrinking core model (Levenspiel, 1999; Yagi and Kunii, 1955). These may indication that the slag leaching reaction is diffusion rate controlled.

In the current study, we will later plot the kinetics data obtained against the equation that belongs to that of rate controlled and investigate the results of the best model-fit. Several researchers (Dickinson and Heal, 1999; Khawam and Flanagan, 2006) have listed the established kinetics equations, which have been used frequently in kinetics studies as the main ones are shown in Table 1. The notations used in the table were suggested by Sharp *et al.* (Sharp et al., 1966), where α is a fraction of progressing

conversion, and function $F(\alpha)$ is an integrated form of the reaction models which depends on the mechanism controlling the reaction, and on the size and shape of the reacting particles. Most of the equations are in the form of $F(\alpha)=(k/r_0^2)\cdot t$, where k is the process rate constant, r_0 is the original radius of the particle. In Kröger and Ziegler's equation, the form is $F(\alpha)=k\cdot lnt$, meanwhile it is $F(\alpha)=k\cdot t$ in Avrami-Erofeev's equation. Assumptions used in the equations are presented in the Table 1.

Table 1. Selected kinetics equations that are used in the current work.

$F(\alpha)$	**Model**	**Assumption of the model**
α^2	One-dimensional	A diffusion-controlled reaction follows the parabolic law, in which the rate of the solid reactant consumption is inversely proportional to the thickness of shell product (Pieraggi, 1987).
$(1-\alpha)\ln(1-\alpha)+\alpha$	Two-dimensional	The equation assumes that the gas or liquid reactant diffuses through a cylindrical surface, in which the thickness of the shell increases as the reaction progress (Holt et al., 1962).
$\left[1-(1-\alpha)^{1/3}\right]^2$	Jander (three-dimensional)	Jander (Jander, 1930) derived a kinetic equation for diffusion-controlled reaction of a spherical particle from the parabolic law, however, Jander used a plane surface (one-dimensional) as the basis of the assumption, which later has been criticized by some researcher.
$1-3(1-\alpha)^{2/3}+2(1-\alpha)$	Ash layer controls (shrinking core model)	The equation considers the flux relationship in a partially reacted spherical particle using Fick's law, and the thickness of the ash layer with the rate of diffusion (Levenspiel, 1999). However, as in Jander equation, the ash layer controls model considers the total volume of the unreacted part and the product is equal to the initial volume of the solid reactant.

$\left[1-\left(2\alpha/3\right)\right]-(1-\alpha)^{2/3}$	Ginstling - Brounshtein	Ginstling and Brounshtein (Ginstling and Brounshtein, 1950) stated that the Jander equation is oversimplified and holds only at low conversion values, i.e. low α. They introduced Fick's first law of steady-state solution for radial diffusion in a sphere to the parabolic law's equation.
$\left[1/\left((1-\alpha)^{1/3}-1\right)\right]^2$	Zhuravlev, Lesokhin and Templeman	The equation is a modification of Jander equation by assuming that the activity of the reacting substance is not constant. It is proportional to the fraction of unreacted material $(1-\alpha)$ (Dickinson and Heal, 1999).
$\left[1-\left(1-\alpha\right)^{1/3}\right]^2$	Kröger and Ziegler	Kröger and Ziegler (Kroger and Ziegler, 1954) proposed the equation by integrating the diffusion equation of a sphere particle, and equating it with the fraction of unreacted solid reactant on volume basis. Their main assumption is that the rate of product layer growth is inversely proportional to the product thickness and time.
$-\ln(1-\alpha)$	Avrami-Erofeev	Avrami-Erofeev equation is not based on a diffusion-controlled reaction. The equation was based on the nucleation and nuclei growth of phases, in which the reaction rate is fast at the beginning of the growth and slows down as nuclei grow larger and impinge on one another.

4. Experimental Methodology

The experiments carried out in this study are elaborated in three different sections, i.e. slag preparation, description of the leaching setups, and techniques used to characterize the samples.

4.1. Slag preparation

The starting material used in this work is a slag that was produced from a smelting-reduction process of a low-grade bauxite from our previous work (Azof et al., 2018). The low-grade bauxite was mixed with lime in a ratio of CaO/Al_2O_3 equals to 1.0. The ratio was chosen so that the produced slag would have leachable phases in a sodium carbonate solution as claimed in literature (Blake et al., 1966). Based on an X-Ray Diffraction (XRD) analysis, the slag consists of C12A7 as the major phase, including CA and C5A3 as the minor phases. The chemical composition of the low-grade bauxite and the produced slag were analysed by X-Ray Fluorescence (XRF) and the results are shown in Table 2.

Table 2. Normalized XRF Analysis of the Low-grade bauxite and the produced slag.

Materials	**Constituents (wt.%)**					
	Al_2O_3	**CaO**	**SiO_2**	**TiO_2**	**Fe_2O_3**	**MgO**
Low-grade bauxite	65.4	4.4	4.1	3.2	22.7	0.2
Slag	46.1	48.1	2.3	1.8	0.9	0.5

Due to a practical reason, we need to use a relatively fine size of slag for the leaching experiment. Therefore, the slag was ground with Retsch™ ring mill for 30 seconds in 700 rpm. The size distribution of the slag was then measured by using Horiba™ LA-960 in a wet analysis, which was isopropanol based with refractive index of 1.378.

4.2. Leaching setups and characterization techniques

There are two different leaching setups used in the current work. First, a setup for the leaching kinetics observation. And, the second setup is for the investigation of the leaching mechanism.

4.2.1. leaching kinetics experimental setup

In the kinetics experiment, 10 g of slag was leached with 200 mL of Na_2CO_3 solution in a borosilicate glass at 30, 45, 60, and 90 °C. No silicon contamination from the glass container was detected on the blank solution. Furthermore, 3 and 10 wt.%Na_2CO_3 solvent concentrations were chosen to observe different concentrations effect to the aluminum recovery. The first concentration represents the Pedersen original leaching process (Pedersen, 1927). Whereas, the latter was chosen according to our

unpublished preliminary trials.

The ratio of solid to liquid is 5 % in mass, and is assumed constant throughout the leaching treatment, as the water evaporation was considered small; less than 10%. The solid and liquid were stirred at 60, 150, and 300 rpm using a magnetic bar stirrer. The leaching time was up to 90 min, and during the leaching 3 ± 0.3 mL of the solution were taken as a sample in different periods. The samples were filtered by using a Büchner funnel and an ashless grade of quantitative filter paper, which then separated the liquor and the solid (grey mud). Also, for the kinetics experiment in a 3 wt.%Na_2CO_3 solution, forty PTFE-balls with a diameter of 6 mm were used to increase the agitation and collision effects. A schematic figure of the leaching setup is shown in Fig. 3.

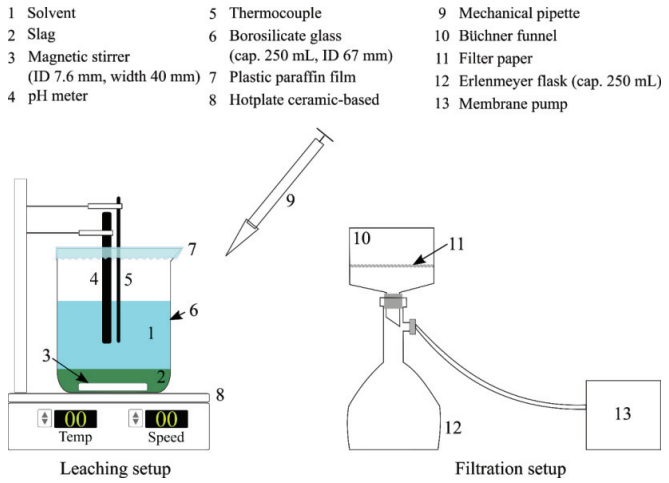

Fig. 3. A schematic of the leaching of the slag using a hotplate ceramic-based and solid-liquid filtration using a Büchner funnel and Erlenmeyer flask.

The chemical compositions of the liquors were analysed using Inductively Coupled Plasma-High Resolution-Mass Spectroscopy (ICP-HR-MS) Agilent 8800™. On the other hand, the grey mud was qualitatively analysed using Bruker D8 A25 DaVinci™ XRD machine with CuKα radiation, between 10 and 75° diffraction angle, 0.01° step size, and 2.5° for both primary and secondary soller slit.

Moreover, we used some digestion reactors that can be shaken to elucidate the effect of various agitation mechanisms on the progress of leaching reactions. A digestion reactor is a Polytetrafluoroethylene (PTFE)-base with the capacity of 45 mL and covered with stainless steel as the outer body. It was placed on a tilting plate that can move ±

45°from the horizontal situation, which gives a shaking effect to the solution inside the reactor. Both the reactor and the plate were installed inside of an oven that can be run under controlled temperature as shown in Fig. 4.

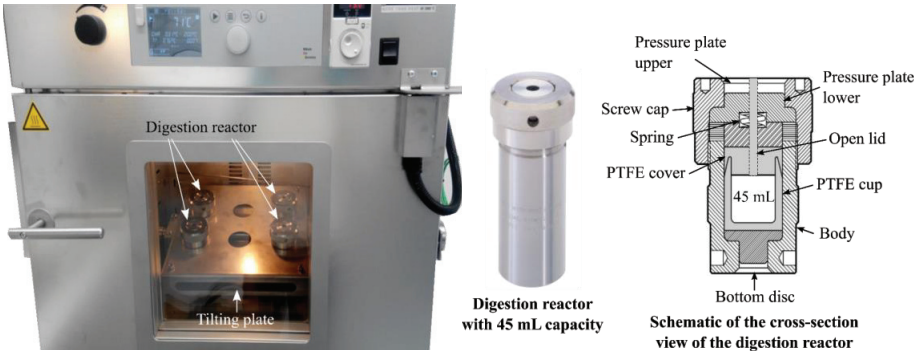

(a) (b)

Fig. 4. (a) Digestion reactors are placed on a plate that can be tilted ± 45° in an oven that gives a shaking effect to the solution. (b) Image of the digestion reactor with 45 mL capacity and the schematic of its cross-sectional view.

4.2.2. leaching mechanism experimental setup

In the current setup, the objective is to study the leaching mechanism and the growth of the solid product (calcium carbonate) that occurs on slag's surface while it is being exposed to Na_2CO_3 solution. To achieve that, we submerged the polished slag, which was previously cast into a resin, into a 10 wt.% Na_2CO_3 solution for short intervals, while the solution was stirred by a magnetic stirrer at 300 rpm. The leaching setup is shown schematically in Fig. 5.

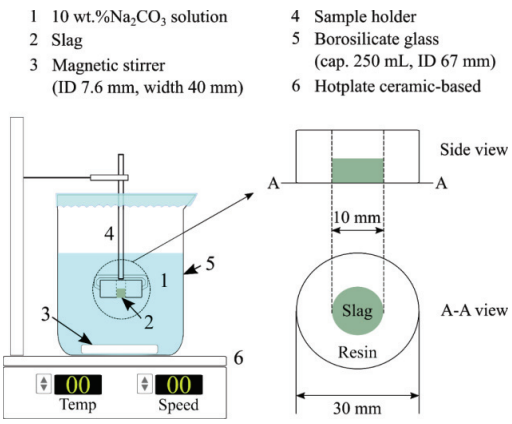

Fig. 5. Leaching mechanism experimental setup.

The morphology of the surface of the slag was investigated using Hitachi SU6600™ Scanning Electron Microscope (SEM) after 30 sec, 1, 5, 10, and 60 min of the leaching treatment. Furthermore, the elemental mapping and chemical composition of the observed phases were studied by X-Ray element mapping and Energy Dispersive Spectroscopy (EDS) in the SEM.

5. Results and Discussion

Results of five different subjects are presented and discussed in the current section; characteristics of the slag, aluminum recovery extent, pH property and thermochemical reactions, leaching kinetics, and characteristics of the leached surface of the slag in different durations.

5.1. Characteristics of the slag

Typical Back-Scattered Electron (BSE) images of the cross-section of the slag at 500× and 1500× magnifications are shown in Fig. 6. Due to the different contrast (light and dark) displayed on the image, at least two distinct phases co-exist and can be identified from the slag. As shown previously in Table 2, the slag has Ca and Al as the dominant elements, and Si and Ti as the minor ones. The light contrast represents a dense phase that may consist Ca-Al-Si-Ti elements. Whereas, the darker one represents a lighter phase that only may have Ca-Al elements, which is the major phase, the C12A7 phase.

Also, Fig. 7 shows the X-ray mapping of major elements in the dashed-square area of the slag. It shows that the phase with light contrast has more of Al, Si, and Ti than the darker one. This phase is an unleachable phase in Na_2CO_3 solution (in the applied

conditions); therefore, for further notation, we use unleachable phase to refer this phase.

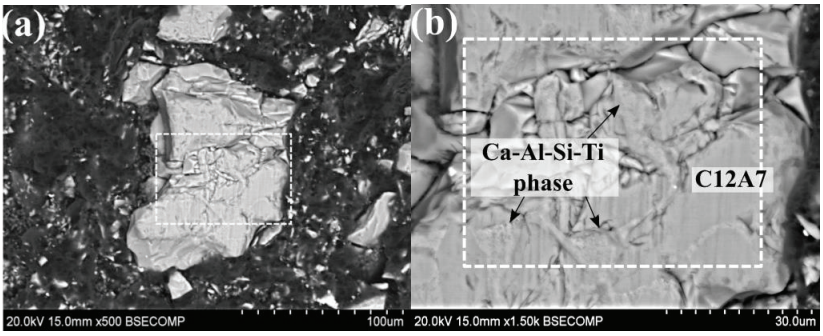

Fig. 6. BSE images of the cross-section of slag at (a) 500× magnification and (b) 1500× magnification.

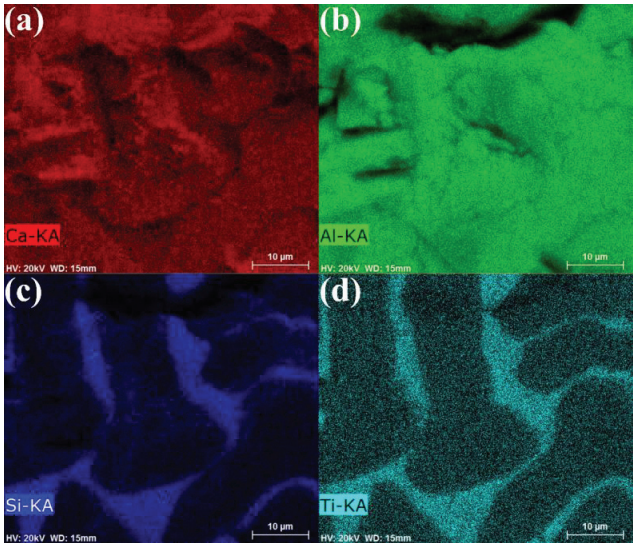

Fig. 7. X-ray mapping elements of the white-dashed square of the slag cross-section in Fig. 6 that shows (a) calcium, (b) aluminum, (c) silicon, and (d) titanium-rich areas.

The size distribution of the ground slag is shown in Fig. 8. The size is less than 100 μm, which is considered as fine particle. Based on the size distribution wet analytical results, the value of D_{10}, D_{50}, and D_{90} of the slag are 7.3, 21.2, and 56.5 μm, respectively.

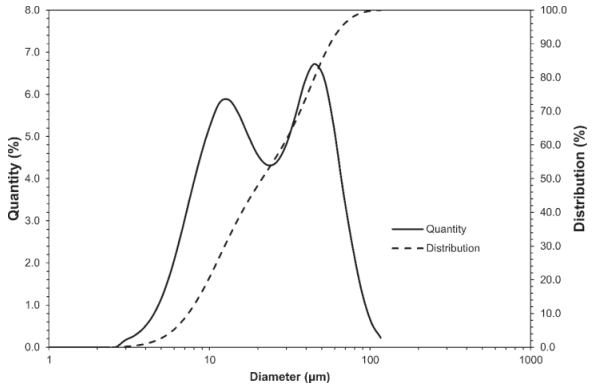

Fig. 8. Size distribution of the slag.

5.2. Aluminum recovery extent

We investigated the effects of different leaching conditions to the aluminum recovery extent, which are temperature, Na_2CO_3 concentration, stirring rate and particle collision.

5.2.1. The effect of temperature and Na_2CO_3 concentration

Fig. 9 shows the effect of different leaching temperatures, 30 and 45 °C, to the aluminum recovery extent, which uses 10 wt.%Na_2CO_3 concentration, at 300 rpm of stirring rate, and in 90 min of leaching time. As seen, the recovery from the slag is considerably high even in the short leaching times, i.e., 15 min; 75 % on 30 °C-sample, and 81.8 % on 45 °C-sample, on average. The result indicates that the leaching reaction starts immediately as the surface of slag is contacted with the solution. The recovery increases slowly as the leaching time progresses. After 90 min of the treatment, the recovery is 90.3 % and 88 % for 30 and 45 °C, respectively. However, as the deviation bar of 45 °C-sample at 90 min is ± 13 %, this suggests that it is possible to recover almost all the soluble aluminum from the slag, except the small portion in the minor unleachable phase. We may conclude that by 10 wt.%Na_2CO_3 solution, the recovery increases 8 – 10% as the temperature rises from 30 to 45 °C.

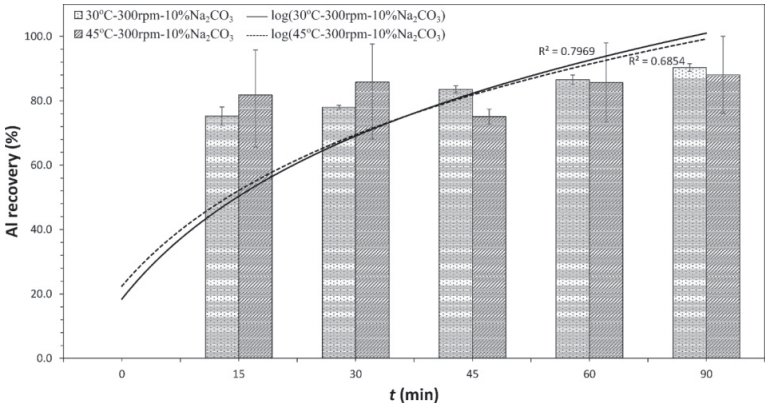

Fig. 9. Aluminum recovery (%) as a function of time (min) at 30 and 45 °C of leaching temperature with following conditions: 300 rpm of stirring rate, use of magnetic stirrer, and 10 wt.% Na_2CO_3 of the solvent's concentration.

Fig. 10 shows the aluminum recovery (%) as a function of time at 45 and 90 °C in leaching trials that 3 wt.%Na_2CO_3 was used as the solvent, at 300 rpm of stirring speed, and as an addition to the magnetic bar stirrer, PTFE-balls were also used to strengthen the agitation. The recovery difference is significant between the two temperatures. At 5 min, the recovery is 56.1 and 74.7 % for 45 °C and 90 °C-samples, on average. The recovery increases slowly as the leaching time progresses, which is like what was occurred on the previous leaching conditions using 10 wt.%Na_2CO_3. At the same solvent and stirring conditions, the recovery increases 43 %, on average, as the leaching temperature rises from 45 to 90 °C. Furthermore, as is seen in Fig. 10, the recovery percentage of 45 °C-sample from 3 wt.%Na_2CO_3 solution is lower compared with that in 10 wt.%Na_2CO_3 solution (Fig. 9). At 30 min, the recovery of 45 °C-sample is 54.8 % in 3 wt.%Na_2CO_3 and 85.8 % in 10 wt.%Na_2CO_3 solution. On average, the recovery increases by 46 % as the Na_2CO_3 concentration changes from 3 to 10 wt.%Na_2CO_3.

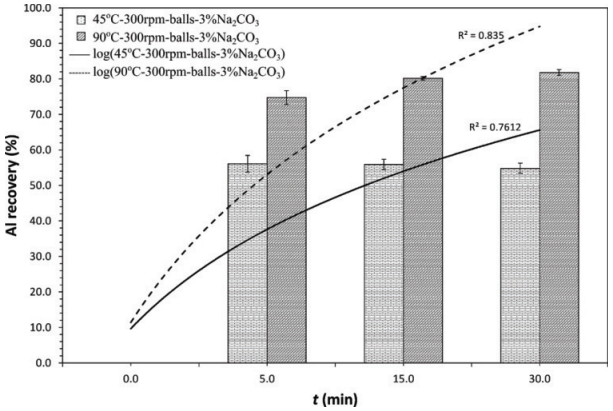

Fig. 10. Aluminum recovery (%) as a function of time (min) at 45 and 90 °C of leaching temperature with following conditions: 300 rpm of stirring rate, use of magnetic stirrer and PTFE-balls, and 3 wt.% Na_2CO_3 of the solvent's concentration.

5.2.2. The effect of stirring speed and particle collision

The slags were leached on different stirring speeds at 45 °C in 10 wt.%Na_2CO_3 solution. The order from the strongest to the mildest agitation is 300 rpm, 60 rpm, and 50 shakings per min (spm). The first two experiments were performed on the hotplate ceramic-based, while the latter was performed on the digestion reactor using the tilting plate. Furthermore, Fig. 11 shows that within the same leaching time, the highest recovery is achieved from the most vigorous agitation. On the other hand, the mildest one results on the lowest recovery.

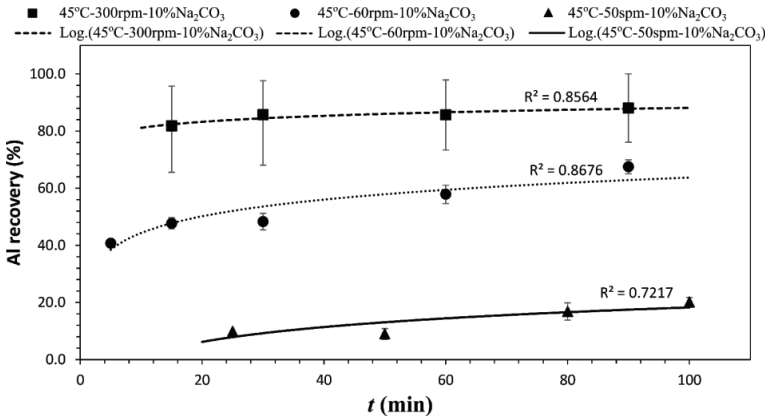

Fig. 11. Aluminum recovery (%) as a function of time (min) at 45 °C of the leaching temperature at different stirring rates in 10 wt.%Na_2CO_3 of the solvent concentration.

It was shown before (Azof et al., 2019b) that the grey mud tends to agglomerate when the leaching was performed in a mild agitation. The crystalline bridges induced by calcite crystal growth causes the agglomeration, which leads to a hard cement-like particle. The cross-section observation of the grey mud residue (Azof et al., 2019b) also proved that the calcite formation and growth on the slag particles might hinder the contact between Na_2CO_3 and the soluble calcium aluminate phases. Therefore, following the result in Fig. 11, it shows that the agitation using a magnetic bar stirrer at higher rate increases the possibility of the collision between both particles and stirrer that breaks the calcite layer, yielding less grey mud agglomeration, which results in better recovery compared to the slow and mild agitations.

5.3. The pH property and thermochemical reactions during the leaching

The pH and temperature measurements on one of the leaching trials at 45 °C, at 150 rpm, in 10 %Na_2CO_3 solution is shown in Fig. 12. The experiment was intended to elucidate the leaching effects on the pH property of the solution and its thermochemical reactions. The notations in the figure is described in Table 3.

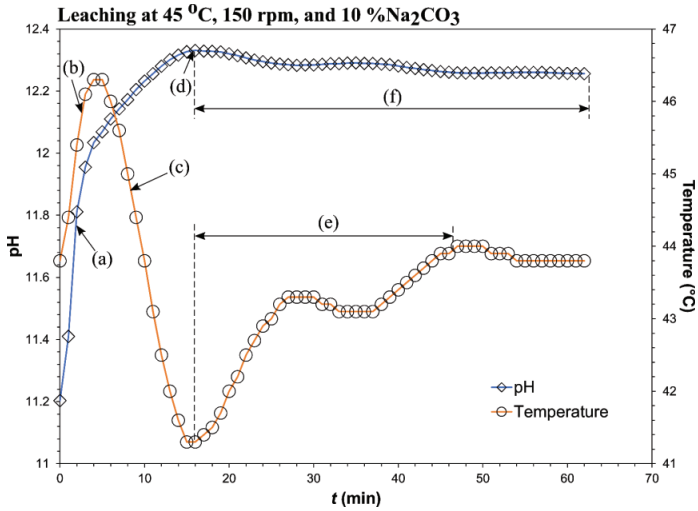

Fig. 12. The pH and temperature (°C) measured of the leaching solution as a function of time (min). The description of notations is presented in Table 3.

Table 3. Description of the Notations in pH and Temperature Measurement.

Notation	Description
(a), (b)	Showing an immediate increase of pH and temperature at the beginning (< 5 min). According to the leaching reaction (2), a reaction between one mole of C12A7 and ten moles of Na_2CO_3 produces 10 moles of NaOH, which is a strong alkali compound that increases the pH. On the other hand, an exothermic reaction between aqueous AlO_2^- and Na^+ phases that produces $NaAlO_{2(aq)}$ as in Equation (3), explains the rise in temperature. $AlO^-_{2(aq)} + Na^+_{(aq)} = NaAlO_{2(aq)}$ (3) $(\Delta H^\circ_{25°C} = -0.9 \text{ kJ/mol} NaAlO_2)$
(c)	Indicating the decrease of temperature as the endothermic reaction, which is shown in Equation (4), starts to occur. In the meantime, the dissolution of soluble C12A7 phase continues as the pH remains increasing at this period (5 – 15 min). $Ca^{2+}_{(aq)} + CO^{2-}_{3\ (aq)} = CaCO_{3(s)}$ (4) $(\Delta H^\circ_{25°C} = 13.6 \text{ kJ/mol} CaCO_3)$
(d)	The highest point of the pH in the reaction is obtained. It occurs after 15 min of leaching. The point also marks the steepest drop of temperature (about 5 °C) and indicates that the leaching reaction (2) may have reached its equilibrium.
(e)	The temperature of the solution increases as the heat supplied by the hotplate rises to target the set point. The hotplate increases the heat of the solution as the temperature was dropped and is lower than its set point.
(f)	Indicating the plateau of the pH as the leaching reaction goes considerably slow. The small changes in the pH are influenced by the correction of the temperature and slow leaching reactions.

5.4. Residue characteristics and the reacting slag surface

Samples of the solid residue (grey mud) were taken after 5, 15, 30, 45, and 60 minutes of leaching at 45 °C, 300 rpm of stirring rate, in 3 wt.%Na_2CO_3 solution. Fig. 13 shows the normalized XRD patterns obtained of samples, which are compared with the unleached slag. As seen, after 5 min of leaching, the calcite exists in the grey mud as the major phase. Other minor phases in the grey mud are C12A7, C5A3, and aragonite (another polymorph of $CaCO_3$). The CA peaks are relatively low and nearly undetected in the grey mud, as it may have already leached.

Another distinct pattern that can be seen from the XRD result is the C12A7 phase, and the intensity of peaks are decreased as the leaching progresses, indicating that the dissolution proceeds, as the calcite nucleates.

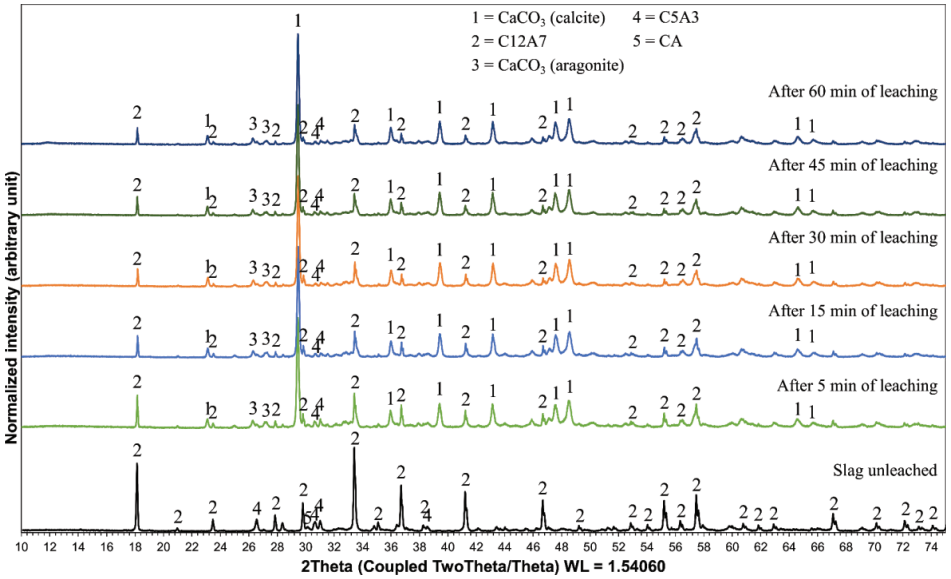

Fig. 13. Normalized XRD patterns of the slag and leached slag within 5, 15, 30, 45, and 60 min at 45 °C, 300 rpm of stirring rate, and 3 wt.%Na_2CO_3 of solvent concentration.

The SEM images of the surface of the slag after being exposed in 10 wt.%Na_2CO_3 solution for 30 sec, 1, 3, 5, and 10 min are shown in Fig. 14. The instrument setup used for the experiment was schematically shown earlier in Fig. 5. Based on the above results and these SEM observations, the leaching mechanism can be described as follows:

(a) The 30-sec images in Fig. 14(a) show that calcite crystals (1 ± 0.5 μm) are nucleated at the surface of unleachable phase. The unleachable phase acts as a precursor of the calcite. And, the topological difference between the surface of C12A7 (slag matrix) and unleachable phase indicates that the C12A7 phase is being depolymerized and dissolved into the solution. Some microcracks on the surface of the matrix are also apparent.

(b) Within 1 min leaching, more calcites are nucleated at the surface of the unleachable phase and in boundaries between resin and slag (see Fig. 14(b)), in which the sites are considerably more stable than C12A7. Meantime, the topological surface between C12A7 and unleachable phase looks more distinct than before.

(c) As shown in Fig. 14(c), after 3 – 5 min leaching the calcite grows up to 100 – 150 % of its previous size. The cracks on C12A7 surface, which are resulted from the leaching, are seemed to be more apparent. Some locations in the

matrix are probably more susceptible to the dissolution, or dissolution occurs in preferred directions of the C12A7 crystal.

(d) The calcites have covered all the available surface of the slag as shown in Fig. 14(d) after 10 min of leaching due to the precipitation, growth, and accumulation of the calcite crystals in plates parallel to the reacting surface. At this period, the rate of leaching reactions might decrease significantly as the calcite is an inert phase and C12A7 phase is not much in direct contact with Na_2CO_3 solution. The calcites growth and networking behavior are similar with the literature observation after Nancollas (Nancollas and Reddy, 1971).

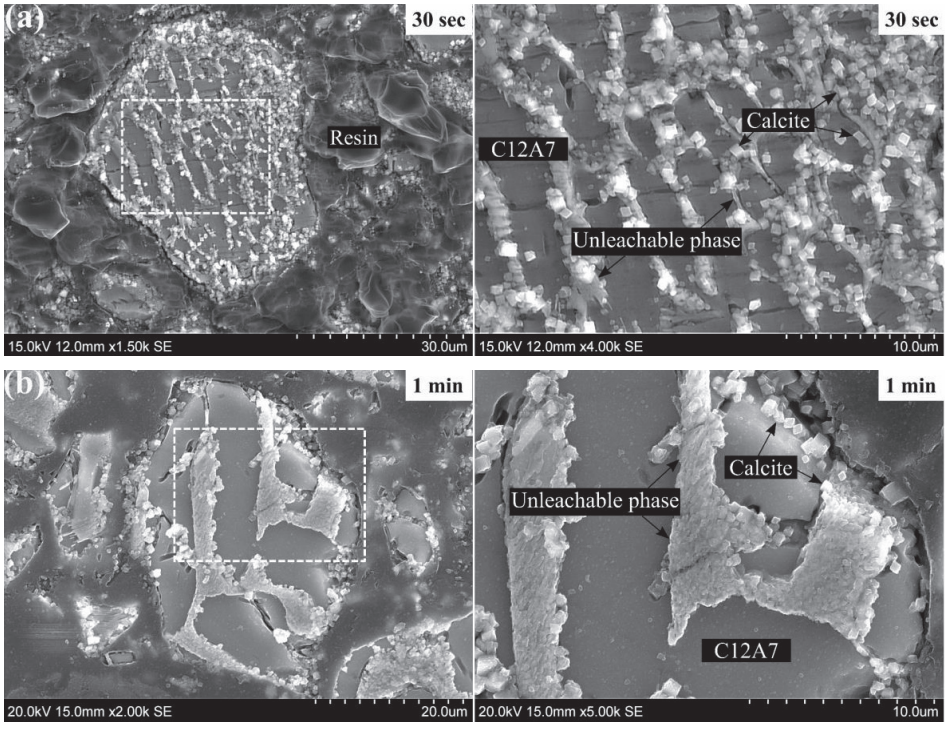

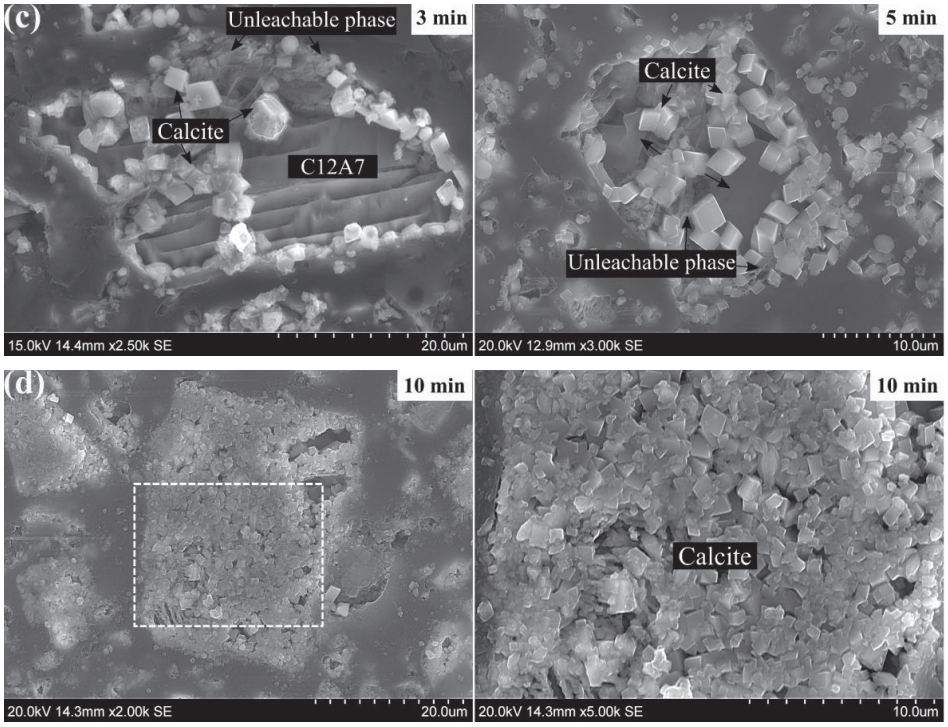

Fig. 14. SEM images of the surface of slag after being exposed to 10 wt.%Na_2CO_3 solution for (a) 30 sec at 1500× and 4000× magnifications, (b) 1 min at 2000× and 5000× magnifications, (c) 3 and 5 min at 2500× and 3000× magnifications, respectively, and (d) 10 min at 2000× and 5000× magnifications.

In addition to the surface morphologies described above, a BSE image and EDS spectrum on the surface of slag after 1 min leaching are shown in Fig. 15(a) – (c). The EDS of points 1 – 4 shows high Ca-Al-Si-Ti-O intensities, which indicates that the observed points are on the unleachable phases. Meanwhile, the EDS of points 5 – 8 show that this phase is C12A7 as only Ca-Al-O intensities are noticeable. The composition of the slag based on EDS point analysis is presented in Table 4.

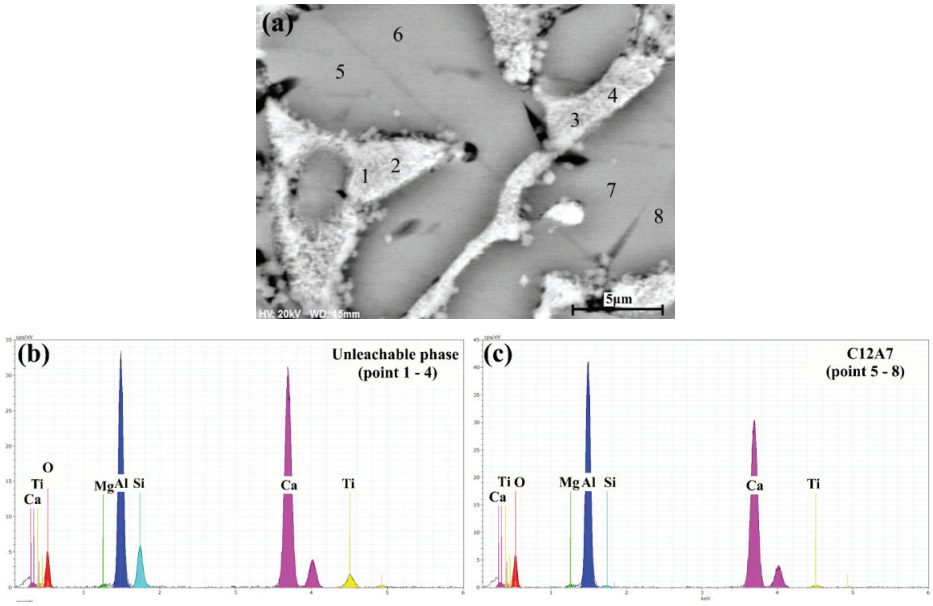

Fig. 15. (a) BSE image of the surface of slag after 1 min of leaching treatment, and the EDS spectrum of (b) unleachable phase, and (c) the C12A7 phase.

Table 4. Composition of the slag based on EDS point analysis in Fig. 15.

Point	Ca (wt.%)	Al (wt.%)	Si (wt.%)	Ti (wt.%)	Mg (wt.%)	O (wt.%)
1 – 4	37.4	22.7	3.9	3.0	0.3	32.8
5 – 8	38.6	30.2	0.3	0.6	0.4	30.1

Also, an X-ray mapping of the slag's surface shown in Fig. 15(a) is provided in Fig. 16. As seen, the extent of silicon and titanium concentrations on the unleachable phase are higher than that of the matrix. On the other hand, the extent of calcium and aluminum concentrations on the unleachable phase are less than that of the matrix, which correlates with the EDS point analysis (Fig. 15). Furthermore, it was shown previously in Fig. 14 that calcite particles nucleated on the surface of the unleachable phase shortly after the leaching starts. However, the calcites are hardly recognizable both in EDS point analysis and X-ray mapping results due to thin thickness.

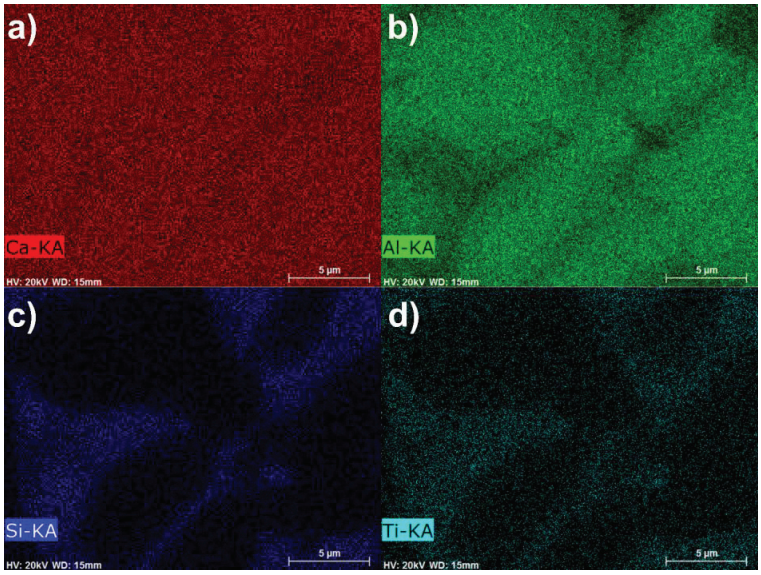

Fig. 16. X-ray mapping element of the surface of slag after 1 min of leaching.

Based on the obtained results, in Fig. 17 we illustrate the mechanism of calcite nucleation and growth on the slag during the leaching of C12A7 in Na_2CO_3 solution from cross-section view. In the beginning of leaching, the mass transfer rate is distinctly high. Meantime, calcite crystal starts to nucleate at the unleachable phase as a proper location and also in a short distance for ions transfer that the reaction proceeds. Thus, when the calcite grows simultaneous with the leaching of the C12A7, the calcite growth occurs in the both directions from over the unleachable phase; in vertical direction to the slag surface and in parallel direction to the slag surface. The latter growth is accompanied with the coverage of the leachable C12A7 phase which eventually covers the entire slag surface. Hence, after the growth of the calcite the leaching reaction is reduced due to less contact between the slag and the solution, and in long reaction times the mass transfer rate is significantly low. Obviously, when the surface is mostly covered by the calcite, the diffusion of the reacting aqueous phases (Ca^{2+}, AlO_2^-, Na^+, CO_3^{2-}) through the product calcite layer controls the rate of reaction.

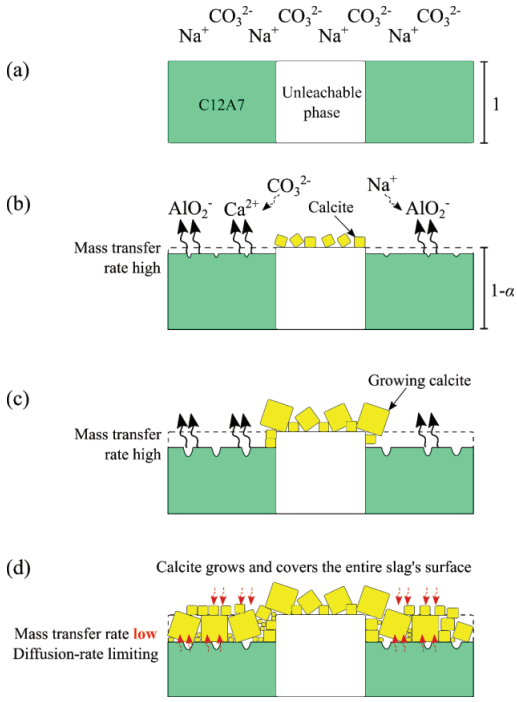

Fig. 17. A cross-section view of calcite formation's mechanism during the leaching of C12A7 in Na_2CO_3 solution.

5.5. Leaching kinetics of the reacting slag

5.5.1. Diffusion models

As described previously on the section 3, α is the fraction of reaction conversion. In the current study, it is convenient to denote the yield of aluminum recovery (%) as the reaction conversion (α). Furthermore, we may plot the integrated form of reaction models, ($F(\alpha)$), against the leaching time from different conditions, as shown in Fig. 18(a) – (c).

In Fig. 18(a) the model of Zhuravlev, Lesokhin, and Templeman (ZLT) and Ginstling – Brounshtein (GB) have a positive correlation and closer interception to the origin, compared with the other models. On the other hand, Fig. 18(b) and (c) show that the model of GB-equation fits better than the other models. These results are in accordance with our previous work, which suggested that GB-equation is one of the most fitted equations for the leaching of the calcium aluminate slag (Azof et al., 2019a).

ZLT model calculates the rate based on Jander-equation for spherical particles and considers that the concentration of penetrating species does not remain constant and is

proportional to the fraction of the unreacted conversion (1 – α). Meanwhile, GB does not consider the change of penetrating species concentration during the treatment. However, they had been derived by introducing the Fick's first law to the parabolic law's equation and been corrected the oversimplified "three-dimensional" calculation made by Jander (Khawam and Flanagan, 2006; McIlvried and Massoth, 1973).

It is worth to note that the slag particles in the present study do not have a spherical shape and are not uniform in size. The irregular shapes and distributed size, obviously, made the models less accurate. In addition, there is evidence from the results of pH property and thermochemical reactions (shown in section 5.3) that different mechanisms occurring during the leaching treatment. This causes that the model, which is only based on one controlled reaction, e.g., diffusion, does not properly fit for a complete leaching process.

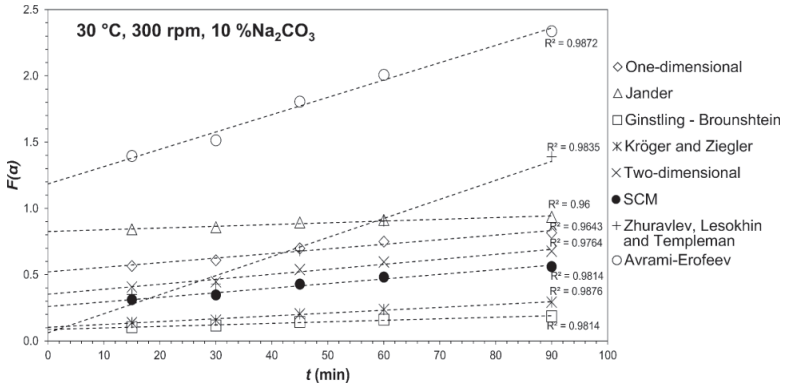

(a)

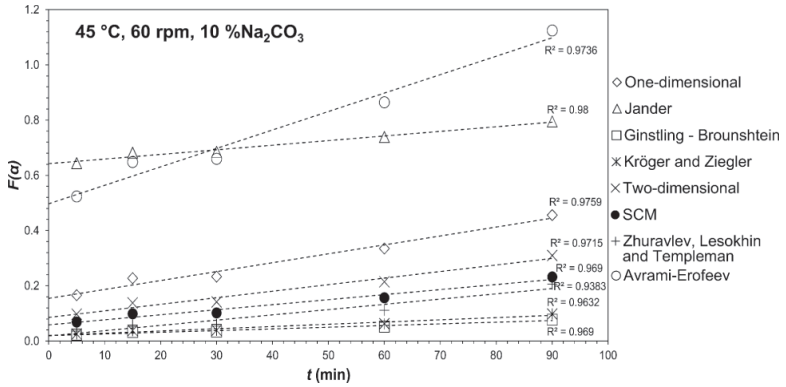

(b)

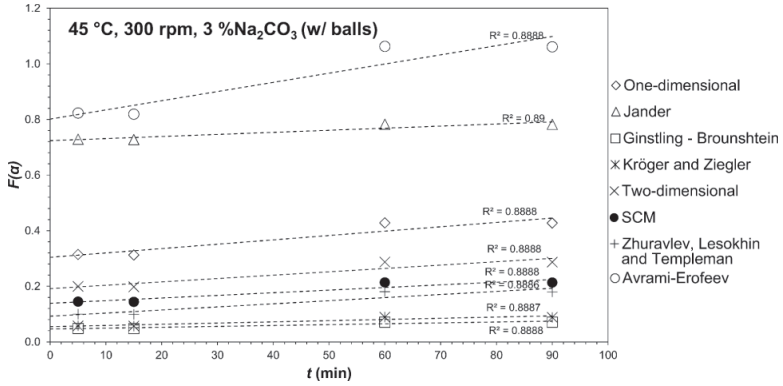

(c)

Fig. 18. Different kinetics rate modelling, *F(α)*, as a function of time (min) in different leaching conditions: (a) 30 °C, 300 rpm, 10 wt.%Na_2CO_3, (b) 45 °C, 60 rpm, 10 wt.%Na_2CO_3, (c) 45 °C, 300 rpm, magnetic bar and PTFE-balls as stirrer, and 3 wt.%Na_2CO_3.

5.5.2. Process rate

As discussed earlier, there are different mechanisms occurring throughout the leaching process. Different mechanisms attributed to different process rate constants. Based on the aluminum recovery extent and pH changes shown earlier in section 5.2 and 5.3., there are up to three different process steps that may occur in series during the leaching process:

1. The chemical reaction rate controlling step (denoted by k_{chem}) between the leachable phases and Na_2CO_3 solution at the surface of slag.
2. The penetration and diffusion of reactants (denoted by $k_{diff.react}$), i.e., Na^+, CO_3^{2-} , H_2O, to the unreacted slag (core) through the calcite layer
3. The outward diffusion of products (denoted by $k_{diff.prod}$), i.e., AlO_2^-, OH^-, through the calcite layer to the leachate. This step may also include the transport of the Ca^{2+}ions from the reaction interface to the proper site for the deposition of $CaCO_3$.

According to Levenspiel (Levenspiel, 1999), we may account the simultaneous steps above as an individual resistance occurring in the process because it is not reasonable to consider that one step controls throughout the whole process, as observed in the present study. At the beginning of leaching process, the calcite does not nucleate at the reacting surface. Therefore, $k_{diff.react}$ and $k_{diff.prod}$ do not exist. Meanwhile, k_{chem} accelerates relatively fast. However, as the calcite layer appears on the reacting surface,

the k_{chem} is decreased, and $k_{diff.react}$ and $k_{diff.prod}$ become progressively more critical. Thus, by eliminating the intermediate concentrations difference between these steps, we can straightforwardly combine the rate constant as an apparent process rate constant ($k_{overall}$) as shown in Equation (5):

$$\frac{1}{k_{overall}} = \frac{1}{k_{chem}} + \frac{1}{k_{diff.react}} + \frac{1}{k_{diff.prod}} \quad (5)$$

Based on the pH measurement in Fig. 12 and SEM results in Fig. 14, we suggest that the k_{chem} value is obtained as the leaching reaction starts. And the rate is expected to decrease significantly after 15 minutes of leaching, as the calcite layers completely cover the slag surface. Subsequently, the reaction is diffusion-controlled as it is mainly dependent on the $k_{diff.react}$ and $k_{diff.prod}$.

The value of k_{chem}^{-1} is suggested to be significantly low as the chemical reaction rate is immediate and, therefore, can be neglected. As the diffusion of reactant and product happen at the same time, it is difficult to separate $k_{diff.react}$ and $k_{diff.prod}$ values. We may use the GB-equation to calculate the $k_{overall}$ based on the experimental results on section 5.2 as shown in Table 5, and suggest that the sum of $k_{diff.react}^{-1}$ and $k_{diff.prod}^{-1}$ is the same as $k_{overall}^{-1}$. It is also worth to note that the diffusion rate of Ca^{2+} and AlO_2^- ions (products) eventually can go slower and slower than Na^+ and CO_3^{2-} ions (reactants), especially when the calcite layer builds upon the surface of the slag, which leads to the accumulation of Ca^{2+} and AlO_2^- ions beneath the calcite layers as illustrated previously in Fig. 17(d).

Table 5. Apparent Process Rate Constant that Corresponds to the Leaching Conditions.

Leaching conditions (temperature, stirring rate, Na_2CO_3 concentration)	Apparent process rate constant ($k_{overall}$)
45 °C, 300 rpm, 3 %	7×10^{-3}
90 °C, 300 rpm, 3 %	18×10^{-3}
30 °C, 300 rpm, 10 %	10×10^{-3}
45 °C, 300 rpm, 10 %	12×10^{-3}
45 °C, 60 rpm, 10 %	6×10^{-3}

As seen in Table 5, the rate of $k_{overall}$ increases with increasing of temperature, stirring rate, and concentration of Na_2CO_3. By increasing the leaching temperature 2

times, we may have up to 2.6 times higher rate, depending on solution concentration. And at the same temperature and stirring rate, we may have 1.7 times higher rate by increasing 3 times of the Na_2CO_3 concentration. Furthermore, as we observed that the leaching reaction rate is influenced by temperature, the relationship between the apparent process rate constant and temperature can be described using Arrhenius equation as given in Equation (6):

$$k_{overall} = A \times \exp\left[\frac{-E}{RT}\right] \tag{6}$$

Where A is a pre-exponential factor, E is the apparent activation energy, R is the universal gas constant 8.3145 J/mol·K, and T is the absolute temperature in K. The apparent activation energy can be calculated by plotting the natural logarithm of $k_{overall}$ against 1000/T as shown in Fig. 19 where the slope represents $-E/R$ ratio. The results show that the apparent activation energy for the leaching process at 3 wt.% and 10 wt.% Na_2CO_3 concentrations are 19.9 and 10.8 kJ/mol, respectively. The value of apparent activation energy is relatively low that supports our hypotheses that the reaction is a diffusion rate limiting. The result is in agreement with Tong and Li (Tong and Li, 2017) where they have calculated the apparent activation energy of a leaching reaction between calcium aluminate slag and Na_2CO_3. It is also confirmed by other studies that the apparent activation energy of hydrometallurgical reactions controlled by diffusion is either <15 kJ/mol (Free, 2013) or <40 kJ/mol (Jackson, 1986). Moreover, the pre-exponential factor is calculated by using Eq. (6), which is 1.18×10^{-2} /min, on average.

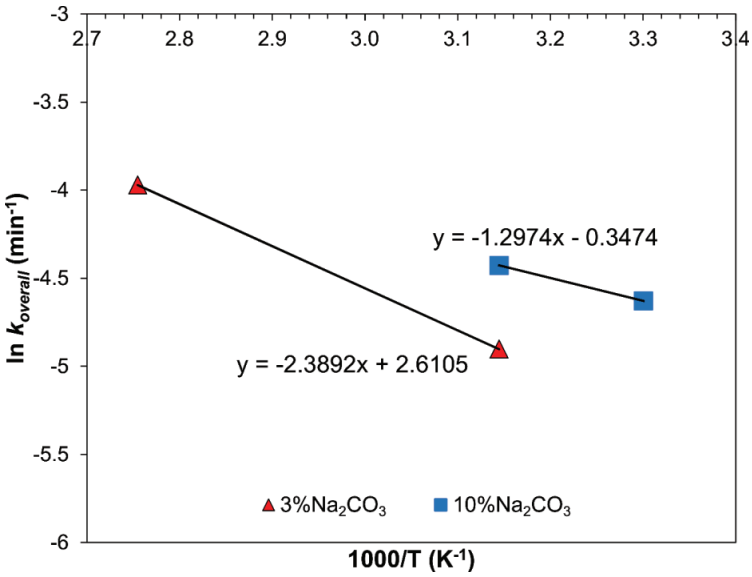

Fig. 19. Arrhenius plot of the slag dissolution at different leaching temperatures and solvent concentrations.

6. Conclusion

A series of leaching treatment of a calcium aluminate slag in Na_2CO_3 solution has been done. The observation on kinetics and leaching mechanism can be summarized as follows:

1. Leaching reactions between leachable phases, e.g. $12CaO{\cdot}7Al_2O_3$, $CaO{\cdot}Al_2O_3$, and Na_2CO_3 are relatively fast. High alumina recovery up to 90.5 % is obtained within 90 min after the slag is leached at 10 wt.% Na_2CO_3 solution, high stirring rates, at 30 – 45 °C.
2. The calcite phase as a solid product of the leaching reaction starts to nucleate at the surface of the adjacent unleachable phase in the slag. Calcite crystals can grow up to large sizes (over 10 micrometre) and bridging occurs between them (agglomeration tendency).
3. The use of stirrer and PTFE-ball during the leaching (wet-grinding) increases the collision frequency between both slag and stirrer that breaks the calcite layer and the agglomerates that leads to higher alumina recovery.
4. Different kinetic models were tried to find out the rate limiting step during the leaching and it was found that the process rate is controlled by the diffusion of reactant and product ions through the product calcite layer.

5. The calculated apparent activation energy of the leaching reaction is 10.8 – 19.9 kJ/mol. The values are relatively low that indicates the reaction is diffusion rate limited.

Acknowledgement

The NTNU has funded the research and the work was supported by the Research Domain 5 – Materials and the Society in SFI Metal Production (Project no. 237738). The support from the ENSUREAL project (EU Horizon 2020) is also acknowledged.

References

Azof, F.I., Kolbeinsen, L., Safarian, J., 2019a. Kinetics of the Leaching of Alumina-containing Slag for Alumina Recovery, in: Proceedings of EMC 2019. pp. 511–526.

Azof, F.I., Kolbeinsen, L., Safarian, J., 2019b. Kinetics of the Leaching of Alumina-containing Slag for Alumina Recovery, in: EMC 2019. Dussedorf, pp. 511–526.

Azof, F.I., Kolbeinsen, L., Safarian, J., 2018. Characteristics of Calcium-Aluminate Slags and Pig Iron Produced from Smelting-Reduction of Low-Grade Bauxites. Metall. Mater. Trans. B Process Metall. Mater. Process. Sci. 49, 2400–2420. https://doi.org/10.1007/s11663-018-1353-1

Azof, F.I., Kolbeinsen, L., Safarian, J., 2017. The Leachability of Calcium Aluminate Phases in Slags for the Extraction of Alumina, in: Travaux 46, Proceedings of 35th International ICSOBA Conference. ICSOBA, Hamburg, pp. 243–253.

Azof, F.I., Vafeias, M., Panias, D., Safarian, J., 2020. The leachability of a ternary CaO-Al2O3-SiO2 slag produced from smelting-reduction of low-grade bauxite for alumina recovery. Hydrometallurgy 191. https://doi.org/10.1016/j.hydromet.2019.105184

Azof, F.I., Yang, Y., Panias, D., Kolbeinsen, L., Safarian, J., 2019c. Leaching characteristics and mechanism of the synthetic calcium-aluminate slags for alumina recovery. Hydrometallurgy 185, 273–290. https://doi.org/10.1016/j.hydromet.2019.03.006

Blake, H.E., Fursman, O.C., Fugate, A.D., Banning, L.H., 1966. Adaptation of the Pedersen Process to the Ferruginous Bauxites of the Pacific Northwest, Bureau of Mines US Department of the Interior.

Dickinson, C.F., Heal, G.R., 1999. Solid–liquid diffusion controlled rate equations.

Thermochim. Acta. https://doi.org/10.1016/S0040-6031(99)00256-7

Free, M.L., 2013. Hydrometallurgy: fundamentals and applications. John Wiley & Sons, Inc., New Jersey.

Fursman, O.C., Blake Jr., H.E., Mauser, J.E., 1968. Recovery of Alumina and Iron from Pacific Northwest Bauxites by the Pedersen Process. Albany.

Ginstling, A.M., Brounshtein, B.L., 1950. Concerning the diffusion kinetics of reactions in spherical particles. Appli chem USSR 23, 1327–1338. https://doi.org/10.1007/10722086_4

Holt, J.B., Cutler, I.B., Wadsworth, M.E., 1962. Rate of Thermal Dehydration of Kaolinite in Vacuum. J. Am. Ceram. Soc. 45, 133–136. https://doi.org/10.1111/j.1151-2916.1962.tb11101.x

Jackson, E., 1986. Hydrometallurgical extraction and reclamation. Chichester: Ellis Horwood.

Jander, W., 1930. Reaktionen im festen Zustande bei höheren Temperaturen. Säureplatzwechsel bei einigen Wolframaten und Molybdaten. Zeitschrift für Anorg. und Allg. Chemie 190, 397–406. https://doi.org/10.1002/zaac.19301900139

Khawam, A., Flanagan, D.R., 2006. Solid-State Kinetic Models: Basics and Mathematical Fundamentals. J. Phys. Chem. B 110, 17315–17328. https://doi.org/10.1021/jp062746a

Kroger, C., Ziegler, G., 1954. Über die Geschwindigkeiten der zur Glasschmelze führenden Reaktionen. III. Reaktionsgeschwindigkeiten im Quarternären System Na2O-CaO-SiO2-CO2. Glas. Ber. 27, 199–212.

Levenspiel, O., 1999. Chemical Reaction Engineering-3rd edition. John Wiley & Sons, Inc.

McIlvried, H.G., Massoth, F.E., 1973. Effect of Particle Size Distribution on Gas-Solid Reaction Kinetics for Spherical Particles. Ind. Eng. Chem. Fundam. 12, 225–229. https://doi.org/10.1021/i160046a014

Miller, J., Irgens, A., 1974. Alumina Production by The Pedersen Process - History and Future, in: Forberg, H. (Ed.), Light Metals. pp. 977–982.

Nancollas, G.., Reddy, M.., 1971. The crystallization of calcium carbonate. II. Calcite growth mechanism. J. Colloid Interface Sci. 37, 824–830. https://doi.org/10.1016/0021-9797(71)90363-8

Nielsen, K., 1978. The Pedersen Process - An old process in a new light. Erzmetall 31, 523–525.

Pedersen, H., 1927. Process of Manufacturing Aluminum Hydroxide. 1618105.

Pieraggi, B., 1987. Calculations of parabolic reaction rate constants. Oxid. Met. 27, 177–185. https://doi.org/10.1007/BF00667057

Safarian, J., Kolbeinsen, L., 2016a. Sustainability in Alumina Production from Bauxite, in: Sustainable Industrial Processing Summit. pp. 75–82.

Safarian, J., Kolbeinsen, L., 2016b. Smelting-reduction of Bauxite for Sustainable Alumina Production, in: Sustainable Industrial Processing Summit. pp. 149–158.

Sellaeg, H., Kolbeinsen, L., Safarian, J., 2017. Iron Separation from Bauxite Through Smelting-Reduction Process, in: Minerals, Metals and Materials Series. pp. 127–135. https://doi.org/10.1007/978-3-319-51541-0_19

Sharp, J.H., Brindley, G.W., Achar, B.N.N., 1966. Numerical Data for Some Commonly Used Solid State Reaction Equations. J. Am. Ceram. Soc. 49, 379-. https://doi.org/DOI 10.1111/j.1151-2916.1966.tb13289.x

Tong, Z., Li, Y., 2017. Leaching Behavior of Alumina from Smelting Reduction Calcium Aluminate Slag with Sodium Carbonate Solution 37–43. https://doi.org/10.1007/978-3-319-51541-0

Tsesmelis, K., 2017. Bauxite Mine Rehabilitation & Bauxite Residue Management: A Global Perspective, in: Proceedings of 35th International ICSOBA Conference. ICSOBA, p. 71.

Vafeias, M., Marinos, D., Panias, D., Safarian, J., van Der Eijk, C., Solhem, Ingeborg; Balomenos, E., Ksiazek, M., Davris, P., 2018. From Red To Grey: Revisiting the Pedersen Process To Achieve Holistic Bauxite Ore Utilisation, in: Proceedings of the 2nd International Bauxite Residue Valorisation and Best Practices Conference. pp. 111–117.

Yagi, S., Kunii, D., 1955. Studies on combustion of carbon particles in flames and fluidized beds. Symp. Combust. 5, 231–244. https://doi.org/10.1016/S0082-0784(55)80033-1

ISBN 978-82-326-4516-9 (printed ver.)
ISBN 978-82-326-4517-6 (electronic ver.)
ISSN 1503-8181

NTNU
Norwegian University of
Science and Technology